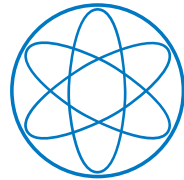


PHYSIK - DEPARTMENT



Development of a low level  
radioactive liquid scintillator and  
of the detector monitoring system  
for the JUNO neutrino experiment

DISSERTATION

VON

HANS THEODOR JOSEF STEIGER



TECHNISCHE UNIVERSITÄT  
MÜNCHEN

TECHNISCHE UNIVERSITÄT MÜNCHEN

Physik-Department  
Lehrstuhl für Experimentalphysik und Astroteilchenphysik

**Development of a low level radioactive liquid  
scintillator and of the detector monitoring  
system for the JUNO neutrino experiment**

Hans Theodor Josef Steiger

Vollständiger Abdruck der von der Fakultät für Physik der Technischen Universität  
München zur Erlangung des akademischen Grades eines

Doktors der Naturwissenschaften (Dr. rer. nat.)

genehmigten Dissertation.

Vorsitzender: Prof. Dr. Alejandro Ibarra

Prüfer der Dissertation:

1. Prof. Dr. Lothar Oberauer

2. Prof. Dr. Peter Fierlinger

Die Dissertation wurde am 26.02.2020 bei der Technischen Universität München  
eingereicht und durch die Fakultät für Physik am 15.06.2020 angenommen.

## Abstract

The Jiangmen Underground Neutrino Observatory (JUNO) is a 20 kton multi-purpose liquid scintillator detector currently being built in a dedicated underground laboratory in Jiangmen (PR China). JUNO's main physics goal is to determine the neutrino mass ordering using electron anti-neutrinos from two nuclear power plants at a baseline of about 53 km. JUNO aims for an unprecedented energy resolution of 3 % at 1 MeV in the central detector, with which the mass ordering can be measured with confidence level of  $3 - 4 \sigma$  within six years of operation. Most neutrino oscillation parameters in the solar and atmospheric sectors can also be measured with an accuracy of 1 % or better. Furthermore, being the largest liquid scintillator detector of its kind, JUNO will monitor the neutrino sky continuously for contributing to neutrino and multi-messenger astronomy. Moreover, JUNO will provide sensitivity in proton decay searches.

Within this thesis a brief overview on the historical milestones of neutrino physics is presented as well as the current knowledge about neutrino oscillations followed by the open questions in the field. After that, the physics goals and the technical design of the JUNO experiment are introduced. As the high-purity liquid scintillator and the liquid handling systems related to it are key technologies for the success of the experiment, this thesis is mainly focused on their development.

The liquid scintillator purification techniques which will be applied to the raw components of the liquid scintillator based on the solvent Linear AlkylBenzene are described in detail as well as their technical realization in purification facilities. Furthermore, an overview on a prototype testing phase with smaller pilot facilities built up at the Daya Bay experimental site is given here as well. One of the Daya Bay antineutrino detectors was filled with  $\sim 24$  t of scintillator produced in the pilot plants. Moreover, a report on the studies of the scintillator purity and performance using the detector can be found in the text.

Based on the experiences from the pilot plant phase, the design of an online monitoring detector (with approximately the size of a Daya Bay antineutrino detector) for the radiopurity of the LS was carried out. The purpose of this detector called OSIRIS (Online Scintillator Internal Radioactivity Investigation System) are measurements of the LS internal radioactivity during the commissioning of the purification plants, LS production phase and the filling of JUNO. OSIRIS which can be placed in the underground liquid scintillator hall at JUNO's experimental site is described in this thesis with a special emphasis on its technical design features.

Since precise handling of the liquids in the detector and the storage tanks requires a precise monitoring of liquid levels, hydrostatic pressures and temperatures requires dedicated sensors, development and characterization of them was a part of the PhD project summarized in this thesis. A test stand for hydrostatic pressure sensors is presented which was set up in the liquid scintillator pit of the shallow underground

---

laboratory in Garching. Furthermore, the thesis contains a report on the characterization of two possible sensor types for the JUNO experiment and OSIRIS. Beyond that, test measurements with a contact-less optical liquid level sensor based on an IR laser distance meter with a precision better than  $\pm 10$  mm over distances up to 50 m are presented. In addition to these developments also a prototype temperature sensor grid based on PT-1000 resistance thermometers is introduced, which was designed to meet the requirement of OSIRIS's liquid handling system prototype currently under construction at the Johannes Gutenberg-Universität Mainz.

For the filling and operation of JUNO, OSIRIS and the LS purification plants pressurized nitrogen will be used. To avoid a contamination of the LS with radon, its content in the nitrogen gas will be monitored. For this purpose an alpha spectrometer in form of a large volume (42.3 l) proportional chamber operated in pure nitrogen will be presented. To efficiently reduce backgrounds in the detector, pulse shape analysis techniques were developed and the pulses' risetimes were identified as powerful cut parameter. With the system sensitivities for the  $^{222}\text{Rn}$  activity below  $2 \text{ mBq/m}^3$  within a 10 h lasting screening measurement was achieved.

The precise knowledge of the scintillator properties is crucial for the interpretation of JUNO's data. Therefore, investigations LS samples were characterized in laboratory measurements using custom-designed experiments. For instance, it is essential to know the typical scintillation quenching and pulse shape for different particle interactions. The pulse shape discrimination (PSD) performance of a liquid scintillator is closely related to differences in the time spectrum of the photon emission of the LS for different particle species. The precise knowledge of the fluorescence time spectrum is a necessity for the implementation of a realistic scintillation model in the global JUNO simulation framework. Furthermore, this knowledge is crucial for event position reconstruction algorithms and tuning of pulse shape analysis algorithms. Beyond that, the fluorescence decay times are highly affecting JUNO's sensitivity in the proton decay search for the channel  $p \rightarrow K^+ + \bar{\nu}$ , since the expected signal shows a narrow double peak structure in time, which could only be resolved with a fast scintillator. To study the fluorescence decay time spectra for gamma and neutron interactions an experimental setup was developed at the Tandem Accelerator of the Maier Leibnitz Laboratorium allowing an irradiation of the LS with a pulsed neutron beam. The decay time spectra were measured within two beamtimes in 2019 for the current JUNO LS mixture. It showed excellent pulse shape discrimination performance with a fastest scintillation component of  $(4.51 \pm 0.61)$  ns found for the LS irradiation with neutrons. The setup is introduced in detail with a special emphasis on the used detectors and readout electronics. Furthermore a description of the accelerator complex and the neutron production facility is presented as well. After that characterization measurements and current results are presented.

---

Reactor neutrinos are detected via the inverse beta decay (IBD) of a proton in the LS. In this reaction a positron and a neutron are generated. The formation of positronium changes the time distribution of the photon emission, which affects positron reconstruction algorithms and allows the application of PSD to distinguish electron from positron events. A novel measurement system for the lifetime and formation probability of ortho-positronium in the liquid scintillator is introduced in this PhD thesis as well. With it the effective ortho-positronium lifetime was determined to be  $(2.98 \pm 0.05)$  ns with a formation probability of  $(44 \pm 3)$  %. As the measurements suffered from a background mainly caused by backscattered high energetic gamma quanta from the used  $^{22}\text{Na}$  positron source, the detectors were substantially upgraded. The measures of the upgrade as well as first test measurements and background studies are also presented in the thesis.

Beyond that, a short summary of measurements related to the LS and realized in other PhD projects is given. Studies on the quenching factors of recoil-protons introduced by the interaction of fast neutrons with the LS are presented. A Birk's factor of  $k_B = (0.0098 \pm 0.0005)$  cm/MeV was determined and the pulse shape discrimination using the tail-to-total method for the scintillation pulses was successfully evaluated. Moreover, attenuation length measurements for the LS at the 430 nm emission wavelength are shown. For the purified LAB sample from the Daya Bay tests an attenuation length of  $\Lambda_{pur}^{430} = (28.07 \pm 2.94)$  m at this wavelength was found, which exceeds JUNO's requirements.

## Zusammenfassung

Das Jiangmen Underground Neutrino Observatory (JUNO) ist ein Mehrzweckdetektor mit 20 kt Flüssigszintillator, der momentan in einem Untergrundlabor in Jiangmen (Volksrepublik China) errichtet wird. Das Hauptziel ist die Bestimmung der Neutrinomassenordnung. Dafür sollen Antineutrinos von zwei Kernkraftwerken in einer Entfernung von 53 km zum Detektor benutzt werden. JUNO plant die Realisierung einer bislang unerreichten Energieauflösung von 3 % für eine sichtbare Energiedeposition von 1 MeV im Szintillator. Damit soll die Massenordnung der Neutrinos mit einer Signifikanz von  $3 - 4 \sigma$  innerhalb einer Messdauer von sechs Jahren bestimmt werden. Die meisten Parameter der Neutrinooszillation können ebenso mit einer Präzision von 1 % (oder besser) bestimmt werden. Mit JUNO als größtem Flüssigszintillator seiner Art sind Beiträge zur Multi-Messenger Astronomie genauso möglich, wie eine effektive Suche nach dem Zerfall von Protonen.

In der vorliegenden Arbeit werden die historischen Meilensteine der Neutrinophysik präsentiert sowie der derzeitige Stand der Forschung. Es wird ebenso auf offene Fragen in diesem Forschungsfeld eingegangen. Danach werden die physikalischen Ziele des JUNO Experiments und seine geplante technische Umsetzung vorgestellt. Da der Flüssigszintillator und alle Systeme, die zu seiner Handhabung benötigt werden, eine Schlüsseltechnologie für den Erfolg des Experiments darstellt, wurde diese Arbeit hauptsächlich deren Entwicklung gewidmet.

Die Komponenten des Szintillators auf der Basis von linearem Alkylbenzol werden mehreren Reinigungsverfahren unterzogen, die im Detail beschrieben werden. Darüber hinaus wird auf die technische Umsetzung dieser Verfahren in Reinigungsanlagen im Industriemaßstab eingegangen. Ebenso wird über die durchgeführte Prototypenphase mit verkleinerten Pilotanlagen am Daya Bay Experiment berichtet. Dabei wurde einer der Antineutrinodektoren vor Ort mit  $\sim 24$  t Szintillator befüllt. In einer anschließenden Messkampagne wurden die Eigenschaften des Flüssigszintillators und der Gehalt an Radionukliden genau untersucht.

Basierend auf den Erfahrungen mit den Anlagenprototypen wurde ein Detektor, der ungefähr die Größe eines der Daya Bay Antineutrinodektoren aufweist, für die Überwachung der Szintillatorproduktion entworfen. Mit diesem Detektor, der OSIRIS (Online Scintillator Internal Radioactivity Investigation System) genannt wird, sollen fortlaufend Messungen der internen Radioaktivität des frisch produzierten Flüssigszintillators vorgenommen werden. Das wird besonders während der Inbetriebnahme der Reinigungsanlagen von großer Wichtigkeit sein. OSIRIS als integraler Bestandteil der Flüssigszintillatorproduktionskette wird in der vorliegenden Arbeit eingehend beschrieben. Dabei wird besonders auf das technische Design der Anlage eingegangen.

Da das Befüllen und der Betrieb des JUNO Detektors präzise Kenntnis der Flüssigkeitsstände, der hydrostatischen Drücke und der Temperaturen der jeweiligen Flüssigkeiten erfordert, wurde in der vorliegenden Arbeit spezielle Sensoren für deren Überwachung charakterisiert. Ein Teststand für hydrostatische Drucksensoren wird vorgestellt, der in einer speziellen Flüssigszintillatorwanne des Garching-Untergrundlabors aufgebaut ist. In dieser Anlage wurden zwei verschiedene Drucksensortypen eingehend getestet. Darüber hinaus wurde auch ein optischer Füllstandsmesser auf der Basis eines optischen Entfernungsmessers getestet. Der IR-Lasersensor erreicht eine Präzision von  $\pm 10$  mm für Distanzen von bis zu 50 m. Im Rahmen der Sensorentwicklung wurde auch ein Temperatursensornetz mit PT1000 Thermometern entwickelt, das im Prototypen des OSIRIS Füllsystems zum Einsatz kommt, der sich gerade an der Johannes Gutenberg-Universität im Bau befindet. Für das Spülen und Füllen sowie für den Betrieb von JUNO, OSIRIS und den Reinigungsanlagen für den Szintillator wird gasförmiger Stickstoff benötigt. Um einer Verunreinigung des Szintillators mit Radon vorzubeugen, muss der Gehalt an diesem radioaktiven Element im Stickstoff überwacht werden. Zu diesem Zweck wurde ein Alphaspektrometer in Form eines großvolumigen (42.3 l) Proportionalzählers entworfen, der in reinem Stickstoff arbeitet. Um den Untergrund in diesem Detektor effizient zu unterdrücken, werden Pulsformanalysetechniken angewandt. Dabei konnte die Anstiegszeit der Pulse als effizienter Diskriminierungsparameter für durch Teilchen verursachte Detektorsignale identifiziert werden. Mit dem Radondetektor wurden Sensitivitäten für die Verunreinigung eines Kubikmeters Stickstoff mit  $^{222}\text{Rn}$  unterhalb von  $2 \text{ mBq/m}^3$  innerhalb einer zehnstündigen Messung erreicht.

Präzise Kenntnisse über die Eigenschaften des Szintillators sind für die Interpretation der JUNO Daten zwingend erforderlich. Daher wurden in dieser Arbeit Experimente im Labormaßstab zur Charakterisierung dieser Eigenschaften durchgeführt. Zum Beispiel sind die Pulsform und das sog. Quenching für die Interaktion verschiedener Teilchen mit dem Szintillator von großer Bedeutung. Die verschiedenen charakteristischen Pulsformen sind dabei in Unterschieden im Zeitspektrum der Photonenemission der jeweiligen Teilchen begründet. Die Form der zugehörigen Fluoreszenzspektren ist daher ein wesentlicher Input eines realistischen Szintillationsmodell und von Rekonstruktionsalgorithmen für die Position eines Ereignisses im Detektor. Darüber hinaus, hat die Form dieses Spektrums auch einen Einfluss auf die Sensitivität des JUNO Detektors bei der Suche nach dem Protonenzerfall im Kanal  $p \rightarrow K^+ + \bar{\nu}$ . Das zu erwartete Signal enthält eine enge Doppelpeakstruktur in der Zeit, die sich nur mit einem ausreichend schnellen Szintillator ausreichend gut auflösen lässt. Um die Zeitprofile der Photonenemission für Neutronen- und Gammawechselwirkungen mit dem Szintillator zu vermessen, wurde ein Experiment am Tandem-Beschleuniger des Maier-Leibnitz-Laboratoriums in Garching errichtet und Szintillatorproben mit gepulsten Neutronen und

---

Gammastrahlung untersucht. In diesen Untersuchungen zeigte sich eine exzellente Diskriminierung zwischen Ereignissen die auf eine Wechselwirkung mit schnellen Neutronen bzw. auf die Streuung von Gammaquanten zurück gingen. Die schnellste Szintillationszerfallszeit wurde mit  $(4.51 \pm 0.61)$  ns in guter Übereinstimmung mit phänomenologischen Vorhersagen gemessen. Im Text der vorliegenden Arbeit, wird neben einer Beschreibung des Experimentes und des Beschleunigers auch auf Charakterisierungsmessungen und die noch andauernde Datenanalyse eingegangen. Neutrinos aus Kernreaktoren werden über den inversen Betazerfall eines Protons im Szintillator nachgewiesen. In dieser Reaktion entstehen ein Positron und ein Neutron. Die Bildung von Positronium beeinträchtigt die Verteilung der Lichtemission, was die Ortsrekonstruktion einer Wechselwirkung im Detektor beeinträchtigt. Darüber hinaus lassen sich Pulsformanalysetechniken anwenden um zwischen Elektronen- und Positronenwechselwirkungen im Szintillator zu unterscheiden. In dieser Arbeit wird ein neuer Messaufbau, der für die Bestimmung der Lebensdauer und Bildungswahrscheinlichkeit von Orthopositronium entwickelt wurde, vorgestellt. Mit diesem Experiment konnte die effektive Orthopositroniumlebensdauer auf  $(2.98 \pm 0.05)$  ns bestimmt werden. Für die zugehörige Bildungswahrscheinlichkeit ergab sich ein Wert von  $(44 \pm 3)$  %. Die Präzision der Messungen mit dem Aufbau ist durch einen quelleninduzierten Untergrund limitiert. Daher wurde das Experiment deutlich überarbeitet und mit schnelleren Detektoren ausgestattet, die eine effiziente Reduktion der störenden Ereignisse erlauben. Sowohl die Messungen mit dem ursprünglichen Aufbau, wie auch die Maßnahmen zu dessen Verbesserung werden in der folgenden Arbeit beschrieben.

Über diese Themen hinaus findet sich eine kurze Zusammenfassung anderer Arbeiten zur Charakterisierung des Flüssigszintillators an der Technischen Universität München in dieser Dissertation. Dazu gehören unter anderem Studien zum sog. Quenching von Rückstoßprotonen, die durch die Wechselwirkung schneller Neutronen im Szintillator entstehen. Für diese Teilchen konnte ein Birks Faktor von  $k_B = (0.0098 \pm 0.0005)$  cm/MeV in einem Experiment am Maier Leibnitz Labor bestimmt werden. In einer weiteren Arbeit wurden Abschwächlängenmessungen für den Szintillator durchgeführt, die auch in dieser Dissertation kurz zusammengefasst werden. Für eine in Daya Bay gereinigte Probe des Szintillatorlösungsmittels LAB konnte eine Abschwächlänge von  $\Lambda_{pur}^{430} = (28.07 \pm 2.94)$  m bestätigt werden, was die Anforderungen an den JUNO Szintillator bereits übersteigt.

# Contents

<b>1</b>	<b>Introduction: historical milestones of neutrino physics</b>	<b>1</b>
<b>2</b>	<b>Neutrino oscillations and neutrino mass ordering</b>	<b>4</b>
2.1	Neutrinos in the Standard Model . . . . .	4
2.2	Neutrino oscillations in vacuum . . . . .	5
2.3	Neutrino oscillations in matter . . . . .	7
2.4	Neutrino mass ordering . . . . .	8
<b>3</b>	<b>The JUNO Experiment</b>	<b>12</b>
3.1	JUNO as multi-purpose neutrino detector: scientific goals . . . . .	13
3.1.1	Reactor neutrino detection . . . . .	13
3.1.2	Sensitivity to the neutrino mass ordering . . . . .	15
3.1.3	Precision measurements of mixing parameters . . . . .	16
3.1.4	Solar neutrinos . . . . .	16
3.1.5	Atmospheric neutrinos . . . . .	17
3.1.6	Supernova burst neutrinos . . . . .	18
3.1.7	Diffuse supernova neutrino background . . . . .	18
3.1.8	Geo-neutrinos . . . . .	18
3.1.9	Proton decay search . . . . .	19
3.2	General overview on the detector design . . . . .	21
3.2.1	The mechanical structure of the detector . . . . .	21
3.2.2	The PMT arrays . . . . .	22
3.2.3	Large PMT testing . . . . .	24
3.2.4	The JUNO liquid scintillator . . . . .	25
<b>4</b>	<b>Liquid scintillator production and purification</b>	<b>28</b>
4.1	Purification pilot plants in Daya Bay . . . . .	31
4.1.1	The Daya Bay experimental site - a brief overview . . . . .	31
4.1.2	The Daya Bay AD design . . . . .	33
4.1.3	Overview on the pilot plant installations . . . . .	34
4.1.4	The distillation pilot plant . . . . .	36

4.1.5	Stripping pilot plant . . . . .	38
4.2	LS production and AD1 filling test . . . . .	40
4.2.1	Achieved $^{238}\text{U}$ and $^{232}\text{Th}$ concentrations . . . . .	41
4.2.2	Results of the light yield optimization study . . . . .	43
4.3	Nitrogen stripping efficiency test . . . . .	45
4.4	Conclusions from the pilot plant phase . . . . .	47
<b>5</b>	<b>The OSIRIS detector project</b>	<b>49</b>
5.1	Overview of the OSIRIS detector design . . . . .	49
5.1.1	Outer steel tank . . . . .	52
5.1.2	PMT holding frame . . . . .	53
5.1.3	Acrylic vessel . . . . .	54
5.1.4	OSIRIS filling and operation modes . . . . .	56
5.1.5	Liquid handling system . . . . .	58
5.1.6	PMTs and readout electronics . . . . .	62
5.1.7	Detector calibration systems . . . . .	64
5.2	OSIRIS sensitivity study . . . . .	66
<b>6</b>	<b>Sensor development for the monitoring of the detector liquids</b>	<b>69</b>
6.1	The characterization facility for hydrostatic pressure sensors . . . . .	72
6.1.1	Mechanical structure . . . . .	72
6.1.2	Sensor readout electronics . . . . .	74
6.1.3	Characterization of a high precision low range sensor . . . . .	76
6.1.4	Characterization of a high range sensor . . . . .	78
6.1.5	Gamma screening of the investigated HPSs . . . . .	81
6.2	Optical liquid level measurement system . . . . .	82
6.2.1	PMT irradiation test . . . . .	84
6.2.2	Sensor readout software and data acquisition . . . . .	85
6.2.3	Test measurements in the laboratory . . . . .	87
6.2.4	Test measurement in the Double Chooz near detector . . . . .	89
6.3	Temperature sensor grid for OSIRIS . . . . .	90
6.3.1	Sensor tests within the OSIRIS prototype . . . . .	90
6.3.2	Multi-channel readout electronics . . . . .	91
6.3.3	Data acquisition software and live-plotting tool . . . . .	93
<b>7</b>	<b>Development of a radon monitor for the nitrogen supply system</b>	<b>94</b>
7.1	The RaMS proportional counter demonstrator . . . . .	96
7.1.1	The detector design . . . . .	96
7.1.2	Readout electronics . . . . .	98
7.1.3	Detector calibrations . . . . .	99
7.1.4	Optimization of the spectrometer's supply voltages . . . . .	104

7.1.5	Trapping of charged Rn daughters . . . . .	105
7.1.6	Monte Carlo simulation and detection efficiency . . . . .	108
7.1.7	Pulse shape analysis . . . . .	109
7.1.7.1	Pulse shapes in P10 . . . . .	109
7.1.7.2	Pulse shapes in N <sub>2</sub> . . . . .	112
7.1.8	Background determination and sensitivity estimation . . . . .	114
7.1.8.1	Backgrounds and sensitivity estimation for P10 . . . . .	114
7.1.8.2	Sensitivity in N <sub>2</sub> . . . . .	115
7.2	The RaMS large volume proportional counter . . . . .	116
7.2.1	Enlarged low background detector design . . . . .	116
7.2.2	Calibrations with radon loaded counting gases . . . . .	118
7.2.3	Background and sensitivity determination . . . . .	121
<b>8</b>	<b>Liquid scintillator characterization experiments</b>	<b>124</b>
8.1	Attenuation lengths measurements . . . . .	124
8.1.1	The PALM setup - a brief overview . . . . .	125
8.1.2	Results for LAB from the purification pilot plants . . . . .	126
8.2	Orthopositronium lifetime and formation probability . . . . .	128
8.2.1	The PoLiDe setup . . . . .	129
8.2.2	Geometry optimization and background studies . . . . .	132
8.2.3	Results for the lifetime and formation probability . . . . .	133
8.2.4	The upgraded PoLiDe setup . . . . .	138
8.2.5	First results from the commissioning tests . . . . .	141
8.3	Fluorescence time profile measurements . . . . .	144
8.3.1	Energy transfer in organic scintillators . . . . .	145
8.3.1.1	Luminescence related to excited $\pi$ -states . . . . .	145
8.3.1.2	Multi-component scintillators . . . . .	147
8.3.1.3	Light output and quenching . . . . .	149
8.3.1.4	Fluorescence time profile . . . . .	150
8.3.1.5	Particle identification . . . . .	151
8.3.2	Experimental setup at the MLL . . . . .	153
8.3.2.1	Overview on the accelerator facility of the MLL . . . . .	153
8.3.2.2	Ion beam production and acceleration . . . . .	154
8.3.2.3	Low energy beam pulsing . . . . .	155
8.3.2.4	Neutron production on a gaseous H <sub>2</sub> target . . . . .	156
8.3.3	Experimental method and detector setup . . . . .	158
8.3.4	Readout electronics for the experiment . . . . .	160
8.3.5	Time resolution determination . . . . .	162
8.3.6	Time of flight particle identification . . . . .	164
8.3.7	Current results for neutron and gamma interactions . . . . .	167
8.3.7.1	Single photon selection . . . . .	167

8.3.7.2	Fluorescence time profiles for neutrons and $\gamma$ s . . .	168
8.3.7.3	Determination of the PDF parameters . . . . .	169
8.4	Proton quenching factor determination . . . . .	171
8.4.1	Detector design with improved light collection . . . . .	172
8.4.2	Experimental setup at the neutron scattering facility . . . .	173
8.4.3	Results for the Birk's factor kB of protons . . . . .	174
8.4.4	Pulse shape discrimination performance . . . . .	176
<b>9</b>	<b>Conclusions</b>	<b>178</b>
	<b>Bibliography</b>	<b>182</b>

# Chapter 1

## Introduction: historical milestones of neutrino physics

In 1914, J. Chadwick reported on his observation of continuous beta spectra of two radon daughter isotopes [1]. Later experiments using  $^{210}\text{Bi}$  by C. D. Ellis [2] and L. Meitner [3] confirmed Chadwick's results. To keep energy and angular momentum conserved in the  $\beta$  - decay process, W. Pauli postulated in December 1930 the existence of an additional hardly detectable neutral spin -  $\frac{1}{2}$  particle [4], which is nowadays called neutrino. The nuclear transition energy is shared between the electron and the neutrino, leading to the observed continuous energy spectrum of beta particles.

First experimental hints for the existence of a neutrino were found by G. W. Rodeback and J. S. Allen in the electron capture (EC) of  $^{37}\text{Ar}$  [5] (and confirmed in 1955 by A. H. Snell et al. [6]). In parallel experiments at the Hanford nuclear reactor were carried out by Cowen and Reines searching for the inverse beta decay reaction

$$\bar{\nu}_e + p \longrightarrow e^+ + n. \quad (1.1)$$

After detecting a promising but still very faint signal in 1953 [7] the experiment was enlarged, further upgraded and repeated in 1956 at the Savannah River reactor. It provided the final proof for the existence of neutrinos [8].

Within two years after this result, Wu demonstrated that parity is maximally violated by beta decays [9] and Goldhaber was able to determine the helicity of the neutrino [10] to be -1.

Based on the work of M. Schwartz [11], high-energy particle accelerators became a further neutrino source. At the AGS (Alternating Gradient Synchrotron) in Brookhaven a nearly pure  $\nu_\mu$  beam was produced by bombarding a beryllium target with 15 GeV protons. With this beam a team around L. M. Lederman, M. Schwartz, G. Danby and J. Steinberger was able to show that  $\nu_\mu$  and  $\nu_e$  are different distinguishable neutrino flavours [12].

---

The first detection of neutrinos from the solar fusion processes succeeded with the radiochemical experiment of R. A. Davis [13, 14], which was operational since 1968 in the Homestake Mine. The experiment pioneered in the field of neutrino astrophysics and observed a deficit in the detected neutrino rate compared to the Standard Solar Model (SSM), leading to the so-called solar neutrino problem [15, 16]. During the nineteen nineties the radiochemical experiments GALLEX/GNO [17] and SAGE [18, 19]) based on  $^{71}\text{Ga}$  confirmed this neutrino deficit. Furthermore, both experiments were sensitive to pp neutrinos and provided direct experimental proofs that the sun's main energy production takes place via hydrogen fusion.

At the beginning of the new century the  $\nu_\tau$  was detected in the DONUT [20] experiment at Fermilab. In a combined analysis of the results of the experiments ALEPH, DELPHI, L3, OPAL and SLD on the  $Z^0$ -resonance width, strong indications for the existence of three neutrino families (in full agreement with the standard model of particle physics) below  $mc^2 \leq 45$  GeV were found [21].

With the 50 kt water Cherenkov detector Super-Kamiokande flavour oscillations of atmospheric neutrinos were observed [22]. This process leads to the existence of non-zero neutrino masses, which can not be explained within the Standard Model (SM) of particle physics.

The oscillation of solar neutrinos and with that the solution of the long lasting solar neutrino problem was found in the SNO (Sudbury Neutrino Observatory) experiment and published in 2002 [23]. Only one year later the KamLAND Collaboration reported the observation of reactor neutrino oscillations [24].

In 2007 the Borexino detector [25] started data taking. During the following 12 years a comprehensive spectrographic measurement of the pp-chain solar neutrinos was gained [26], while the experiment is nowadays aiming for the first measurement of neutrinos from the CNO process. These measurements are possible because breakthroughs in the liquid scintillator technology (especially with respect to the radiopurity) were achieved during the long R&D phase of the experiment.

With IceCube, an observatory for high-energy neutrinos of cosmic origin started its operation in 2010 after six years of construction. Three years later the detection of neutrinos with PeV energies were published [27] and in 2017 the detector was triggered by a neutrino event coincident in direction and time with the occurrence of a gamma-ray flare from the blazar TXS 0506+056 [28].

In the same year, the COHERENT Collaboration provided the first observation of the standard model predicted coherent scattering of neutrinos on atomic nuclei at  $6.7 \sigma$  confidence level. Therefore, a low-background, 14.6-kilogram CsI[Na] scintillator detector was exposed to the neutrino emissions from the Spallation Neutron Source at Oak Ridge National Laboratory [29]. Two promising experiments with complementary detector technology are currently being developed with the CONUS [30] and  $\nu$ -cleus [31] projects to further investigate this phenomenon.

At the end of the second decade of the new century, neutrino oscillations are a well-established process in particle physics and to this day the only one ever observed beyond the predictions of the SM. While all mixing angles have been experimentally determined with high precision, the questions about the absolute neutrino mass, the order of the mass eigenstates and the search for the neutrinoless double beta decay and sterile neutrinos remain important challenges for the future.

The JUNO (Jiangmen Underground Neutrino Observatory) experiment [32], described in the present thesis, aims (beside other goals) for a precise study of reactor neutrino oscillations at a medium baseline of 53 km in order to determine the mass ordering of the neutrino mass eigenstates, within the coming decade.

# Chapter 2

## Neutrino oscillations and neutrino mass ordering

The following chapter gives a brief overview of the role of neutrinos in the SM, the theoretical description and formalisms of neutrino oscillation in vacuum and effects caused by the  $\nu$ 's passage through matter. In addition, the yet unsolved problem of the unclear neutrino mass ordering is discussed.

### 2.1 Neutrinos in the Standard Model

The SM is a theoretical unification of three fundamental forces namely the strong, the weak and the electromagnetic force. Within this model the weak and the electromagnetic interactions are described via a spontaneously broken local gauge symmetry  $SU(2) \times U(1)$  [33]. The fields of left-handed fermions are doublets

$$\begin{pmatrix} \nu_e \\ e^- \end{pmatrix}_L, \quad \begin{pmatrix} \nu_\mu \\ \mu^- \end{pmatrix}_L, \quad \begin{pmatrix} \nu_\tau \\ \tau^- \end{pmatrix}_L, \quad (2.1)$$

while right-handed fields are represented by singlets

$$e_R, \quad \mu_R, \quad \tau_R. \quad (2.2)$$

The three neutrino flavors interact only weakly in neutral current (NC) interactions, mediated by the  $Z^0$ -boson or in charged current (CC) processes via the  $W^\pm$ -bosons. As a consequence of the high boson masses ( $m_W \approx 80.3$  GeV and  $m_Z \approx 91.2$  GeV [34]) ranges and cross-sections of the weak force are very small. For neutrinos in the MeV energy regime, this leads to typical cross-section values of  $10^{-8}$  up to  $10^{-7}$  pb [35, 36]. Since the conservation of parity is maximally violated, the  $W^\pm$ -bosons

couple only to left-handed particles and right-handed antiparticles. From this point of view, it seems plausible that neutrinos are generated as pure left-handed, while antineutrinos should exist only right-handed. For these neutrinos, the standard Higgs-mechanism can not be applied and neutrino masses can not be generated within the SM [33].

## 2.2 Neutrino oscillations in vacuum

The existence of neutrino masses is a compelling requirement for the phenomenon of neutrino oscillations, observed by several experiments. While undergoing these oscillations, neutrinos change their flavor (periodically in time) depending on their energy and travelled distance [37, 38, 39]. The neutrino-flavor eigenstates (of the weak interaction) are denoted as  $\nu_e$ ,  $\nu_\mu$  and  $\nu_\tau$  while the mass eigenstates of their propagation Hamiltonian are written as  $\nu_1$ ,  $\nu_2$  and  $\nu_3$ . Mass and corresponding flavor eigenstates are in general not equal. Nonetheless, the flavour states can be expressed by a superposition of the orthogonal mass eigenstates. Using the unitary Pontecorvo-Maki-Nakagawa-Sakata (PMNS) matrix  $U$  this can be denoted as [36, 40, 41]

$$\begin{pmatrix} \nu_e \\ \nu_\mu \\ \nu_\tau \end{pmatrix} = U \begin{pmatrix} \nu_1 \\ \nu_2 \\ \nu_3 \end{pmatrix} = \begin{pmatrix} U_{e1} & U_{e2} & U_{e3} \\ U_{\mu1} & U_{\mu2} & U_{\mu3} \\ U_{\tau1} & U_{\tau2} & U_{\tau3} \end{pmatrix} \begin{pmatrix} \nu_1 \\ \nu_2 \\ \nu_3 \end{pmatrix}. \quad (2.3)$$

Introducing three mixing angles  $\theta_{12}$ ,  $\theta_{23}$ ,  $\theta_{13}$  and a CP violating phase  $\delta$  the matrix  $U$  can be parameterized as

$$U = \begin{pmatrix} 1 & 0 & 0 \\ 0 & c_{23} & s_{23} \\ 0 & -s_{23} & c_{23} \end{pmatrix} \begin{pmatrix} c_{13} & 0 & s_{13}e^{-i\delta} \\ 0 & 1 & 0 \\ -s_{13}e^{i\delta} & 0 & c_{13} \end{pmatrix} \begin{pmatrix} c_{12} & s_{12} & 0 \\ -s_{12} & c_{12} & 0 \\ 0 & 0 & 1 \end{pmatrix} \quad (2.4)$$

with the abbreviations  $c_{ij} = \cos(\theta_{ij})$  and  $s_{ij} = \sin(\theta_{ij})$  [40, 41].

By the introduction of two additional CP violating phases, this can be adapted in case of the Majorana nature of neutrinos [34]. Since the phases have no influence on the oscillation probability, they are neglected in the descriptions within this chapter. In the following, the concept of neutrino oscillations is derived using the assumption that the neutrino mass eigenstates can be treated as plain waves. The nature of the neutrino production and detection reactions are not taken into account. For a detailed and theoretically more accurate formulation see [42].

Since  $\nu_i$  is an eigenstate of the free Hamiltonian, its time evolution is given by

$$|\nu_i(t)\rangle = e^{-iE_i t} |\nu_i(0)\rangle \quad (2.5)$$

where  $E_i$  is the energy associated with the mass eigenstate  $\nu_i(t)$ . It follows directly

$$P_{\nu_\alpha \rightarrow \nu_\beta}(t) = |\langle \nu_\beta | \nu_\alpha(t) \rangle|^2 = \left| \sum_{i=1}^3 U_{\beta i}^* e^{-iE_i t} U_{\alpha i} \right|^2 \quad (2.6)$$

for the time dependent probability  $P_{\nu_\alpha \rightarrow \nu_\beta}(t)$  to observe a neutrino in the flavor state  $|\nu_\beta\rangle$  which was generated as  $|\nu_\alpha\rangle$ . Replacing  $U$  by  $U^*$  modifies equation 2.6 for anti neutrinos [43, 44].

With the ultra-relativistic approximation  $E_i > m_1$  the flavor eigenstate's energy  $E_i$  can be expressed by

$$E_i = \sqrt{p_i^2 + m_i^2} \approx p_i + \frac{m_i^2}{2p_i} \approx E + \frac{m_i^2}{2E}. \quad (2.7)$$

As a consequence, the distance  $L$  that a neutrino has traveled from its initial position at  $t = 0$ , can be approximated as

$$L \approx t, \quad (2.8)$$

which leads to a distance dependent formulation of equation 2.6 [45]

$$P_{\nu_\alpha \rightarrow \nu_\beta}(L) = \left| \sum_{i=1}^3 U_{\beta i}^* e^{-\frac{im_i^2}{2E}L} U_{\alpha i} \right|^2. \quad (2.9)$$

Transforming this equation in SI units and using the unitarity of matrix  $U$  results in [44, 45]

$$P_{\nu_\alpha \rightarrow \nu_\beta}^{(-) (-)} = \delta_{\alpha\beta} - 4 \sum_{i>j} \Re(U_{\alpha i}^* U_{\beta i} U_{\alpha j} U_{\beta j}^*) \sin^2 \left[ 1.27 \frac{\Delta m_{ij}^2}{eV^2} \frac{L/km}{E/GeV} \right] \\ (-) \Im(U_{\alpha i}^* U_{\beta i} U_{\alpha j} U_{\beta j}^*) \sin \left[ 2.54 \frac{\Delta m_{ij}^2}{eV^2} \frac{L/km}{E/GeV} \right] \quad (2.10)$$

with  $\Delta m_{ij}^2 = m_i^2 - m_j^2$ .

The matrix elements define the oscillation's amplitude by the mixing angles and the

CP-violating phase  $\delta$ , while its frequency is proportional to  $\Delta m_{ij}^2$ . Since neutrino oscillations were observed,  $|\Delta m_{ij}^2| > 0$  is compelling for at least one tuple  $(i, j)$  and at least one mass eigenstate is different from zero. However, the neutrino oscillation probability only depends on mass-squared differences, thus no information on the absolute neutrino masses can be gained from oscillation studies.

Since  $\nu_\alpha \rightarrow \nu_{\bar{\alpha}}$  and  $\nu_\beta \rightarrow \nu_{\bar{\beta}}$  are CP-transformations, CP is only conserved if  $\Im(U_{\alpha i}^* U_{\beta i} U_{\alpha j} U_{\beta j}^*)$  vanishes and there is no difference in the oscillations of neutrinos and their antiparticles [44]. In the PMNS matrix  $\delta$  can be identified as the only parameter affecting the appearance of imaginary terms in the oscillation function and so CP is only violated in the neutrino sector if  $\delta \neq 0$  and  $\delta \neq \pi$ . As a consequence  $\delta$  can not be measured in disappearance experiments (e.g. Double Chooz or Daya Bay), because the survival probability of a flavor  $P_{\nu_\alpha \rightarrow \nu_\alpha}$  is independent of  $\delta$ . In this case the imaginary part

$$\Im(U_{\alpha i}^* U_{\beta i} U_{\alpha j} U_{\beta j}^*) = \Im(|U_{\alpha i}|^2 |U_{\alpha j}|^2) = 0 \quad (2.11)$$

vanishes. Challenging neutrino beam based appearance experiments (e.g. T2K [46] published a first result in 2018 and the future DUNE project [47]) can shade light on this important question.

## 2.3 Neutrino oscillations in matter

The oscillation probability was derived in 2.2 under the assumption, that the neutrino travels through vacuum. When it travels through matter, additional coherent forward scatterings with protons, neutrons and electrons have to be considered [48]. Since NC processes have equal cross sections for all flavors, the oscillations are not affected, while only electron neutrinos can undergo CC reactions, resulting in an asymmetry between the coherent scattering amplitudes for  $\nu_e$  and the other flavors [49].

To take this fact into account, an additional potential  $V$  exclusively influencing electron neutrinos can be introduced as

$$V = \sqrt{2} G_F N_e, \quad (2.12)$$

where  $G_F$  denotes the Fermi constant and  $N_e$  the electron number density of the matter traversed by the  $\nu_e$ . In the case of  $\bar{\nu}_e$  the sign of the potential changes ( $V \rightarrow -V$ ). This so-defined potential (acting only on the  $|\nu_e\rangle$  flavor state) leads directly to non-independent neutrino mass eigenstates. As a consequence, the PMNS matrix has to be re-diagonalized using effective mixing angles and mass differ-

ences [49]. For simplicity this concept will be presented here, using a two-neutrino flavor model with just one mixing angle  $\vartheta$  and the mass-squared difference  $\Delta m^2$  ( $\vartheta_M$  and  $\Delta m_M^2$  as effective quantities in matter).

In this scenario the effective mass-squared difference can be expressed by

$$\Delta m_M^2 = \Delta m^2 \sqrt{\sin^2(2\vartheta) + (\cos(2\vartheta) - A)^2} \quad (2.13)$$

while the effective mixing angle is given by

$$\sin^2(2\vartheta_M) = \frac{\sin^2(2\vartheta)}{\sin^2(2\vartheta) + (\cos(2\vartheta) - A)^2} \quad (2.14)$$

and  $A$  represents

$$A = \frac{2\sqrt{2}G_F N_e E}{\Delta m^2}. \quad (2.15)$$

$A$  and with that the matter effects are dependent on the neutrino energy and the electron density. Thus  $A$  scales according to  $1/\Delta m^2$ . Therefore, the sign of  $\Delta m^2$  has direct implications on the neutrino oscillation probabilities in matter, however in first order, they are not influenced by the CP violating phase  $\delta$  [50].

## 2.4 Neutrino mass ordering

Solar neutrino experiments (e.g. Super-Kamiokande [51] and SNO [52]) showed that  $|\nu_2\rangle$  is more massive than  $|\nu_1\rangle$ , i. e.  $m_2 > m_1$ . Since the oscillations of solar neutrinos are mainly determined by  $\Delta m_{21}^2 > 0$ , it can be concluded that  $\Delta m_{sol}^2 = \Delta m_{21}^2 > 0$  [53]. The solar mass-squared difference was measured in these experiments as  $\Delta m_{sol}^2 = 7.5 \times 10^{-5} (eV)^2$ . The absolute value of the so-called atmospheric mass difference  $\Delta m_{atm}^2 \approx |\Delta m_{31}^2| \approx |\Delta m_{32}^2| \approx 2.5 \times 10^{-3} (eV)^2$  (measured by e.g. KamLand, T2K, Double Chooz) is about two orders of magnitude larger but its sign could not be determined yet. Due to the unknown sign, there are (in case of three-neutrino mixing) two independent mass-squared differences:  $\Delta m_{31}^2 = \Delta m_{32}^2 + \Delta m_{21}^2$ . This results in two possible orderings of the neutrino mass eigenvalues, the normal (NO)  $m_1 < m_2 < m_3$  and the inverted ordering (IO)  $m_3 < m_1 < m_2$ . The relation between the parameters and their differences in the two scenarios are summarized in Table. 2.1 and illustrated schematically in Figure 2.1.

Normal Ordering (NO)	Inverted Ordering (IO)
$m_1 < m_2 < m_3$	$m_3 < m_1 < m_2$
$\Delta m_{sol}^2 = \Delta m_{21}^2$ $\Delta m_{atm}^2 = \Delta m_{32}^2$	$\Delta m_{sol}^2 = \Delta m_{21}^2$ $\Delta m_{atm}^2 = \Delta m_{13}^2$
$ \Delta m_{31}^2  =  \Delta m_{32}^2  +  \Delta m_{21}^2 $ $\rightarrow \Delta m_{31}^2 > \Delta m_{32}^2$	$ \Delta m_{31}^2  =  \Delta m_{32}^2  -  \Delta m_{21}^2 $ $\rightarrow  \Delta m_{31}^2  <  \Delta m_{32}^2 $

**Table 2.1:** Differences in the relations of the neutrino mass eigenvalues and mass squared differences for the two possible neutrino mass orderings.

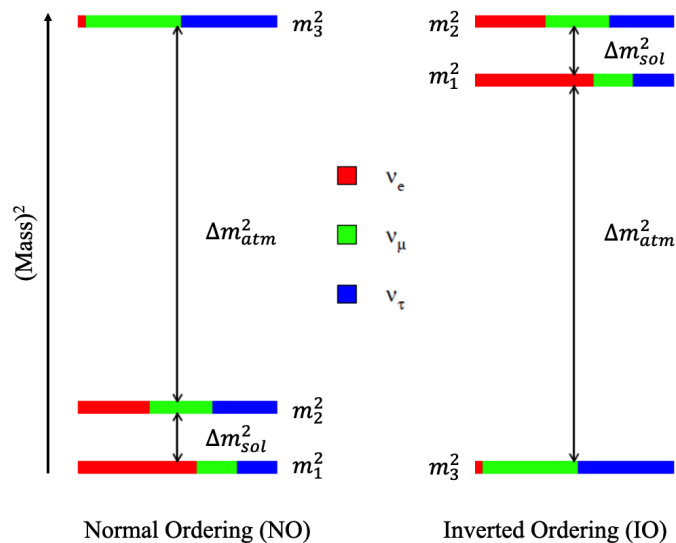


**Figure 2.1:** Normal and inverted mass ordering of the mass eigenstates. The colors represent the admixture of the corresponding flavor eigenstate. The distances are not to scale. Figure adapted from [41].

Currently, there are two complementary experimental approaches to answer the open question, which neutrino mass ordering is realized in nature. One uses the matter effects on atmospheric neutrinos, while the other is a precision measurement of the oscillation pattern in the energy spectrum of reactor neutrinos on a medium baseline of 50-60 km [54]. Both require new detectors.

In the IceCube Upgrade experiment (or in the planned Precision IceCube Next Generation Upgrade (PINGU)) the matter effect on atmospheric neutrinos in the energy range between 5 and 15 GeV will be studied [55]. Future long baseline experiments (e.g. DUNE [47]) using particle accelerators as neutrino sources are based on a similar strategy, since they are exploiting the matter effects on the neutrinos traversing the earth on their way from the accelerator to the detector. JUNO will follow the second approach, measuring the oscillation of reactor neutrinos

on a medium baseline ( $\approx 53$  km) with high energy resolution ( $\sigma \approx 3\%$  at 1 MeV) [32, 41]. For the  $\bar{\nu}_e$  emitted with a certain energy  $E$  from a reactor, the survival probability  $P$  is

$$P_{\bar{\nu}_e \rightarrow \bar{\nu}_e}(E) = 1 - P_{21} - P_{31} - P_{32} \quad (2.16)$$

with the solar term

$$P_{21} = \cos^4(\theta_{13}) \sin^2(2\theta_{12}) \sin^2(\Delta_{21}) \quad (2.17)$$

and two atmospheric terms

$$P_{31} = \cos^2(\theta_{12}) \sin^2(2\theta_{13}) \sin^2(\Delta_{31}) \quad (2.18)$$

$$P_{32} = \cos^2(\theta_{12}) \sin^2(2\theta_{13}) \sin^2(\Delta_{32}) \quad (2.19)$$

where  $\Delta_{ij} = 1.27(m_i^2 - m_j^2)[eV]^2 \frac{L[m]}{E[MeV]}$ .  $L$  denotes the distance to the neutrino source, while  $\theta_{12}$  and  $\theta_{13}$  represent neutrino mixing angles in the standard parametrization of the PMNS matrix [56, 57, 58].

At the baseline length foreseen for JUNO, the neutrino energy spectrum (see Figure 2.2) is modulated at a rather low frequency by  $P_{21}$  because of the large  $\sin^2(2\theta_{12})$  and the relatively small  $\sin^2(\Delta_{21})$  values.

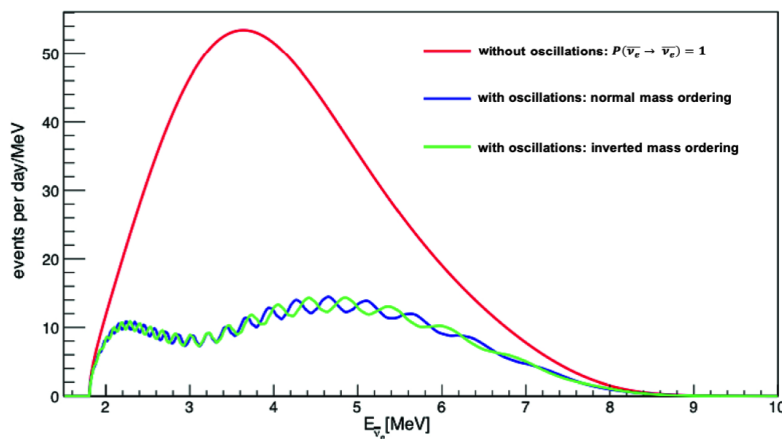


**Figure 2.2:** The neutrino energy spectrum calculated for the JUNO detector at a distance of  $\approx 53$  km to the reactor cores. In this medium baseline experiment the fast oscillations will be resolvable, which will allow a discrimination between normal (blue) and inverted neutrino mass ordering (green). The red curve shows a hypothetical scenario without neutrino oscillation. Plot adapted from [41].

---

Overlaying are  $P_{31}$  and  $P_{32}$  with high frequencies  $\sin^2(\Delta_{31})$  and  $\sin^2(\Delta_{32})$  but with a small amplitude  $\sin^2(2\theta_{13})$ . In short baseline experiments (e.g. Double Chooz or Daya Bay), which provided precise knowledge of the mixing angle  $\theta_{13}$ , the solar oscillations are not enough pronounced. With larger baselines (e.g. in KamLand or DUNE) the fast oscillations are no longer resolvable [41].

# Chapter 3

## The JUNO Experiment

The Jiangmen Underground Neutrino Observatory (JUNO) is a 20 kton multi-purpose liquid scintillator (LS) detector currently being built in a dedicated underground laboratory ( $\approx 600$  m deep) in Jiangmen (PR China). JUNO's main physics goal is the determination of the neutrino mass ordering using electron anti-neutrinos from two nuclear power plants at a baseline of about 53 km (see also Table 3.1). The total installed thermal power of  $26.6 \text{ GW}_{th}$  will be available from the beginning of data taking in 2021, while a final power of  $35.8 \text{ GW}_{th}$  will be realized during following years.

Cores	YJ-C1	YJ-C2	YJ-C3	YJ-C4	YJ-C5	YJ-C6
Power ( $\text{GW}_{th}$ )	2.9	2.9	2.9	2.9	2.9	2.9
Baseline (km)	52.75	52.84	52.42	52.51	51.12	52.21
Cores	TS-C1	TS-C2	TS-C3	TS-C4	DYB	HZ
Power ( $\text{GW}_{th}$ )	4.6	4.6	4.6	4.6	17.4	17.4
Baseline (km)	52.76	52.63	52.32	52.20	215	265

**Table 3.1:** The table (taken from [32]) lists the reactor cores of the corresponding nuclear power plants with their distance to the JUNO detector as well as their installed thermal power. Currently, all six reactors of Yangjiang (YJ) are operational. In Taishan (TS) two of the four planned EPR (European Pressurized Reactors) are operational, while the realization of the two others (TS-C3 and TS-C4) is delayed. The nuclear power plants in Daya Bay (DYB) and Huizhou (HZ) are also listed, because they are the closest other plants. Currently in Huizhou two of six  $2.9 \text{ GW}_{th}$  cores are under construction, while the other four are still in the planning phase.

Besides this high reactor power, JUNO aims for an unprecedented energy resolution of 3% at 1 MeV for the central detector, to be able to determine the mass ordering with 3 - 4  $\sigma$  significance within six years of operation [32].

Besides this fundamental aim, JUNO will have a rich physics program. It includes the measurement (at a sub-percent level) of the solar neutrino oscillation parameters, the detection of low-energy neutrinos coming from galactic core-collapse supernovae, the first measurement of the diffuse supernova neutrino background, the detection of neutrinos coming from the sun, the earth and the earth's atmosphere. Moreover, JUNO will provide sensitivity in searches for nucleon decays and neutrinos resulting from potential dark matter annihilation in the sun [59].

The present work is devoted to the production and characterization of the high-purity liquid scintillator (LS) based on the solvent LAB (Linear Alkyl-Benzene), which is foreseen for the JUNO experiment. A second focus of the present thesis, is on the handling of the ultra pure liquids (35 kt water and 20 kt LS) for the JUNO detector. For the liquid handling system, a broad variety of monitoring sensors were developed. From the experience, also gained during the first phases of the present work, a quality control detector (Online Scintillator Internal Radioactivity Investigation System - OSIRIS) for the LS purity (in terms of radioactivity) has been proposed. The technical design, the scientific goals, the integration of the detector into the liquid handling system of JUNO and the current status are also presented in this thesis.

In the following chapter, an overview of the scientific goals of the JUNO project is given, followed by their requirements for the detector design, which will be discussed afterwards.

## 3.1 JUNO as multi-purpose neutrino detector: scientific goals

The JUNO detector will carry out many scientific studies during the planned 30 years of operation. Within this section the reactor neutrino based experimental programme is discussed, followed by the investigations with neutrinos from other sources as well as the proton decay search potential.

### 3.1.1 Reactor neutrino detection

The electron antineutrinos in the energy range of a few MeV, as emitted by the nuclear reactor cores, are detected within JUNO by their interaction with a proton of the LS in the so-called inverse beta decay (IBD) reaction

$$\bar{\nu}_e + p \longrightarrow e^+ + n. \quad (3.1)$$

A positron  $e^+$  and a neutron  $n$  are generated by this CC process. The energy

threshold for this reaction is  $\approx 1.8$  MeV. The  $e^+$  deposits its kinetic energy  $E_{e^+}$  in the scintillator, which leads to a prompt scintillation signal. By the annihilation of the positron with an ambient electron two 511 keV  $\gamma$  quanta are generated, depositing their total energy (1.022 MeV) within the LS quickly. The neutron is thermalized and finally captured by a proton, which releases 2.2 MeV in  $\gamma$  radiation as a delayed second signal (about 236  $\mu$ s after the prompt  $e^+$  signal). The so called delayed coincidence of prompt and delayed signals is a distinctive antineutrino signature. The initial energy of the neutrino  $E_{\bar{\nu}_e}$  can be reconstructed from the energy visualized by scintillation  $E_{vis}$  using

$$E_{vis} \approx E_{\bar{\nu}_e} - (m_n + m_e - m_p) + 2m_e \approx E_{\bar{\nu}_e} - 0.78 \text{ MeV} \quad (3.2)$$

where  $m_e$  is the electron mass,  $m_p$  and  $m_n$  are representing the masses of the proton and neutron respectively. Since the mass of the positron is much smaller than the mass of the neutron, the positron carries almost the complete kinetic energy of the neutrino. Therefore, the recoil energy of the neutron produced in the IBD reaction can be neglected.

The cross section of the IBD reaction as shown in Figure 3.1 can be expressed using the neutron lifetime  $\tau_n$  and the phase space factor  $f_{ps}$

$$\sigma_{\bar{\nu}_e} = \frac{2\pi/m_e^5}{\tau_n f_{ps}} E_e p_e \sim 0.98 \cdot 10^{-43} \text{ cm}^2 (E_e p_e / (\text{MeV})^2) \quad (3.3)$$

where  $E_e$  denotes the positron's energy and  $p_e$  its momentum [41].

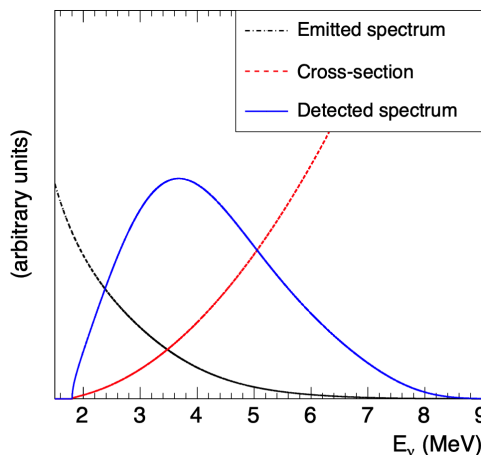


**Figure 3.1:** The visible neutrino spectrum (in a detector) neglecting neutrino oscillation effects (blue solid line), which is a convolution of the IBD cross section (red dashed curve) and the emitted spectrum from the reactor core (black dashed dotted line). The plot is taken from [60].

### 3.1.2 Sensitivity to the neutrino mass ordering

In the Geant4-based Monte Carlo studies for JUNO's sensitivity to the neutrino mass ordering, a total thermal power of  $36 \text{ GW}_{th}$  for the two reactor complexes in Yangjiang and Taishan were assumed as well as a data taking campaign of six years (2000 effective days). The IBD detection efficiency was previously estimated by simulations to be  $\approx 73\%$ . Under the assumption of a detector energy resolution of  $3\%/\sqrt{E(\text{MeV})}$  for the visible energy of the positron, the  $\nu$  mass ordering can be determined with a significance of  $3.3 \sigma$  with the NO realized in nature and  $3.4 \sigma$  in case of a true IO. By including future precision measurements of  $|\Delta m_{\mu\mu}^2|$  from long baseline muon (anti)neutrino disappearance experiments this sensitivity would be further improved. In case of a 1% constraint on  $|\Delta m_{\mu\mu}^2|$  a significance of  $4.4 \sigma$  can be obtained. A detailed description of this study with all parameters identified to influence JUNO's sensitivity to the mass ordering as well as the used background models can be found in "Neutrino physics with JUNO" [59].

Since measuring the mass ordering within JUNO means to resolve the fine structure on the energy spectrum of the reactor neutrinos, it is expected that the detector's energy resolution is a crucial parameter, which influences the sensitivity severely. This influence was studied for an IBD detection efficiency of 80% and different energy resolutions. The resulting iso- $\Delta\chi_{MH}^2$  contour plot is shown in Figure 2.3 [59].

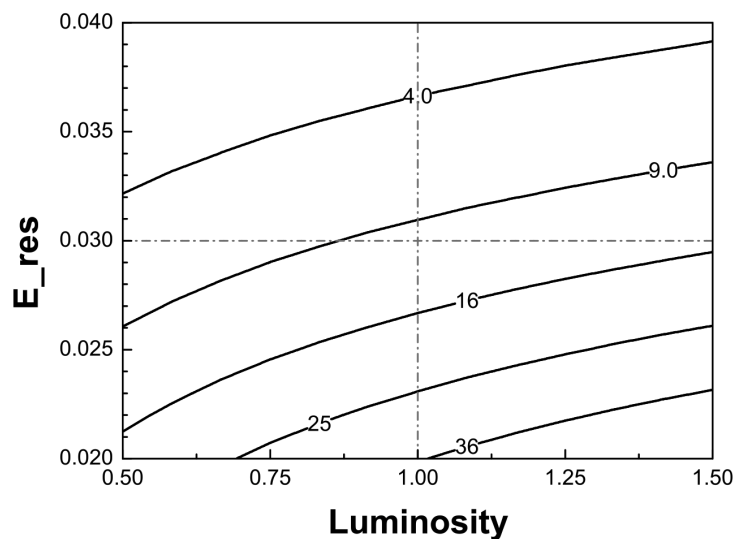


**Figure 3.2:** The iso- $\Delta\chi_{MH}^2$  contour plot as a function of the event statistics (luminosity) and the energy resolution. The vertical dash-dotted line represents the nominal run time of six years with an IBD signal detection efficiency of 80%. With the  $3\%/\sqrt{E(\text{MeV})}$  energy resolution JUNO aims for and  $36 \text{ GW}_{th}$  thermal reactor power, the  $\Delta\chi_{MH}^2 = 9.0$  line is well exceeded. Plot adopted from [59].

Furthermore, by a combined analysis of JUNO and the planned PINGU experiment a sensitivity of the neutrino mass ordering determination of  $5\sigma$  is possible within 2 years of data taking. If the available reactor power of JUNO will not exceed the initial  $26.6\text{GW}_{th}$  and there will be no further upgrade from IceCube Upgrade to PINGU the  $5\sigma$  significance of a combined analysis can be reached within 7 years of data taking [55].

### 3.1.3 Precision measurements of mixing parameters

Besides the determination of the neutrino mass ordering, the  $\mathcal{O}(10^5)$  IBD events recorded within the first six years of JUNO's operation can be used for studies of the fundamental properties of neutrino oscillations and will give access to four parameters  $\theta_{12}$ ,  $\theta_{13}$ ,  $\Delta m_{21}^2$  and  $|\Delta m_{ee}^2|$  for the neutrino flavour mixing. Table 3.2 gives an overview of the current precision achieved in the leading experiments and results of global analyzes.

Parameter	$\Delta m_{21}^2$	$ \Delta m_{31}^2 $	$\sin^2\theta_{12}$	$\sin^2\theta_{13}$	$\sin^2\theta_{23}$
Dominant Exp.	KamLAND	T2K	SNO+SK	Daya Bay	NO $\nu$ A
Individual $1\sigma$	2.4%	2.6%	4.5%	3.4%	5.2%
Global $1\sigma$	2.4%	1.3%	4.0%	2.9%	3.8%

**Table 3.2:** The precisions ( $1\sigma$ ) achieved by the leading experiment as well as by global analyzes for selected parameters of neutrino oscillations (as of 2019). All values were taken from NuFit 4.0 [61].

JUNO with the foreseen energy resolution of 3 % at 1 MeV and energy scale uncertainty below 1 % will be able to determine  $\theta_{12}$ ,  $\Delta m_{21}^2$  and  $|\Delta m_{ee}^2|$  with a  $1\sigma$ -precision of 0.7 %, 0.6 % and 0.5 % respectively [59]. Moreover, the unitarity of the neutrino mixing matrix  $U_{PMNS}$  can be probed with 1 % accuracy. The  $\theta_{13}$  measurement from JUNO will be less accurate than that of Daya Bay because the medium baseline is much larger than the optimized one ( $\sim 2$  km) of the Daya Bay experiment. However, JUNO would be the first experiment to simultaneously observe neutrino oscillations from two different frequencies and be the first experiment to observe more than two oscillation cycles [59].

### 3.1.4 Solar neutrinos

There are currently three open issues in the solar neutrino field of great relevance for astrophysics and elementary particle physics, where JUNO's contribution could become crucial [59]:

- The discrepancies between the solar and the reactor experimental data in the measurement of the  $\Delta m_{21}$  oscillation parameter;
- the solar metallicity problem, regarding a discrepancy between the Standard Solar Model (SSM) predictions and the solar data which would require either a revision of the SSM inputs or a modification of the core abundances of some elements in the sun;
- the analysis of the energy dependence of the  $\nu_e$  survival probability to study the transition between the vacuum-dominated and the matter-dominated oscillation regions.

As described in the previous section, JUNO aims for a determination of  $\Delta m_{21}$  with sub-percent precision. Furthermore, if the precision in measurement of the solar neutrino oscillations could be improved by JUNO, the tension on the  $\Delta m_{21}$  oscillation parameter measurements could be investigated in one single detector for the first time by detecting reactor and solar neutrinos simultaneously [59, 62]. A more accurate measurement of the  ${}^7\text{Be}$  and  ${}^8\text{B}$  neutrino fluxes from the sun will shade light on the solar metallicity and could lead to a solution of this central problem of nuclear astrophysics. Furthermore, the continuous solar  ${}^8\text{B}$  neutrino spectrum will be useful for an investigation of the transition from vacuum- to matter-dominated oscillations in the relevant energy region between 1 and 3 MeV [62]. The main detection channel for solar neutrinos of all flavors (neutrino oscillations) is the elastic scattering on electrons with the observable being the electron's kinetic energy. The impact of JUNO in the solar neutrino field will depend crucially on the achieved background level. Here, in contrast to the IBD reaction, no coincidence signature can be applied directly [32, 62]. A detailed description of JUNO's solar neutrino programme can be found in [59].

### 3.1.5 Atmospheric neutrinos

The JUNO Collaboration plans to perform measurements of atmospheric neutrinos. The advantages of the detector will be the low energy detection threshold, excellent energy resolution, the foreseen particle identification performance and moreover the event reconstruction capabilities with respect to the direction of the charged leptons of a neutrino interaction. JUNO's investigations can be expected to improve the predictions on the atmospheric neutrino fluxes at low energies. Furthermore, they will provide a complementary approach to other detector types (e.g. Cherenkov detectors). As described beforehand, atmospheric neutrinos are a very important source for neutrino oscillation investigations, which can provide an independent determination of the mass ordering via matter effects [59]. Moreover, precise knowledge of the atmospheric neutrino flux is crucial for some rare event

searches (e.g. diffuse supernova neutrino background search), since atmospheric  $\nu$ s will cause the main background for this type of studies [59, 62].

### 3.1.6 Supernova burst neutrinos

A core-collapse Supernova (SN) emits its energy mainly in the form of neutrinos. In the Milky Way, three core-collapse SN per century are expected. JUNO aims for measuring both, the energy spectrum and the time evolution of the burst, which will be beneficial for testing the different existing theoretical SN models. As liquid scintillator detector, JUNO can measure all neutrino flavors via charged current (CC) and neutral current (NC) interactions as well as via elastic scattering, with a possible energy threshold of  $\sim 200$  keV. The dominant signal of a SN burst will come from the IBD and the detection can be considered to be practically background-free since the SN event duration is very short ( $\sim 10$  s). About 5000 IBD events are expected in JUNO from a core-collapse SN located at 10 kpc distance from earth. JUNO will be able to make areal time detection of the neutrino burst and is therefore being eligible to participate at the international SN alert networks [32, 59].

### 3.1.7 Diffuse supernova neutrino background

The integrated neutrino flux from all past core-collapse SN events in the visible universe forms the diffuse supernova neutrino background (DSNB). The DSNB intensity provides information on the average core-collapse neutrino spectrum, cosmic star-formation and the failed SN rate. JUNO is aiming for a first observation of DSNB at the level of  $3\sigma$  significance. The most critical background for this measurement will be created by NC interactions of atmospheric neutrinos. Using pulse-shape discrimination (PSD) techniques and given excellent PSD performance of the detector, this background might be reduced efficiently. A non-detection would strongly improve current limits and exclude a significant range of DSNB parameter space. A detailed description of JUNO's DSNB detection goals is given in [59], while a full background and sensitivity study can be found in [63].

### 3.1.8 Geo-neutrinos

Geo-neutrinos are important messengers to explore the composition of the earth. They will help in an estimation of the amount of radiogenic power driving the earth's engine. In JUNO most of the detected geo-neutrinos will come from the earth crust. Present models of the earth's bulk silicate composition predicting different mantle neutrino fluxes can be evaluated. On the other hand, the detector will not be able to discriminate the earth crust contribution from the mantle one.

Currently, an interdisciplinary team of physicists and geologists is working in the development of a local refined crust model around the JUNO site in Jiangmen [62]. About 400-500 IBD events per year are expected from  $^{238}\text{U}$  and  $^{232}\text{Th}$  geoneutrinos. The neutrinos emitted by the nuclear reactors near by will be the main background source. The IBD related reaction threshold of  $\sim 1.8$  MeV prevents a detection of neutrinos emitted in the decay of  $^{40}\text{K}$ . However, the excellent precision in the measurement of the oscillation parameters, JUNO is aiming for, should efficiently reduce the uncertainty of the expected antineutrino flux, thus allowing a measurement of the U/Th ratio in the earth at percent level [59].

### 3.1.9 Proton decay search

Baryon number violation is one of the prerequisites to explain the observed matter-antimatter asymmetry in the universe [64]. In particular, for the search of the two body proton decay

$$p \longrightarrow K^+ + \bar{\nu} \quad (3.4)$$

into a kaon and an antineutrino, which is favored by SUSY theories, JUNO will be competitive with present and future experiments using either water Cherenkov or liquid argon detectors [32].

In the 20 kt of JUNO's LS, the number of free protons (in hydrogen) can be estimated to be  $\sim 1.45 \times 10^{33}$ , while  $\sim 5.30 \times 10^{33}$  protons are bound in carbon nuclei [32]. In case of a proton decay, a prompt signal of 105 MeV energy in case of a free proton will be visible, while for a bound one the binding energy and Fermi motion modify the decaying proton's effective mass and momentum, which leads to a different kinematics of the decay process. The energy of the prompt bound proton decay signal will range from 25.1 MeV up to 207.2 MeV [65]. The kaon has a lifetime of 12.4 ns and decays via the following major channels (branching ratios in brackets):

- $K^+ \longrightarrow \mu^+ + \nu_\mu$  (63.43%)
- $K^+ \longrightarrow \pi^+ + \pi^0$  (21.13%)
- $K^+ \longrightarrow \pi^+ + \pi^+ + \pi^-$  (5.58%)
- $K^+ \longrightarrow \pi^0 + e^+ + \nu_e$  (4.87%)
- $K^+ \longrightarrow \pi^+ + \pi^0 + \pi^0$  (1.73%).

In case the  $K^+$  decays into a muon and a neutrino (for the expected signal shapes see Figure 3.3), a delayed signal of 152 MeV produced by the  $\mu^+$  travelling through the LS will occur. The muon decays subsequently ( $2.2 \mu\text{s}$  lifetime) via

$$\mu^+ \longrightarrow e^+ + \nu_e + \bar{\nu}_\mu \quad (3.5)$$

in a positron and two neutrinos. By this reaction the third even more delayed signal (shown in Figure 3.3) will be visible with a well known Michel electron energy spectrum [32, 65].

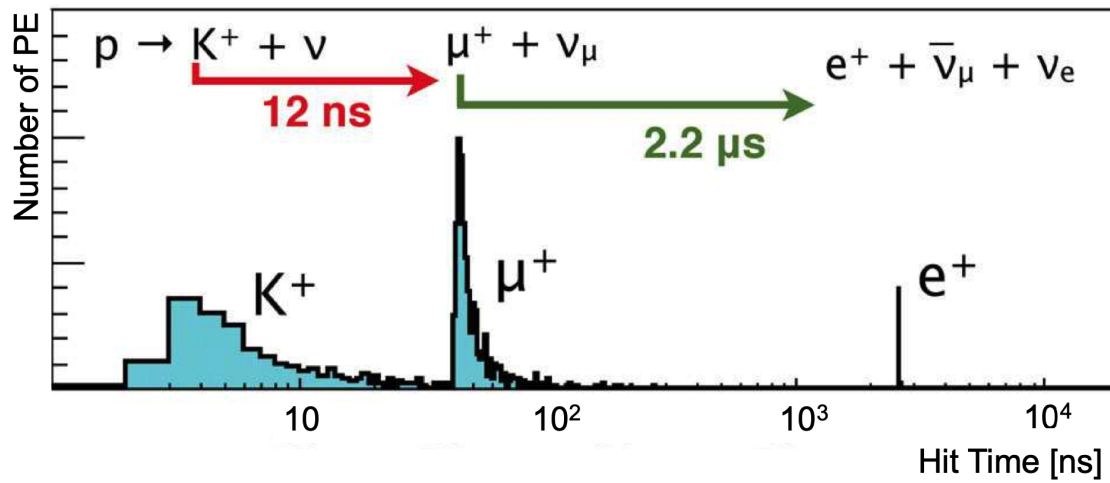


**Figure 3.3:** The hit time distribution of photoelectrons from a  $K^+ \rightarrow \mu^+ + \nu_\mu$  example event as simulated for the JUNO Conceptual Design Report [32]. Note, that the fast coincidence of the  $K^+$  and the muon is only resolvable if the fluorescence decay of the LS is fast enough.

If the  $K^+$  decays in two pions, the positive one deposits its energy (108 MeV) directly in the LS, while the neutral pion decays subsequently in two  $\gamma$ s with the combined energy of 246 MeV, which is the total  $\pi^0$  energy. The  $\mu^+$  produced in the decay of the  $\pi^+$  (low kinetic muon energy of 4.1 MeV) provides in its own decay according to equation 3.5, again a relatively long delayed signal, due to the  $2.2 \mu\text{s}$  lifetime of the muon. In conclusion, the three-fold coincidences and sharply-defined energies provide a powerful tool to tremendously reduce the background, which is crucial in the search for proton decays.

The sensitivity in a proton decay search using the JUNO detector along the runtime of the experiment was estimated in a preliminary Monte Carlo study. The result is shown in Figure 3.4 (assumed background model and detector performance can be found in [32]). According to this simulations JUNO's sensitivity will be superior to

Super-Kamiokande's within 3 years of data taking. This is mainly because the  $K^+$  does not reach the Cherenkov threshold and therefore can not be directly detected in this kind of detectors.

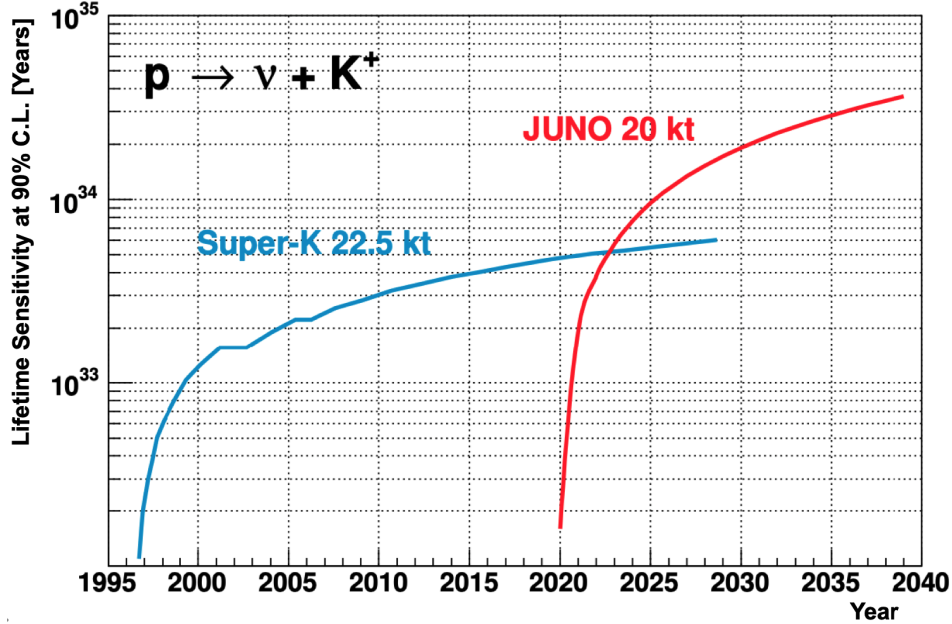


**Figure 3.4:** Simulated sensitivity (at 90 % confidence level) to the proton lifetime in JUNO compared with a projection of Super-K's sensitivity to 2029 [32].

## 3.2 General overview on the detector design

Since the JUNO experiment has a rich physics program and the detector is foreseen to participate in numerous rare-event searches, this results in numerous requirements for the detector design. The technical design of the experiment, which takes these requirements into account, will be explained in the following section, focusing on selected aspects of great importance for this thesis.

### 3.2.1 The mechanical structure of the detector

After the completion, JUNO will be the largest liquid scintillator detector ever built, containing 20 kt target mass made of Linear Alkyl-Benzene (LAB) based liquid scintillator, monitored by  $\sim 17600$  twenty-inch high quantum efficiency (QE) photomultiplier tubes (PMTs) and  $\sim 25600$  three-inch PMTs providing a total photo coverage of  $\sim 78\%$ . According to the conceptual design report [32] the LS will be stored in a 12 cm thick highly transparent acrylic hollow sphere with a diameter of

35.4 m. This construction is immersed in a  $\sim 44$  m deep pool containing  $\sim 35$  kt of ultra-pure water (see Figure 3.5). The water volume is instrumented with  $\sim 2400$  additional twenty-inch PMTs acting as a Cherenkov detector to tag and veto cosmic muons. Above the central part of the pool an additional (muon) tracking detector will be placed [32, 66].

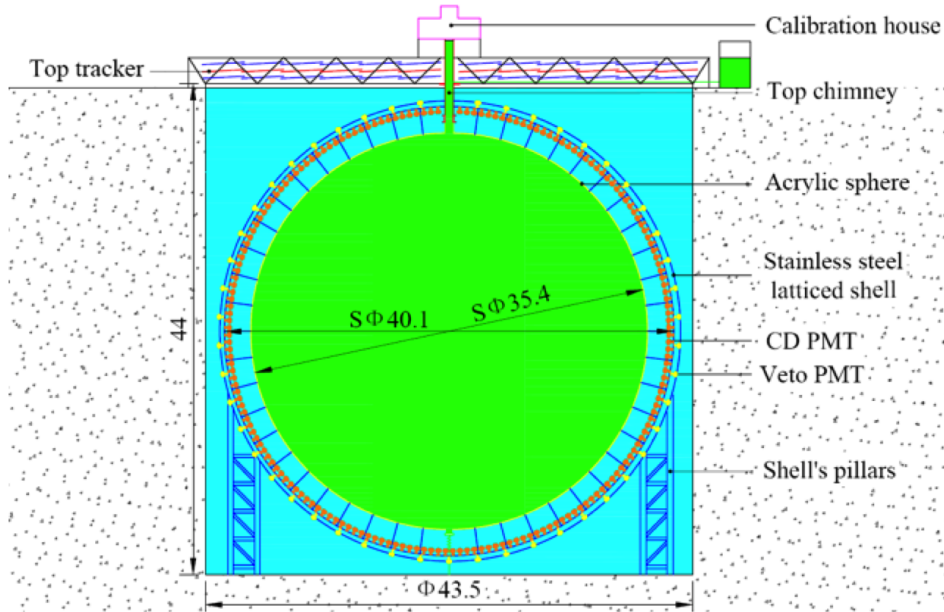


**Figure 3.5:** Scheme of the JUNO central detector. A 35.4 m acrylic sphere will contain 20 kt of LS inside a stainless steel latticed shell (inner diameter: 40.1 m). Inside this shell,  $\sim 17600$  twenty-inch and approx. 25600 three-inch PMTs (see CD PMT) are foreseen to detect the scintillation photons. A water pool (44 m deep and 43.5 m wide) instrumented with PMTs (see Veto PMT) acts as Cherenkov detector to tag and veto muons. An additional tracking detector (Top tracker) will be placed above the pool.

### 3.2.2 The PMT arrays

The scintillation light is read out in JUNO via two independent PMT arrays, one consisting of  $\sim 17600$  twenty-inch high-quantum efficiency PMTs and a second independent one with  $\sim 25600$  small three-inch PMTs. Their arrangement can be seen in Figure 3.6 [32].

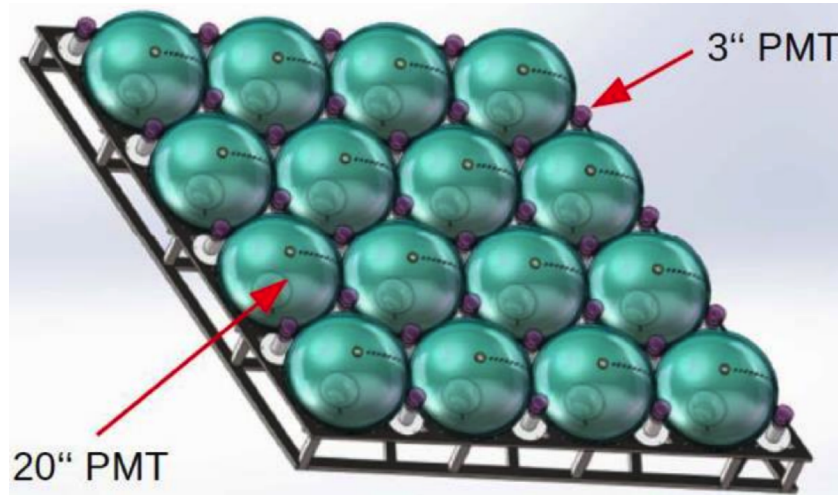


**Figure 3.6:** Arrangement of the PMTs on one of the scaffolding panels. The 20-inch PMTs are drawn in green. The small 3-inch PMTs (in purple) will be mounted in the gaps of the laying pattern of the large tubes to optimize the photo-coverage to an absolute value of  $\sim 78\%$ .

Specifications	MCP-PMT (NNVT)	R12860HQE
Det. Efficiency (QE · CE)	26.9% (new Type: 30.1%)	28.1%
Peak to Valley (SPE)	3.5 (> 2.8)	3.0 (> 2.5)
TTS (on top point)	12 ns (< 15 ns)	2.7 ns (< 3.5 ns)
Rise time	$\sim 2$ ns	$\sim 5$ ns
Fall time	$\sim 12$ ns	$\sim 9$ ns
Anode Dark Count	20 kHz (< 30 kHz)	10 kHz (< 50 kHz)
After Pulse Rate	1% (< 2%)	10% (< 15%)
Radioactivity (glass)	$^{238}\text{U}$ : 50 ppb $^{232}\text{Th}$ : 50 ppb	$^{238}\text{U}$ : 400 ppb $^{232}\text{Th}$ : 400 ppb

**Table 3.3:** Specifications of the two 20-inch PMT types. Since 2018 NNVT is providing a new PMT with enhanced detection efficiency. Numbers in brackets represent the acceptance criteria of PMTs for JUNO, while all other numbers represent typical values for the according specifications. With respect to the timing properties, the R12860HQE from Hamamatsu is superior to the NNVT tube. However, the glass used for the MCP-PMT contains significantly less uranium and thorium [66].

The large PMT array contains two 20-inch PMT types, the Hamamatsu R12860HQE optimized for high quantum efficiency (QE) and tubes using the multi-channel plate technology manufactured by Northern Night Vision Technology (NNVT). The large PMTs represent 75% optical coverage of the central detector. The specifications for both types can be found in Table 3.3. The small PMT array will be used as a second handle on the energy determination (double calorimetry) of an event [66]. This will be beneficial for cross-calibration of the large PMT system, will reduce nonlinearities and will give the detector a greater dynamic range and granularity. For example, muon tracking and shower calorimetry, as well as supernova readout and solar oscillation parameter measurements are supposed to gain from the small PMTs. In the array a 3-inch PMT custom design (XP72B22) provided by HZC-Photonics (Hainan, PR China) with 24 % QE, a single photon peak to valley ratio of 3.0:1 and a transition time spread of 2-5 ns will be used. The earth magnetic field will be compensated by dedicated coils in the detector [66].

### 3.2.3 Large PMT testing

While the small PMTs are tested by HZC in corporation with the JUNO Collaboration at the factory site, the large PMTs are stored and tested in Zhongshan Pan-Asia. There dedicated performance testing systems were installed. Two container test systems with electromagnetic shielding are currently used for mass acceptance tests. Each of them consists of 36 individual drawers (see Figure 3.7 a and b). The PMTs can be pulsed with a self-stabilized LED or a picosecond laser, both with 420 nm wavelength. A commercial switched-capacitor ADC (CAEN V1742) is used for waveform readout. Triggering and noise counting is realized via VME based leading edge discriminators (CAEN V895B) and latching scalers (CAEN V895AC). Using a PCIe computer bridge card and a custom made LabView based software, the entire system is controlled [66, 67].

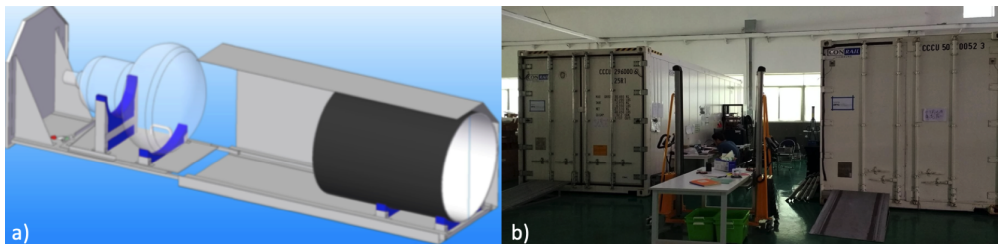


**Figure 3.7:** a) One of the PMT drawers as CAD Model. b) The two PMT testing containers in Zhongshan Pan-Asia.

In the containers the parameters charge resolution, single PE peak/valley ratio, operating voltage necessary for a gain of  $10^7$ , dark count rate (DCR), single PE

rise and fall time as well as pre-pulsing and after-pulsing rate are determined. The photon detection efficiency (PDE) of the PMTs already tested up to July 2019 (5000 Hamamatsu and  $\sim 7500$  NNVT) are shown in Figure 3.8 (the other parameters can be found in [68]).

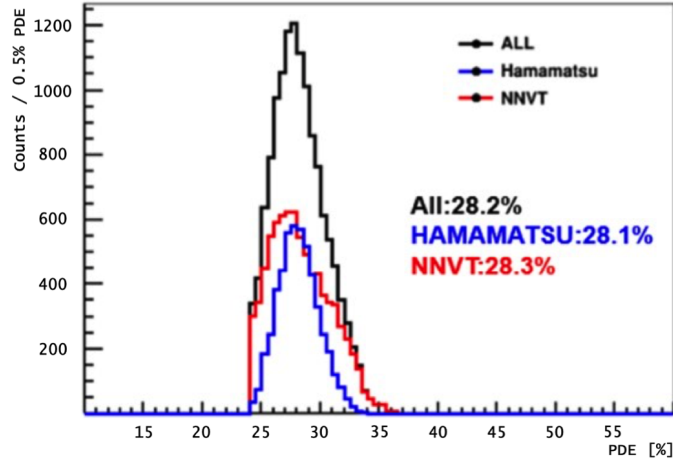


**Figure 3.8:** PDE of 5000 Hamamatsu (blue) and  $\sim 7500$  NNVT (red) 20-inch PMTs tested in the container system. The black curve represents the sum over the histograms for both PMT types.

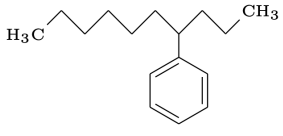
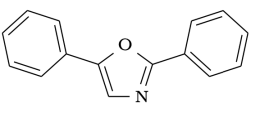
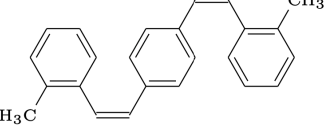
Beside the containers, two scanning stations were set up to irradiate the photo cathodes from 168 point-like sources. The scanning provides information about the non-uniformity of PMT parameters, as well as their earth magnetic field dependence (for a detailed description see [68]).

### 3.2.4 The JUNO liquid scintillator

JUNO's LS will consist of Linear AlkylBenzene (LAB) as solvent (density:  $0.863 \text{ g/cm}^3$ ) doped with 2,5-Diphenyloxazole (PPO 2.5 g/l) as fluor and 1,4-Bis(2-Methyl-Styryl)Benzene (BisMSB 3 mg/l) as secondary wavelength shifter (see also Table 3.4). LAB is a family of organic compounds with the formula  $\text{C}_6\text{H}_5\text{C}_n\text{H}_{2n+1}$ . For JUNO, a specific selection of carbon chain lengths ( $n=10-13$ ) will be used. Detailed descriptions of the energy transfer mechanisms for multi-component LSs can be found in [69], [70] and [71]. Moreover, a brief introduction is also presented in section 8.3.1 of the present thesis.

To meet the requirements (e.g. detector resolution) of the physics programme, a light yield above  $10^4$  photons per MeV has to be achieved in JUNO. In order to reach the necessary light collection (1100 p.e./MeV) in the detector, the attenuation length for the light emitted by the LS has to be comparable to the diameter

of the acrylic target holding sphere. As a consequence, the goal for JUNO is the realization of an attenuation length for 430 nm light above 22 m.

Function	Solvent	Fluor	Wavelength Shifter
Substance	LAB	PPO	BisMSB
Structure	 (typ. representative)		
Formula	$C_6H_5C_nH_{2n+1}$ (typ.: $n = 10-13$ )	$C_{15}H_{11}NO$	$C_{24}H_{12}$
Abs. max.	$\sim 260$ nm	303 nm	345 nm
Em. max.	$\sim 283$ nm	365 nm	420 nm

**Table 3.4:** The three substances used in the future JUNO LS. The table shows the wavelengths of maximum absorption (Abs. max) and emission (Em. max) taken from [72] and [73] in combination with the chemical structure and formula of the corresponding substance.

Low-background conditions are crucial for the success of JUNO. For the LS, this means that the concentration of radioactive impurities inside the liquid should result in an radioactivity of the same level or below the rate of neutrino events. For the determination of the NMO the IBD reaction (see also 3.1.2) provides a fast coincidence signature that can be used to suppress single-event backgrounds efficiently. For  $\nu_e$  detection (e.g. solar neutrino spectrography) this is not possible and the requirements on the LS purity are stricter. According to the Conceptual Design Report [32] the following mass concentrations for the corresponding isotopes have to be reached:

- $\bar{\nu}_e$  induced IBD detection:  
 $C(^{238}\text{U}) < 10^{-15}$  g/g,  $C(^{232}\text{Th}) < 10^{-15}$  g/g,  $C(^{40}\text{K}) < 10^{-16}$  g/g
- Solar Neutrino Spectrography:  
 $C(^{238}\text{U}) < 10^{-17}$  g/g,  $C(^{232}\text{Th}) < 10^{-17}$  g/g,  $C(^{40}\text{K}) < 10^{-18}$  g/g

To keep the pile-up rate provided by the low energetic background of the  $^{14}\text{C}$ -decays (Q-value: 156.5 keV) low and to allow JUNO's operation with acceptable trigger rates at low energy detection thresholds, the content of  $^{14}\text{C}$  in the detector should be kept below  $C(^{14}\text{C})=10^{-17}$  g/g.

This thesis is dedicated to the production of the high-purity scintillator of JUNO with low radioactivity and to the handling of this liquid in the filling system of the central detector. Furthermore, laboratory experiments were developed to characterize the LS in detail and to refine its recipe.

# Chapter 4

## Liquid scintillator production and purification

The optical performance of the LS is mainly affected by the solvent production and transportation methods. Furthermore, the attenuation length of the LS is influenced also by the different absorbance and cleanliness of each solute. The raw LAB attenuation length from high quality industrial production is  $\sim 15$  m [74]. However, if LAB is produced for standard industrial applications, the attenuation lengths stays below 10 m. Nevertheless, it remains to be noted that any oxidation of the LAB worsens substantially its optical properties. So for JUNO it is mandatory to avoid any contact between oxygen and LAB by keeping any transportation and storage vessel under a nitrogen blanket.

In order to achieve the stringent requirements on the LS optical and radioactive purity described in chapter 3, a composite purification system (see Figure 4.1) is foreseen, realizing a broad variety of purification steps. This system, which will be able to produce up to 10.000 l of purified LS per hour, is based on the technologies developed for scintillator production in the frame of previous neutrino experiments such as Borexino, SNO+ and KamLAND. Nevertheless, it will be the largest facility ever built for this purpose.

LAB, PPO and BisMSB are provided by trucks to the JUNO site in Jiangmen. In the above-ground storage area the entire amount of LAB will be stored in dedicated tanks. From this storage the liquid is pumped into the LS purification building. There the LAB is purified in two plants:

- **Filtration column filled with  $\text{Al}_2\text{O}_3$ :**

Alumina column filtration is intended to remove optical impurities from LAB. Alumina is very effective in removing optical contaminants through absorption mechanisms in the slightly acidic substrate with a grain size of  $\sim 100$   $\mu\text{m}$  [75].

- **A vacuum distillation column:**

Optical impurities, in principle, can be removed also through a distillation process by retaining in the lower part of the column the high boiling point compounds as well as dust, metal particles and usually oxides that can affect the light transmittance of the LAB. However, the main purpose of the vacuum distillation column is the removing of potentially radioactive heavy metals such as uranium and thorium. This distillation process is based on the heat and mass transfer between a gas stream and a liquid, due to the equilibrium conditions reached on each stage of a fractional distillation column. The equilibrium depends on the difference of volatility between the components of the input stream and on the pressure and temperature in the column. The high volatility components are concentrated on top of the column while the low volatility constituents will concentrate at its bottom [75].

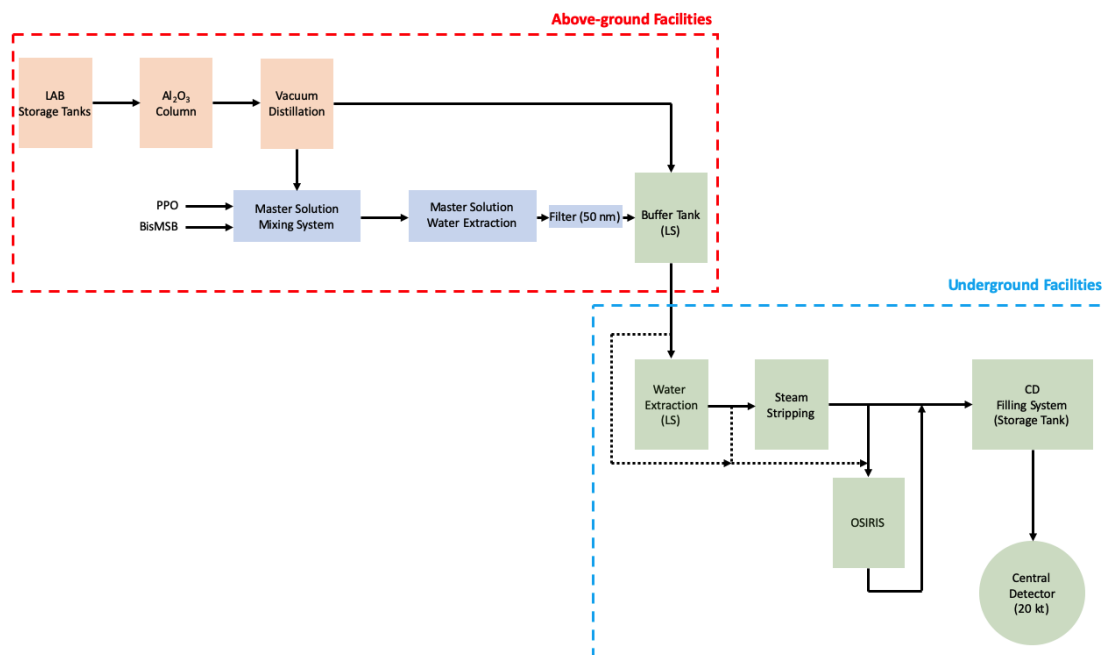


**Figure 4.1:** Simplified scheme of the JUNO LS production facilities. Above ground (facilities in red dashed box) the LAB will be purified by  $\text{Al}_2\text{O}_3$ -column filtration and vacuum distillation. PPO and BisMSB will be mixed with the distilled LAB to the so called master solution (LAB with 120 g/l PPO and 144 mg/l BisMSB), which undergoes a threefold water extraction process and fine filtration. Then the solution is diluted in a buffer tank to reach a PPO mass concentration in LAB of 2.5 g/l with 3 mg/l BisMSB. Afterwards, the mixture is sent underground (facilities in blue dashed box). There, the LS is treated with water extraction and steam stripping. After quality controls with respect to the optical purity a part ( $\sim 15\%$ ) of the LS is investigated on its radioactivity by OSIRIS (Online Scintillator Internal Radioactivity Investigation System) while the remaining 85 % will be transferred directly to the central detector filling facilities.

---

PPO and BisMSB are mainly purified by the supplying company. On the JUNO site the substances are mixed with LAB from the distillation plant in the master solution (MS) mixing station (see Figure 4.1). Subsequently this solution with 120 g/l PPO and 144 mg/l BisMSB undergoes a threefold water extraction process in the MS water extraction system using ultra pure water, which is produced on-site. After the extraction, the MS is sent through a 50 nm fine filter into the above ground LS buffer tank, where the MS is diluted with  $\text{Al}_2\text{O}_3$ -filtered and distilled LAB. The concentrations of PPO and BisMSB are adjusted to 2.5 g/l and 3 mg/l respectively in this tank. The LS cocktail will be finally sent underground through a 1.3 km long pipe to the final purification plants:

- **Water Extraction:**

Water extraction is an equilibrium stage process where LS and water are brought into close phase contact and then they are allowed to re-separate. The purification efficacy is based on the significant difference in solubility between water and LS for the contaminants. For JUNO a multistage extraction process is realized in form of a so called “Scheibel column” design where the heavy and light phases flow counter-current. Ionic heavy metal species such as U, Th, Ra and Pb will be removed as well as potassium and suspended ultrafine dust particles, which tends to be charged [75, 76].

- **Steam Stripping:**

The steam stripping is a variant of the gas stripping method where (instead of the conventionally used  $\text{N}_2$  gas) a variable mixture of superheated steam and nitrogen is used. The steam is generated from ultra pure water provided by a dedicated water purification system underground. The steam stripping technique was selected due to safety reasons in the underground LS hall. Furthermore, it can be considered to be more cost effective. Gas or steam stripping is a separation process in which one or more dissolved gases are removed from the liquid phase and transferred to the gas phase by desorption. Radioactive gases (mainly  $^{39}\text{Ar}$ ,  $^{85}\text{Kr}$  and  $^{222}\text{Rn}$ ) as well as oxygen are removed efficiently from the LS [75].

After the steam stripping the LS has passed all purification steps. To ensure a sufficiently low radioactivity and the required optical performance the LS will undergo several quality controls. Beside the checks for optical purity with LS samples of some 100 ml, the LS internal radioactivity will be tested. Therefore,  $\sim 15\%$  of the produced LS will be filled into the OSIRIS detector (discussed in detail in the dedicated chapter of this thesis) and screened with a sensitivity necessary to ensure the radioactivity levels required for efficient IBD detection in JUNO. The

remaining 85 % of the LS are directly filled in the CD, if there are no indications for a contamination or bad optical quality. In case the requirements to the LS are not reached, the purification steps underground can be repeated and furthermore the liquid can be circulated to the plants multiple times in an internal loop mode.

Currently, the technical designs of the  $\text{Al}_2\text{O}_3$ -filtration system, the MS mixing and purification stations and the water extraction plant are finalized by Chinese Collaborators at the IHEP (Institute for High Energy Physics) in Beijing. The distillation and stripping plants, for which the INFN (Istituto Nazionale di Fisica Nucleare) section of Milano is in charge, are already under construction at POLARIS in Monza. This company is specialized to the construction and fabrication of separation systems for process industry. After completion the composite purification system with all six plants will have a nominal LS production capacity of 7000 l per hour [75]. The OSIRIS monitoring detector with a screening capacity of  $\sim 20$  tons per day is in the final design phase by the German Research Unit JUNO.

## 4.1 Purification pilot plants in Daya Bay

When designing such complex facilities, it is mandatory to have a dedicated prototype phase with pilot plants to evaluate the feasibility of reaching all required purity parameters and the desired reliability of the systems. However, to determine reliably the expected low concentration of radioactive contaminants in the LS, a highly sensitive detector filled with several tons of LS, preferably located well shielded in an underground laboratory, is needed. Since the Daya Bay Collaboration [77], which currently operates 8 suitable antineutrino detectors (ADs) with  $\sim 20$  t of LS target mass each at Daya Bay (close to Shenzhen), is closely connected to the JUNO collaboration, the experimental site was chosen for the location of the pilot plants of all future purification systems. The pilot plants installed there in 2016/17 and tested, commissioned and operated in 2017 and 2018 realize a LS purification capacity of  $\sim 100$  l per hour.

The results of these pilot plant phase are discussed in the following sections as well as technical details on distillation and stripping system, since the participation in their installation, commissioning and operation over months was also part of this thesis.

### 4.1.1 The Daya Bay experimental site - a brief overview

The Daya Bay nuclear power complex is located in south China, 55 km northeast of Hong Kong. It consists of three nuclear power plants (NPPs), Daya Bay, Ling Ao and Ling Ao-II. Each NPP consists of two reactors, with  $2.9 \text{ GW}_{th}$  power per core.

There, the Daya Bay collaboration constructed an experiment for high precision reactor neutrino oscillation measurements at short baselines. The experimental facility consists of surface support buildings, three underground experimental halls (EH1-EH3) with two antineutrino detectors (ADs) in EH1 and EH2 and four ADs in EH3. Furthermore, there are two additional underground halls for LS production (LS Hall) and water purification (Water Hall) [77].

EH1 has an overburden of  $\sim 280$  meter-water-equivalent (mwe) and is about 360 m from the center of the twin cores of the Daya Bay NPP. EH2 has an overburden of  $\sim 300$  mwe and is placed some 500 m away from the four cores of the Ling Ao NPPs. EH3 is the deepest hall with 880 mwe in a distance of about 1910 m from Daya Wan and 1540 m from the Ling Ao NPPs [77]. A map of the experimental site with the NPPs can be seen in Figure 4.2.

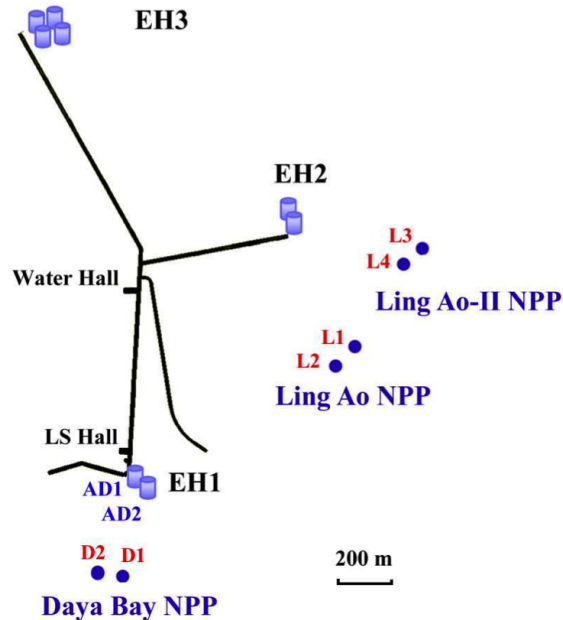


**Figure 4.2:** Map of the Daya Bay experimental site. Blue dots are indicating the reactor cores of Daya Bay, Ling Ao-I and Ling Ao-II NPPs. The experimental halls EH1-EH3 are containing two or four ADs respectively, which are indicated by blue cylinders. The water hall and the LS hall are shown as black rectangles. All underground halls are connected by horizontal tunnels with a 0.3 % slope to allow water drainage. The surface-access tunnel has a downward slope of 10 % slope and a length of 267 m, allowing the transportation of large and heavy equipment underground. Figure taken from [77].

### 4.1.2 The Daya Bay AD design

The Daya Bay ADs have three cylindrical volumes separated by concentric acrylic vessels as shown in Figure 4.3. The innermost acrylic vessel (called neutrino target) with  $\sim 3$  m diameter contains 20 t of Gd-loaded (0.1 % by weight) LS. The space between this cylinder and the 4 m acrylic vessel, called gamma catcher, is filled with 21 t of Gd-free LS. The outermost vessel (SSV) is constructed of stainless steel. Between SSV and gamma catcher 37 t of mineral oil are used to provide optical homogeneity and radiation shielding [77].

Three automated calibration units (ACU-A, ACU-B, and ACU-C) are installed at the top of the SSV in dedicated stainless steel domes. Each ACU is equipped with a pulsed LED based light source for detector timing calibration as well as two sealed capsules with radioactive isotopes that can be lowered individually into the neutrino target [77, 78].

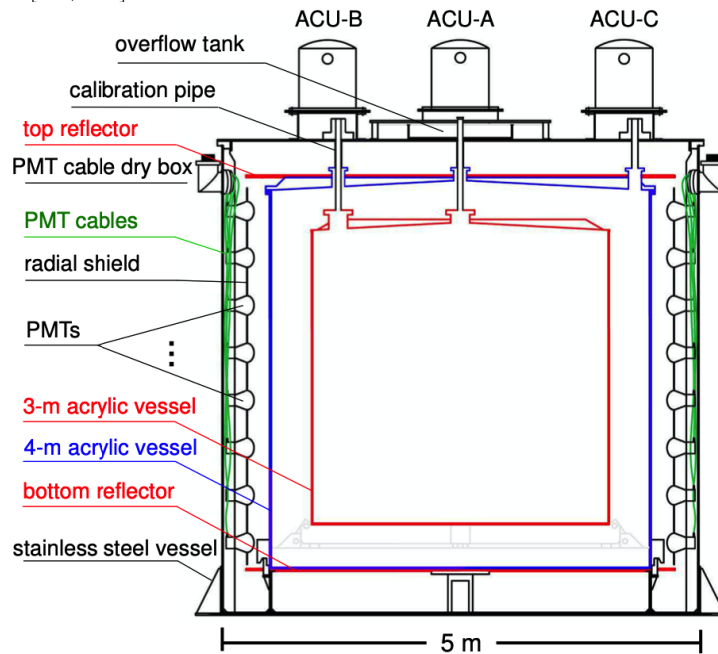


**Figure 4.3:** Schematic sectional view of a Daya Bay AD, which consists of three nested cylindrical vessels. The innermost hollow cylinder (made from acrylic) contains the neutrino target. The gamma catcher liquid is stored between the 3 m (red) and 4 m (blue) acrylic cylinder. 192 PMTs with 8-inch diameter are detecting the scintillation light while specular reflectors (drawn in red) at the bottom and top of the gamma catcher improve the photon collection efficiency. The outermost vessel made from stainless steel (black) is submerged in a water pool equipped with PMTs acting as water Cherenkov muon veto. The figure was adopted from [77], where a fully detailed description of the ADs can be found.

Two specular reflective panels with 4.5 m diameter are placed at the bottom and top of the gamma catcher vessel to improve the light collection efficiency. The scintillation light is read out by 192 PMTs (Hamamatsu R5912, 8 inch) mounted on eight ladders installed along the circumference of the SSV in contact with the mineral oil volume [77, 78].

The complete detector vessel is submerged in a pool filled with purified water produced with  $18 \text{ M}\Omega/\text{cm}$ . The water pool realizes at least 2.5 m of water surrounding for each AD in every direction. The pools in EH1 and EH2 containing two ADs are filled with  $\sim 1200 \text{ t}$  of water each, while in the pool with four ADs in EH3  $\sim 1950 \text{ t}$  are used. The pools consist of an inner and an outer optically separated part. Each one is equipped with PMTs and operates as independent water Cherenkov detector. The pool detects muons, neutrons produced by spallation and other cosmogenic backgrounds. Furthermore, the water moderates neutrons and attenuates gamma radiation emitted by the surrounding rock and other construction materials in the proximity of the detector [77, 78, 79].

### 4.1.3 Overview on the pilot plant installations

To test the technical design of the JUNO purification system, pilot plants for  $\text{Al}_2\text{O}_3$  filtration, vacuum distillation, water extraction and steam stripping were installed in the Daya Bay LS Hall. These systems are realizing a purification capacity of 100 l/h LAB or LS respectively. The connections of the plants to each other and the liquid handling and storage systems of the Daya Bay experiment are shown in Figure 4.4 while a photo of the finalized pilot plants installed in the LS Hall can be found in Figure 4.5. After purification, the LS can be filled into AD-1 in EH1 to allow a determination of the scintillator's internal radioactivity down to the required levels for the effective detection of the IBD reactions in JUNO. Beforehand, the Gd-loaded LS of the Daya Bay experiment has to be replaced by ultra pure water to avoid mixing of the two organic liquids and to pre-clean the detector. The purified LS is filled from the top into the neutrino target, while the water is pressed (and also pumped) out from its bottom. The LS in the gamma catcher and the mineral oil buffer can be reused without any exchange for this screening campaigns. The liquid handling system (LHS) allows the circulation of the LS from the central acrylic vessel through the entire purification chain and back to the detector. Also internal loop operations of each plant or a series of plants are possible.

All pipes and metal parts in contact with the LS were made of stainless steel (type: AISI 316L). To avoid leaks in the system, the connections between tubes have been realized by orbital welding. Before the distillation and stripping plants were shipped to Daya Bay, they have been previously mounted in their scaffolding by POLARIS in Monza. The inside of the plants and tubes were pickled and passivated as well as electro-polished to keep the contamination of the LS with  $^{222}\text{Rn}$  emanated from

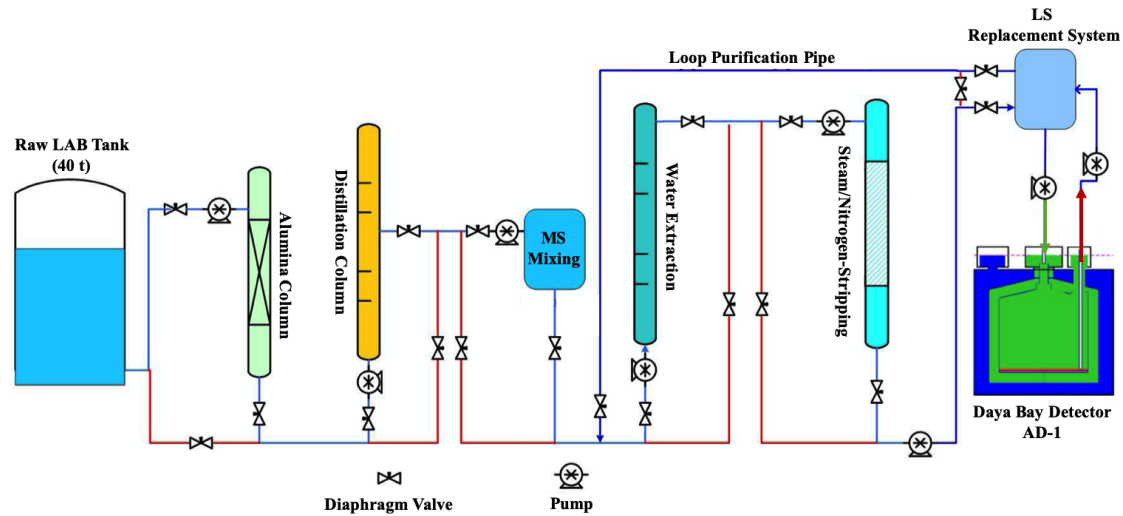


**Figure 4.4:** Schematics of the connections between the pilot plants and the Daya Bay LS infrastructure of EH1. Blue lines indicate the way of the liquids in normal operation conditions, while the red lines are indicating bypass connections. The raw LAB storage tank filled with 40 t of specially selected LAB for the test, is connected to the alumina column via a pump. The output of the filtration is led into the distillation column and from there into the MS mixing plant, which can also be bypassed. After water extraction and steam stripping the mixed LS is sent to the LS replacement system of AD1 in EH1. By the usage of a draining (red arrow) and a filling (green arrow) pump in the LS filling system of the detector, the LS can be filled into the detector. Before doing this, the previously used Gd-loaded LS in AD1 was replaced by ultra pure water to clean the detector and to avoid mixing of the two organic scintillators in direct contact to each other. Image taken from [80] (modified).

the steel surfaces and other radionuclides detached from it as low as possible. For the distillation and stripping facility simple mounting of the pre-assembled parts in the LS Hall and brief leak checking down to leak rates below  $10^{-6}$  mbar l/s were possible. During the commissioning all plants, pumps and pipes were rinsed with deionized water and finally extensively purged with pure nitrogen. After that a first LAB batch of some 300 l was circulated for purification in extensive loop operations of all plants. This LAB was finally drained out of the systems. The following two sections give an overview on the distillation and stripping pilot plants as well as their operation in 2017/18, since the participation in their installation and cleaning on-site, as well as their commissioning and operation over several months in dedicated testing campaigns were parts of this PhD project.



**Figure 4.5:** Photo of the pilot plants as they were installed in the LS Hall in Daya Bay in 2016/17. In the foreground, the water extraction system (left) and the filtration facility (right) can be seen. Behind them (on the left) are the stripping and distillation units in their blue assembly frames.

#### 4.1.4 The distillation pilot plant

The three major components of the distillation plant (schematic shown in Figure 4.6) are the 6 m high and 2 m wide column with six sieve trays, the condenser and the reboiler. The liquid LAB is fed in the column at a flow rate of  $\sim 100$  l/h in the middle tray section (see 1 in Figure 4.6). Beforehand, the LAB is preheated to  $\sim 160$  °C in the vapour condenser (see 2 in Figure 4.6) on the column top. By gravity the liquid stream is falling through the sieve trays and subsequently reaching the reboiler, which evaporates the LAB with  $15 \text{ kW}_{th}$  electric heating power (resistors immersed in the liquid). This generates a counter current flow of vapor and liquid in the system. The temperature in the reboiler is kept around 200 °C depending on the pressure in the column. A close contact between the liquid stream and the gas stream for a sufficient period of time to allow mass and heat transfer between the phases is realized by the tray design. During the contact of the two streams the liquid is enriched with less volatile components and the vapors are cooling down in the column [75].

The condenser in the column's top is cooled by the LAB input flow. This allows an energy recovery during the phase change from vapor to liquid. The product stream is split up by the condenser in two currents, one (the reflux) is reinserted into the column to increase the distillation efficiency and the other is directly sent to the heat-exchanger (see 3 in Figure 4.6) where the product liquid is cooled down to some 30 °C and subsequently filled in the product tank of the plant. The pressure inside the distillation column as well as in the bottom and product tanks is kept at  $\sim 5 \text{ mbar}_a$  using a oil free scroll vacuum pump (VP in Figure 4.6). Furthermore,

the facility is continuously purged with pure gaseous nitrogen to avoid oxidation inside the column. By this measure the risk of fire is also banned effectively. The vacuum condenser (see 4 in Figure 4.6) liquefies all remaining LAB vapors dragged out of the column by the nitrogen stream. The distilled LAB can be pumped back by a diaphragm pump (P in Figure 4.6) to the input tank. This allows an operation of the plant in an internal loop mode. By this pump, sending the product to the next purification plant is possible as well. In both cases the LAB passes a 50 nm pore filter, which can be bypassed if necessary. In order to recover the discharged liquid from the bottom of the column recirculation between the bottom tank and the input tank is possible via an additional diaphragm pump [75].

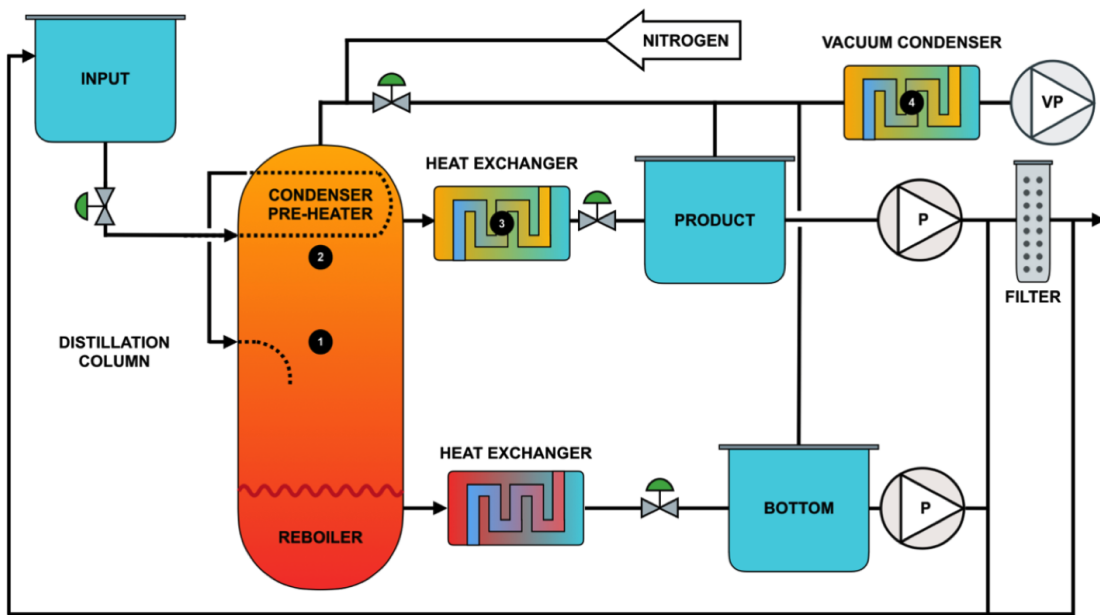


**Figure 4.6:** Drawing of the LAB fractional vacuum distillation pilot plant installed in the Daya Bay LS Hall. The input tank has a volume of  $\sim 1 \text{ m}^3$  and is continuously filled with raw LAB from the storage in the LS Hall during the LS production phase. The nominal input flow in the 6 m high and 2 m wide column is 100 l/h of LAB. The temperature in the top of the column reaches  $160 \text{ }^\circ\text{C}$  while a temperature of  $200 \text{ }^\circ\text{C}$  is typical for the reboiler. Two heat exchangers with a total cooling power of  $14 \text{ kW}_{th}$  are cooling the column's output flows. The liquid drained from the bottom goes to the bottom tank (with  $0.5 \text{ m}^3$  volume), while the purified product leaves the column on top and is led through the corresponding heat exchanger into the product tank (volume:  $0.5 \text{ m}^3$ ). Continuous nitrogen purging is realized in the system. A detailed description of the liquid and gas flows as well as the working principle of the column can be found in the text. The figure was taken from [75].

### 4.1.5 Stripping pilot plant

As mentioned before, in the pilot facilities LAB is purified by the alumina column and the distillation plant according to the final procedure for JUNO. After this purification step, the plants are no more purifying pure LAB, but LS mixtures with fluor and wavelength shifter. After the distillation the MS has been mixed using the pre-purified LAB. In the Daya Bay pilot plant mass concentrations of 100 g/l solvent for PPO and 280 mg/l for BisMSB are commonly used to meet the requirements of the LHS and the MS plant. The MS was water extracted in a batch mode using a dedicated stirring plant. After that the MS has been diluted with the pre-purified LAB to the final LS cocktail. Note, that for the first production tests, the content of MS in the LS was slowly increased to study the light emission of the LS for different PPO/BisMSB concentrations. The so produced LS is then led through the water extraction. The product tank of this plant is directly connected to the feed tank on the input of the stripping plant (see Figure 4.7).

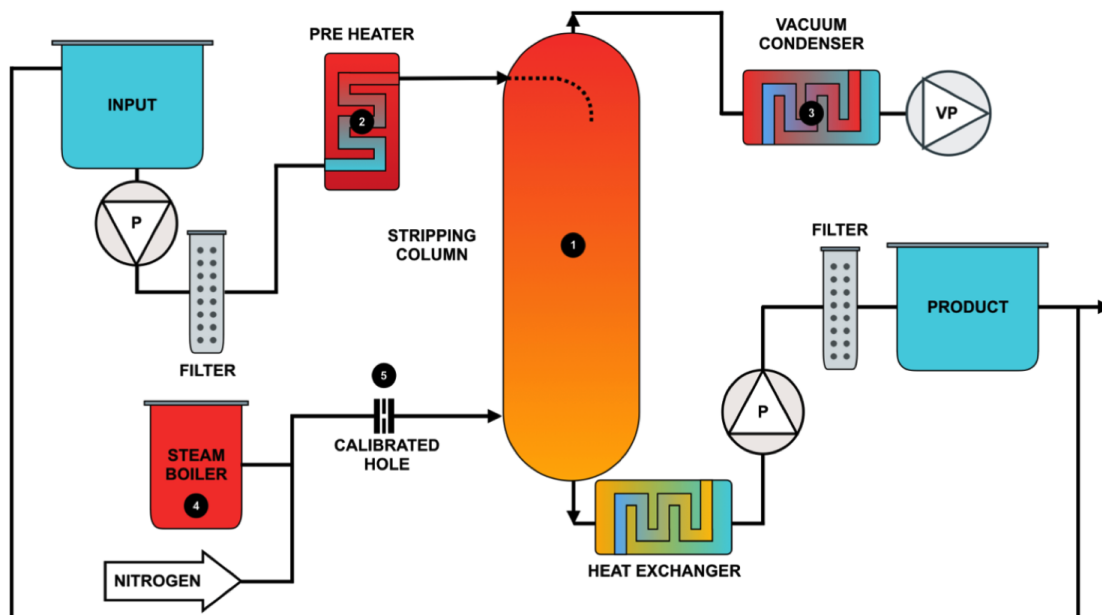


**Figure 4.7:** Schematic drawing of the steam stripping pilot plant. The input and product tanks have a volume of  $0.5 \text{ m}^3$  each. The input tank is connected via a diaphragm pump (P), a fine filter and a pre-heater for the LS to the top of the column (1). The product LS is extracted from the column's bottom, chilled by a heat exchanger and pumped using a diaphragm pump (P) through a filter into the product tank. The steam of high purity water is generated in the steam boiler (4) and subsequently mixed with nitrogen. The flow of steam and nitrogen is controlled by a calibrated hole (5) in the steam feed line. Also stripping without steam using pure nitrogen is possible. The drawing was adopted from [75].

---

A schematic drawing of the stripping plant is shown in Figure 4.7. The LS is pumped (diaphragm pump) from the input tank through a 50 nm pore filter into a pre-heater (see 2 in Figure 4.7). The pre-heated liquid stream ( $\sim 80$  °C) enters the stripping column (1 in Figure 4.7) from the top and falls down through an unstructured packing in the form of Pall rings. This ensures a high contact surface between the liquid and the gas coming from the column's bottom. The gas flow (counter current to the falling LS) is an adjustable mixture of steam and nitrogen. The absolute quantity of the  $N_2$ /steam-mixture, which is fed into the column is controlled by a calibrated hole (5 in Figure 4.7) in the steam feed line. In the normal operation mode a mixture of steam produced in the steam boiler (see 4 in Figure 4.7) and nitrogen is used. In a second operation option (without steam) only nitrogen from the  $N_2$  plat of the Daya Bay experiment is used. The stripped liquid is collected at the column's bottom and sent through a heat exchanger and another fine filter to the product tank. The LS can be sent back to the input tank for an internal loop operation of the plant or it can be pumped directly to the filling station of AD1 [75].

## 4.2 LS production and AD1 filling test

After the installation, cleaning and commissioning of all systems in the purification chain (at the end of 2016) a first full scale LS production test with filling of AD1 was scheduled for February and March 2017. A month before the test, the old Gd-loaded LS in the detector was replaced by ultra pure water. During the following month the radon introduced by the diffusion into the LHS as well as by emanation from the LHS itself had the time to decay.

For the production of  $\sim 24 \text{ m}^3$  of LAB based scintillator (comparable with the JUNO recipe) the raw LAB storage tank of the LS hall in Daya Bay was filled with 40 t of a special high quality LAB produced by SINOPEC Jinling Petrochemical Company with a selection of typical carbon chain length  $n$  between 10 and 13. The detailed composition can be found in Table 4.1.

Components $\text{C}_6\text{H}_5\text{C}_n\text{H}_{2n+1}$	Concentration [%]
$n = 9$	$\sim 0 \%$
$n = 10$	$\sim 10 \%$
$n = 11$	$\sim 35 \%$
$n = 12$	$\sim 35 \%$
$n = 13$	$\sim 20 \%$
$n = 14$	$\sim 0 \%$

**Table 4.1:** LAB is a mixture of molecules with the formula  $\text{C}_6\text{H}_5\text{C}_n\text{H}_{2n+1}$ . For the LAB used in the LS production test SINOPEC Jinling Petrochemical Company specified the concentrations of each molecular species by the given numbers in the right column. The LAB is not containing chain length shorter than 10 or longer than 13 carbon atoms. All numbers of the table were taken from [75].

As mentioned before, the Gd-LS in AD1 was replaced by pure water within 7 days using the LS replacement system, mounted to the LHS in EH1. The amount of residual Gd-LS can be estimated to be  $\sim 10 \text{ l}$ . After two weeks of waiting, the LS production facilities were started and operated in an internal loop mode until nominal operation conditions were reached. During the first three days of nominal purification, pure LAB was produced and filled into AD1. After that, the MS plant started its operation and the LAB in AD1 was mixed with MS to reach a PPO concentration of  $\sim 0.5 \text{ g/l}$  PPO without BisMSB. Since then, the purification plants produced LS with a rate of  $\sim 100 \text{ l/h}$ . The liquid was directly filled, using the LS replacement system, into the detector until the nominal filling level was reached (on 03/07/2017). The measurements with the filled detector had two major goals: the determination of the radioactive contamination in the LS and the optimization

of the PPO and BisMSB concentrations with regard to the light yield of the LS mixture [79].

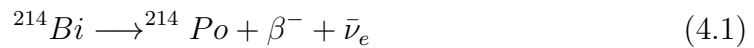
To obtain the radiopurity of LS with 0.5 g/l PPO the replacement system was shut down after ten additional days of self circulation. In the following, the radon load in the detector was decaying over two month. After that the content of uranium- and thorium-chain contaminants was determined.

After this phase of sealed detector operation, the light yield of the mixture was determined with a  $^{60}\text{Co}$  calibration source deployed at the detector center. Since May 20., PPO and BisMSB were added to the LS in the detector in 12 steps as summarized in Table 4.2. In each step the replacement system was working in an internal loop with the detector and a buffer tank of the water extraction system in the LS Hall with a circulation rate of 300 l/h. The PPO and BisMSB was slowly added to the buffer tank. Then the replacement system continued its operation in the self circulation mode for 36 h, which results in a circulation of the half detector LS volume. This measure was taken to produce a uniform distribution of fluor and wavelength shifter. Their concentrations have been measured every 12 hours with a commercial UV/Vis spectrometer. After two days of self circulation the concentration could be considered stable at the target value [79].

### 4.2.1 Achieved $^{238}\text{U}$ and $^{232}\text{Th}$ concentrations

Since the reconstruction and analysis of the data from AD1 requires profound knowledge and experience with the detector as well as access to the Daya Bay Monte Carlo framework, the analysis is currently carried out exclusively by scientists of the Daya Bay Collaboration. While writing this thesis, the final results are prepared for publication. Here, only a first overview of the analysis methods and the results can be given.

To determine the concentration of  $^{238}\text{U}$  and  $^{232}\text{Th}$  in the LS, the fast coincidences of bismuth and polonium decays in the corresponding decay chains were exploited. In the uranium decay chain  $^{214}\text{Bi}$  has a half-life of  $\sim 19.9$  min and decays with a branching ratio of 99.98 % via



in polonium. The half-life of this daughter isotope is with  $164.3 \mu\text{s}$  so short, that the subsequent alpha decay via



provides a very well resolvable delayed signal for the frontend electronics (FEE) [81]

of AD1. This delayed coincidence allows an efficient background reduction. In the thorium chain the corresponding coincidence of



with a branching ratio of 64.06 % and



is due to the  $\sim 299$  ns half-life of  $^{212}\text{Po}$  significantly faster. To allow an efficient detection of this fast coincidence a FADC system, which is able to record 1000 ns long traces of the connected PMTs, has been used in parallel to the conventional FEE readout electronics of AD1.

After a detailed event selection and efficiency estimation (described in [82]) the following plot (see Figure 4.8) for the  $^{222}\text{Rn}$  event rate obtained from the  $^{214}\text{Bi}/\text{Po}$  coincidences in AD1 was generated for the days after the detector filling test.

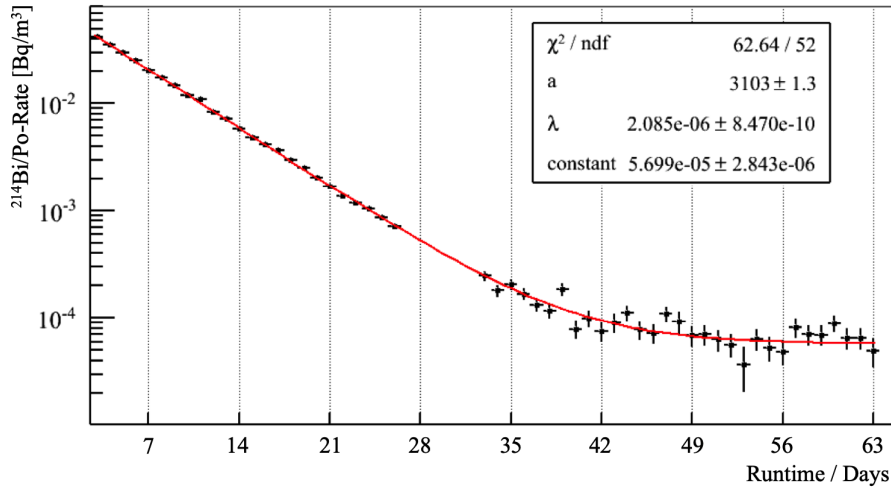


**Figure 4.8:** Plot of the  $^{214}\text{Bi}/\text{Po}$  coincident event rate in AD1 in the 63 days after the filling with purified LS. The red curve represents a fit of the data using an exponential function with an additional constant background. The half-life of the decay rate was calculated to be  $\sim 3.8$  days in well agreement with the half-life of  $^{222}\text{Rn}$ . Plot adapted from [82]

It can be seen directly, that the LS was loaded with radon during the detector filling. Over a time of approx. 4 weeks the radon decayed down to a constant level. By fitting the data points with an exponential decay function (red curve in Figure 4.8)

$$R(t) = N_0 e^{-\lambda t} + \text{constant} \quad (4.5)$$

with  $N_0 = e^a$  a half-life of  $T_{1/2} = (3.847 \pm 0.002)$  days (uncertainty purely statistical) was obtained [82] in well agreement with the literature value for the  $^{222}\text{Rn}$  decay.

According to [82] the constant  $^{222}\text{Rn}$  decay rate  $R_c$  was determined to be

$$R_c = (5.70 \pm 1.07(\text{sys.}) \pm 0.28(\text{stat.})) \times 10^{-5} \text{Bq/m}^3. \quad (4.6)$$

Assuming a density of  $0.85 \text{ g/cm}^3$  for the liquid, the mass concentration of  $^{238}\text{U}$  in the LS was estimated in [82] to be

$$C(^{238}\text{U}) = (7.52 \pm 1.41(\text{sys.}) \pm 0.37(\text{stat.})) \times 10^{-15} \text{g/g}. \quad (4.7)$$

The corresponding values for the  $^{220}\text{Rn}$  event rate and the contamination of the LS from the  $^{232}\text{Th}$ -chain are according to the analysis of Zhang, Wu and Yu [82]

$$R_c = (7.83 \pm 2.41(\text{stat.}) \pm 1.58(\text{sys.})) \times 10^{-6} \text{Bq/m}^3 \quad (4.8)$$

and

$$C(^{232}\text{Th}) = (3.24 \pm 1.00(\text{stat.}) \pm 0.66(\text{sys.})) \times 10^{-15} \text{g/g}. \quad (4.9)$$

In an independent analysis by A. Formozov and E. Meroni [83], using the reconstructed data set of AD1, these values were confirmed.

### 4.2.2 Results of the light yield optimization study

After the measurement of the scintillator's internal radioactivity with a sealed detector over 2 month, a calibration using a  $^{60}\text{Co}$  source deployed by one of the ACUs into the detector center was performed. During the following weeks the PPO and BisMSB concentrations were increased in twelve steps according to Table 4.2. After the fluor and wavelength shifter have reached a homogeneous distribution in AD1 a new calibration was carried out. The concentrations of fluor and wavelength shifter were measured every 12 hours with a commercial UV/Vis spectrometer. The light yield of the corresponding LS mixture is obtained by dividing the fitted  $^{60}\text{Co}$  peak position of each calibration with 2.505 MeV, which is the total energy of the two gamma quanta emitted by  $^{60}\text{Co}$  decays. During the entire campaign

Step	PPO Concentration [g/l]	BisMSB Concentration [mg/l]	Light Yield [p.e./MeV]
0	0.5	0.0	$123.7 \pm 0.7$
1	1.0	0.0	$150.3 \pm 0.8$
2	2.0	0.0	$167.7 \pm 0.8$
3	2.0	0.1	$177.2 \pm 0.9$
4	2.0	1.0	$183.2 \pm 0.9$
5	2.0	4.0	$184.3 \pm 0.9$
6	2.0	7.0	$184.3 \pm 0.9$
7	2.5	7.0	$188.7 \pm 0.9$
8	3.0	7.0	$191.6 \pm 1.0$
9	3.5	7.0	$192.6 \pm 1.0$
10	4.0	7.0	$192.6 \pm 1.0$
11	4.0	10.0	$193.0 \pm 1.0$
12	4.0	13.0	$193.3 \pm 1.0$

**Table 4.2:** Table of the tested LS mixtures in the Daya Bay LS purification pilot plant tests. The concentrations of PPO and BisMSB were increased in 12 steps. The resulting light yields obtained by a  $^{60}\text{Co}$  calibrations of AD1 are denoted in the right column. All numbers were taken from [79].

the temperature of the LS was kept stable within 0.2 °C. With pure PPO in the LS mixture the light yield increases by more than 40 % from 0.5 g/l to 2 g/l. By adding 1 mg/l a further increase of  $\sim 10$  % was achieved. For higher admixtures of BisMSB no significant increase could be observed. The result is also shown in Figure 4.9 (left) illustrating all 13 data points, while a detailed study of all systematic uncertainties can be found in [79].

After reaching the final concentration of the light yield study with 4 g/l PPO and 13.0 mg/l BisMSB, the stability of the light yield was evaluated in series of calibrations from August 2017 to January 2019. In this long term study no indication for ageing of the LS could be found. The light yield as shown in Figure 4.9 (right) was stable within a  $\pm 0.5$  % band.

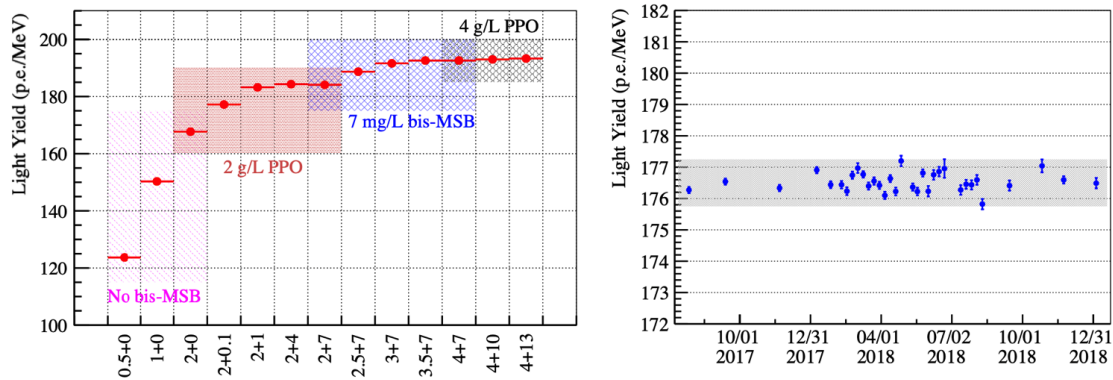


**Figure 4.9: Left:** The measured light yields for the corresponding admixtures of PPO and BisMSB to LAB in AD1. The labels of the horizontal axis denote the concentrations of PPO (g/L) and of BisMSB (mg/L). The statistical error bars for the light yields are too small to be visible. The coloured boxes indicate measurements with equal PPO or BisMSB amounts respectively. **Right:** The right plot shows the result of the long term stability study of the light yield of LAB with 4 g/l PPO and 13 mg/l BisMSB. From the first measurement in August 2017 to the last one in January 2019 the obtained light yield was stable within a  $\pm 0.5\%$  band (grey shaded region). Both plots were adopted from [79] in courtesy.

### 4.3 Nitrogen stripping efficiency test

In order to evaluate the efficiency of the radon removal by  $N_2$  stripping of the LS, an evaluation test of this system was carried out in November 2017. Therefore, the LS was loaded with nitrogen beforehand in a water extraction process by using water with a higher radon load than the one during the LS production. Before the water extraction, the LS was circulated through the LS replacement system in EH1. Subsequently, the radon count rate in AD1 started to increase, due to the accumulation of radon from the system. The count rate in the neutrino target of AD1 during these measures is shown in Figure 4.10.

When circulating back LS after the water extraction from the plant to AD1 (45 h after the beginning of the test) a steep rise by more than one order of magnitude in the  $^{222}\text{Rn}$  count rate occurred. After the nominal filling level of the detector was reached, the stripping test started. During this  $N_2$  stripping campaign, half of the LS volume was circulated in a loop of the stripping pilot plant and the detector with a flow rate of  $\sim 115$  l/h.

The visible  $^{222}\text{Rn}$  count rate during the stripping test is shown in Figure 4.11. Before the flow of nitrogen and with that the stripping in the column was started, the leak rate was evaluated by circulating LS for  $\sim 24$  hours through the system

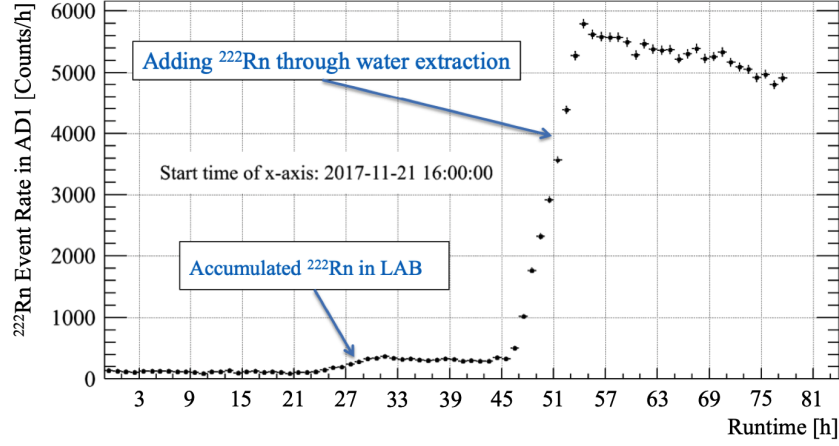


**Figure 4.10:** The radon decay rate in the neutrino target of AD1 during the water extraction process intended to load the LS with radon. After a rise due to accumulated radon in the LS replacement system around 27 h after the beginning of the test, the water extraction started. When circulating back LS from the water extraction system to the detector a steep rise of the  $^{222}\text{Rn}$  decay rate occurred. The aim of the following stripping tests was to reduce the radon load faster than the natural decay and by doing so to evaluate the efficiency of this purification process. The plot was taken from [84] and modified.

(8h-32h runtime). 32 hours after the beginning of the test, the stripping column started its nominal operation.

According to [84] the stripping efficiency can be obtained from the visible decays in AD1. By using the equation

$$N_t^{ex} = N_{t-1h}^{ex} \cdot (e^{-\lambda\Delta T} - F \cdot \eta \frac{\Delta T}{FV}) + leak \quad (4.10)$$

the number of expected decays within one hour  $t$  can be calculated from the number of decays within the previous hour  $t-1$ . In this model  $\lambda$  denotes the decay constant of  $^{222}\text{Rn}$  and  $\eta$  represents the stripping efficiency. All times  $t$  and time intervals  $\Delta T$  are binned (1 h bin width), while the leak rate is also given in 1/h. FV is the fiducial volume selected in AD1. For this study the entire neutrino target with  $23.5 \text{ m}^3$  volume was used [84]. By a  $\chi^2$  minimization of

$$\chi^2 = \sum_t \frac{(N_t^{ob} - N_t^{ex})^2}{N_t^{ex}} \quad (4.11)$$

where  $N_t^{ob}$  denotes the observed number of counts in an hour  $t$ , the data can be

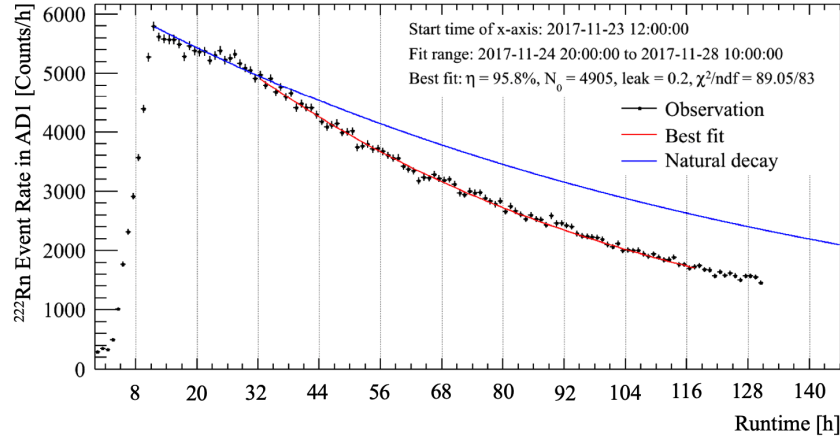


**Figure 4.11:** Event rate in AD1 during the stripping pilot plant test. From 8 h to 32 h the leak rate of the system was evaluated by circulating LS from the detector through the column without nitrogen flow. After that the stripping plant was operated under normal conditions with a flow rate of  $\sim 115$  l/h of LS. The blue curve represents the event rate in AD1 expected from the natural radon decay, while the data points during the stripping fall clearly below this line. The red curve represents a fit of the data with a model described in the text. Approximately 95 % of the radon load in the LS was removed within the stripping column. The plot was taken from [84] and modified.

fitted (see red line in Figure 4.11). By doing so, the stripping efficiency  $\eta$  was estimated to be  $\eta = (95.8 \pm 1.1) \%$  [84].

## 4.4 Conclusions from the pilot plant phase

In Daya Bay, pilot plants with a purification capacity of 100 l/h LAB (or LS) were successfully set up, commissioned and operated during a dedicated testing campaign for more than a year. This confirmed the technical feasibility and the mode of operation of all systems. In particular the distillation and the stripping plant showed excellent reliability and leak tightness. Nevertheless, refilling the  $\text{Al}_2\text{O}_3$  column proved to be difficult and the life of the alumina substrate until its saturation with impurities from the LAB has not been fully understood yet. Operating the water extraction pilot plant, especially when loading the LS with radon (when less pure water was used) demonstrated clearly the need for excellent ultra-pure water systems of sufficient capacity for the JUNO experiment at the Jiangmen site. The distillation and the stripping plant for JUNO are already under construction by POLARIS in Monza and will be shipped to China in the first half of 2020. The plans for the  $\text{Al}_2\text{O}_3$  column and the water extraction system are

currently revised with subsequent collaboration internal reviews. Nevertheless, it should be mentioned that the goals of the LS production test could be reached only partially. While the optical transparency [85] and light yield of the JUNO LS was measured to comply with the specifications, the radiopurity levels did not reach the required  $10^{-15}$  g/g for the uranium and thorium concentrations. This discrepancy is at least partially due to certain inadequacies of the AD and the filling setup that were not designed to support a detector reaching such low background levels. All flanges, pipes, pumps as well as the cover gas and N<sub>2</sub> support system of the LS storage tanks and the detector itself were not designed to fulfill the strict radon tightness requirements of JUNO. The pilot plant phase shows clearly that, despite of the substantial experience gathered in Borexino, reaching the radiopurity required for JUNO should not be taken as given. During the two years of extensive testing, each individual plant was evaluated using the detector and important informations for the improvement of the pilot systems were gained. In the dedicated stripping test in November 2017 the efficiency for the radon removal by stripping was evaluated to be  $\sim 95$  %. Furthermore, this test demonstrated clearly the advantages of a radioactivity monitoring detector (with approximately the target mass of AD1) for the commissioning of the purification systems with greater complexity and dimensions in Jiangmen. The installation of such a detector as an integral part of the purification and filling system chain of the JUNO experiment seems very appropriate. This LS radioactivity monitoring detector should be designed to allow LS screening measurements down to uranium and thorium concentrations of  $10^{-16}$  g/g as well as investigations of the <sup>14</sup>C, <sup>85</sup>Kr and <sup>210</sup>Po contents.

# Chapter 5

## The OSIRIS detector project

To address the conclusions from the Daya Bay purification pilot plant tests the OSIRIS (Online Scintillator Internal Radioactivity Investigation System) task force was formed within the LS working group of the JUNO Collaboration. The goal of the OSIRIS project is to construct a LS radiopurity monitoring detector with a  $\sim 19$  t LS target as an integral part of the JUNO purification and CD filling chain. There are three major purposes of the OSIRIS facility: to provide radiopurity data during the commissioning of the LS purification plants, to ensure their faultless operation by continuous monitoring of the LS radiopurity during the CD filling and to act as a test bed for JUNO detector subsystems [86].

The detector's dimensions are optimized to screen the LS internal radioactivity down to mass concentrations of  $10^{-16}$  g/g for  $^{238}\text{U}$  and  $^{232}\text{Th}$  within one day of measurement. Therefore, exploiting the fast Bi/Po-coincident decays is foreseen. In this chapter a brief overview of the global facility design, OSIRIS' integration in the JUNO liquid handling and purification system as well as the current status of the Monte Carlo studies will be presented.

### 5.1 Overview of the OSIRIS detector design

The OSIRIS detector will be constructed in the underground Scintillator Hall (SH) in immediate proximity to the underground plants of the purification system. This ensures short piping to the JUNO purification and also detector filling system.

The SH is tunnel-shaped with a maximum height of 15 m. The hall crane for lifting heavy equipment is running on a single bar oriented along the ceiling. The clearance below the hook is  $\sim 13$  m. Access to the hall crane will be blocked by the height of the installation of the water extraction plant as soon as it is constructed. Therefore, the order of installing facilities in the SH is determined by the availability of this crane. As shown in Figure 5.1, the area foreseen for OSIRIS is a square of

$\sim 9$  m by  $\sim 9$  m in the central section of the SH. Firstly, the steam stripping plant will be constructed by using the hall crane (see Figure 5.1). After that, the heavy part installation (requiring a crane) of OSIRIS will be carried out followed by the installation of the water extraction and ultra pure water plant.

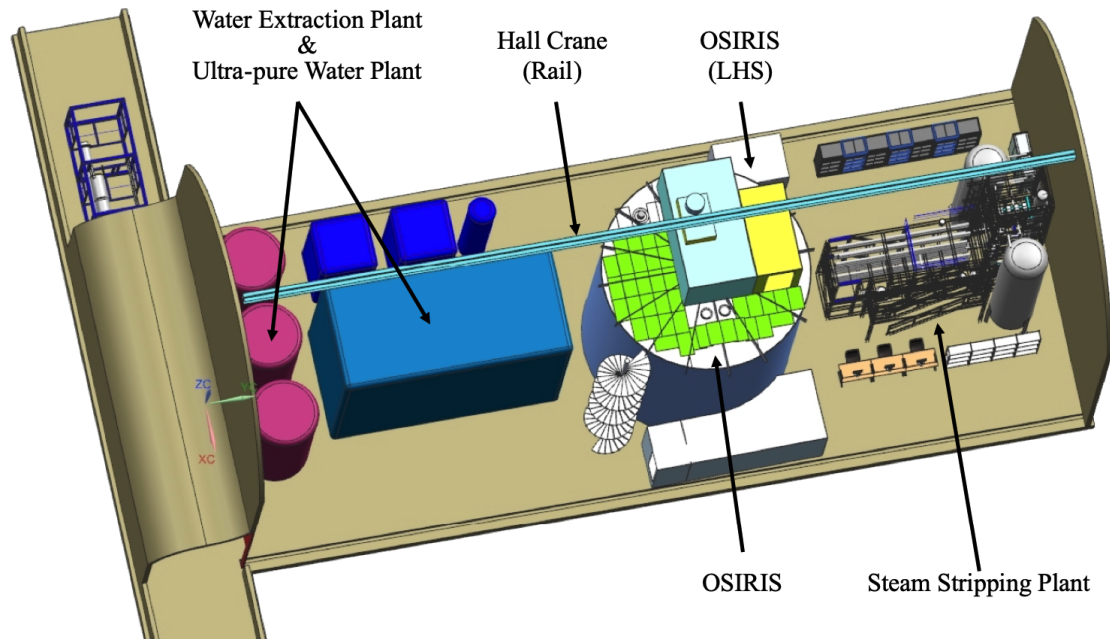


**Figure 5.1:** Current planning status of the underground scintillator hall. Firstly the steam stripping system will be installed at the closed end of the hall. After that, the installation of OSIRIS (mainly the outer structure) will be done in the middle section of the hall. Subsequently, the water extraction plant and the ultra-pure water system (only place holders in the drawing) will be mounted in the hall.

The basic dimensions of the OSIRIS facility are given by the requirements of the BiPo coincidence searches and the available space in the SH. A CAD model of the current technical design of the OSIRIS detector is presented in Figure 5.2. The outer dimensions of the setup are determined by the carbon steel tank, with 9 m high and diameter, holding the water buffer which is acting also as active muon veto. Since welding must be avoided underground due to strict clean room requirements, the tank is joined with bolts and sealed with an HDPE (High Density Polyethylen) liner [86].

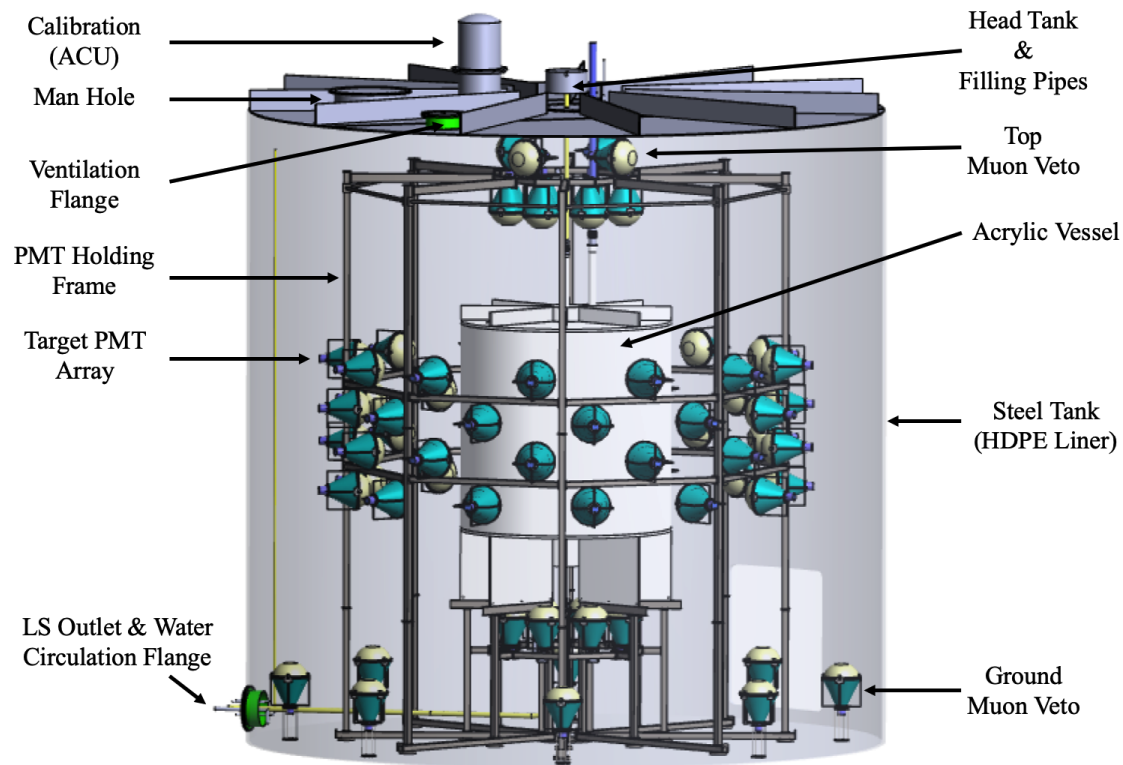


**Figure 5.2:** Simplified 3D-model of the OSIRIS detector. The drawing shows the overall cylindrical dimensions of the outer water buffer tank as well as the inner acrylic vessel. The PMTs for reading out the light of the LS target and the cherenkov veto are indicated as well. Furthermore, some interfaces, the head tank and the calibration system dome are shown. A full description is given in the text. The drawing was adopted and modified from [87].

The water volume is instrumented with 12 Hamamatsu R12860HQE PMTs with 20 inch photo cathodes as used in the CD of JUNO. Eight of them are placed on the bottom and four on the top of the water tank. 68 PMTs of the same type will read out the scintillation light from the LS target. To hold them in place a stainless steel frame is foreseen. In the frame's center, the LS batch under investigation will be held by a highly transparent  $\sim 3$  cm thick acrylic vessel (AV) equipped with a star-shaped foot. The 3 m high cylindrical AV with 3 m diameter will contain  $\sim 19$  t of LS. For calibration one of the ACUs [78] from the Daya Bay experiment is overhauled, modified and placed under a steel dome on the detector lid. The head tank for stabilizing the LS filling level in the AV is also installed there [86]. The major components essential for the operation of OSIRIS will be discussed in the following sections.

### 5.1.1 Outer steel tank

As mentioned before, the SH will realize an ISO8 standard cleanroom environment. Therefore, welding of the tank underground would be in conflict with lab cleanliness requirements. As a consequence, the tank will be constructed in a modular way. Previously produced steel panels (from carbon steel Q235A) will be bolted together piece by piece instead of welding the structure. To withstand the hydrostatic pressure of the water buffer, the tank walls are made of 16 mm strong material, while bottom and top lid are from 20 mm strong plates additionally reinforced by steel ribs [86]. The following list briefly explains the main design features of the tank.

- **HDPE Liner:**

The tightness of the tank will be ensured by an internal HDPE liner. This material is foreseen for walls and bottom of the tank. The several millimeter thick sheets of HDPE can be bonded together either by pressure or heat. After that, this water and gas tight material will be fastened by steel batten stripes on the inside of the tank. This procedure is equivalent to the sealing used for the water pool of JUNO's CD. Due to the large number and variety of connections necessary in the tank's lid, the liner will not be applied there. Air and water tight sealing will be provided by mounting the uppermost liner fastening ring on the periphery of the tank lid [88].

- **Tank Lid:**

The tank lid will support a lot of infrastructure: a cleanroom (CR), liquid handling equipment, calibration systems and an electronics platform as well as a crane for lifting heavy equipment in late construction phases. Moreover, a staircase will allow access to the tank top during construction and operation of OSIRIS. The following interfaces are also realized in the tank lid:

- **Central flange:** A flange in the middle of the top lid with a diameter of 1 m will be the primary access for the LHS and other instrumentation. The flange will realize feed-throughs for the inlet pipes connected to the AV and water tank, as well as for the cabling of AV and buffer sensor instrumentation and a slightly off-center access pipe for a contact-less optical level measurement system.
- **Top man hole:** During the construction phase, access to the inside of the detector will be possible from the top and bottom of the tank by two dedicated man holes. The man hole in the lid will allow access to the tank towards the end of the detector construction phase when the ground one is already closed.

- **Cable feed-throughs:** The PMT cables will be fed out of the tank via crimp connectors that are placed concentrically along the verge of the tank lid. These connectors will provide water and gas tight sealing of the tank with the cables.
  - **Ventilation ports:** During installation of equipment within the buffer ventilation of the volume is required for the personnel and to maintain clean room conditions. For this purpose a 500 mm flange in the lid is foreseen.
  - **Calibration Flange:** A dedicated flange is foreseen for the ACU with which the calibration of OSIRIS will be performed, using radioactive sources. The flange and the lid is designed to hold a gas and liquid tight stainless steel dome for the system that fully encloses the calibration unit.
- **Bottom Flange:**

The outflow for LS from the AV as well as water circulation for the buffer is realized by the pipes through the bottom flange in the tank's side wall. The HDPE liner will be used here as well to protect the carbon steel from corrosion.
  - **Bottom man hole and airlock:**

A man hole in the side of the tank at ground-level with sufficient size to transport elements of the PMT holding frame, the PMTs themselves and parts of the calibration and liquid handling system into the tank, is planned. A small clean room mainly acting as airlock but also usable for quality control and final equipment cleaning will be constructed around the man hole. During the final construction phase the tank access will be closed and covered from inside with HDPE. Currently, it is still under discussion, if the airlock will be extended to a larger and permanent cleanroom for the entire LS plant installation and quality control in the SH.

The technical design of the water tank is currently advanced enough, that the bidding process for suitable companies has already been started. The JUNO Collaboration will review the first quotes during March 2020.

### 5.1.2 PMT holding frame

The PMTs of OSIRIS will be mounted to a frame made of stainless steel profiles surrounding the Acrylic Vessel at about 1 m distance (see also Figure 5.2). This close distance is a compromise between maximizing the optical coverage of the AV for the given limited number of photo sensors and the external gamma ray background

mainly caused by  $^{40}\text{K}$  and  $^{208}\text{Tl}$  present in the PMT glass. The frame will consist of stainless steel profiles with a quadratic cross-section (50 mm  $\times$  50 mm). The profiles will be joined by plug connectors, which will be subsequently secured with stainless steel screws to avoid welding. Two rings are attached halfway up the frame using similar profiles, to which the PMTs with their magnetic shield are mounted, using dedicated holders currently developed at the RWTH Aachen. The design of the frame allows an extension with additional PMT rings for possible later phases of the OSIRIS project. The PMTs that are facing the AV from above and below are placed in the middle of the frame. At the top of the frame, the four upper muon veto PMTs are mounted centrally so that the photo cathodes are facing diametrically outwards in all four directions. Cables from the PMTs as well as from sensors monitoring the liquid in the buffer will be led out along the vertical bars of the frame. A free traverse from the top of the frame to the crimp connectors of the cable feed-throughs in the tank lid is foreseen. Beyond that, the frame has to provide a holding structure for the AV. Currently, similar stainless steel profiles in a star-shaped arrangement are foreseen for this purpose. In order to optically decouple the outer water cherenkov detector from the LS target, Monte Carlo studies are currently carried out for the design of an optical separation layer that will be mounted on the outside of the PMT holding frame [89, 90].

### 5.1.3 Acrylic vessel

With a diameter of 3 meters and a height of 3 meters, the AV will hold  $\sim 19$  t of liquid scintillator. These dimensions are mainly determined by the necessity to produce the vessel almost completely off-site and transport it as a single piece underground. However, according to Monte Carlo studies [91] using the 9 m diameter of the water tank, the size of the fiducial volume within the AV is fully determined by the external  $\gamma$ -background. Thus, a larger AV is not expected to be of advantage. The AV will stand on eight vertical acrylic plates arranged as a concentric star (see Figure 5.3). The plates will be directly bonded to the lower lid of the cylindrical vessel. By the usage of steel bolts pushed through corresponding holes in the acrylic plates the vessel will be fixed to the steel holding frame. For the cylinder top and bottom lid 4 cm of material thickness and 3 cm for the cylinder wall are foreseen. In addition, central rings of 50 cm inner diameter will be bonded to top and bottom lids [89]. Furthermore, eight radial reinforcement ribs on the top lid as well as the eight acrylic footing plates on the bottom will increase the mechanical stability. During operation, the hydrostatic pressure inside the AV can be fine-adjusted to compensate the water pressure from outside by raising the liquid level in the scintillator head tank to  $\sim 50$  cm above the water level [86]. Currently, the stability of the AV under normal operating conditions and in emergency situations is being investigated in a Finite-Element Analysis (FEA) study by Chinese collaborators at the Sun-Yat Sen University in Guangzhou.

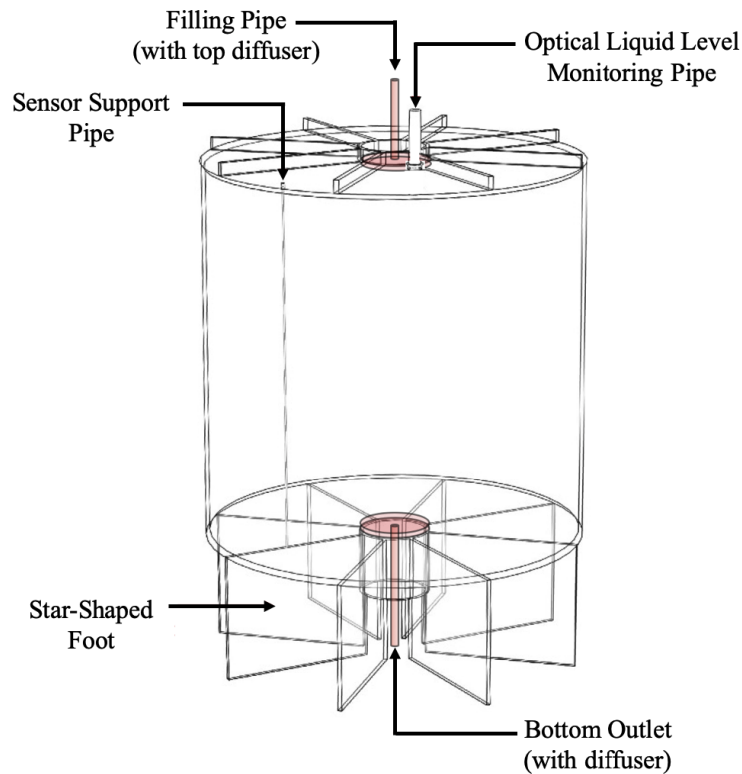


**Figure 5.3:** Drawing of the AV, which will contain  $\sim 19$  t of LS. The scintillator will be filled via an acrylic glass pipe from the top. To ensure a slow, broad and laminar flow of the liquid into the AV a diffuser (drawn in red) is glued directly to the end of the pipe and additionally fixed on the inside of the vessel's lid. For the outlet the same system will be used (also highlighted in red). The pipe for the optical liquid level monitoring, the sensor support pipe as well as the foreseen star-shaped foot of the vessel are also shown in the drawing. Figure adopted from [86].

The AV will be filled with LS through the LS filling pipe located at the center of the top lid. On the end of this pipe a diffuser will be placed to ensure broad and slow flow of LS inside the whole width of the AV. A similar diffuser will be placed at the outlet for the LS at the bottom of the AV [86]. This measures were taken to allow several different filling and operation modes for the detector. They will be described on later sections of this chapter. Through the top lid the liquid level inside the AV will be monitored. Therefore, a dedicated pipe will provide support for hydrostatic and gas pressure sensors as well as for thermometers. An additional tube will provide a direct line of sight to the liquid surface in the AV to allow the installation of a contact less optical level measurement system [90].

### 5.1.4 OSIRIS filling and operation modes

This subsection describes the operation and the corresponding filling scenarios for OSIRIS as well as the resulting requirements for the Liquid Handling System (LHS).

When the construction of the detector is finished, it will be filled initially following the procedure listed below and illustrated in Figure 5.4.

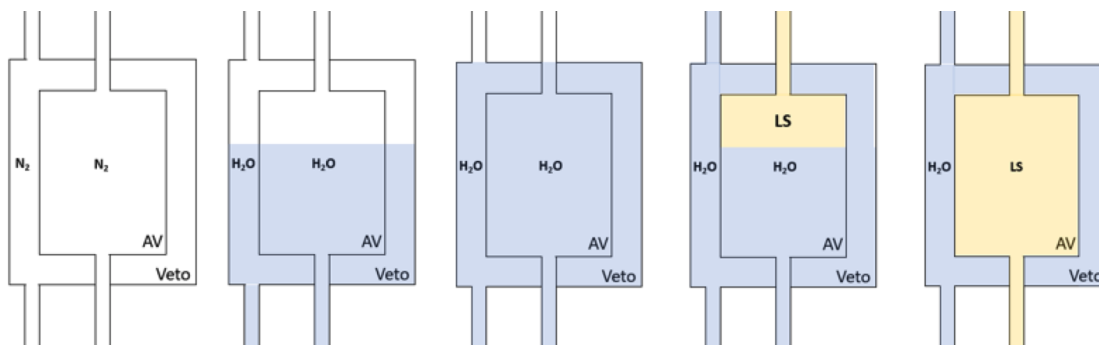


**Figure 5.4:** From left to right the chronological sequence of the major steps of the filling process is shown. Volumes filled with ultra-pure nitrogen are drawn in white, while blue represents water and yellow LS. When the filling procedure is finished, the acrylic vessel (AV) is filled with LS. One operation mode foresees the continuous exchange of the LS volume during detector operation.

- **N<sub>2</sub> pre-filling:**

For the initial filling of the buffer and the AV, a pre-fill and extensive flushing of both volumes with ultra-pure nitrogen gas is foreseen in order to avoid direct contact of water with air, which could result in a subsequent contamination of the water with radon. Since the radon affinity of LAB is much higher than that of water this measure can be considered as mandatory. Note: When the entire detector filling is completed, protective N<sub>2</sub> blankets will be created over all liquids.

- **Water filling:**

After the nitrogen pre-fill, the buffer and the AV are filled simultaneously with ultra-pure water. The water is pumped into the detector via the bottom tube system so that the detector is slowly filled from the bottom to the top. To avoid harmful stress on the thin AV walls caused by hydrostatic pressure differences inside and outside the AV, the water levels in both volumes have to be controlled within  $\pm 10$  cm [86]. After completion of this filling step a

waiting time of  $\sim 40$  days will ensure a low residual radon concentration in the water before the LS filling begins.

- **LS filling:**

The LS will be filled into the AV from the top of the detector. The water is pressed out slowly through the lower outlet diffuser and pipe. As the buoyancy of the AV increases during this exchange process, the LS flux has to be controlled precisely. Later exchanges of the LS sample are possible with a much higher flow rate of  $\sim 1000$  kg/h.

During operation of OSIRIS as LS screening detector, two operating modes will be possible:

- **Batch Mode:**

The LS is filled in large uniform batches of  $\sim 19$  t into the AV. To allow screening of a large fraction of the produced LS, the detector filling process has to run fast. For this purpose LS flows of 4 t/h are currently investigated in hydrodynamic simulations. If radon had been introduced in the LS sent to OSIRIS, this mode will give the opportunity for a decay of the radioactivity excess, allowing highly sensitive measurement of the U/Th content in the LS batch. So the batch operation will be preferable in the commissioning phase of OSIRIS and the purification systems to provide very accurate measurements of the radiopurity levels even in the presence of ambient radon [86, 92].

- **Continuous filling mode:**

The LHS of OSIRIS will be able to continuously exchange the LS in the AV with a rate of 1 ton per hour. This method enables a highly efficient early warning for severe pollution events during the LS production. Furthermore, a time-integrated radioactivity measurement of the LS guided through OSIRIS is gained. For this kind of operation, it is crucial that only a negligible amount of environmental radon is fed into the LS during production and in the piping connecting the purification plants and OSIRIS. Radon introduced in this way will provide a similar slowly decaying background as in the Daya Bay pilot plant tests with AD1. The sensitivity of the Bi/Po coincidence screening might be severely decreased [86, 92].

Both filling schemes require a creation of a temperature difference between newly filled and already present LS in the AV. Therefore, a positive temperature gradient (illustrated in Figure 5.5 left) will be established over the height of the AV. This gradient is expected to suppress the intermixing of fresh and already screened LS. For maintaining this gradient in the liquid, active heating of the LS input and cooling of the LS inside the AV is required. Moreover, the LS output temperature

of OSIRIS will have to match the requirements of the JUNO CD filling system. In addition to the temperature gradient, the diffuser system (shown in Figure 5.5 right) in the AV will lower the injection speed of the LS and broadens its flow. By this measure the occurrence of turbulences at the LS inlet and outlet is suppressed [92].

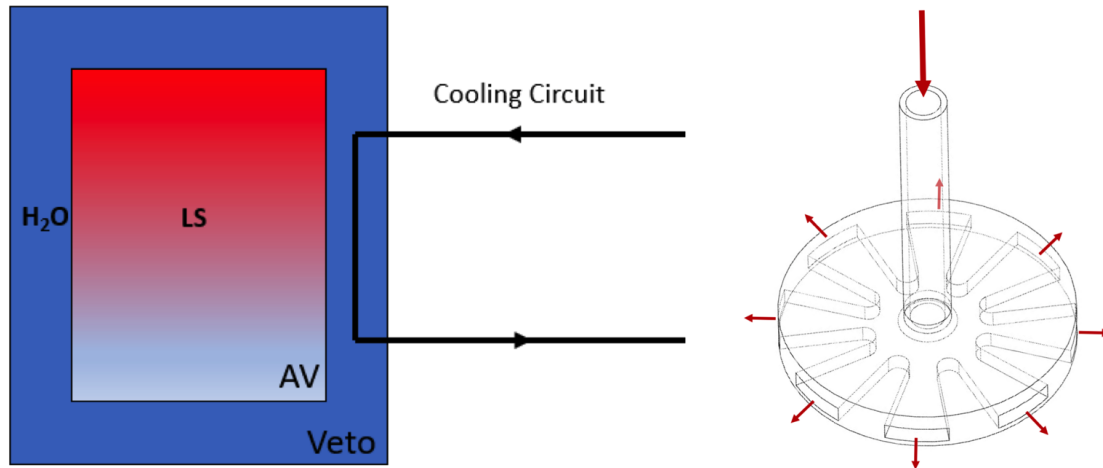


**Figure 5.5: Left:** The temperature gradient in the AV is illustrated as a color transition from red (warm) to gray (cooler). The water buffer (blue) serves as a heat sink, with an active temperature stabilizing cooling circuit. **Right:** Shown is a simple 3D schematic of the diffuser system mounted at the input and output of the AV. The LS flow is indicated by red arrows. The flow diameter is increased within the diffuser by a factor of  $\sim 10$ , while the flow speed decreases by one order of magnitude. The schematic was taken from [87].

### 5.1.5 Liquid handling system

While LS neutrino detectors like those at Double Chooz and Daya Bay were filled over several weeks, fast filling and LS exchange procedures will be essential for the effective operation of OSIRIS as LS screening detector. The LHS should allow detector operation in batch-mode as well as a continuous flow of LS through the AV during data taking.

Due to the complexity and the large number of functionalities, that the LHS necessarily has to have, only a brief description of the essential functions is possible here using simplified diagrams. Nevertheless, the essential components and special design features for OSIRIS will be discussed. Figure 5.6 shows a simplified diagram of the liquid scintillator and water handling structures for OSIRIS as integrated part of JUNO's LS purification plants and CD filling system.

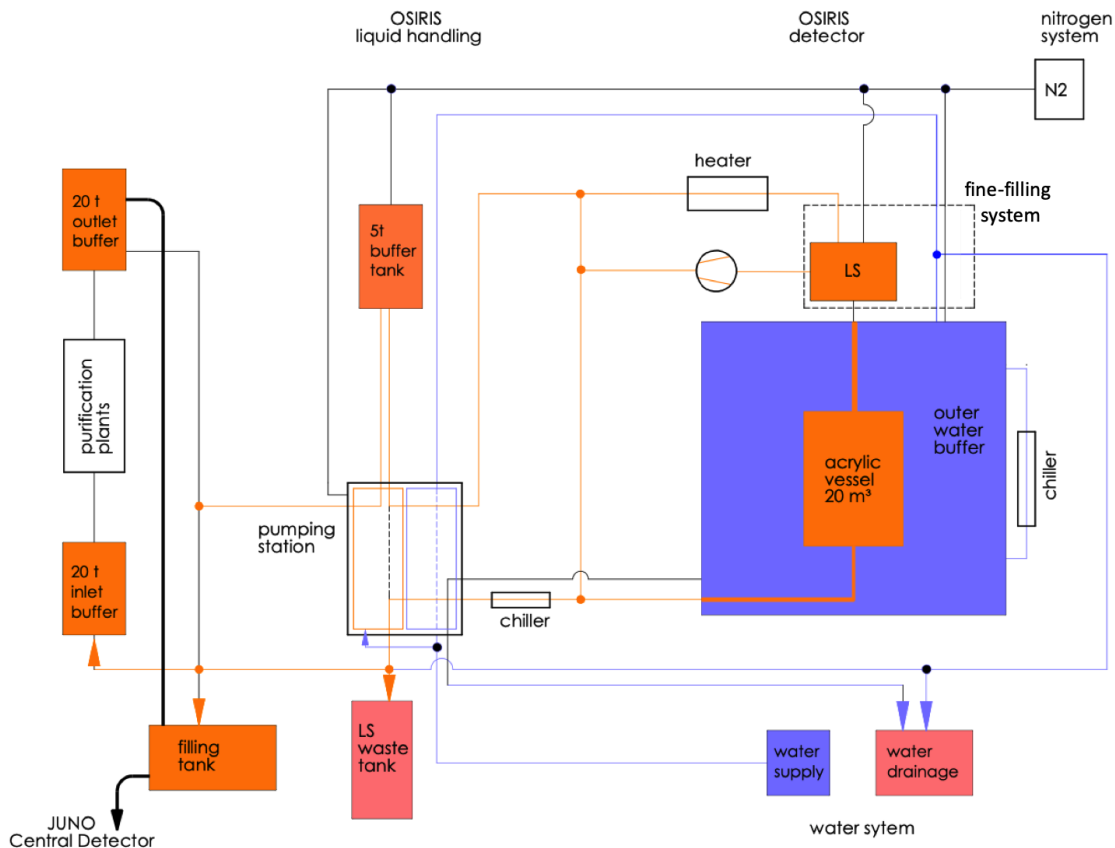


**Figure 5.6:** The conceptual layout of the OSIRIS LHS in a simplified scheme. Parts of the system dedicated to water are drawn in blue, while orange lines represent the connections foreseen for the filling of LS. A LS buffer tank (capacity  $\sim 5$  t of LS) provides independence from the operation status of the purification plants and CD filling systems. Where possible, flanges, valves and pumps of the OSIRIS LHS are placed in a dedicated pumping station, which is constantly flushed with nitrogen to prevent loading the liquids with radon. Figure adapted from [93].

The purification systems have their own LS product tank (LS outlet buffer, capacity: 20 t LS) at the end of the purification chain after the steam stripping column. This system is directly connected to the CD filling system. The OSIRIS LHS represents a bypass to this main filling line, allowing to divert a fraction of the LS for the screening in OSIRIS while the major amount of the LS proceeds directly to the filling system. Furthermore, due to internal bypasses of the purification systems, LS can also be taken directly out of the LS pipe from above ground and from the water extraction plant. Beyond that, also a circulation of LS in a loop connecting the stripping plant and OSIRIS is foreseen.

The following list describes the main elements of the LHS.

- **Buffer tank:**

Directly connected to the LS input from the JUNO main filling line, a buffer tank with a storage capacity of 5 t LS provides independence from the operation status of the purification plants and CD filling systems. By this tank, a constant inflow into the AV of OSIRIS can be maintained for several hours (without LS supply from the purification plants) before the buffer tank runs dry [86].

- **Pumping Station:**

To reduce the number of active components required in the system and to better protect pipe connecting flanges from ambient radon, most of this equipment is placed in a single unit called pumping station. This station will contain two magnetic centrifugal pumps for the LS, one for the water system and at least one additional spare pump. The pumps will realize a LS flow above 1 m<sup>3</sup>/h for the LS system and 3 m<sup>3</sup>/h for the water circuit. By several valves, these pumps can be connected to different LS and water circuits. In addition, the pumping station will be equipped with a number of liquid flow meters, thermometers and gas pressure sensors. It is foreseen to prefabricate, assemble, test and clean the entire pumping station in Germany. After shipping this complex part to China, installation in the piping system of the LS hall is expected to be done by mounting a few flanges. By this measure welding underground is avoided. The pumping station will be enclosed by an acrylic cabinet flushed continuously with nitrogen. Therefore, all active elements have to be controllable remotely [86, 93].

- **Fine-filling system and head tank:**

The fine-filling system containing the LS head tank (capacity: ~100 l) is shown in a dashed rectangular box in Figure 5.6. Since water and LS expand by temperature increases, it can be expected that the OSIRIS filling levels will vary during the entire measuring duration. Furthermore, it will be necessarily to keep slightly different filling levels of the AV and water buffer in order maintain the equality between hydrostatic inward and outward pressures. To ensure this fine-filling, the LS head tank is mounted at a defined height above the top lid of the water tank. Its filling level will be monitored carefully by dedicated sensors [90].

- **LS heater loop:**

In order to generate and maintain a temperature gradient within the LS contained in the AV, the scintillator has to be pre-heated before it is filled. Therefore, a flow heater in the form of a heat exchanger using hot oil (from

the LS hall hot oil system) as heating media is foreseen. Heater and head tank will be additionally connected in a dedicated circuit with a pump to allow leading back LS to the flow heater. By that, short interruptions in the LS flow from the pumping station can be compensated without draining the heater [86, 94].

- **LS chiller:**

Since it is mandatory, that the LS coming from OSIRIS will reach the temperature requirements of the JUNO filling system, a flow chiller is foreseen at the outlet of the AV. Nonetheless, it can be expected that most of the excess heat of the LS caused by the pre-heating will be dissipated to the buffer water.

- **Buffer water cooling circuit:**

To dissipate the heat introduced into the water by the heated LS and to keep the buffer temperature stable, a cooling loop is foreseen in the water tank. The cooling media in the loop will run through an external flow chiller.

- **Drainage:**

The LHS of OSIRIS is equipped with numerous bypasses for drainage of (polluted) LS and water. While the later can be fed directly into the waste water facilities of the underground laboratory, the LS has to be collected in mobile tanks that will be returned to the surface. Currently, there is no pipe from the underground laboratory to the surface for pumping out waste LS. In case the LS showed slightly reduced purity in OSIRIS, it is foreseen to be returned to the inlet buffer tank of the water extraction or steam stripping plant. There the LS can undergo a further purification.

- **N<sub>2</sub> gas handling system:**

OSIRIS will be connected to JUNO's nitrogen supply system. There N<sub>2</sub> gas with 6-10 bar pressure is produced from high purity liquid nitrogen. In OSIRIS this pressure will be decreased to ~4 bar for the operation of pneumatic valves and pumps. By further reducing the pressure to 100 - 600 mbar (relative), nitrogen is gained for flushing the pumping station, tanks, AV, buffers and special flanges. A further pressure reducer provides low pressure nitrogen (3-10 mbar relative) which is used to maintain the blankets in AV, buffers and tanks over the liquid surfaces. Moreover, the small overpressure should prevent air from entering the system [94].

- **Nitrogen purged flanges:**

For connections in the liquid-carrying tubes that cannot be placed in the pumping station, special flanges (see Figure 5.7) flushed with N<sub>2</sub> will be used.

By the barrier of pure nitrogen between two rubber o-rings the radon entry from the ambient air into the LHS should be minimized.

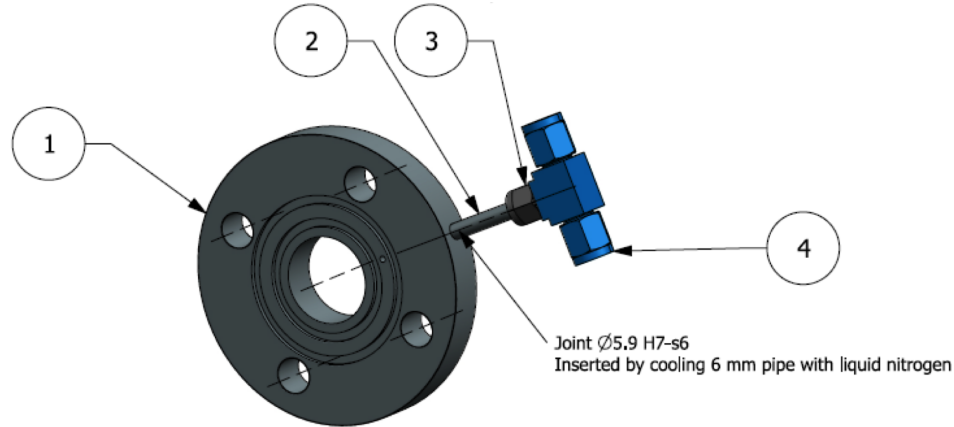


**Figure 5.7:** CAD Model of a nitrogen purged flange developed at the INFN for the LS purification plants. 1) Milled stainless steel (SAE 316L) flange with two grooves for rubber O-rings, 2) Nitrogen support tube, 3) Swagelok patented screwing (1/4 inch), 4) Connector to the nitrogen support line with a Swagelok patented T-screwing (1/4 inch) [95].

Based on this preliminary design and the requirements formulated in the Preliminary Design Report of OSIRIS [86], a technically feasible and fully detailed design for the LHS is worked out with the support of a technical consultant company. Draft designs foreseen for the bidding process will be submitted to the JUNO Collaboration for internal review in spring 2020.

### 5.1.6 PMTs and readout electronics

As mentioned before, the OSIRIS detector will use the same 20 inch Hamamatsu R12860HQE PMTs as the JUNO CD. Twelve tubes will be used for reading out the Cherenkov radiation of the muon veto, while 68 will be placed around the AV. For the readout of these PMTs a new concept developed at the University Aachen and the Forschungszentrum Jülich, which is called the iPMT (intelligent PMT) will be used. The OSIRIS detector serves as a test bed for this new technology. The iPMT system allows a digitization of the pulses from the PMT directly behind the tube without long cables. For the intelligent PMTs all electronics necessary for their operation and readout is mounted directly within a water tight stainless steel pot attached to the tube. A scheme of the pot with all the PCBs (Printed Circuit Board) is presented in the left part of Figure 5.8 while a prototype of the holder

for mounting the PMT to the holding frame in the water tank of OSIRIS is shown on the right.

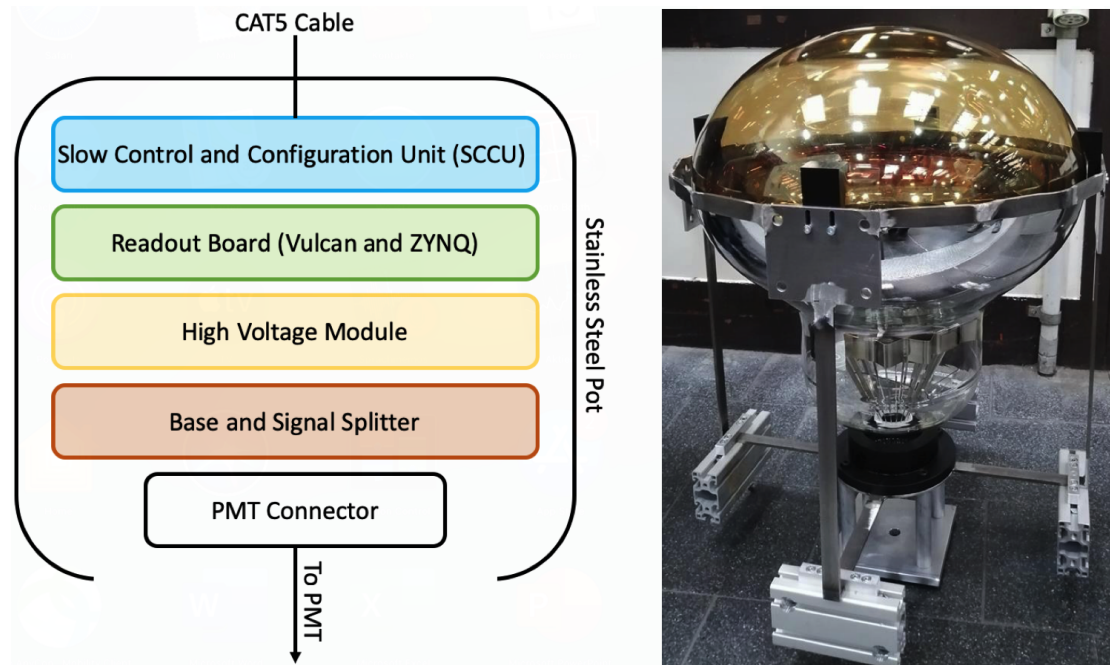


**Figure 5.8:** **Left:** Scheme of the PCBs for the iPMT system as stacked in the stainless steel pot. The four boards allow the PMT operation and digitization of the pulses directly at the tube. A single CAT5 Ethernet cable is required to route the digital data out of the pot, control the electronics and provide power to all systems. **Right:** The right photo shows a Hamamatsu R12860HQE PMT within a prototype holder for the mounting on the PMT holding frame. The mu-Metal shield is still under development and is not shown on the photo. The aluminium blocks on which the PMT rests on the photo are only used as stands on the laboratory floor and are not comparable to the profiles of the PMT holding frame. Photo taken with courtesy from [96].

On the backside of the PMTs a stack of four circuit boards has to be mounted. For an easier potting the PCBs will be round with a diameter of  $\sim 100$  mm. In the following list the boards are described starting from the PMT (see also [86]).

- **Base and Signal Splitter:**  
The heart of the base is the resistive voltage divider which splits the high voltage to the PMT's dynodes. The signal splitter also on this board separates the supply high voltage and the signal.
- **High Voltage Module:**  
The purpose of the high voltage board is twice: it contains the high voltage

module and all infrastructure for its operation and acts as a shielding layer against high frequency noise possibly generated on the following digital boards.

- **Readout Board:**

On the readout board the analogue signal coming from the signal splitter is digitized using an ADC chip developed under the name VULCAN at the Forschungszentrum Jülich. This chip has an input bandwidth of 500 MHz with maximum sampling rate of 1 GSample/s. The resolution is 8 bit in each of three selectable gain regions [97]. The digital waveform is processed by a Xilinx ZYNQ 7000 chip [98], which unifies a FPGA and a dual core ARM processor in a single chip. It is foreseen to reconstruct the number of photo electrons from the waveform directly on this PCB. The ZYNQ is connected via Ethernet to the SCCU (Slow Control and Configuration Unit) board.

- **Slow Control and Configuration Unit:**

The SCCU provides the possibility to program VULCAN and the ZYNQ. In principle a reprogramming (in situ) is possible at any time during the operation of OSIRIS. This PCB controls the high voltage module, as well as it provides the slow control. Moreover, I<sup>2</sup>C ports for the communication with optional monitoring sensors (e.g. thermometers) are foreseen. Furthermore, the SCCU board hosts an Ethernet switch to split the data traffic from the backend electronics to the SCCU and the readout board. Additionally, the Ethernet connection is used to transmit the power to all iPMT systems via PoE (Power over Ethernet). The major advantage of this power distribution is that only one single CAT5 cable has to be fed into the pot. Sealing problems at the cable feed-throughs are reduced to a minimum. In the final design of the iPMT boards, the power transformation electronics is fully integrated in the SCCU. The 48 V from PoE will be transformed to the main supply voltage 5 V for all boards and to 24 V to power the high voltage module [86].

### 5.1.7 Detector calibration systems

Currently there are two kinds of calibrations foreseen for OSIRIS. One is based on radioactive sources deployed into the LS, while the other will use the injection of defined light pulses into the LS. The calibration with radioactive sources will provide information about the detector's response to a defined energy deposition. The available isotopes that will be ordered for JUNO and can be used in OSIRIS are <sup>22</sup>Na, <sup>40</sup>K, <sup>54</sup>Mn, <sup>60</sup>Co and <sup>137</sup>Cs. The activity of this sources will be defined mainly by the maximum trigger rate of the DAQ system and possible pile-up effects. However, calibrations using radioactive sources are not well suited for studying

the timing behaviour of the detector since the light emission from the scintillator follows a complex multi-component decay in time. This process is circumvented by injecting light pulses with a defined start time. Two systems are currently being developed for this purpose. One of them is based on a pulsed LED with a diffuser deployed in the LS [67], the other uses an external pulsed laser which will be coupled to an optical fiber fed into the AV [99].

For OSIRIS it is foreseen to modify one of the ACUs (shown in Figure 5.9) developed for the Daya Bay experiment. A detailed description of the system can be found in [100], while in this section just a brief overview of the functionality and the necessary modifications is presented.

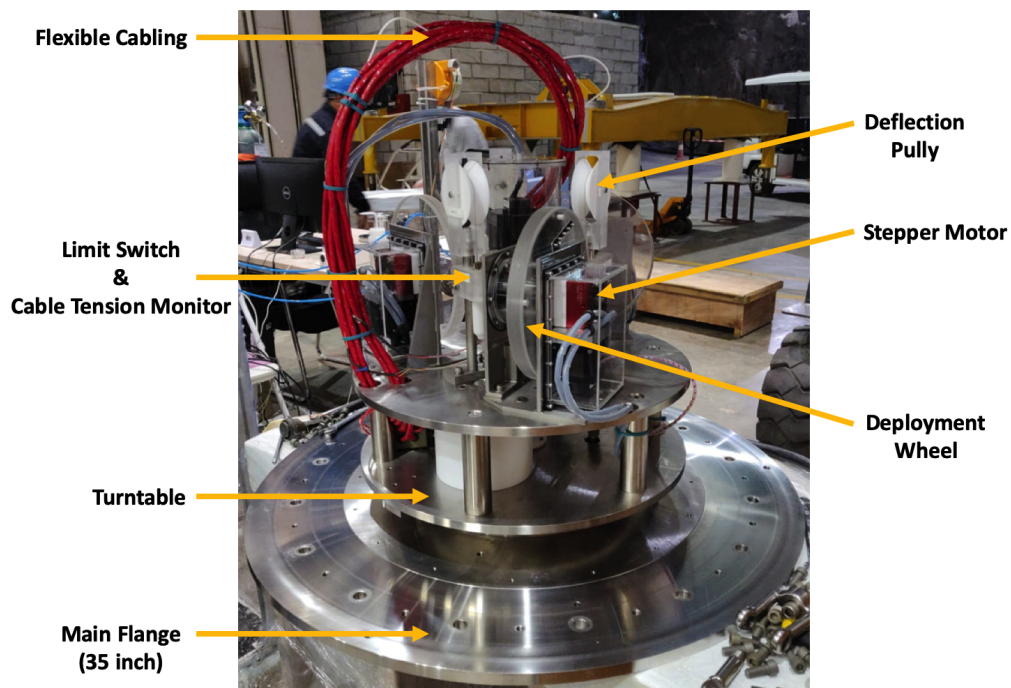


**Figure 5.9:** Photography of one ACU from the Daya Bay experiment. During operation the ACU is placed on top of a Daya Bay AD and connected to it via the 35 inch stainless steel main flange. This flange also provides connection to the dome (not on the photo) enclosing the unit. The turntable can be rotated to three different positions allowing a selection between three different radioactive sources or light injectors to be deployed in the detector. The deployment wheel, over which the respective holding rope is guided, is driven by a stepper motor. The lateral displacement of the cable unwinding from the wheel is absorbed by the deflection pulley. To prevent cable breakage, the ACU contains a cable tension monitor and a level switch that would stop the motor when the uppermost or lowermost point of the possible source position is reached [100].

The ACU matches well the major requirements of OSIRIS. It is able to deploy radioactive sources along one vertical axis to well defined positions. Moreover, the entire unit is placed below a gas and liquid tight stainless steel dome, which provides a fully enclosed system. The ACU is equipped with a turntable with three possible positions for the source deployment wheels. By that, different calibration sources can be deployed into the detector without opening the sealed steel dome. For OSIRIS two of this deployment systems will be used for radioactive sources mounted in dedicated capsules and held by PTFE coated stainless-steel wires. The third wheel is foreseen to be used for a light injection system [99]. All three deployment systems feature a wire load monitoring system, which is able stop the motors of the ACU automatically before a source holding cable breaks in case of sticking somewhere in the detector [100]. All other systems of the ACU can be remotely operated by a LabView software provided by the Daya Bay collaboration. However, to match the software environment of JUNO and OSIRIS it has to be modified and reprogrammed in EPICS. The major features as controlling the motor motions, logging and live plotting of the source positions as well as security checks are currently adapted at the Forschungszentrum Jülich [99].

## 5.2 OSIRIS sensitivity study

In order to evaluate the potential of OSIRIS as a radiopurity monitor exploiting the Bi/Po coincidences an extensive Monte Carlo study was carried out and described in detail in [99]. The signal expected from the scintillator's internal contamination is expected to be rare and has to be detected in the presence of background events caused by other radioactivity. This radiation can cause events in the same energy range as the signal events. Moreover, the coincidence signature can be mimicked by two unrelated events.

For the external backgrounds the  $\gamma$ s emitted by the isotope  $^{40}\text{K}$  and by the entire  $^{238}\text{U}$  and  $^{232}\text{Th}$  chains are taken into account.  $\alpha$  and  $\beta$  radiation have been neglected for all volumes except for the AV itself, since they can not penetrate the acrylic. For the stainless steel structures as well as for the acrylic the requirements for the CD of JUNO [101] were implemented into the simulation. The values for the radionuclide content of the PMT glass and the surrounding rock of the LS hall were based on laboratory measurements summarized in the JUNO-internal radioactivity database [102].

Events caused by residual decays in the LS are referred to as internal background. The radioactive carbon isotopes produced by cosmic radiation in the LS as well as the natural abundant  $^{14}\text{C}$  were considered. For the content of  $^{40}\text{K}$  an upper limit (based on the JUNO requirement for effective solar neutrino spectrography) of  $10^{-17}$  g/g was used.

Given the fact that OSIRIS is screening the LS only for a couple of hours up to a few days and assuming the low mass concentration requirements for the uranium and thorium chains of  $10^{-16}$  g/g (which results in a LS activity of  $\sim 10^{-9}$  Bq/kg) are reached by the LS, approximately two Bi/Po-coincidence events per day within the entire 19 t target are expected. Considering a reduction of the target mass by a fiducial volume cut and a realistic non perfect efficiency for the selection of Bi/Po events make obtaining a null result for the observed decays possible. In order to obtain meaningful values for limits of the internal LS radioactivity achievable in 24 h, the method of G. Feldman and R. Cousins [103, 104] was applied in [99].

Assuming that the LS was not loaded with radon when filling the detector, the limits for the  $^{214}\text{Bi}/^{214}\text{Po}$ -coincidence rate of  $3.4 \times 10^{-9}$  Bq/kg at a 90 % confidence level can be set according to the Monte Carlo simulation within the first 24 h of screening. This value corresponds to a mass concentration of  $C(^{238}\text{U}) = 2.8 \times 10^{-16}$  g/g of  $^{238}\text{U}$  within the LS. For the  $^{212}\text{Bi}/^{212}\text{Po}$  decays an activity limit of  $2.9 \times 10^{-9}$  Bq/kg with a corresponding  $^{232}\text{Th}$  mass concentration of  $C(^{232}\text{Th}) = 7.3 \times 10^{-16}$  g/g was obtained at the same confidence level. These values can be obtained in the presence of a radon contamination of the water buffer with an activity of  $550 \text{ mBq/m}^3$  for  $^{222}\text{Rn}$  and  $3.9 \text{ mBq/m}^3$  for  $^{220}\text{Rn}$ , which can be considered as a worst case scenario [99].

The increase of OSIRIS' sensitivity along the runtime of a screening measurement is shown in Figure 5.10. The simulation study shows that OSIRIS will be able to screen the LS down to the JUNO IBD requirement within a few hours of measurement, if the LS is not loaded with radon during production and filling. It can be concluded, that due to the limited target mass of OSIRIS and the defined size of the water shield, reaching the solar spectroscopy limits of JUNO require more than one day of data taking. Nevertheless, under these assumptions OSIRIS will be able to evaluate the nominal purification capabilities of the LS production plants during their commissioning and operation. During the filling process of the CD, OSIRIS has the potential to detect critical increases in the radon load of the LS almost in real-time.

However, it should be noted that a significant radon loading of the LS as observed in the Daya Bay pilot plant test will require waiting for several half-lives of  $^{222}\text{Rn}$  to decrease this dominant background. Otherwise, only severely worsened limits for the residual LS contamination would be obtained. In a batch mode requiring weeks of waiting for the radon decay, only small quantities of the entire LS production can be screened within OSIRIS and the detector would lose its early warning capabilities. Therefore, avoiding any source of contamination will be one of

the main challenges during the construction and operation of the OSIRIS detector. Minimizing the radon emanation of all detector materials as well as ensuring a low radon content in the nitrogen gas in contact with the LS is essential.

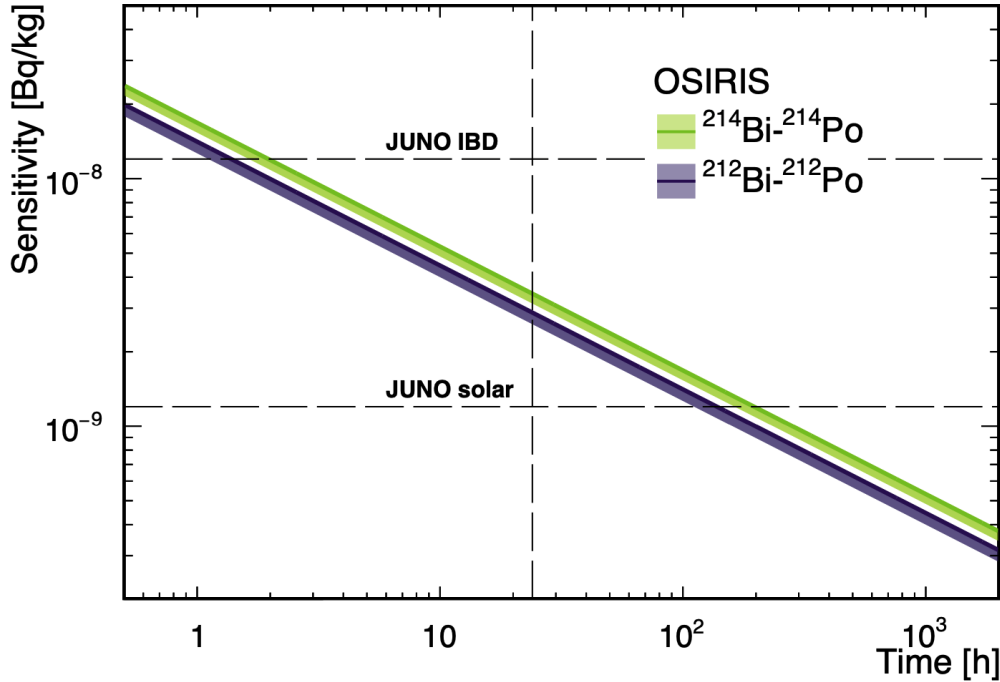


**Figure 5.10:** Projection of OSIRIS' sensitivities in searches for  $^{214}\text{Bi}/^{214}\text{Po}$  (green) and  $^{212}\text{Bi}/^{212}\text{Po}$  (purple) coincident decays within the LS along the time. The coloured bands represent upper limits for the corresponding activities within 1 kg of LS at a 90% confidence level. While the upper edge of the bands represent a worst case scenario for the radon activity in the water buffer the width of the band shows the improvement of the sensitivity up to radon free water. The LS purity limits set in the Conceptual Design Report of JUNO [32] for the effective detection of neutrino induced IBD events as well as for solar neutrino spectrography are indicated by two dashed horizontal lines. An additional dashed vertical line is placed at 24 h of measuring time. Plot taken with courtesy from [99].

# Chapter 6

## Sensor development for the monitoring of the detector liquids

Handling the large quantities of liquids in JUNO and OSIRIS requires precise knowledge of the filling levels, gas pressures and temperatures in all vessels of the liquid handling systems. Furthermore, the liquids in the water pool and the acrylic sphere of the JUNO detector and the corresponding volumes in OSIRIS have to be monitored as well. Due to the size of the detector facilities and the fragility of the acrylic vessels, high demands must be made on the sensor's range and precision. To avoid any contamination of the detector liquids all sensor materials have to be compatible with LS and ultra-pure water. Beyond that, all parts have to fulfill JUNO'S radiopurity requirements.

While the detector filling system is developed at the IHEP (Institute for High Energy Physics, Beijing), the Sun-Yat Sen University in Guangzhou and Chinese partner companies, various sensors were tested and characterized with respect to their suitability for the JUNO experiment in the frame of the present thesis at the Technical University of Munich. Figure 6.1 shows the planned liquid level measurement sensors of the CD. Redundancy should be achieved by using numerous sensors of different types.

Since liquid level differences between the outer and inner side of the 12 cm thick acrylic hollow sphere might cause harmful stress to the vessel during the filling and operation of JUNO, a precise and reliable determination of this levels is mandatory. The goal for the detector filling system is to guarantee a stability of the filling levels within  $\pm 20$  cm, which corresponds to a safety factor of 10 for the hydrostatic pressure difference in case of a water filling of veto pool and target sphere [105].

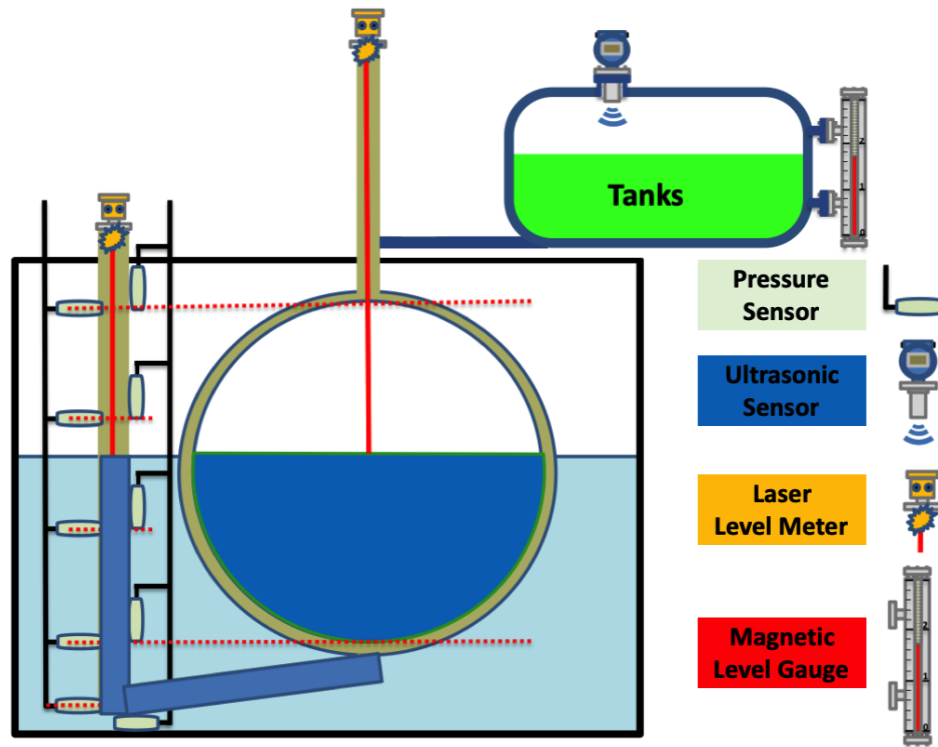


**Figure 6.1:** Scheme of the JUNO CD with indicated monitoring sensor position and types. Dashed horizontal red lines are indicating critical filling levels at the lower and uppermost points of the acrylic sphere where the so called chimneys for large diameter access pipes (mainly for filling and calibration) are attached. At the bottom of the sphere the liquid Level Measurement Pipe (LMP) is connected, in which all Hydrostatic Pressure Sensors (HPS) in direct contact with the LS are installed (drawn in horizontal direction). By this measure exploiting the principle of communicating vessels, building in a potentially radioactive sensor in the target volume can be avoided. The HPSs for the water pool will be attached from outside to the walls of the LMP (drawn in vertical direction). An optical laser based liquid level sensor is foreseen to be placed in the LMP providing high precision measurements (laser beam indicated by vertical solid red line). If the laser wavelength and intensity is compatible with the operation of PMTs, such a level meter should be placed directly in the upper chimney and if possible in the water pool (not indicated in the drawing). For the external tanks of the filling system, sensors based on ultrasonic waves or guided radar are considered in combination with magnetic level gauges. Drawing adapted from [105].

The liquid level measurement sensor types foreseen for the usage in the JUNO detector as well as their required performances are listed in the following. The list also refers to the mounting positions in the detector.

- **High range hydrostatic pressure sensors:**

As the depth of the water pool is  $\sim 45$  m, hydrostatic pressure sensors with a large range are required. Moreover, they should be able to determine liquid levels with a precision of  $\pm 20$  cm water depth. The high range sensors should be used in the Level Monitoring Pipe (LMP) attached to the target volume as well. By mounting the sensors in the external pipe, the installation of potentially background-causing components directly in the LS target volume can be avoided. The HPSs for the water tank can be mounted on the outside of the LMP, which is foreseen to be equipped with a support structure for the sensor heads and cabling.

- **High precision hydrostatic pressure sensors:**

At critical points, such as the highest and lowest point of the acrylic sphere, pressure sensors of smaller range (0-3 m) but higher precision (better than  $\pm 10$  cm water depth) should be used. A mounting on and in the LMP would be preferable as well.

- **Laser-based optical liquid level meter:**

The high precision liquid level measurement with an accuracy better than  $\pm 2.5$  cm will be realized by a laser based optical distance meter. The laser is planned to be mounted in the LMP and if an operation is possible in the presence of running PMTs also in the water pool and directly in the upper chimney of the detector. Despite small turbulences in the liquid surfaces and despite of the high transparency of LS and ultra-pure water, contact-less measurements should be possible without the deployment of a target float.

- **Other level meters for external tanks:**

In principle, the level meters already described can be used in the outer tanks of the LHS as well. Nevertheless, the use of sensors that are widely used in industrial process plants for liquids is advantageous in terms of reliability and cost. Ultrasonic sensors, as provided by Endress+Hauser, Siemens or Sisen Automation reach typically precisions in distance measurements to a liquid surface of  $\pm 15$  cm over measurement distances of 30 m. However, their usage is difficult in narrow pipes. The same applies to devices on the basis of guided radar. Magnetic level indicators, on the other hand, provide a cost-effective, reliable (and possibly power supply-independent) solution for monitoring tank levels with precisions of  $\pm 1$  cm. However, their application is only possible in vessels of relatively low height and therefore they can hardly be used in vertical storage tanks of large capacity.

## 6.1 The characterization facility for hydrostatic pressure sensors

It cannot be taken for granted that commercially available hydrostatic pressure sensors meet the strict requirements for range and precision of the LHSs of JUNO and OSIRIS. Testing many different sensors in a controllable laboratory environment is essential to select the best possible types. Furthermore, the materials of the HPSs should be investigated with respect to their radiopurity and compatibility with ultra-pure water and LS. Therefore, a testing facility for HPSs was developed within the frame of this thesis. The test stand allows to simulate the pressure conditions in JUNO up to a maximum water depth of 45 m. Furthermore, flexible custom made readout electronics and dedicated software for the used micro-controllers were developed for this facility. This allows the testing of sensors with different bus types. These efforts are described in detail in the following sections as well as tests of two HPS types (Sisen Automation, BST6600, PS3 and PS36 [106]) provided by the Chinese JUNO collaborators from the Sun-Yat Sen University.

### 6.1.1 Mechanical structure

For the testing and characterization of the HPSs a pressure vessel in form of a DN65 (outer diameter 74.75 mm) stainless steel pipe with a height of 2.20 m was used. A schematic drawing of the setup is presented in Figure 6.2 while the left part of Figure 6.3 shows a photography with highlighted main components. At the upper end of the measuring pipe a lid with a 6 mm pipe socket for the connection of a mechanical gas pressure gauge was welded on. A manometer with a range up to 5 bar (relative) and a 100 mbar scale division provided by Swagelok [107] was mounted. If a finer division is required, a second gauge with a range of 1 bar and a scale division of 50 mbar can be mounted to an already attached T-connector. Using a pressurized nitrogen bottle, pressure up to 4 bar can be built up in the pipe via a manual valve. Water or LAB are filled into the system from the bottom. The principle of communicating vessels is exploited to realize a continuously adjustable filling level. An external transparent liquid storage tank made of acrylic glass is connected to the pressure vessel via a 3 m long PTFE hose. The liquid level can be determined on this movable tank with a measuring tape attached to an ITEM profile behind it (see Figure 6.3 middle). To equalize the pressures in the storage tank and the measurement pipe, both volumes have to be opened to the surrounding air. In case of the tank, this is ensured by a small hole ( $d = 1$  mm) drilled in the lid. For the pressure vessel, a dedicated draining valve mounted on a 6 mm pipe socket on top of the tube has to be opened. The entire facility is mounted on a vibration-decoupled platform, which is equipped with an ITEM scaffolding to hold all components in place.

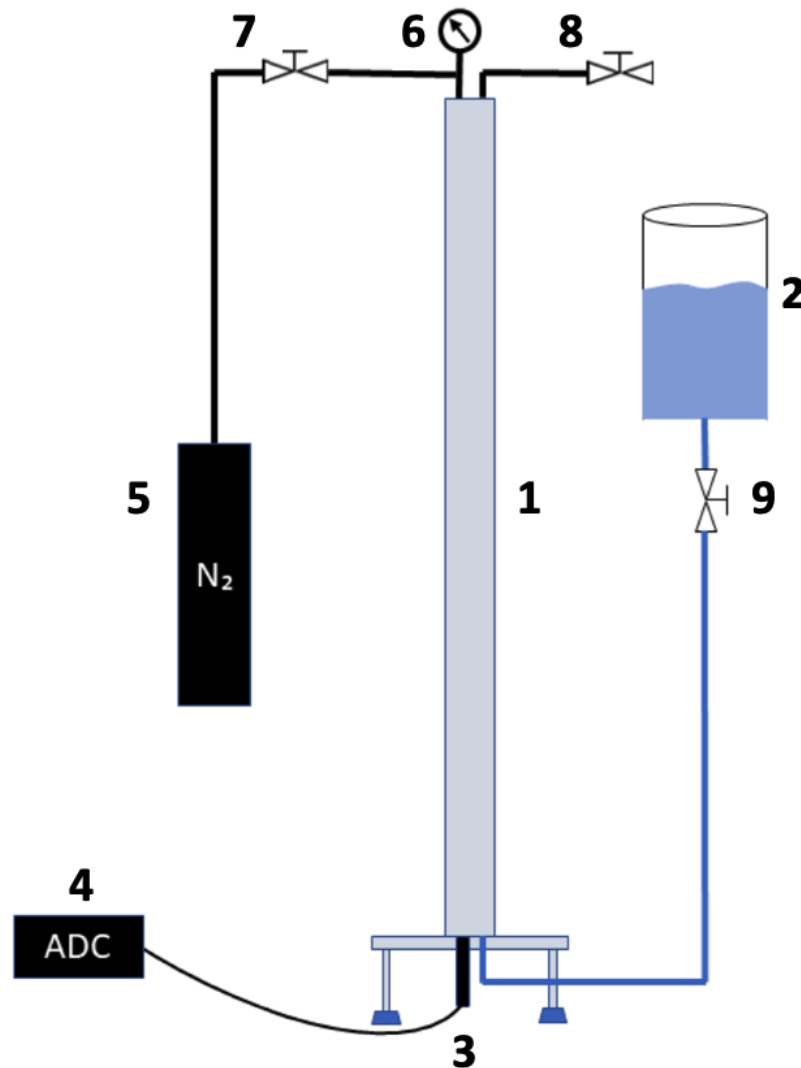


**Figure 6.2:** Schematic drawing of the HPS characterization facility with its major components: 1. stainless steel pipe, 2. movable water or LS storage tank, 3. hydrostatic pressure sensor under investigation, 4. data acquisition system with power supply, ADC and micro-controller, 5. nitrogen gas supply, 6. pressure gauge, 7. gas supply valve, 8. gas drain valve, 9. liquid flow control valve.

In order to ensure fast exchanges of HPSs and to ensure the usability of the setup for any kind of sensor head, a flange is welded on the bottom of the pressurized tube which allows the usage of exchangeable inserts for different dimensions of sensor housings. The insert is fixed with eight M4 stainless steel screws on the pipes bottom flange plate (see Figure 6.3 right). Water and gas tight sealing is provided by dedicated pressure resistive PTFE shaft sealing rings.

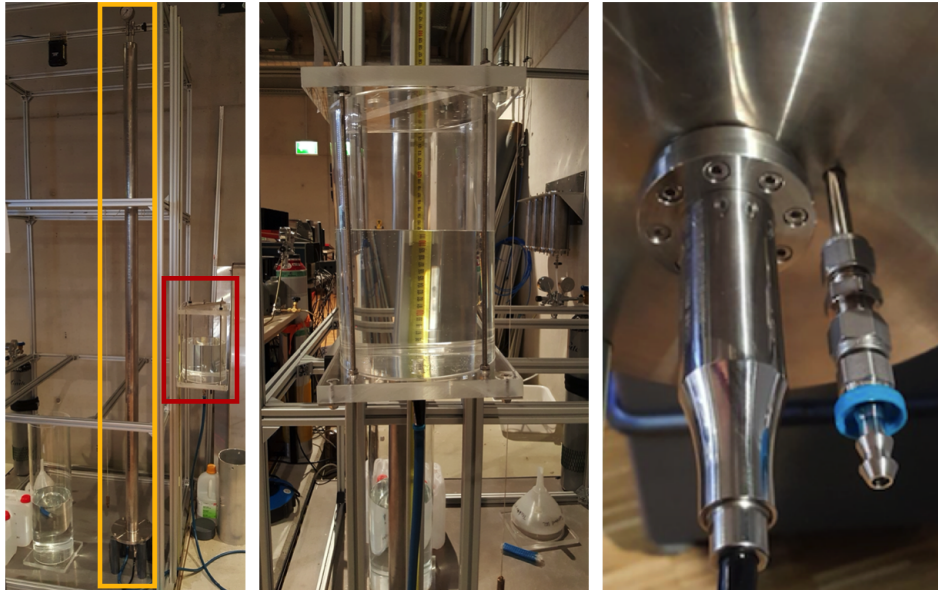


**Figure 6.3: Left:** A photograph of the HPS characterization facility mounted in an ITEM scaffolding placed on a vibration decoupled platform. By the yellow rectangular box the pressure pipe is highlighted, while the red one indicates the movable liquid storage tank. **Middle:** Shown is the liquid reservoir mounted on three ITEM profiles allowing upward and downward movements. A measuring tape is attached on the central profile behind the vessel. **Right:** The photograph shows one of the multipurpose inserts with a built in sensor head. Sensor and insert are fixed by screws on the bottom flange of the tube. To the right, the 6 mm pipe socket with a Swagelok patented connector equipped with a tubing olive for the filling hose is shown as well.

### 6.1.2 Sensor readout electronics

Currently, the 4-20 mA current loop system and the HART (Highway Addressable Remote Transducer) bus system based on it, represent the standard commonly used for the readout and communication of sensors of any kind in industrial applications. If a passive pressure sensor is used, it is installed in an electric current loop. The output signal of the sensor is then given as the current in the circuit. The advantage is that the sensor itself is equipped with a minimum of potentially radioactive analogue or digital electronics, which could spoil the LS purity. Furthermore, the sensor is powered by the voltage (typically 10-40 VDC) applied to the circuit. Therefore, only two cables to the sensor are needed.

In order to ensure a great flexibility of the test facility's electronics, no commercially available power supplies, readout devices, transducers and data loggers were used. A dedicated custom made readout system (scheme shown on the left side of Figure

6.4) for the 4-20 mA signals was developed on the basis of the single-board computer Raspberry Pi 3b. An easy and fast conversion to the 0-5 VDC (or similar) sensor signal standard, which is also common in industrial applications, should be ensured.

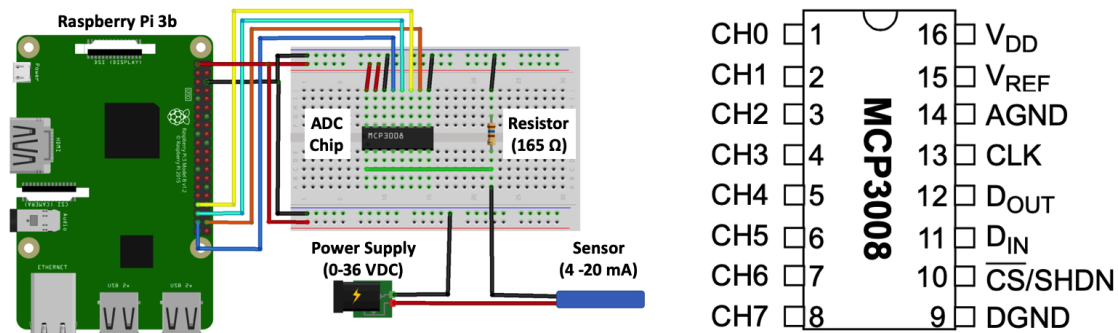


**Figure 6.4: Left:** Schematic drawing of the readout electronics and data recording of the HPS characterization facility. The HPS is powered by a highly stable DC power supply. A resistor connected in series is used for the generation of a voltage signal in the range of the MCP3008 ADC chip. The digitizer is read out using the SPI bus of Raspberry PI single-board computer. **Right:** Shown is the MCP3008 pin configuration. CH0 - CH7 are 8 individual analogue input pins, The digital ground is connected via pin 9 while the analogue ground is separated from it on pin 14. The Chip Select/Shutdown Input (CS/SHDN) is placed on 10, the serial data is fed in via 11, and fed out on pin 12. Pin 13 connects the serial clock while pin 15 can be used as voltage reference input. Pin 16 is used for the power supply connection. The drawing of the configuration was taken from [108], where a detailed description of the chip can be found.

For powering a broad variety of sensors, a flexible multi-purpose laboratory power supply STATRON 3250.1 is used. It can maintain stable DC voltages between 0 V and 36 V with a residual ripple of  $\sim 1$  mV<sub>eff</sub> [109]. Since the Raspberry Pi 3b is not equipped with analogue inputs, the output signal of the sensor has to be digitized externally. This is done via a MCP3008 Analog-to-Digital Converter (ADC) with a voltage resolution of 10 bits and a maximum sampling rate of 200 kS/s [108]. Note, that the ACD has 8-Channels, which allow an enlargement of the system to read data from multiple sensors. The pin configuration of the ADC is shown on the right side of the Figure 6.4.

As shown in Figure 6.4 (left) the ADC is connected to the Raspberry Pi via the SPI (Serial Peripheral Interface) pins on the one-board computer. The GPIO (General Purpose Input/Output) pins of the SPI on the Raspberry work with a voltage of 3.3 V and can be harmed severely by long lasting higher voltages [110]. Therefore, the voltage read of the ADC must be limited to a maximum of 3.3 V. The current

signal of the sensor between 4 mA and 20 mA is converted into voltages of 0.66 V up to 3.3 V by a 165  $\Omega$  resistor connected in series. The readout of the ADC, saving, processing and displaying of the data is realized by simple Python scripts (described in [111]).

### 6.1.3 Characterization of a high precision low range sensor

From the Juno collaborators working on the detector filling system, two types of sensors were suggested for a first investigation, one for high precision measurements and the other for reaching an increased range. The sensor head BST6600 PS3 provided by SISEN Autmotation is considered as low range sensor with high precision. As mentioned in section 6.1 this HPS type has to reach a precision of  $\sim \pm 10$  cm with a range corresponding to a few meters of water depth. According to SISEN's homepage [106], the BST6600 PS3 silicon piezoresistive sensor, is expected to have a range of 3 m and can be ordered with an accuracy of  $\pm 0.25$  %. The sensor is placed within a stainless steel (possible types: 304, 316) capsule which can be exchanged by a PTFE housing on demand. This device makes use of the two-wire 4-20 mA readout and powering system, with a DC supply voltage of 17 V up to 36 V. Numerous different cable types are available. The tested sensors were equipped with a kink-protected 8 mm thick two-wire cable with an additional internal capillary for the relative pressure measurement. Besides PTFE and silicone, the cable jacket can be selected from a wide range of materials depending on the application of the device [106]. The tested BST6600 PS3 sensor is shown in Figure 6.5.

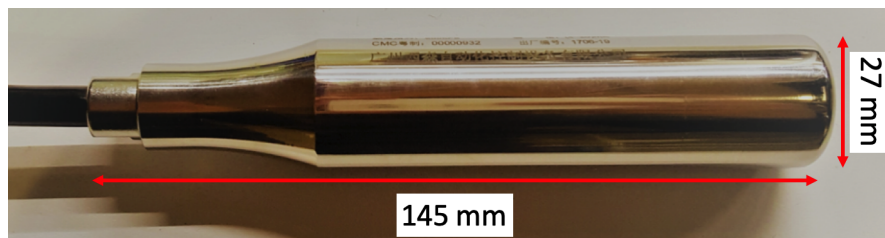


**Figure 6.5:** Photo of the characterized BST6600 PS3 sensor head. The cable is attached to the sensor from the left. The feed-through into the stainless steel housing is sealed by a PTFE gasket. The stainless steel housing has a length of 145 mm and a diameter of 27 mm which allows the usage of a simple insert with a pressure resistive shaft sealing ring for the sensor mounting into the pressure vessel of the characterization facility. Note, that the sensor with its insert is shown in Figure 6.3 (right). To allow the liquid to enter the sensor head, the circular part of the cylindrical housing features four holes.

During the characterization measurement the pipe was filled with water in 10 cm steps from the bottom up to 210 cm. The water level in the pipe was determined via the filling level in the liquid reservoir using the measuring tape. As shown

on the left side of Figure 6.6, the filling height was increased slowly during  $\sim 2$  h. Since filling via the hose and equalizing of the levels in the pipe and tank takes time, the voltage signal corresponding to a defined filling height was obtained from the horizontal parts of the measurement curve. By plotting the mean value of the voltage readings versus the values read off the measuring tape, the calibration points shown on the right side of Figure 6.6 were obtained. Data fitting by means of a linear function (drawn in red)

$$\text{Liquid Level} = m \cdot U_{\text{Signal}} - c \quad (6.1)$$

provides the calibration parameters

$$m = (1.136 \pm 0.001) \frac{m}{V} \quad (6.2)$$

and

$$c = (0.750 \pm 0.001)m \quad (6.3)$$

where the uncertainties are purely statistical.

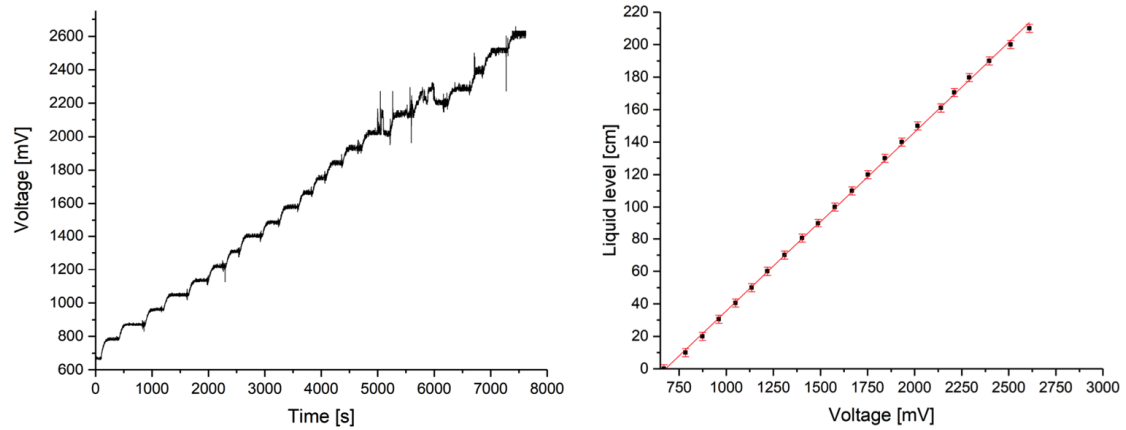


**Figure 6.6: Left:** Voltage response of the sensor head, while the liquid level in the measuring pipe was increased in steps of 10 cm during the course of  $\sim 2$  h. The voltage increases are clearly visible in the form of steps. Spikes in the voltage curve are mainly caused by digital noise due to unshielded cabling. Some fluctuations are caused by moving the water reservoir without closing the liquid control valve as well as by subsequent vibrations. **Right:** Liquid level in the tube versus the voltage response of the sensor head. The red line represent a linear fit of the data points. The horizontal error bars for the averaged voltage are too small to be visible, while the vertical ones correspond to a reading accuracy of  $\pm 2$  cm for the measuring tape.

The offset  $c$  is caused by the fact that the minimal pressure reading (atmospheric pressure) corresponds to a current signal of 4 mA and with that to a non-zero voltage for an empty measuring pipe. The calculated coefficient of determination  $R^2=99.94\%$  for the linear regression underlines the excellent linearity of the sensor response over its entire operating range.

The measurements have shown that changes of  $\pm 10$  cm filling height (water) can be resolved with the PS3 sensor. The stability of the voltage source as well as the limited 10 bits resolution of the ADC were identified as limiting factors for the achievable precision. By averaging 100 sampling points of the voltage measurement a resolution of  $\pm 1$  cm for filling height differences was achieved [111]. The results exceed the specification of the sensor given by SISEN Automation and fulfil JUNO's requirements for linearity and precision.

#### 6.1.4 Characterization of a high range sensor

The second sensor provided for characterization by the JUNO filling system working group is foreseen to allow liquid level measurements with a precision better than  $\pm 20$  cm with a range up to some 40 m water depth. Therefore, the BST6600 PS36 sensor head from SISEN Automation was selected. This sensor is identical to the PS3 described above in terms of dimensions, housing design and wiring. However, the conversion of the resistance change of the piezoresistive crystal to the 4 - 20 mA signal is adapted by modified internal electronics in such a way that higher ranges are achieved at the expense of resolution. For the investigation of this sensor two separate measurement series were carried out. The first was focused on the determination of low liquid levels using a pure water filling in the tube. The second study was dedicated to the sensor's response to greater hydrostatic pressures.

##### **Sensor response from 0 - 2.1 m water depth:**

Starting with a filled tube, the liquid level of 220 cm was decreased in steps of 10 cm slowly over the course of  $\sim 100$  min until the pipe was empty. The signal voltage values along the runtime of this measurement are shown in the left plot of Figure 6.7. When comparing with the measurement series of the PS3 sensor head (Figure 6.6 left), the significantly reduced resolution of the filling height steps is clearly visible. To obtain stable voltage values, 100 voltage sampling points were averaged from the central area of the steps. These mean values were plotted with their standard deviation as uncertainty versus the liquid level in the pipe obtained from the measuring tape with an assumed reading uncertainty of  $\pm 2$  cm. On the right-hand side of Figure 6.7, a linear fit of the data (red line) according to equation 6.1 is also shown.

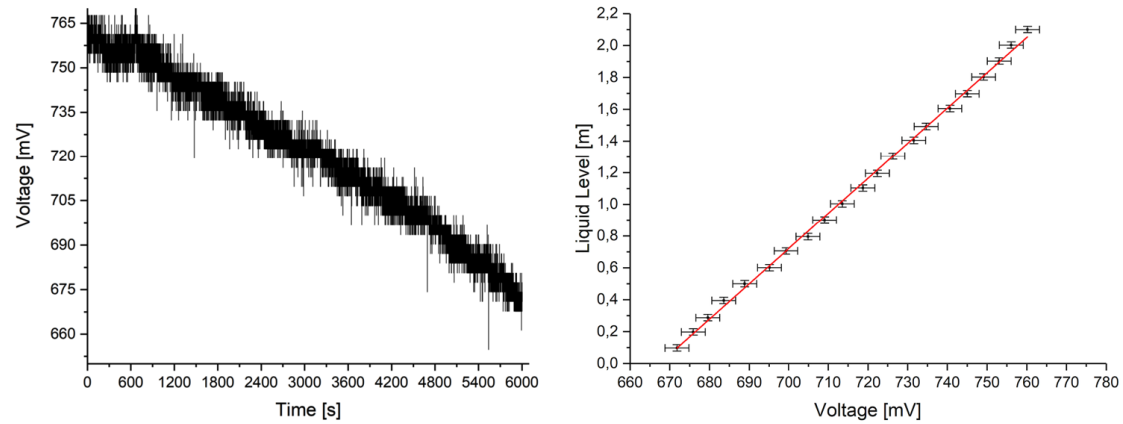


**Figure 6.7:** **Left:** Voltage values recorded while lowering the liquid level in the pipe from 220 cm in steps of 10 cm plotted over a total measurement runtime of  $\sim 100$  min. **Right:** The liquid level values are plotted versus the measured voltage. The voltage was calculated as mean of 100 sampling points from every fill height step. The horizontal error bars correspond to the standard deviation of this mean value, while the vertical uncertainties are governed by the reading accuracy of the tape measure which was conservatively estimated to be  $\sim \pm 2$  cm.

For the calibration parameters in this lower pressure region  $m_{low} = (22.15 \pm 0.02) \frac{m}{V}$  and  $c_{low} = (14.79 \pm 0.14) m$  was calculated from the linear fit with a coefficient of determination of  $R^2 = 99.86\%$ . A constant resolution of  $(8.5 \pm 0.6) cm$  water depth achieved in this study confirms the value of 9.0 cm presented in the sensor's data sheet [106].

### Sensor response from 3 - 22 m water depth:

To determine the sensor response at greater water depths, the pipe was filled with water up to a height of  $\sim 1$  m. Then the pressure in the pipe was increased in steps of approx. 200 mbar with the help of the nitrogen supply. The measured voltage values for each step of the investigation are plotted on the left in Figure 6.8. The overshooting voltage values at the beginning of each stage are caused by the measuring procedure. The pressure was built up in the pipe via the pressure reducer on the  $N_2$  bottle and subsequently fine-adjusted by draining excess gas using the gas drain valve and the pressure gauge. By averaging 100 measuring points from the central horizontal parts of the steps, stable values for the sensor response to a certain pressure were determined. The simulated water depth was calculated from the inertial liquid level of 1 m and the applied gas pressure. The uncertainty of this quantity is no longer determined by the reading accuracy of the tape measure, but is governed by that of the pressure gauge, which was assumed to be  $\pm 20$  mbar. As shown in the right plot of Figure 6.8, the sensor response is also linear in the

range between 3 m and 22 m water depth. To avoid damage of the sealing rings in the pressure vessel, no further measuring points were recorded at higher pressures. The linear fit of the data according to equation 6.1 provides  $m_{high}=(22.16\pm 0.02) \frac{m}{V}$  and  $c_{high}=(14.61\pm 0.22) m$  with a coefficient of determination of  $R^2=99.94\%$ . A constant resolution of  $(8.5\pm 0.6) cm$  water depth, identical to the value obtained from lower filling levels, was determined in this higher part of the sensor range. This matches well the value of 9.0 cm presented in the sensor's data sheet [106].

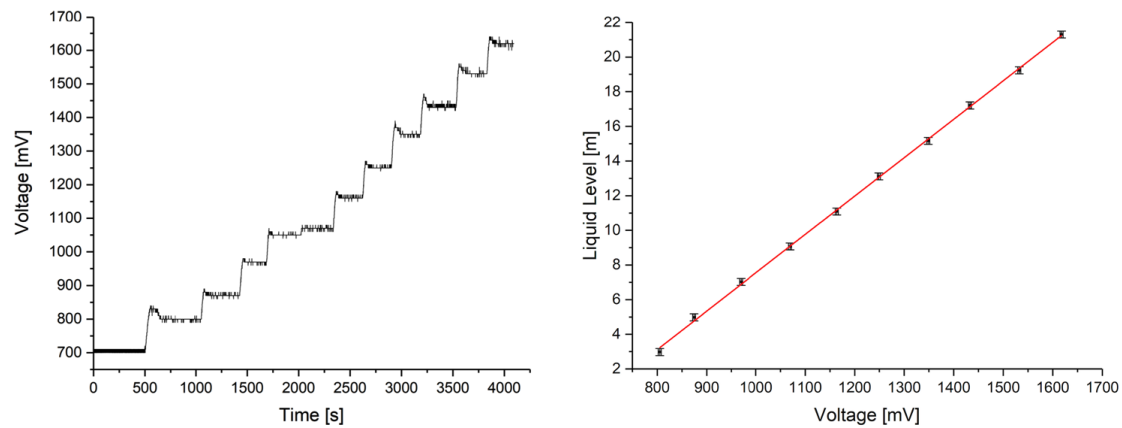


**Figure 6.8: Left:** The PS36 calibration data measured with a fixed water level in the pipe and additional gas pressure above the liquid. The pressure was increased in steps of 200 mbar (corresponding to an increased water depth of 2.04 m). Overshooting voltage at the beginning of each step are caused by the fine-adjustment procedure of the gas pressure. **Right:** The measured liquid level plotted versus the sensor signal voltage. The greater water depths were simulated by building up additional gas pressure above the fixed water level in the pipe. The red line represents a linear fit of the data according to equation 6.1.

#### Global sensor linearity and response function:

By combining the two measurement series (see Figure 4.9) the global (0 - 22 m water depth) sensor response function was determined. The calibration parameters  $m_{PS36}=(22.34\pm 0.01) \frac{m}{V}$  and  $c_{PS36}=(14.92\pm 0.07) m$  were determined from a linear fit (red line in Figure 4.9) according to equation 6.1. The coefficient of determination  $R^2=99.94\%$  underlines the excellent linearity of this sensor head in the investigated range.

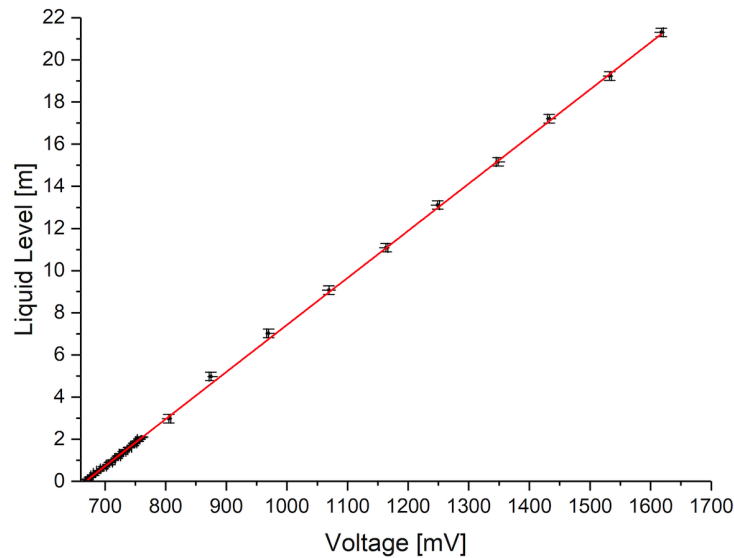


**Figure 6.9:** Data points from both measurement series in one plot. The liquid levels below 2.2 m were investigated by using water in the pipe under atmospheric gas pressure. The greater filling levels of the pipe were simulated using pressurized nitrogen. The red line represents a linear fit of the data.

### 6.1.5 Gamma screening of the investigated HPSs

In the frame of a Bachelor's thesis [111] the two sensor heads provided by SISEN Automation BST6600 PS3 and PS36 were investigated in terms of radioactivity in a low background  $\gamma$  radiation screening facility (described in detail in [112, 113]) in an underground laboratory at shallow depth in Garching. For the screening both sensors were placed in front of the High Purity Germanium Detector (HPGe) of the facility. The detector is enclosed by an anti-Compton veto consisting of sodium-iodide scintillation crystals within a copper shielding, was used. The whole setup is placed inside several layers of lead bricks. On the outside an active muon-veto system consisting of six plastic scintillator panels equipped with photomultiplier tubes was used. Unfortunately, during this screening campaign a large part of these panels failed due to a broken multichannel acquisition interface module. Only the upper part of the veto was usable. Nevertheless, upper limits for the activities of several radio-isotopes shown in Table 6.1 could be determined for the sensors.

Isotope	Activity [mBq/Sensor]
$^{40}\text{K}$	$< 103.21 \pm 2.33$
$^{60}\text{Co}$	$< 6.57 \pm 0.17$
$^{208}\text{Tl}$	$< 8.72 \pm 0.65$
$^{212}\text{Bi}$	$< 3.18 \pm 0.51$
$^{212}\text{Pb}$	$< 17.22 \pm 0.29$
$^{214}\text{Bi}$	$< 99.33 \pm 1.70$
$^{214}\text{Pb}$	$< 349.04 \pm 7.03$
$^{228}\text{Ac}$	$< 28.48 \pm 1.88$

**Table 6.1:** Screening result for the HPSs from the BST6600 series provided by SISEN Automation. In this  $\gamma$ -screening campaign only upper limits for the activity of the isotopes listed in the left column could be set [111].

## 6.2 Optical liquid level measurement system

In the Double Chooz experiment, a laser-based distance measuring system was already used to determine the filling level of the detector vessels. A precision of  $\pm 0.5$  mm [114] could be achieved by the optical measurement. However, the wavelength ( $\lambda = 650$  nm) of the used laser sensor M10L/100 [115], provided by MEL-Mikroelektronik, was in the visible range. Due to the high intensity of the laser light, operation of the system was incompatible with the simultaneous operation of the detector's PMTs without an optical separation. This prevented the system from being used directly in the chimney of the detector. Therefore, a mounting in liquid level measurement tubes, connected to the corresponding detector vessels, was made (for details please refer to [114]). Furthermore, it was not possible to realize a contact-less measurement. A guided float in direct contact with the liquids had to be used as target for the laser beam [114].

With regard to the requirements of JUNO for a contact-less optical measurement of distances up to  $\sim 50$  m to highly transparent liquids, the market for commercially available sensors was investigated. The company Laser Technology Inc. supplied a prototype sensor which measures the distance by means of a pulsed IR (infra-red) laser ( $\lambda = 905$  nm [116]) using the time of flight (TOF) technique. The system, which is now sold under the name TruSense S310 (shown in Figure 6.10), was characterized and tested in this work. The operational safety in the presence of running PMTs was also evaluated.

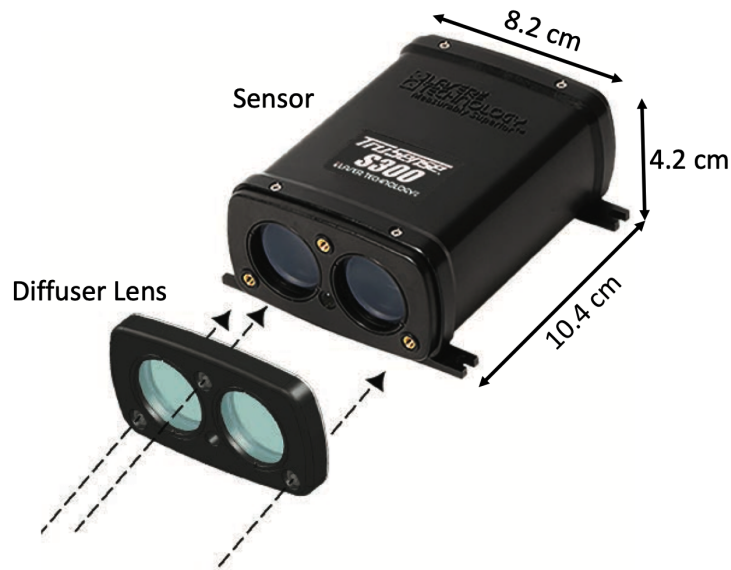


**Figure 6.10:** Photo of the TruSense S300 series distance meter with its diffuser lenses, which can be attached to the optics of the sensor with three M3 screws. The class 1 IR laser, the detector and optics as well as readout and support electronics are housed in glass-filled polycarbonate. The assembly has a total mass of  $\sim 139$  g. However, the sensor is available in an OEM version without housing. The zero point for the distance measurement is located at the front edge of the housing and is only slightly displaced by the usage of the diffuser lenses. Any offset for the measured values can be set via the control software [116]. Figure adapted from [117].

According to the supplier, the distance meter can determine distances to surfaces from 0.46 m up to 50 m with a precision of  $\pm 10$  mm [116]. In case the levels of liquids with turbulent motion or major vibrations on the monitored surface the usage of the additional diffuser lenses provided by Laser Technology Inc is required (see also Figure 6.10). To ensure precise alignment of the sensor to the target and orthogonal to the liquid surface the sensors are equipped with visible alignment lasers. If required, these can be switched on and off via communication software. The TruSense S300 series of laser distance meters offers a 4-20 mA output with HART communication capabilities. In addition to a standard serial RS-232 for configuration, the S300 and S310 types provide also a standardized SDI-12 serial interface for data readout and sensor configuration. The sensor is powered with 12 - 24 VDC and requires 1.8 W while measuring and 0.48 W during standby.

### 6.2.1 PMT irradiation test

To ensure that the laser sensor can be mounted directly in JUNO's CD without being hazardous to the PMTs, one of the Hamamatsu H12860HQE PMTs was irradiated in the single channel test stand (for details see [118, 119]) at the University of Tübingen. The laser irradiated the photo cathode through 12 cm highly transparent acrylic glass, what corresponds to the thickness of JUNO's CD acrylic sphere. The sensor and the acrylics were placed in a distance of  $\sim 1$  m to the PMT. For the irradiation test the laser was operated without diffuser lenses (divergence 3 mrad [116]) and with the highest possible measurement repetition rate of 14 Hz [116]. The arrangement, which can be considered as worst case scenario for the usage in JUNO, is shown on the right side of Figure 6.11. Due to several reflections on the liquid and acrylics in the detector as well as the use of diffuser lenses (resulting divergence 44 mrad [116]) during the operation in JUNO, the intensity of the laser in the CD is always distributed over several PMTs.

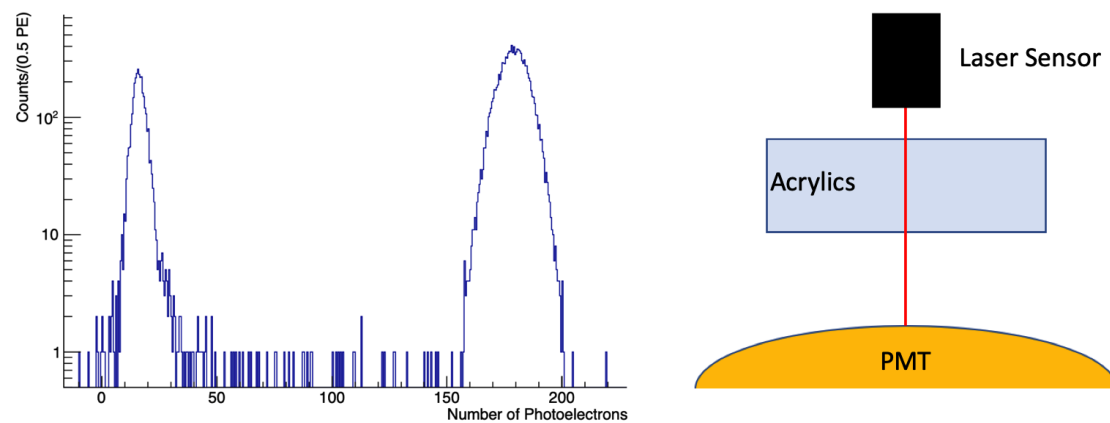


**Figure 6.11: Left:** Charge spectrum of the PMT obtained from the IR laser pulses shining through 12 cm of highly transparent acrylic glass. The peak at  $\sim 180$  p.e. corresponds to radiation directly hitting the photo cathode, while the left peak is caused by IR photons undergoing previous reflections on the interfaces between acrylics and air. **Right:** Shown is the arrangement used for the PMT irradiation test. The laser sensor was placed at a distance of  $\sim 1$  m to the central part of the PMT photo cathode. Within the laser beam a 12 cm thick block of highly transparent acrylics was placed to simulate the impact of JUNO's CD sphere. Note, in JUNO the IR light will be further attenuated by  $\sim 2$  m of water between the PMTs and the acrylic sphere.

The ADC of the test stand (CAEN V1742) has a limited dynamic range of  $1 V_{pp}$  with an adjustable offset of  $\pm 1$  V [120]. Since multi-photon pulses with the height of several volts were expected (PMT gain:  $\sim 10^7$ ) a 20 dB attenuator was placed in the signal line from the PMT to the DAQ system. The ADC was triggered

by a leading edge discriminator (CAEN V895, see also [121]), which was set to a threshold of -7 mV corresponding to  $\sim 7$ -9 photoelectrons.

The recorded charge spectrum (see Figure 6.11 left) containing 15109 events was calibrated to the number of photoelectrons using previous single photon calibration data measured during the commissioning phase of the single channel PMT test stand in 2016 [119]. IR laser pulses directly hitting the photocathode cause intensive events with a charge corresponding to 160-200 photoelectrons. Radiation reflected at the interfaces between acrylic glass and air, which reaches the photocathode, causes a second peak in the spectrum at about 17 photoelectrons.

Although the events caused by the laser are intense pulses, they do not harm the functionality of the PMT. Since the intensity in JUNO will be distributed over a larger area and about 2 m of the water buffer lie between the tubes and the acrylic sphere, it can be assumed that even continuous operation of the laser, with the photomultipliers switched on, does not pose a risk of destruction. Based on these measurements, the TruSense S310 was considered for further laboratory characterization and the development of a complete non-contact optical liquid level measurement system with a micro-computer as data logger and controlling device.

### 6.2.2 Sensor readout software and data acquisition

The distance meter is powered and read out using the dedicated PCC (Power Comm Cable) provided for the TruSense series by Laser Technology Inc [116]. The sensor is connected via the DB9 pin serial connector to a serial I/O device. The usage of an DB9 to USB adapter is foreseen. For this type of connection, the manufacturer provides readout and communication software with a graphical user interface (see Figure 6.12 left) requiring Microsoft Windows. However, the software is incompatible with JUNO's requirements and does not allow direct access to the data stream from the sensor.

Similar to the hydrostatic pressure sensor test facility, the Raspberry-Pi 3 was foreseen as data logger and controlling device. The investigated TruSense S310 was connected to the Pi via RS232 using a DB9 to USB adapter. For the serial communication with the sensor a dedicated software was developed. The program called TUM/JUNO TruSense Tool was written in C++ with embedded headers for serial communication programmed in C. The software contains a graphical user interface (see Figure 6.12 right), which was implemented using the Qt GUI module, that provides classes for windowing system integration, event handling, OpenGL and OpenGL ES integration, 2D graphics, basic imaging, fonts and text [122]. The software is compatible with all sensors of the TruSense series (S200/S300). The data output of all this types contains three measurement values obtained from the first, the last and the most intensive IR laser reflex. This readings are written into

a .txt file as delimiter separated values. Furthermore, the control of the visible alignment laser and the data acquisition rate is also possible by the tool.

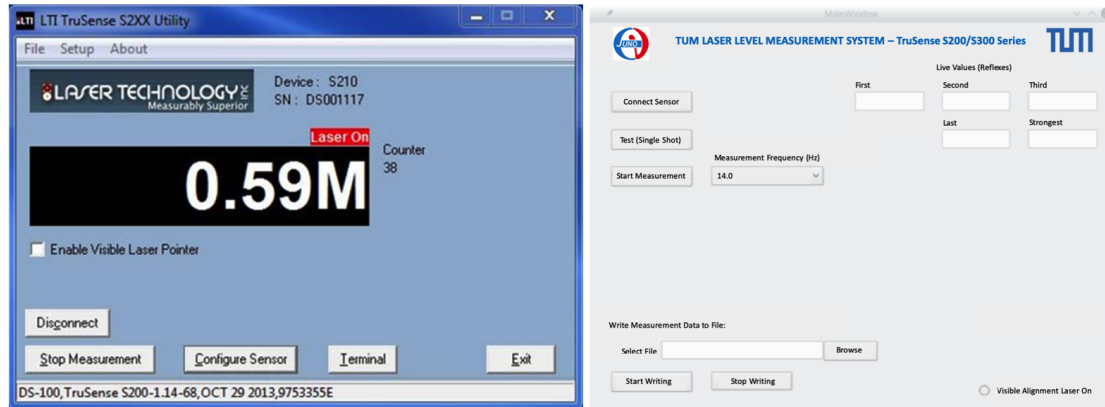


**Figure 6.12: Left:** Screenshot of the GUI (Graphical User Interface) of the laser sensor software provided by the manufacturer Laser Technology Inc. The software requires a Microsoft Windows infrastructure. The data is stored in a .txt file as delimiter separated values. A live access to the data stream of the sensor for further processing is not possible. The user can select between the imperial and metric units. Sensor configuration can be done in a separate tab. The figure was taken from the TruSense S200 manual [123]. **Right:** Screenshot of the TUM/JUNO TruSense Tool GUI. By simple clicking on the button "Connect Sensor" the Raspberry-Pi is connected automatically to the sensor. In case the procedure fails an error message will show up. The "Test" button allows a single measurement. The measurement frequency for the continuous mode can be selected before starting the measurement. The obtained distance values for the first, last and strongest detected laser reflex are shown. If the internal data logger of the sensor is further upgraded by the manufacturer, two more values (see "Second" and "Third") can be displayed. The selection of a path for the data file storage can be done easily via a dedicated browsing tab. Writing the data to the selected .txt file can be started and stopped by clicking on the dedicated buttons. The visible alignment laser is controlled via a radio button in the lower right edge of the window.

Beyond the sensor testing in the laboratory, the software allows the usage of the Raspberry-Pi for direct laser level meter control and intermediate storage of sensor readings in the LHSs of JUNO and OSIRIS. Therefore, compatibility with EPICS (Experimental Physics and Industrial Control System) was ensured during the development of the tool. EPICS, which is foreseen as global control software for JUNO's LHS, can be fed directly with the data stream written into the .txt file.

### 6.2.3 Test measurements in the laboratory

To investigate the reliability of the sensor data, especially with respect to the resolvable liquid level changes, the TruSense S310 with its diffuser lenses was mounted into the ITEM scaffolding already used for the characterization of the HPSs. A cylindrical acrylic vessel, which can be filled with liquids such as distilled water or LAB, was placed on the vibration-decoupled stainless steel base plate. The distance from the sensor to the liquid surface (within the vessel) can be increased by using different mounting positions for the sensor on the horizontal braces. The scaffolding offers three possible options up to its total height of  $\sim 2.5$  m. In Figure 6.13 A the TruSense S310 is mounted in the middle height at a distance of  $\sim 1.6$  m to the bottom plate. The precise adjustment of the laser central into the acrylic pipe and orthogonal to the liquid level was ensured by means of a plumb bob and the visible adjustment laser.

#### **Short-term measurement with LAB as target liquid:**

In a first test measurement using pure LAB, the sensor was operated with a repetition rate of 1 Hz for  $\sim 20$  min. Figure 6.13 B shows the measured values for the most intense laser reflex. The mean value of the measured data points gives a distance of  $(1252 \pm 0.05)$  mm, which is in well agreement with the rough cross-check by means of a meter rule. All measurement values lie within a  $\pm 10$  mm band around the mean value, which corresponds to the maximum reading fluctuation specified by Laser Technology Inc. Except for a few single data points, all values are within a band of  $\pm 5$  mm around the mean. The readings for the first and last reflex correspond to those shown here within  $\pm 1$  mm.

#### **Long-term measurement with distilled water as target liquid:**

To evaluate the long term stability of the sensor and the capability to measure the level of pure water the LAB was replaced by distilled water. For this investigation, the laser was placed in the uppermost position within the scaffolding resulting in an increased distance of  $\sim 2$  m above the water surface. Before the measurement was started, the water level was marked on the acrylic pipe by means of a felt-tipped pen. Subsequently, data was taken with a sampling rate of 1 Hz for 30 h with the TruSense S310. In order to make the fine changes in the level clearly visible, the mean values calculated from 100 sampling points were plotted in Figure 6.13 C. Starting at a distance to the water surface of  $\sim 2079.5$  mm the readings slightly increased during the 30 h to  $\sim 2082.4$  mm. This discrepancy was confirmed comparing the marked water level on the tube before and after the measurement using a vernier calliper. Since the temperature in the laboratory was kept stable within  $\pm 0.2$  °C by the air conditioning system, it can be assumed that the falling liquid level is caused by evaporation of water from the pipe. The small fluctuation of the

mean values obtained from the data demonstrates the feasibility of resolving filling level changes of  $\pm 100 \mu\text{m}$ .

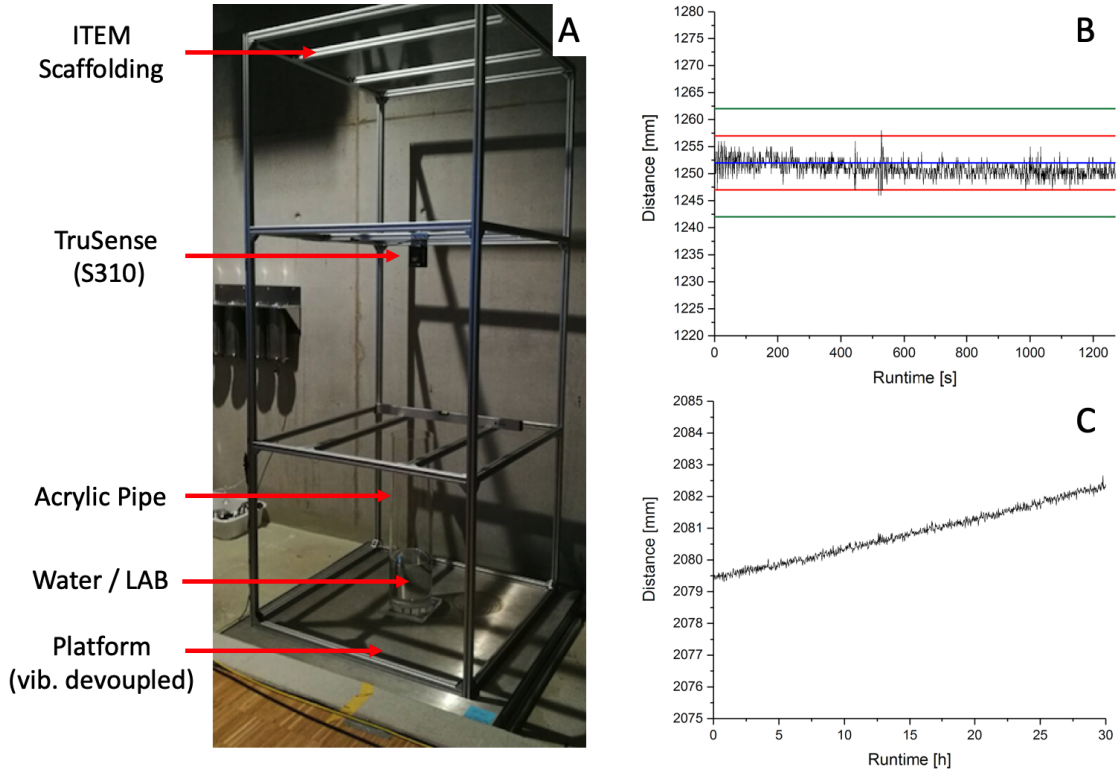


**Figure 6.13:** **A:** Setup used for the test of the TruSense S310 contact-less optical liquid level meter. The sensor is mounted in the ITEM scaffolding, which was also used for the HPS characterization facility. The scaffolding is placed on a vibration decoupled stainless steel bottom plate. On this plate, directly below the sensor, a pipe shaped acrylic vessel for water and LAB was placed. **B:** Distance values to a LAB surface with a sampling rate of 1 Hz. The mean value of the raw sensor readings is plotted as blue solid line, while the red lines indicating the edges of a  $\pm 5$  mm band around the mean. The green lines represent the maximum fluctuation of the sensor readings of  $\pm 10$  mm specified by Laser Technology Inc. **C:** Long-term measurement of the distance to a water level in the acrylic pipe. The data points in the plot are the mean values obtained from 100 sampling points for the distance recorded at a rate of 1 Hz. Clearly visible is an increase in the distance corresponding to a falling water level in the pipe due to evaporation of water during the 30 h of measurement duration.

### Interpretation of the laboratory tests:

Both scenarios are well comparable to the measurement situation in a filled JUNO or OSIRIS detector either with water or LS. During the test using LAB, the excellent stability of the raw sensor readings (even at short distances) was demonstrated. Moreover, the additional stray light from the room lighting did not influence the

measurements noticeably. The long-term test has shown that the resolution of level changes far exceeds the requirements. The available measuring rate of 14 Hz for single distance samplings enables the calculation of stable mean values within a few seconds. The implementation of filter algorithms (e.g. for vibration compensation) for the sensor data as well as the used mean value calculation can be integrated easily into the TUM/JUNO TruSense Tool as selectable options.

#### 6.2.4 Test measurement in the Double Chooz near detector

During the dismantling of the Double Chooz (DC) near detector, the opportunity arose for a sensor test under operating conditions perfectly matching the foreseen usage for the laser in the OSIRIS detector and in the LMP of the JUNO CD. Since a precise measurement of filling level changes is necessary for filling as well as draining the scintillator from the fragile thin-walled neutrino target (NT) vessel in DC, a mechanical system called Tamago (Proservo NMS5, for details see [114]) was installed in the chimney of the detector.

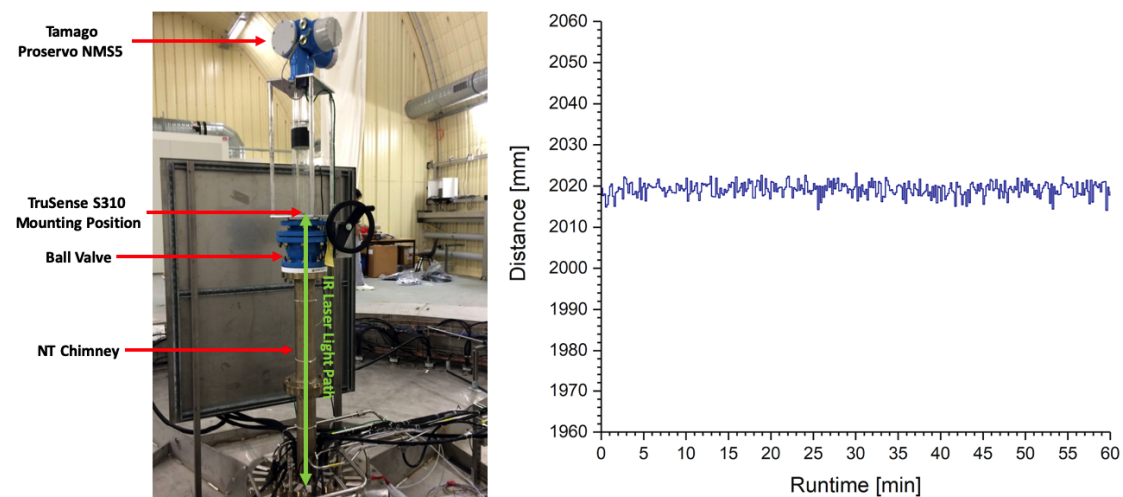


**Figure 6.14:** **Left:** NT chimney of the DC near detector. For the test the Tamago float based mechanical level measurement system was removed with its holding structure and replaced by the TruSense S310 level meter with diffuser lenses. The level was measured through the opened ball valve. The green double-arrow is indicating the light path of the IR laser. **Right:** Distance to the LS surface measured with a sampling rate of 1 Hz during a sensor runtime of 1 h. The data shown in the plot are the mean values of 10 sampling points.

The system shown on the left side of Figure 6.14 failed during the years of detector operation and was removed. It is no longer available for emptying the detector in 2020. In a test during the first phase of detector dismantling in November 2018,

the usability of the TruSense S310 laser system with the TUM/JUNO Raspberry-Pi based readout solution was evaluated. Therefore, the remaining holder of the Tamago above the ball valve (see Figure 6.14 left) was replaced by a holding structure for the laser sensor.

The level meter was operated during one hour in the NT chimney. On the right plot of Figure 6.14 the result of the test measurement is shown. The obtained distance to the LS of  $(2019.2 \pm 0.1(\text{stat.}))$  mm is in well agreement with the expectation  $(200 \pm 15)$  cm calculated from the live readings of the hydrostatic pressure sensors on the bottom of the NT.

The stability of the sensor readings is remarkable, since the sensor mount had no vibration decoupling. Moreover, during the measurement dismantling work was done by several men on the cabling flanges mounted on the upper detector cover. During the test, no contradictions could be found regarding the usability of the sensor in JUNO and OSIRIS. Beyond that, the TUM/JUNO laser-based level measurement system meets the strict requirements to the Double Chooz detector's precision filling level monitoring system for the final liquid removal.

## 6.3 Temperature sensor grid for OSIRIS

As pointed out in chapter 5, generation and maintenance of a fine adjusted temperature gradient within the OSIRIS detector volume is essential for the success of the project. To ensure this, precise control of the heating and cooling systems for the detector liquids is necessary. That requires a precise grid of numerous thermometers in the water buffer as well as inside the acrylic vessel. Moreover, the sensors monitoring the temperature layering within the AV will be in direct contact with the LS. Therefore, strict requirements must be placed on the material compatibility as well as the radio purity of the thermometers and the related cabling. How many sensors are required for the grid as well as the identification of the optimal sensor positions is the subject of simulations currently carried out at the University of Mainz.

### 6.3.1 Sensor tests within the OSIRIS prototype

To investigate the feasibility of temperature layering in the LS and the influence of different diffuser geometries (see also Section 5.1.4) on its stability during the continuous filling process, a small simplified prototype of the OSIRIS detector is being built at the Johannes Gutenberg University in Mainz. For this purpose the water and LS volumes of the prototype shown on the left of Figure 6.15 will be instrumented with four PT-1000 thermometers. Three of them will be deployed in the LS volume, while one is installed in the buffer vessel. The PT-1000 thermometers

of this type (shown in Figure 6.15 right) are intended for later use in OSIRIS. Therefore, detailed tests of this sensors within the prototype are planned.

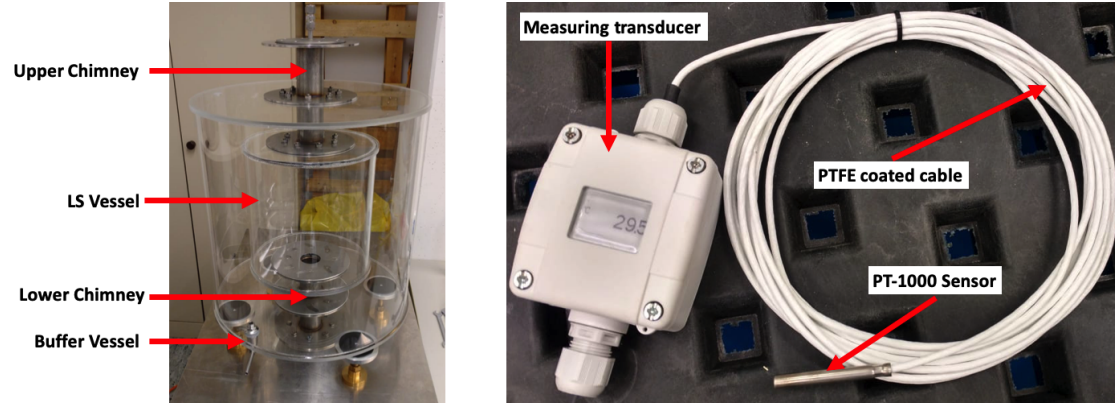


**Figure 6.15:** **Left:** Photo of the OSIRIS prototype currently set up at JGU Mainz. The LS vessel as well as the water buffer can be filled through the chimneys. Their ends can be equipped with diffusers in various geometries. In order to study the temperature gradient stability for several filling schemes and diffusers, it is planned to deploy three PT-1000 sensors into the LS vessel and to install a further one in the buffer. **Right:** Shown is one of the PT-1000 sensors equipped with a 6 m long PTFE coated cable. The resistance thermometer is housed in a stainless steel mantle with 6 mm diameter and a length of 50 mm. For sensor readout a measuring transducer with an additional display showing the live readings was attached to the PT-1000. The transducer uses the 4-20 mA standard for the output.

To ensure compatibility with the LS and water, a sensor with the passive PT-1000 resistor enclosed in a stainless steel housing (V4A 1.4571) was chosen [124]. The sensor is connected with a two wire PTFE coated cable. The selected precision class A type realizes an absolute accuracy  $\Delta\vartheta$  of

$$\Delta\vartheta = 0.15^{\circ}\text{C} + 0.002 \cdot |\vartheta| \quad (6.4)$$

where  $\vartheta$  denotes temperature in  $^{\circ}\text{C}$ .

### 6.3.2 Multi-channel readout electronics

The passive PT-1000 sensor with the 2 wire readout system is embedded in a current loop similar to the HPSs. Typical measurement currents range from  $\sim 400 \mu\text{A}$  to  $\sim 5 \text{ mA}$  to keep the power loss at the resistor as low as possible. To reach a sufficient precision of the readings as well as a sufficient resolution of the small res-

istance changes in the temperature regime between 0 °C and 40 °C, a measurement transducer [125] is connected to the sensors. This device allows a modification of the measuring current according to the required temperature range. Furthermore, it converts the voltage signal to the 4-20 mA sensor communication standard. The transducer is powered with 15-36 VDC and furnishes the current of the sensor as well. For the prototype tests a Statron 3250.1 laboratory power supply [109] will be used. To be able to readout the four sensors of the OSIRIS prototype, the single channel 4-20 mA scheme used in characterization facility for HPSs (see also section 6.1.2) was modified. The four current signals are converted into voltage signals by means of four 165  $\Omega$  resistors. The voltages are digitized using four of the eight channels of the MCP3008 ADC chip [108]. The entire system was mounted in a metal casing (see Figure 6.16), which is foreseen for the installation on the prototypes support scaffolding.

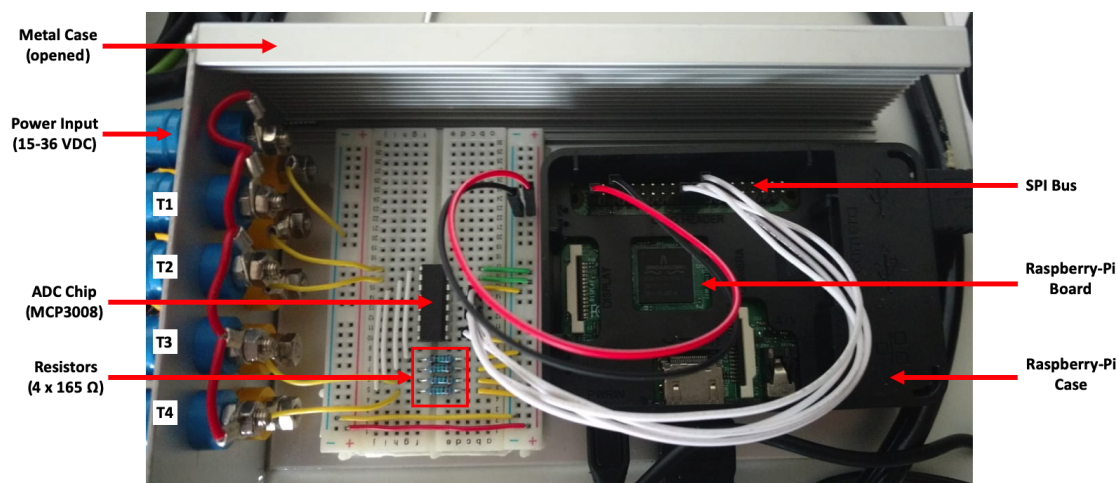


**Figure 6.16:** Shown is the 4-20 mA readout system with four channels on the basis of a Raspberry-Pi 3b. The entire setup is placed within a metal case. On the front panel the input connectors for the sensors (T1 to T4) are placed as well as the power input connectors. The current signal from the measurement transducers are transferred in a voltage signal between 0.66 V and 3.30 V by one 165  $\Omega$  per channel. This voltages are digitized using four of the eight input channels of the MCP3008 chip. The digital values from the ADC are read out via the Raspberry-Pi’s SPI bus.

Currently the liquid handling system of the prototype (with pumps, heaters and chillers for the liquids) is set up at JGU. In parallel a holding structure for the sensors in the LS vessel is under construction at TUM. First filling and sensor tests with the prototype are planned for the forthcoming spring.

### 6.3.3 Data acquisition software and live-plotting tool

The data acquisition software used for the readout of HPSs, which was developed in Python during the bachelor's thesis of M. Walter [111], was modified and its functionality upgraded to match the requirements of the temperature sensor grid with four sensors. By command line inputs calibration data can be acquired and the temperature readings can be equalized before the start of the filling test. The sampling rate can be selected from 0.1 Hz up to 1 kHz in steps of 0.1 Hz. Moreover, mean calculation algorithms were implemented for more stable sensor readings as well as for efficient data reduction for very long measurement series. The data stream of the four channels including timestamps is saved in form of comma separated values in a .csv file which can be accessed directly by other programmes, e.g. heater and chiller as well as pump control software in LabView or EPICS.

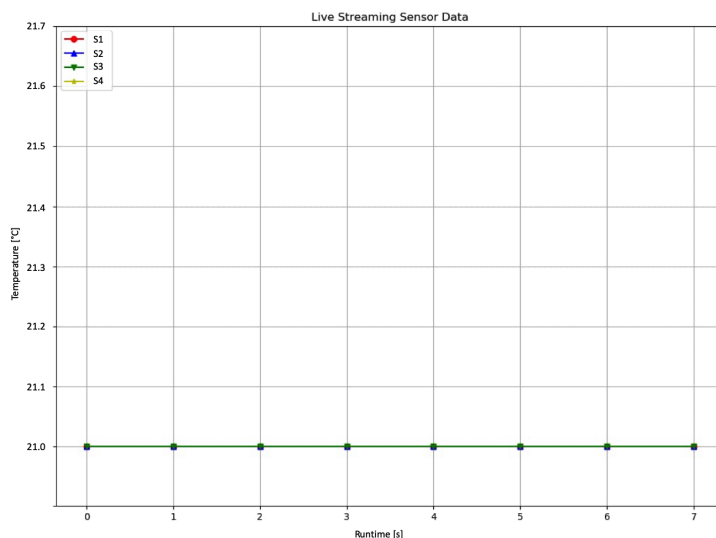


**Figure 6.17:** Shown is a screenshot from the live plotting window of the thermometer readout software developed in Python with the libraries NumPy and Matplotlib as well as with the "drawnow" tool. Eight data points for each of the channels were recorded in the laboratory with all four sensors placed next to each other at an equal temperature.

Especially for the prototype filling tests, a live plotting tool based on the python libraries NumPy, Matplotlib with the live graph updating software "drawnow" was developed. This libraries allow easy implementation of a live plotting window (as shown in Figure 6.17) for a stream of data. The readout software is now able to read and plot data from all four channels simultaneously. Also continuous plotting of mean values from a selectable number of sampling points is possible. Saving live plots to a file in the .png format is also foreseen.

# Chapter 7

## Development of a radon monitor for the nitrogen supply system

As already mentioned in the previous chapters, the plants for the production and handling of LS as well as ultra-pure water require a constant supply of high purity nitrogen. In addition, nitrogen is required to flush the storage tanks and the OSIRIS detector before filling. During the entire operation of JUNO and OSIRIS, nitrogen blankets must be maintained above the LS and the ultrapure water volume. This measure is essential to protect the LS from oxidation. Moreover, it should keep the entry of radon from the ambient air into the ultra-pure liquids to a minimum. Since these substances with high affinities to radon will be in direct contact with this protective nitrogen layer, it is essential to ensure low radon concentrations in the nitrogen.

Radon, which is naturally present in the environment, consists mainly of the isotopes  $^{222}\text{Rn}$  ( $\sim 90\%$ ) and  $^{220}\text{Rn}$  ( $\sim 9\%$ ). Since all decays following  $^{224}\text{Ra}$  in the thorium chain have short half-lives below  $\sim 10.6$  h (from  $^{212}\text{Pb}$ ), the entry of  $^{220}\text{Rn}$  will not provide long-lived backgrounds in the JUNO detector. In contrast, the uranium series contains the isotope  $^{210}\text{Pb}$  (see Figure 7.1), which has a half-life of 22.2 a [126]. So once the detector liquids are loaded with radon,  $^{210}\text{Pb}$  stays for the entire runtime of the experiment in the detector providing backgrounds mainly by daughter decays. The  $\beta$ s emitted from  $^{210}\text{Bi}$  ( $Q = 1161.2$  keV [126]) overlap the region of interest for the detection of CNO and  $^7\text{Be}$  neutrinos from the sun. Moreover,  $^{210}\text{Po}$  causes a correlated background for JUNO's main goal, the measurement of the NMO via IBD events. This background for IBD events (see also the publication by the KamLAND Collaboration [127]) originates from  $^{210}\text{Po}$ , which undergoes an alpha decay ( $E_\alpha(^{210}\text{Po}) = 5.304$  MeV [126]). The  $\alpha$  reacts with  $^{13}\text{C}$  in the LS via



to an excited  $^{16}\text{O}^*$  nucleus and a neutron. The de-excitation of the nucleus happens nearly instantaneous, leading to a prompt signal, while the neutron capture in the LS provides a delayed signal, similar to IBD events.

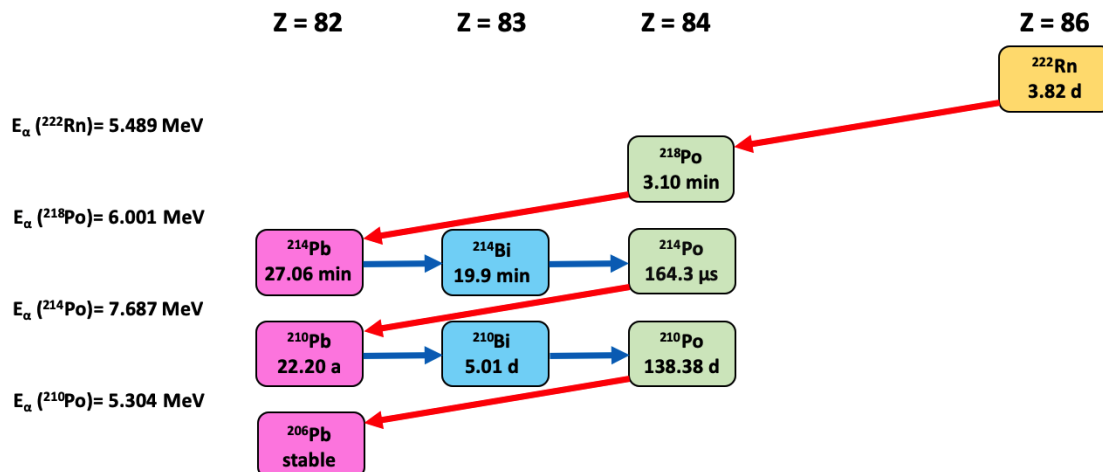


**Figure 7.1:** Part of the uranium series from  $^{222}\text{Rn}$  to the stable  $^{206}\text{Pb}$  (rare branchings with ratios below 0.1 % not shown). The alpha decays are indicated by red arrows (corresponding  $\alpha$  energies listed on the left), while beta decays are illustrated by blue ones. Since  $^{210}\text{Pb}$  has a half-life of 22.2 years, it can be considered to be present in the detector during its entire operation time. Subsequent decays are causing multiple backgrounds, even for the IBD detection in JUNO. Therefore, any contamination of the LS with radon has to be avoided. All figures in the drawing were taken from [126].

In JUNO's  $\text{N}_2$  gas supply system (NGSS), which is in its early design phases (by the IHEP in Beijing), the gas will be produced by boiling it off from LN (Liquid Nitrogen). For radon removal activated carbon traps operated in LN at 77 K are foreseen [128]. To allow efficient solar neutrino spectrography with the JUNO detector, the design goal for the NGSS is a radon activity below  $100 \mu\text{Bq}/\text{m}^3$ . However, according to simulations [128] the reactor neutrino detection for the NMO determination via IBD is considered to be possible up to  $1 \text{ mBq}/\text{m}^3$ . To ensure that these low activities are achieved and constantly maintained, a sensitive Radon Monitoring System (RaMS) for  $\text{N}_2$  is required. Since air leaks in the NGSS and associated radon contaminations usually occur suddenly, the measurement time should be as short as possible. Moreover, it would be beneficial if the RaMS has early warning capabilities.

For this purpose an alpha spectrometer based on a large-volume proportional chamber was developed in a two phase program as part of this thesis. In the demonstrator phase, the feasibility of the detector operation using pure nitrogen was

evaluated. Furthermore, a characterization of this gas sampling detector with  $\sim 4.3$  l active volume as well as the development of background suppression techniques were carried out. In the second phase (during the last year) a first low background detector with the final active volume of  $\sim 42$  l was built and tested. This chapter gives an overview of both phases and their results.

## 7.1 The RaMS proportional counter demonstrator

Proportional chambers are commonly used gas sampling detectors for the measurement of low radioactivity. This detector type features a high efficiency for the detection of alpha particles and can provide a spectral measurement of their energies. To allow the usage of a proportional counter in the NGSS, it has to be adapted to the requirements of the operation with pure nitrogen as counting gas. Avoiding the admixtures of noble gases or quenchers was one of the design goals for the RaMS detector. Furthermore, the operation at the blanket and flushing pressure of JUNO (a few mbar above atmospheric pressure) should also be ensured. All this requirements were considered during the design of the RaMS demonstrator detector.

### 7.1.1 The detector design

The cylindrical proportional chamber (see Figure 7.2) was made from a copper tube with an outer diameter of 152 mm and a wall thickness of 2 mm with a length of 250 mm. On the ends of the tube, stainless steel CF flanges (DN125) were fixed by brazed joints. The pipe is closed with two identical copper lids in the form of blind flanges, which are sealed by rubber O-rings embedded in dedicated grooves in the modified DN125 flanges. Both lids are equipped with a DN25 KF flange from brass on a brass pipe socket. While one flange is used for the connection to a dry vacuum pump (Edwards nXDS10i [129]) via the main valve, the HV connection is guided through the other. Each of the lids features two 6 mm pipe sockets with valves provided by Swagelok. One of these ports is connected to a pressure gauge, two others are foreseen for the connection of pressurized gas bottles with an argon/methane mixture or nitrogen respectively.

The internal structure of the proportional counter is shown in Figure 7.3. The holding structure for the counting wire consists of two copper bars mounted in counterbores on the faces of the CF flanges. A PTFE insulator with a central brass pin is inserted in the middle of each bar. The 20  $\mu\text{m}$  thin gold coated tungsten counting wire was spanned between the pins (using a mass of  $\sim 4$  g) and subsequently soldered to them. The high voltage connection is realized by a MHV feedthrough (for panel mounting, sealed by rubber O-ring) mounted on a DN25

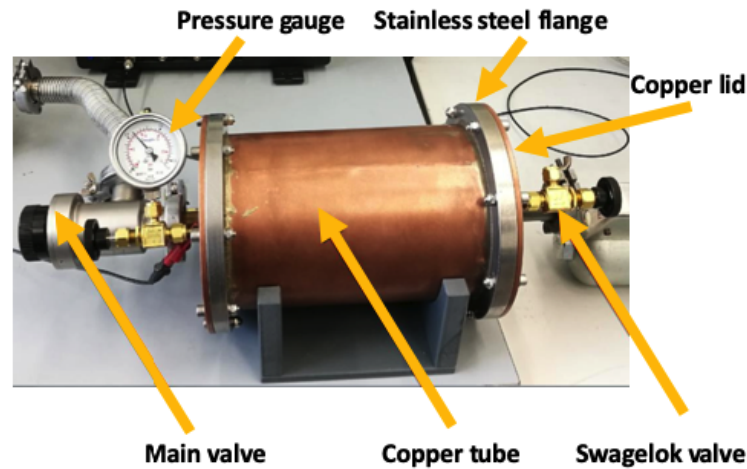


**Figure 7.2:** Photo of the proportional counter demonstrator, which was constructed during the Master's Thesis of Philipp Landgraf [130]. The detector with an active volume of  $\sim 4.3$  l, which was made from a cylindrical copper tube, can be filled with gas through 6 mm pipe sockets sealed by Swagelok valves. The internal gas pressure can be read from a manometer attached to one of these valves. The proportional chamber can be evacuated through the main valve by a dry scroll pump (not on the photo). For a more detailed description refer to the text.

blind flange from stainless steel. With this blind flange one of the DN25 ports on the lids is closed. A cable with a polyethylene (PE) jacket provides the electrical connection between the MHV feedthrough and the counting wire.

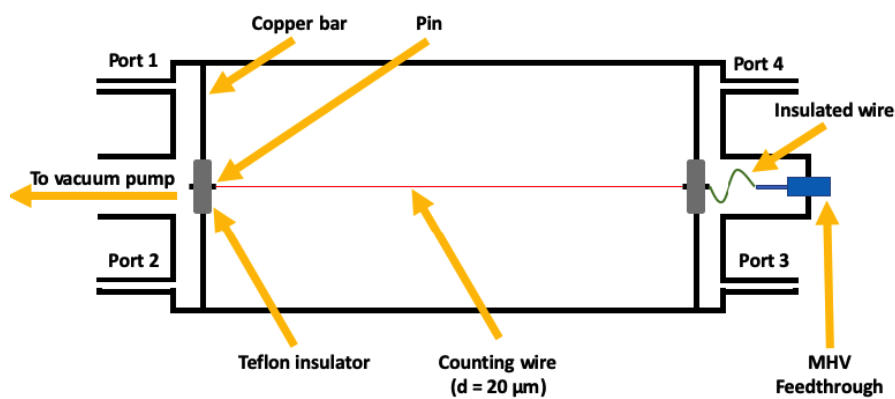


**Figure 7.3:** Scheme of the internal structure of the proportional counter demonstrator. The counting wire is soldered to two brass pins fixed within PTFE insulators. Copper bars hold them in place. The electrical connection is furnished through a vacuum tight MHV feedthrough and a copper wire with a PE jacket. A comprehensive description can be found in the text.

### 7.1.2 Readout electronics

To allow precise spectrography of the expected small pulses from a nitrogen-filled gas detector (in the proportional regime), a dedicated readout electronics was developed. As shown in the block diagram (see Figure 7.4), a charge sensitive preamplifier (ORTEC 142PC) is connected to the detector [131]. In addition to amplifying the signal, the high voltage is also furnished to the proportional counter through the device. To minimize the distortion of the small signal, the coaxial cable between detector and preamplifier is kept as short as possible (10 cm).

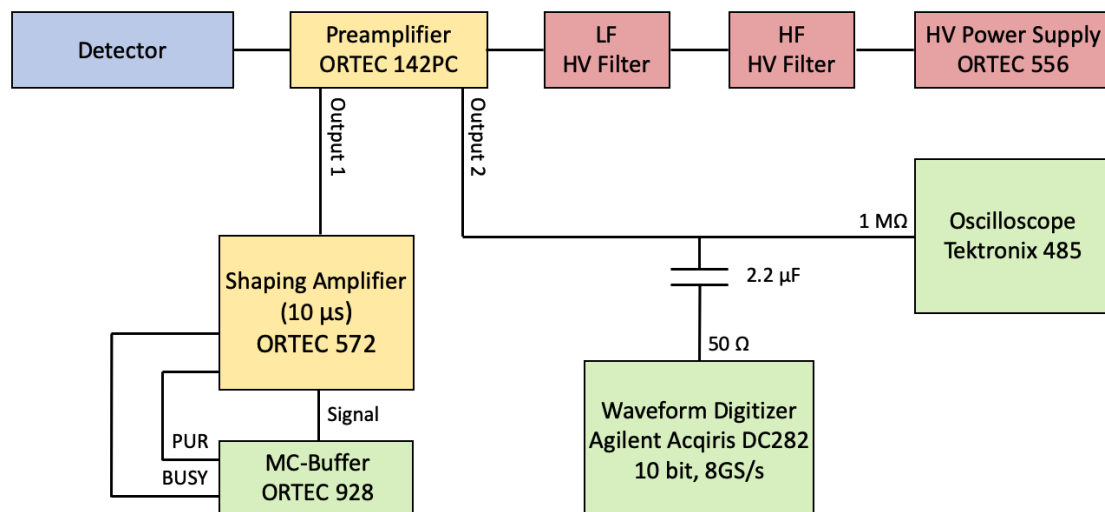


**Figure 7.4:** Block diagram of the readout electronics of the RaMS proportional counter. The HV supply system is drawn in red while the analogue pulse processing electronics (pre- and shaping amplifier) is shown in yellow. The pulses can be monitored by a 350 MHz oscilloscope (green). A pulse height spectrum for the shaped pulses can be recorded with a multichannel analyzer with a buffer memory (called MC Buffer), while the unshaped signals are digitized using a waveform digitizer (highlighted in green). A detailed description of the setup is given in the text.

The NIM module ORTEC 556 serves as a high voltage source, which provides stable voltage up to 3 kV (drift less than 0.03 % per day). The low ripple ( $<15 \text{ mV}_{pp}$ ) is of particular importance for the stability of the detector pulses' baseline. Beyond that, the device allows resetting the voltage after a shut down to its previous value with a precision of 0.1 %, which ensures the reproduction of the gain in different measurements [132]. To further reduce the noise on the HV, two filters were installed in the supply line. A bidirectional passive HV filter (A483 provided by CAEN [133]) featuring a typical ripple rejection of 20 dB (26 dB at 36 kHz) was added for noise reduction. Since this measure was found to be insufficient at

low frequencies, an additional HV low-pass filter (scheme shown in Figure 7.5) was built and inserted in the detector bias line.

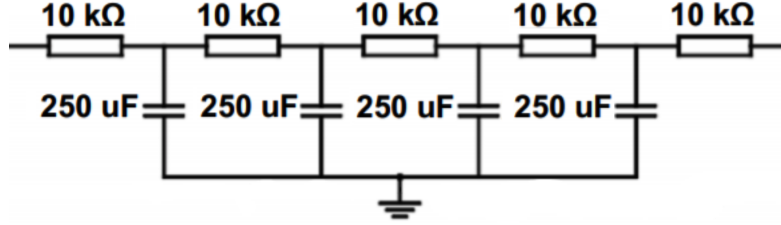


**Figure 7.5:** Circuit diagram of the custom made high voltage low-pass. The filter was realized by a series of identical RC elements with resistors of  $10\text{ k}\Omega$  and HV capacitors with  $250\text{ }\mu\text{F}$ . The entire circuit is mounted into a standard NIM cassette with SHV input and output connectors on the front panel. Note, that due to the voltage limitations of the capacitors, the filter can only be used up to  $2\text{ kV}$ .

The detector pulses are decoupled from the HV within the charge sensitive preamplifier and subsequently amplified. The device features two signal outputs. One of them is connected to an ORTEC 572 shaping amplifier [134] (shaping time:  $10\text{ }\mu\text{s}$ , gain: 20). The pulse heights of the gaussian shaped signals are recorded by a multichannel analyser with buffer memory (ORTEC Easy NIM 928 MCB [135]) providing a live spectrum of the recorded events. By the usage of the PUR (Pile-Up Rejector) and the BUSY output of the the main amplifier, pile-up events are rejected and the dead time of the system can be determined. The MCB's internal rate meter allows recording and live monitoring of the rate in previously defined pulse height ranges. This can be beneficial if the RaMS detector has to act as early warning system for severe radon leaks in the NGSS.

The second output of the preamplifier is connected to an analogous oscilloscope for live signal inspection. In parallel the pulses are fed into an Agilent U1065A Acqiris DC282 waveform digitizer [136] which is triggered by its internal discriminator. On the input of this ADC (terminated with  $50\text{ }\Omega$ ) a  $2.2\text{ }\mu\text{F}$  capacitor is used as an additional high-pass signal filter. To store the rare unshaped pulses from the preamplifier allows a detailed offline analysis as well as the application of background suppression techniques (such as pulse shape discrimination).

### 7.1.3 Detector calibrations

To facilitate the detector characterization and to have a comparison for the spectra in nitrogen, all measurements were performed first in a mixture of 90 % argon and 10 % methane (referred to as P10) and then in nitrogen. For the calibration of the detector with radon gas, an additional pot-shaped recipient had to be connected via a KF 3-way tee and a further valve in the vacuum system. A  $^{226}\text{Ra}$  source

with an activity of 3.7 kBq was placed in this vessel. Before the measurements, the detector (as well as the source pot) was evacuated to a pressure below  $10^{-3}$  mbar, subsequently flushed with the respective gas and then pumped down again. After that, the detector and the source pot are finally filled with the counting gases nitrogen or P10. An absolute pressure of 1.2 bar was chosen to avoid leaking of oxygen from the ambient air into the detector as well as to simulate the slight overpressure in JUNO's NGSS. Once the valve between detector and source pot is opened,  $^{222}\text{Rn}$  emanated from the source diffuses into the detector volume. After waiting approximately one day an activity sufficient for the calibration has built up.

### $\alpha$ calibration with $^{222}\text{Rn}$ -loaded P10:

Before taking calibration data, the optimal detector supply voltage in terms of linearity and resolution in the energy range of the alpha decays, caused by radon and its daughters, was determined roughly. Therefore, test spectra at different voltages were recorded, containing some hundred events. Due to simplicity, this was done with the live spectrography electronics (shaping amplifier and MC-Buffer). Then the voltage was set to the determined value of 720 V and calibration data was taken with the waveform digitizer. The threshold of the internal discriminator of the ADC was set to 30 mV, while a trigger delay of  $-10 \mu\text{s}$  ensures recording a sufficiently long baseline. The absolute trace lengths was limited to  $50 \mu\text{s}$  while using a sampling rate of 1 GS/s. With these settings 30.000 pulses were recorded during 114 min of measurement runtime.

To obtain a measure for the charge deposited in the counting wire and with that the energy of the events, the pulses were integrated from their onset, determined by a constant fraction timing algorithm, up to the end of the acquisition window ( $\sim 40 \mu\text{s}$  integration time). In the scatter plot shown in Figure 7.6, the obtained values for each event are plotted along the runtime of the measurement. Three clearly defined bands occur which can be assigned to  $^{222}\text{Rn}$  and the two short-lived alpha emitters  $^{218}\text{Po}$  and  $^{214}\text{Po}$  in the decay chain. Due to the long half-life of  $^{210}\text{Pb}$  and the associated low decay rate of  $^{210}\text{Po}$ , the alpha line of this isotope is not visible. As visible in the scatter plot, the populations of the three lines run horizontally, indicating a stable gain during the  $\sim 2$  h of measurement.

The positions of the overlapping  $^{222}\text{Rn}$  and  $^{218}\text{Po}$  peaks in the charge histogram of the detector pulses were determined by fitting the data with a sum of two Gaussian functions and an additional constant. The  $^{214}\text{Po}$  peak was fitted separately using a single gaussian with an additional linear background component. The energy spectrum shown in Figure 7.7 was calibrated using the linear regression of the three measuring points.

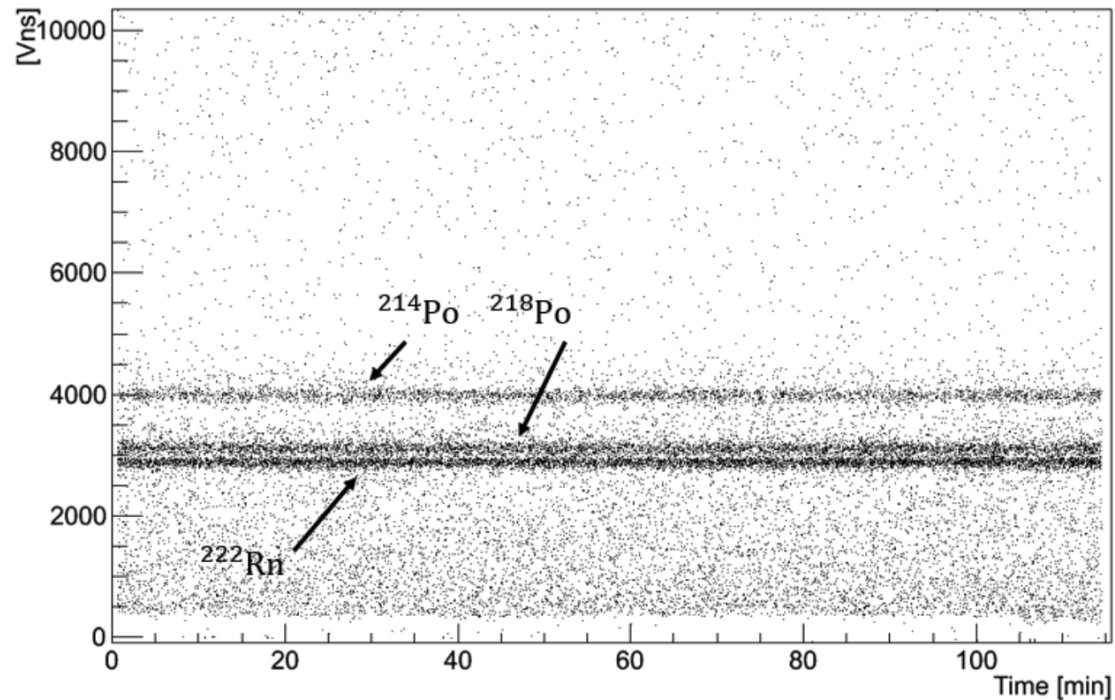


**Figure 7.6:** Scatter plot showing the values obtained from pulse integration, which are a measure for the deposited charge, along the runtime of the data taking. A radon loaded P10 counting gas at 1.2 bar absolute pressure was measured using a detector supply voltage of 720 V. Three defined populations occur, which can be assigned (as indicated in the plot) to the alpha decays of  $^{222}\text{Rn}$  and the short-lived nuclei following in the decay chain. As the horizontal course of the three lines shows, sufficient stability of the gain was achieved for alpha spectroscopy in this energy range.

The energy spectrum shows the expected peaks of  $^{222}\text{Rn}$  and the two short lived Po daughters. The unequal intensities of the lines are caused by different detection efficiencies for the corresponding decays. This can be explained by a model based on the trapping of charged daughter ions of radon on the counting wire, which is discussed in detail in the following sections. The background to the left of the peaks towards low energies can be explained by degraded alpha signals (e.g. emission of the particles from surfaces or inhomogeneities in the electric field of the detector) and micro-discharges in the detector. This aspect is also discussed in more detail later in this chapter. The resolutions at the three lines as well as their position in the calibrated spectrum are listed in Table 7.1.

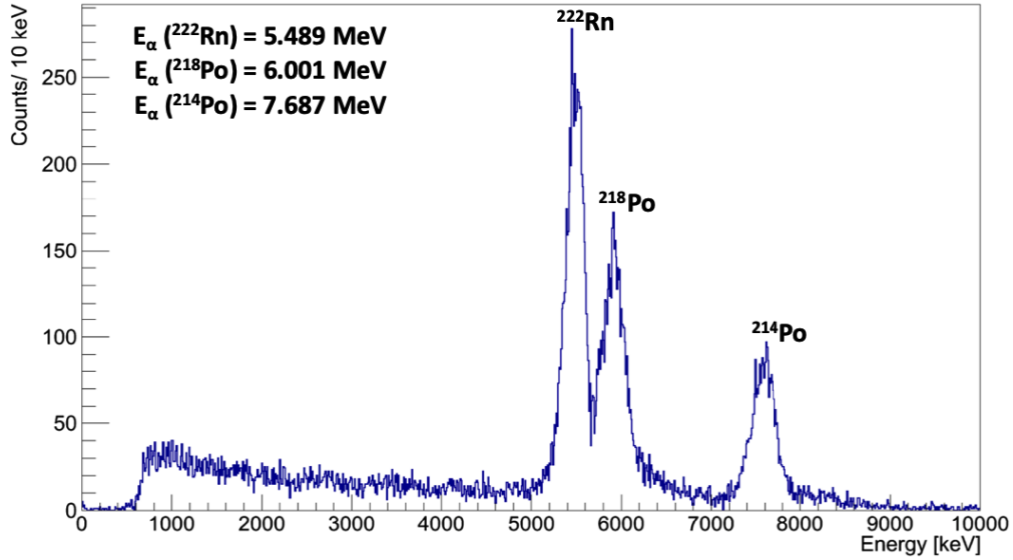


**Figure 7.7:** Spectrum of the radon-loaded P10 counting gas measured at a detector supply voltage of 720 V. The expected lines from  $^{222}\text{Rn}$  at  $\sim 5.5$  MeV,  $^{218}\text{Po}$  at  $\sim 6.0$  MeV and  $^{214}\text{Po}$  at  $\sim 7.7$  MeV are resolved. The background towards lower energies is caused by micro-discharges as well as by alphas not depositing their full energy in the counting gas. The missing intensity of the Po-peaks is caused by trapping of the charged Rn daughters on the counting wire. A detailed explanation of this effect is presented in the following sections.

Isotope	Real $\alpha$ energy [keV]	Visible $\alpha$ energy [keV]	Resolution (FWHM) [keV]
$^{222}\text{Rn}$	5489	$5517 \pm 2$	$256 \pm 5$
$^{218}\text{Po}$	6001	$5959 \pm 3$	$350 \pm 9$
$^{214}\text{Po}$	7687	$7695 \pm 3$	$367 \pm 7$

**Table 7.1:** The table lists the isotopes with their alpha energies from [126]. The third column contains the visible energies in the RaMS proportional counter prototype filled with P10 gas ( $p_{abs} = 1.2$  bar) and operated at 720 V. The resolution (FWHM) of these lines are shown in the right column.

### Calibration with $^{222}\text{Rn}$ -loaded nitrogen:

The detector filled with pure nitrogen instead of P10 was calibrated following the same procedure. After the source pot and the counter were filled with the  $\text{N}_2$  a waiting time of  $\sim 24$  h ensured a sufficiently high alpha activity for a rough adjustment of the supply voltage using the live spectrography electronics. The best energy resolution and linearity of the detector response was observed between

600 V and 800 V in this brief test measurements. Therefore, the voltage was set to 700 V for a first calibration. To allow a digitization of the small pulses in nitrogen, the trigger threshold of the ADC was lowered to 7 mV.

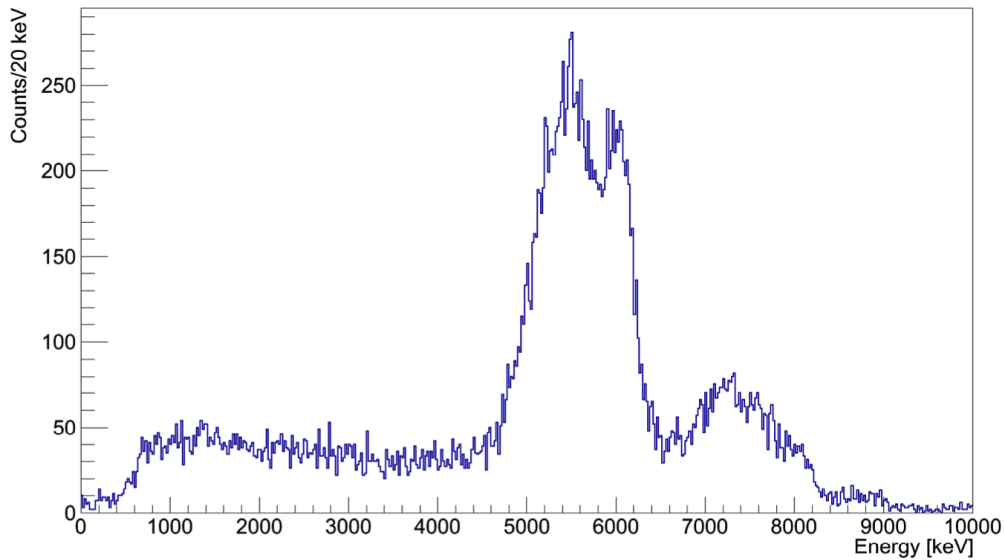


**Figure 7.8:** Spectrum of the radon-loaded nitrogen counting gas measured at a detector supply voltage of 700 V. The peaks of  $^{222}\text{Rn}$  and  $^{218}\text{Po}$  overlap each other. However, the 6 MeV line is clearly visible as shoulder of the radon peak. The  $^{214}\text{Po}$  events overlap with the high-energy part of the double peak as well. Therefore, the maximum of the broad peak seems to be shifted to  $\sim 7.35$  MeV. The background towards lower energies has the same origin as in P10. It is mainly caused by micro-discharges as well as by alphas not depositing their full energy in the counting gas. Furthermore, due to the usage of the molecular (and therefore electron quenching)  $\text{N}_2$ , the energy resolution is reduced by dependencies of the charge amplification on the electrons' drift path within the detector.

In the energy spectrum, obtained from the calibration, the three alpha lines are visible (see Figure 7.8). The peaks of  $^{222}\text{Rn}$  and  $^{218}\text{Po}$  are overlapping each other. Due to the usage of the electron quenching  $\text{N}_2$ , the gas amplification for an alpha event is more dependant on the drift path of the electrons in the detector. This means a dependence of the detector response on the position of the  $\alpha$  particle interactions within the gas. The resolution of the 5.49 MeV radon line is decreased (compared to P10) to a value of  $918 \pm 19$  keV. Nonetheless, it should be mentioned, that an energy threshold below 1 MeV was achieved by the reduced trigger threshold of 7 mV (about twice the observed baseline RMS of  $(3.40 \pm 0.01)$  mV).

### 7.1.4 Optimization of the spectrometer's supply voltages

As part of Alexander Gardanow's Bachelor's thesis [137], the proportional regime with linear energy response of the detector was determined in a series of calibrations at different supply voltages. The HV was raised from 520 V up to 1020 V in steps of 100 V. For each HV setting 30.000 pulses were recorded with an ADC trigger threshold of 30 mV (7 mV for N<sub>2</sub>). Figure 7.9 shows the energy spectra of the measurement series using P10 gas. For the calibrations the position of the 5.49 MeV radon line was used.

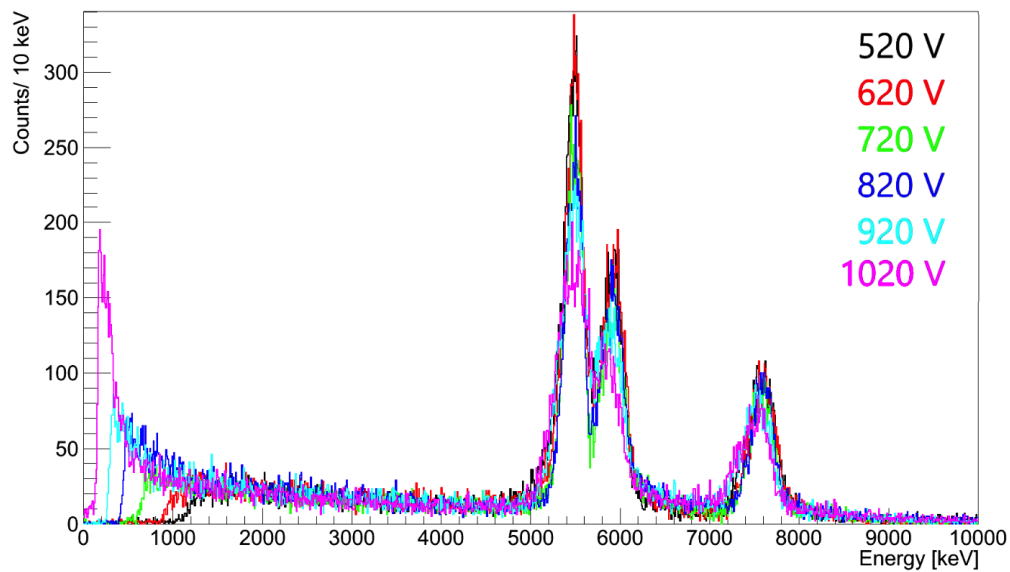


**Figure 7.9:** Energy spectra obtained with different supply voltages. Obviously, a voltage variation from 520 V up to 1020 V has just a minor influence on the linearity of the detector within the investigated energy range from 5 MeV to 8 MeV. However, the energy resolution is getting worse towards higher voltages, while an optimum between 620 V and 820 V was identified. Note, that the energy detection threshold is significantly reduced while increasing the HV. For 1020 V the proportional chamber becomes sensitive to  $\beta$  radiation. Also  $\gamma$ s contribute events in the form of secondary betas produced in the copper. Cosmic muons traversing the detector contribute as well to the steep increase of this spectrum at low energies.

In the whole calibration series no HV setting caused severe nonlinear energy response of the detector. In contrast, the energy threshold of the detector is significantly influenced (values for the peak positions of <sup>218</sup>Po and <sup>214</sup>Po shown in Table 7.2). Due to the higher gas amplification, it decreases with increased voltage. As already shown in Philipp Landgraf's thesis [130], the detector becomes sensitive to secondary  $\beta$  radiation, which can be caused by  $\gamma$  interactions in the detector wall.

Furthermore, beta radiation from the inside of the detector (e.g. emitted from the radon daughter  $^{214}\text{Bi}$ ) as well as cosmic muons traversing the counting gas provide low energetic events.

As shown in Table 7.2, the HV has a significant influence on the energy resolution. While a rather flat optimum was found between 620 V and 820 V, there is a clear worsening towards higher voltages visible.

Voltage [V]	Resolution (FWHM) at 5.49 MeV [keV]	$^{218}\text{Po}$ peak position [keV]	$^{214}\text{Po}$ peak position [keV]
520	$287\pm 5$	$5944\pm 3$	$7682\pm 3$
620	$269\pm 5$	$5952\pm 3$	$7690\pm 3$
720	$256\pm 5$	$5959\pm 3$	$7695\pm 3$
820	$262\pm 5$	$5944\pm 2$	$7696\pm 3$
920	$404\pm 9$	$5947\pm 6$	$7722\pm 5$
1020	$537\pm 17$	$5906\pm 10$	$7712\pm 6$

**Table 7.2:** Summary of the results from the calibration series with P10 at a pressure of 1.2 bar. The resolution of the radon line is shown as well as the positions of the peaks caused by  $^{218}\text{Po}$  and  $^{214}\text{Po}$  decays. The recorded spectra were previously calibrated to the radon line only.

In [137], a similar investigation with comparable results was carried out for  $\text{N}_2$  as a counting gas. A optimum for the energy resolution and linearity of the energy scale was determined to be between 600 V and 800 V. In general, a balance must be made in nitrogen between the number of micro-discharges, which increases with voltage and the achievable gas amplification. Therefore, the 700 V used in the first calibration measurement can be considered as a good compromise.

### 7.1.5 Trapping of charged Rn daughters

As already mentioned, the calibration spectra in both gases show reduced intensities of Po decays compared to the Rn line. This effect reduces the detection efficiency of the corresponding decays. Compared to the  $^{218}\text{Po}$  peak, the intensity of the  $^{214}\text{Po}$  line is even lower. In order to determine the detection efficiency, the following model was developed for the processes in the detector:

It is well known that radon daughters in gases are often present as charged ions. Assuming that the radon atom was not ionized, the alpha decay produces a negatively charged  $^{218}\text{Po}$  ion in the inert detector gases. Due to the high electric fields, the  $^{218}\text{Po}$  ions are attracted by the counting wire and accumulate on its surface. As  $\alpha$ s which pass through parts of the wire will lose huge quantities of energy in

the dense metal over small distances, only reduced amounts of energy are deposited by them in the counting gas. Due to the nuclear recoil of the  $^{214}\text{Pb}$  nucleus produced in the alpha decay of  $^{218}\text{Po}$ , a certain amount of lead nuclei is implanted into the wire. Moreover, this causes a further reduction of the efficiency for the  $^{214}\text{Po}$  events. Beyond that, the corresponding peak should have a more pronounced non-Gaussian shaped left side towards lower energies, which was observed already in the the calibrations using P10 [137].

In order to substantiate these assumptions, a further measurement was carried out. Therefore, the detector was operated beforehand for three days at 720 V with the source pot attached to the gas volume, which caused a high activity in the counter. After that, the HV was shut down and the wire was grounded. In an approximately 15 min lasting procedure the contaminated counting gas was replaced by fresh P10. Subsequently the HV was switched on again and data was taken for  $\sim 500$  min. In a hurry, closing of the source pot valve was omitted so that small amounts of radon were released into the counting gas during the 8 hour measuring period. Figure 7.10 contains the resulting energy spectrum with a clearly visible  $^{214}\text{Po}$  peak. Small amounts of  $^{222}\text{Rn}$  and  $^{218}\text{Po}$  are also visible, due to the open valve.

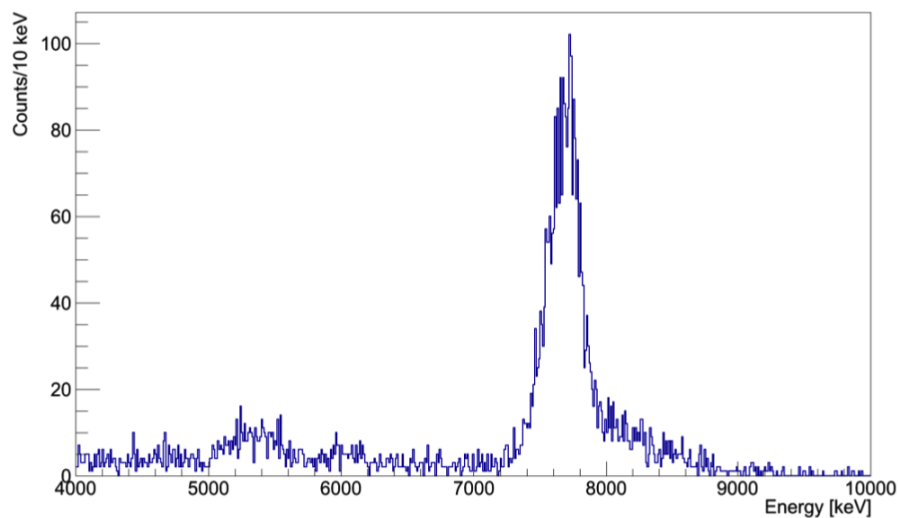


**Figure 7.10:** Spectrum of the contaminations trapped in the tube during a previous calibration. Before recording this spectrum, the counting gas used for the calibration was replaced by a fresh one. A  $^{214}\text{Po}$  peak dominates the spectrum. Minor contributions of  $^{222}\text{Rn}$  and  $^{218}\text{Po}$  in the energy range of 5-6.5 MeV are visible, which is due to an open valve to the source pot.

To ensure that the  $^{214}\text{Po}$  events have their origin in implanted  $^{214}\text{Pb}$ , the activity in the peak (between 7200 and 8200 keV) was plotted against the the runtime of the measurement (see Figure 7.11). The data was fitted using a model for the

two coupled decay processes of  $^{214}\text{Pb}$  and  $^{214}\text{Bi}$ . Since the gas refill lasted some 5 half-lives of  $^{218}\text{Po}$ , the contamination left in the counter can be assumed to be present in the form of  $^{214}\text{Pb}$  and partly as its daughter  $^{214}\text{Bi}$ . Because the half-life of  $^{214}\text{Po}$  is very small ( $164.3 \mu\text{s}$ ) compared to that of  $^{214}\text{Pb}$  (27.06 min) and  $^{214}\text{Bi}$  (19.9 min), it need not be considered separately.  $^{210}\text{Pb}$ , on the other hand, can be considered stable ( $T_{1/2} = 22.20 \text{ a}$ ) compared to  $^{214}\text{Bi}$  and  $^{214}\text{Pb}$ . Moreover, its line is far off the investigated energy regime.

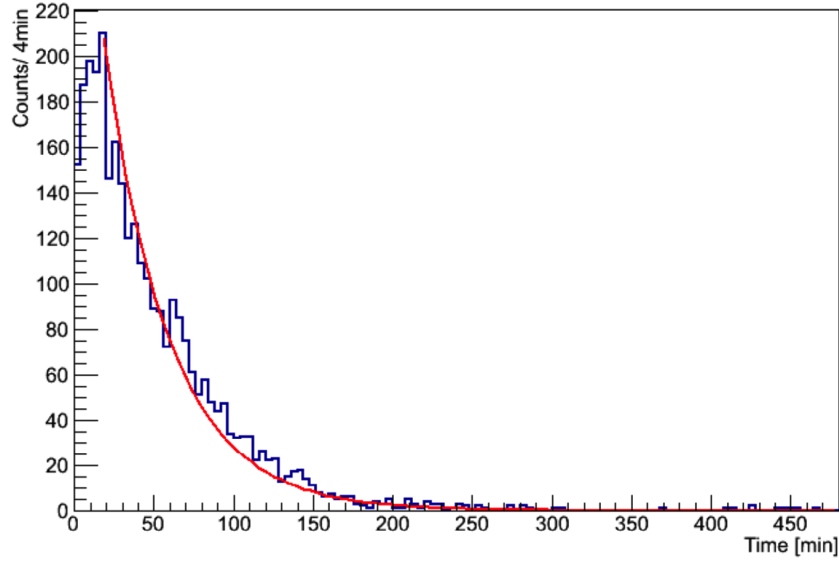


**Figure 7.11:** Event rate in the  $^{214}\text{Po}$  peak along the runtime of the measurement. The red curve represents a fit to the data based on two exponential decay functions for the isotopes  $^{214}\text{Pb}$  and  $^{214}\text{Bi}$ .

Using these simplifications, the rate of alpha decays of  $^{214}\text{Po}$  can be denoted as

$$A_{Po}(t) = A_{Bi}(t) = A_{Pb}(0) \frac{\lambda_{Bi}}{\lambda_{Bi} - \lambda_{Pb}} (e^{-\lambda_{Pb}t} - e^{-\lambda_{Bi}t}) + A_{Bi}(0)e^{-\lambda_{Bi}t} \quad (7.2)$$

where  $\lambda_{Pb}$  and  $\lambda_{Bi}$  are representing the corresponding decay constants. To account for the background of micro-discharges causing a constant activity, a constant was added to the above equation before fitting it to the data. The values for the half-life of  $^{214}\text{Pb}$  and  $^{214}\text{Bi}$  obtained from the fit (red line in Figure 7.11)

$$T_{1/2}(^{214}\text{Pb}) = (26.56 \pm 1.50) \text{ min} \quad (7.3)$$

$$T_{1/2}(^{214}\text{Bi}) = (20.27 \pm 1.78) \text{ min} \quad (7.4)$$

are in well agreement with the literature values from [126].

### 7.1.6 Monte Carlo simulation and detection efficiency

Based on the model of daughter ion trapping on the wire, a simple Monte Carlo simulation was set up. Therefore,  $\alpha$  events with an initial energy of 5489 keV were generated homogeneously distributed in the counting gas. The corresponding 6.001 keV events were generated on the surface of the counting wire. To simulate the implantation of the daughters of  $^{218}\text{Po}$  into the counting wire (simulated as solid tungsten cylinder), the 7.687 keV  $\alpha$ s were generated randomly in depth from 0 to 5  $\mu\text{m}$  below the surface. The resolution of the detector was realized by Gaussian smearing of the Monte Carlo truth.

For the spectrum in Figure 7.12 a total number of  $10^6$  Events were simulated. The spectral shape agrees well with the calibration data. The reduction of the intensities in the lines of the two Po isotopes could be reproduced by the simulation. Furthermore, the background events from the alpha peaks down to the threshold are visible as well. However, in this region the simulated spectrum is nearly flat while in the calibrations a slight increase towards lower energies was visible. The additional events in the measured spectra can be explained by micro-discharges in the proportional chamber (see also the following section).

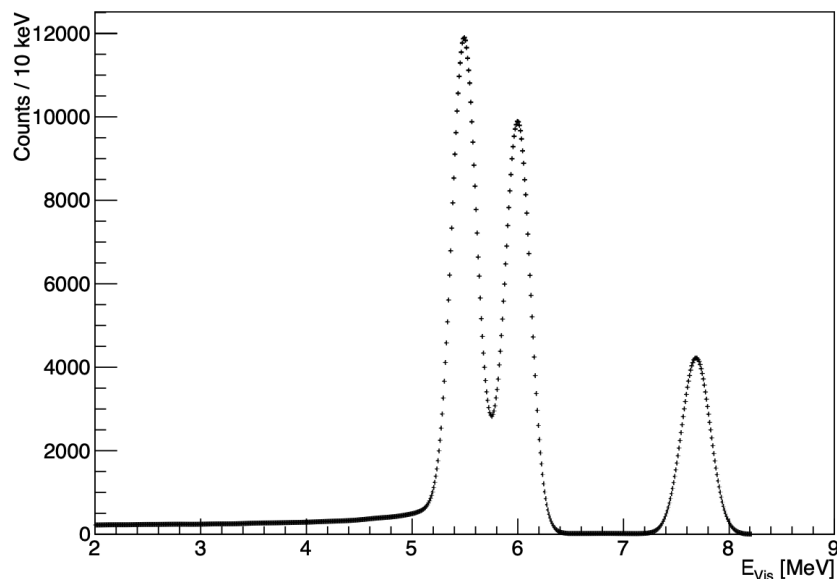


**Figure 7.12:** Simulated  $\alpha$  spectrum containing  $10^6$  events. The spectral shape of the calibration spectra (for comparison see Figure 7.7) was reproduced using the assumption of trapped radon daughters at the counting wire. Furthermore, the implantation of the  $^{218}\text{Po}$  daughters in the counting wire decreases the intensity of the  $^{214}\text{Po}$  line compared to the peak at 6.001 MeV even further. A flat background component down to lower energies was reproduced by the simulation as well.

According to the calibrations, the ROI (Region Of Interest) for  $^{222}\text{Rn}$  and related daughter  $\alpha$  decays can be defined as the energy range from  $\sim 5.0$  MeV up to  $\sim 8.2$  MeV. To determine the efficiency of detecting  $\alpha$  events from the three isotopes within this energy window,  $3 \times 10^4$  events for each species were simulated separately. For  $^{222}\text{Rn}$  an efficiency of  $(96.5 \pm 0.6) \%$  was calculated.  $^{218}\text{Po}$  is detected with  $(74.9 \pm 0.5) \%$  while observing a  $^{214}\text{Po}$  event in this range has the lowest probability of  $(58.3 \pm 0.5) \%$ .

### 7.1.7 Pulse shape analysis

Micro-discharges are a well known background in proportional counters for low event rate measurements. The rate of such events can vary significantly for different detectors and filling gases. To address this problem in neutron counters filled with pure  $^3\text{He}$ , Langford et. al [138] applied successfully pulse shape analysis techniques to the unshaped pulses from the connected charge sensitive pre-amplifiers. In order to benefit from these techniques with the RaMS detectors, the possibilities for  $\alpha$  event discrimination from backgrounds were investigated in both P10 and  $\text{N}_2$ .

#### 7.1.7.1 Pulse shapes in P10

In the calibrations using P10, two main pulse forms can be distinguished, which are illustrated by corresponding examples in Figure 7.13.

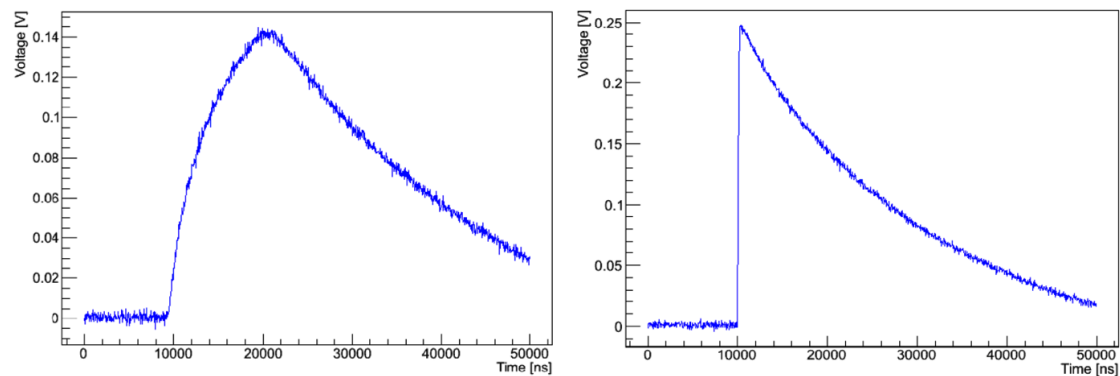


**Figure 7.13: Left:** A pulse from one of the alpha peaks in the energy spectrum of the calibration in P10 gas at a voltage of 720 V. The pulse clearly shows a rounded rising edge. According to [138] this can be attributed to an  $\alpha$  interaction with the counting gas. **Right:** Second pulse species identified in the calibration. Clearly visible is a steep short rise of the pulse to its maximum height. According to [138], this is a clear indication for a background event caused by a micro-discharge.

Pulses taken from the alpha peaks mostly show the shape of the left pulse in Figure 7.13. The risetime of the pulse shows a value of several microseconds, which was found to be typical for this pulse species. The rising edge is clearly rounded towards the maximum. This second slower risetime component can be attributed to the lower drift velocity of the positive gas ions produced by the electron avalanche. The later and extended arrival times of the ions dominate this region of a signal caused by particle interactions in the detector [139]. The second event class identified in the calibration data has a very steep rise. For the pulse shown on the right side of Figure 7.13 the event's maximum amplitude is reached within 100 ns. The exponential return to the baseline is identical for both event classes since it is mainly determined by the electronic components used in the pre-amplifier's circuitry. The supplier specifies a typical value of 75  $\mu$ s for reaching the baseline[131].

To determine the pulses' risetimes, the time difference between reaching two different certain fractions of the pulses amplitude on the rising edge was used. The lower determination limit was set to 10 % of the maximum voltage. As mentioned in [138], avoiding a strong contribution of the positive gas ion drift to the determined risetime value allows the discrimination between different particle species like muons, betas and alphas. Since N<sub>2</sub> filled proportional counters are sensitive to fast neutrons, which could cause an additional background for the alpha spectroscopy, this aspect was considered here as well. Therefore, the upper determination limit for the risetime has to be carefully balanced to ensure a sufficient discrimination power against micro-discharges and subsequently not spoiling the capabilities for identifying different particles.

Figure 7.14 shows different risetime spectra for the calibration measurement with radon loaded P10. In all graphs two risetime populations are visible. As expected, the separation between discharges (left peak) and the particle candidate events (right peak) is reduced for smaller upper risetime determination limits. If more of the rising edge is included in the risetime determination (see 10 % - 60 % or 10 % - 70 % in Figure 7.14), a pronounced long tail towards higher values occurs on the right peak. The boundaries of 10 % - 40 % and 10 % - 50 % were identified to be a good compromise with similar discrimination powers for discharges in A. Gardanow's thesis [137]. This values are in well agreement with the study of Langford [138].

In order to assess the signal acceptance without using a calibrated radon source, the risetime cut has to be applied to a calibration spectrum for a conservative estimation. The comparison of a raw and a cut spectrum is shown in Figure 7.15. The cut accepts risetime values (calculated from 10 % - 50 % of the maximum pulse height) between 350 ns and 3500 ns.

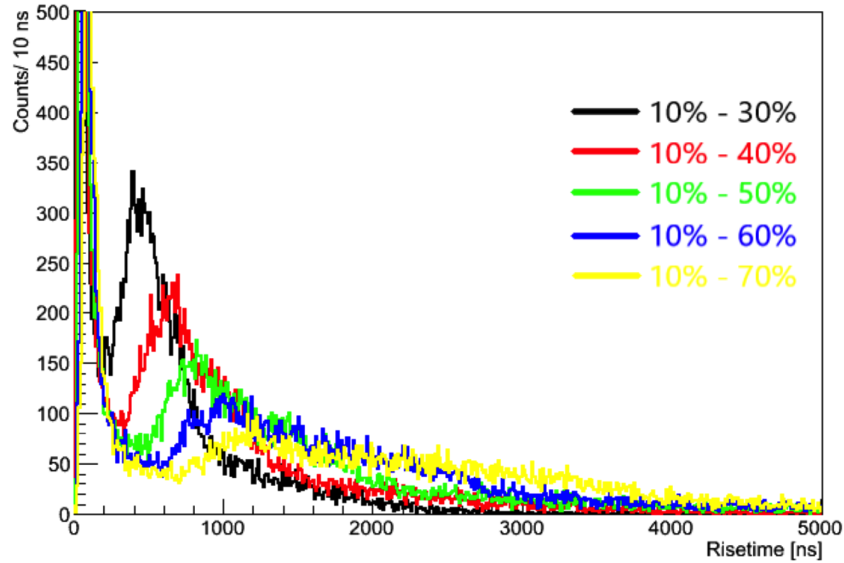


**Figure 7.14:** Risetime spectra for all events recorded during a calibration with radon loaded P10. The risetime of a pulse was determined using the time difference between a lower and an upper constant fraction of the maximum voltage on the rising edge. The upper and the lower fraction used for obtaining the corresponding coloured graphs are indicated in the plot. In all spectra, one population at low rise times (up to  $\sim 200$  ns) and another at higher values are clearly visible. Likewise, the influence of the slow drift of the positive ions on the right peak increases with enlarging the upper fraction of the pulses' maximum voltage. Especially for 60 % and 70 % as upper determination limit the peak shows a pronounced tail towards higher risetimes.

To estimate the signal acceptance for the alpha peaks, the raw and the cut spectrum were integrated between 5200 keV and 6200 keV as well as between 7200 keV and 8000 keV. The raw spectrum contains in this two ranges 14453 entries, while the cut one has 12552. With the conservative assumption that the cut has removed alpha events exclusively, a lower limit of  $(86.8 \pm 1.5)$  % can be set for its signal acceptance. Comparing the background on the left side of the alpha peaks, it becomes obvious that the cut has removed the rise in the spectrum towards low energies. The resulting flat shape of the spectrum in this energy range is now in well agreement with the Monte Carlo simulation. Therefore, it can be concluded, that the remaining events are caused by alphas partially depositing their energy in the counting gas. It has to be mentioned that the cut showed only a small effect on the energy resolution which was slightly improved to  $(242 \pm 3)$  keV at 5.49 MeV compared to the uncut spectrum with  $(256 \pm 5)$  keV.

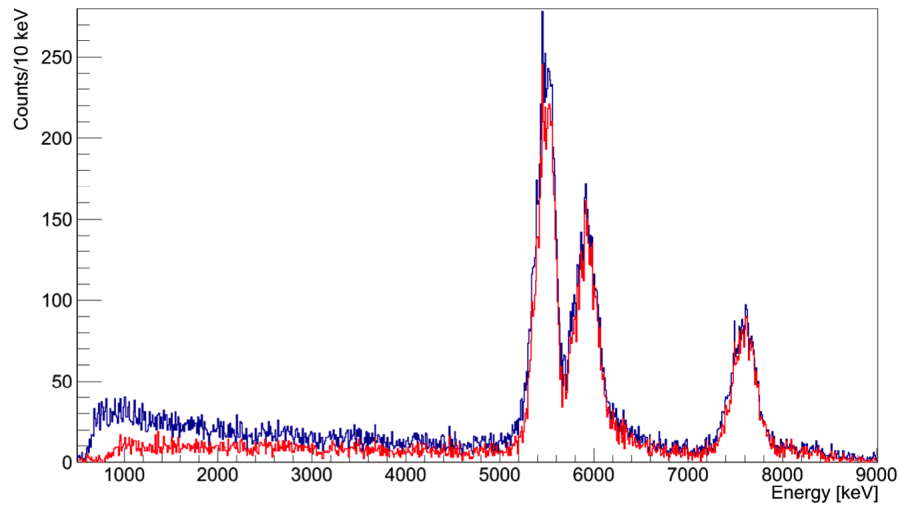


**Figure 7.15:** Comparison of a raw (blue) and a cut (red) calibration spectrum. The cut removes the rise in the spectrum from the radon peak down towards lower energies. The remaining flat spectral shape is due to  $\alpha$ s which are depositing only a part of their initial energy in the counting gas. As the intensities of the raw and cut  $\alpha$  peaks show, the signal acceptance of the cut is close to 1. However, the cut has only a minor influence on the resolution of the recorded  $\alpha$  lines.

### 7.1.7.2 Pulse shapes in $N_2$

The same study for the feasibility of micro-discharge discrimination via the pulses' rising edges was carried out using the calibration data in  $N_2$  for the bias voltage of 700 V. Figure 7.16 shows the resulting spectra for different risetime determination boundaries.

All spectra show a clear separation of the slowly and rapidly rising pulses. However, using larger upper boundaries for the determination of the risetimes leads to more pronounced tails in the right peak towards higher values. Due to the good separation and due to the fact that  $N_2$  filled proportional counters are sensitive to fast neutrons, which might cause backgrounds in the alpha regime, the risetime was determined in the following from 10 % to 40 % of the pulses maximum voltage. Figure 7.17 shows a comparison of the uncut and a cut energy spectrum of radon loaded nitrogen. For the cut one, only risetimes between 400 ns and 4000 ns were accepted.

Clearly visible is the significant reduction of micro-discharges from the energy threshold up to the radon peak. Since the ratio of discharges to alpha decays was significantly higher (compared to the P10 measurement) during the calibration in  $N_2$ , an estimate of the signal acceptance by comparing raw and cut spectrum would provide values that are by far too low. However, due to the even better separation of alpha events and micro-discharges, the assumption of the same signal acceptance as in P10 can be considered as conservative estimate.

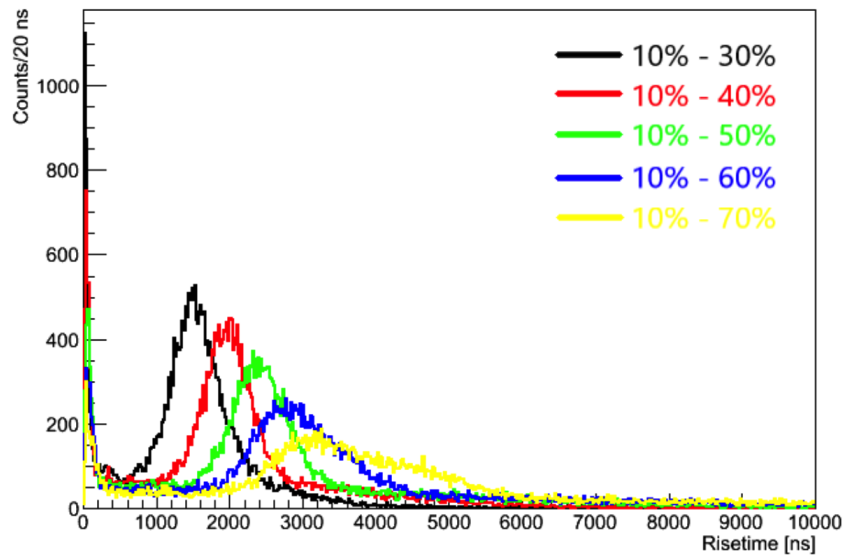


**Figure 7.16:** Risetime distribution obtained from radon loaded  $N_2$  calibration for different risetime determination boundaries. The lower boundary was fixed at 10 % of the pulses' amplitude while the upper limit was varied from 30 % to 70 % in steps of 10 %. All spectra show two well separated populations, where the larger upper determination boundaries result in long tails of the alpha candidate events towards high risetimes. Moreover, it has to be mentioned that the separation of  $\alpha$ s is even more pronounced compared to the measurement in P10.

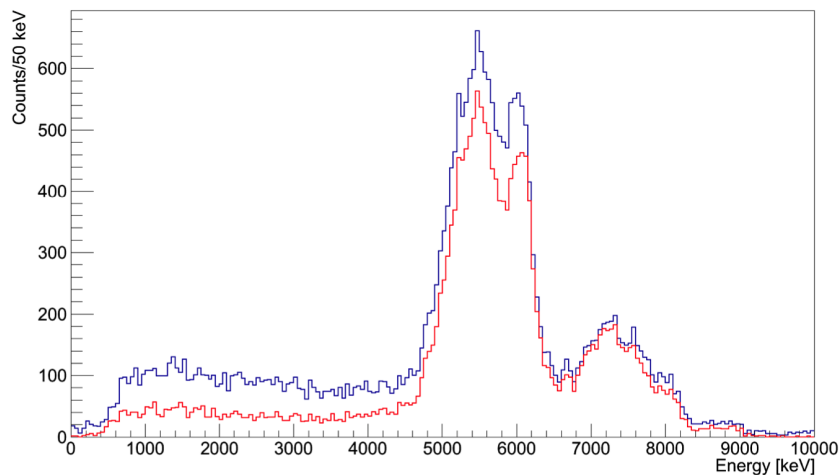


**Figure 7.17:** Comparison of a raw (blue) and a spectrum cut on the risetime of the pulses (red). The risetimes were determined from 10 % to 40 % of the pulses amplitude. Micro-discharges are reduced significantly, while the alpha peaks are nearly unaffected by the cut.

### 7.1.8 Background determination and sensitivity estimation

Since the future RaMS detector should have early warning capabilities and effective screening should be possible within 10 h measurement time, the background and its reduction by PSD was investigated and the achievable sensitivity was estimated also for the demonstrator. In order to be able to assess the influence of the use of nitrogen on the achievable sensitivity, the backgrounds in both P10 and N<sub>2</sub> were determined. Currently it is assumed that RaMS will not be used in flow-through mode (constant flow of gas through the counter), but batches of N<sub>2</sub> (possibly with pre-concentrated radon) will be screened over a few hours. The investigations shown here are therefore dedicated to the minimum measurable radon activities in batch mode.

#### 7.1.8.1 Backgrounds and sensitivity estimation for P10

To evaluate the sensitivity for a radon screening, the proportional chamber was pumped down to  $2 \times 10^{-4}$  mbar and kept at this pressure for 3 days. After flushing the detector with the argon methane mixture and pumping the chamber down again to  $\sim 5 \times 10^{-4}$  mbar it was filled with a P10 batch at a pressure of 1.2 bar. The bias voltage was set to 720 V.

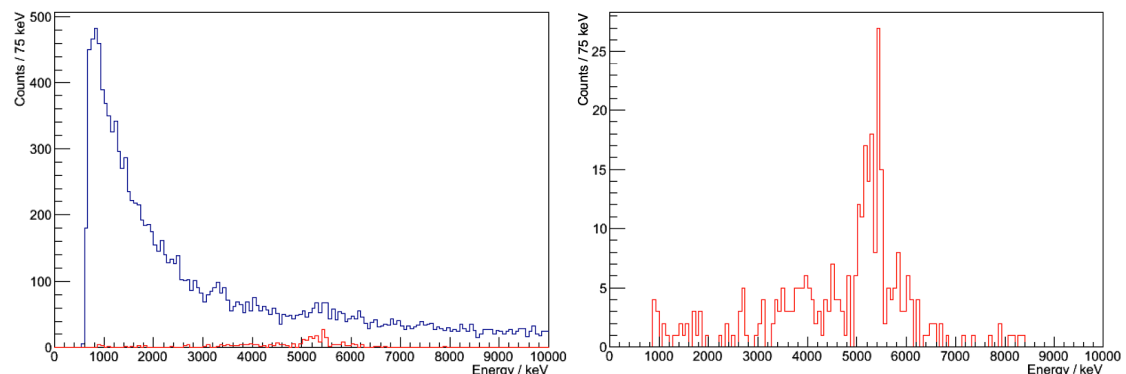


**Figure 7.18: Left:** Background in the demonstrator recorded in P10 during a 4.5 h measurement. The blue curve represents the raw data while the red histogram shows the spectrum after the application of the risetime cut described in 7.1.7.1 with a signal acceptance close to 1. **Right:** Magnification of the histogram obtained with PSD. It shows an excess of entries around 5.3 MeV, which can be attributed mainly to  $^{210}\text{Po}$ . There is no indication visible for the three peak structure of  $^{222}\text{Rn}$ ,  $^{218}\text{Po}$  and  $^{214}\text{Po}$ .

The spectrum (blue histogram in Figure 7.18 left) which has been recorded during the first 4.5 h after the filling is completely dominated by the background from micro-

discharges. Applying the PSD cut described in 7.1.7.1 reduced this background. The remaining entries show a spectrum (see Figure 7.18 right) with an excess at 5.3 MeV which is the position of the  $\alpha$  line from  $^{210}\text{Po}$ . The presence of this line was expected due to the large number of previous calibrations with radon-loaded counting gases. As the daughters of  $^{218}\text{Po}$  were found to be implanted into the counting wire material,  $^{210}\text{Pb}$  accumulates there, which leads to  $^{210}\text{Po}$  decays. Although peaks of  $^{210}\text{Po}$  and  $^{222}\text{Rn}$  cannot be separated, it can be assumed that the line was not mainly caused by emanated radon, since the characteristic daughter peaks of  $^{218}\text{Po}$  and  $^{214}\text{Po}$  are missing.

Within the 16000 s of screening the sample, 182 events were recorded within the ROI (5.0 MeV - 8.2 MeV). This corresponds to a visible total  $\alpha$  activity of  $(11.4 \pm 0.9)$  mBq. Assuming a constant radon activity in the batch of gas during the measurement and further assuming that all observed counts are caused by background and not by a radon contamination of the counting gas, the sensitivity of this 4.5 h radon screening can be estimated to be  $\sim(142 \pm 12)$  mBq/m<sup>3</sup> (95 % C.L.) for P10 at atmospheric pressure. The uncertainty takes beside counting statistics also the reading uncertainty from the manometer, the not perfectly known active detector volume and the uncertainties from the efficiency simulation into account. Just using the lines from  $^{218}\text{Po}$  and  $^{214}\text{Po}$  results in a lower limit, but requires a modification of the detection efficiency simulation ( $^{218}\text{Po}$ :  $(71.8 \pm 0.5)$  %,  $^{214}\text{Po}$ :  $(53.9 \pm 0.5\%)$ ). Within the energy range of 5.7 MeV - 6.3 MeV 37 Events were observed and 5 between 7.2 MeV and 8.1 MeV. This leads to a sensitivity of  $\sim(124 \pm 8)$  mBq/m<sup>3</sup> (95 % C.L.) using both lines and  $\sim(101 \pm 7)$  mBq/m<sup>3</sup> (95 % C.L.) obtained from the  $^{214}\text{Po}$  regime alone.

### 7.1.8.2 Sensitivity in N<sub>2</sub>

Also a background run was carried out for a detector filling with N<sub>2</sub> (1.2 bar abs.) provided by the Westfalen AG with a purity specified to 5.0. The spectrum shown in Figure 7.19 (left) was recorded during 14 h and is dominated by the micro-discharge background. Events visible below the energy threshold of the detector were caused by noise triggers due to the low threshold (7 mV) setting of the ADC. As the red histogram in this plot illustrates, the background is greatly reduced by the cuts on the pulses' risetime which was described in 7.1.7.2.

The right plot in Figure 7.19 shows a zoom-in on the background reduced histogram. It contains the  $^{210}\text{Po}$  peak observed before in P10. Due to the worse resolution compared to P10, the peak completely overlays the  $^{222}\text{Rn}$  region and furthermore, the high energetic tail of the peak contributes to the counts around the  $^{218}\text{Po}$  line. During the 14 h lasting measurement 876 Events were recorded within the ROI (4.8 MeV - 8.2 MeV). This leads to a total  $\alpha$  activity of  $(17.4 \pm 0.6)$  mBq in this energy range. The higher activity compared to the P10 measurement is caused by

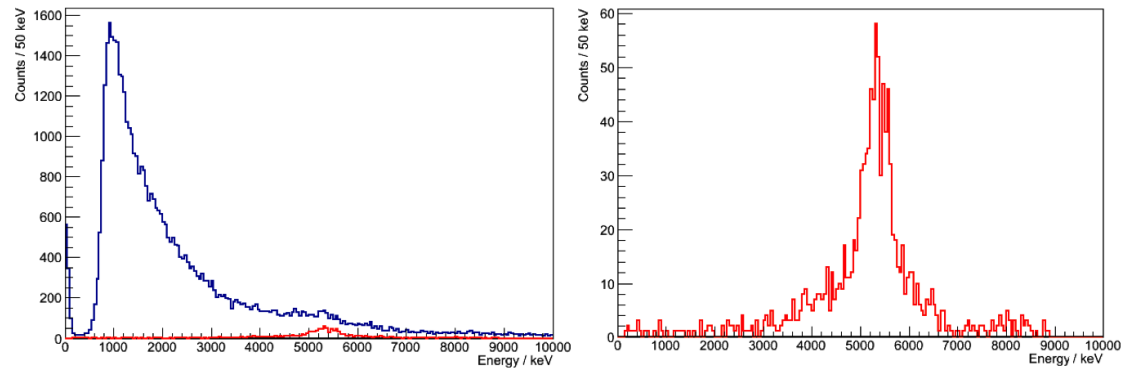


**Figure 7.19: Left:** Background in the demonstrator recorded in  $N_2$  during a 14 h measurement. The blue curve represents the raw data while the red histogram shows the spectrum after the application of the risetime cut described in 7.1.7.2. **Right:** Magnification of the histogram obtained with PSD. It shows also the  $^{210}\text{Po}$  peak. There is no indication visible for the three peak structure of  $^{222}\text{Rn}$ ,  $^{218}\text{Po}$  and  $^{214}\text{Po}$ .

the fact, that the  $N_2$  background measurement was the last of all measurements carried out with the RaMS detector demonstrator after large calibration campaigns. Therefore, the amount of accumulated  $^{210}\text{Po}$  can be considered to be higher. Using the same assumptions as for the P10 measurement, the sensitivity to  $^{222}\text{Rn}$  decays can be estimated to  $\sim(98.7\pm 9.2)$  mBq/m<sup>3</sup> (95 % C.L.). If the limit was calculated from the 39  $^{214}\text{Po}$  event candidates alone (7.2 MeV - 8.2 MeV), a value of  $\sim(82.5\pm 8.7)$  mBq/m<sup>3</sup> (95 % C.L.) was obtained for the minimal detectable radon activity within 1 m<sup>3</sup> nitrogen at atmospheric pressure. As in the calculations presented beforehand for P10, counting statistics, the reading uncertainty from the manometer, the not perfectly known active detector volume and the uncertainties from the efficiency simulation are taken into account.

## 7.2 The RaMS large volume proportional counter

Due to the promising results of the demonstrator phase, the detector design was upgraded. The objective was to increase the active volume by a factor of 10 while reducing the background. The following section describes this design and its realization as well as calibrations and background measurements.

### 7.2.1 Enlarged low background detector design

The large volume counter (shown in Figure 7.20) consists of a 2.3 m long tube with 159 mm outer diameter and a wall thickness of 3 mm made of high purity oxygen

free copper. This increases the gas volume in the detector to 42.3 l. On both ends of the detector, flanges made from the same copper are welded on. Each flange lid is equipped with a KF-16 flange socket and two 6 mm copper pipe sockets. The sockets are equipped with valves made from stainless steel provided by Swagelok. Behind one of these valves a manometer is mounted, while two others were used for connecting the counting gas support via steel reinforced PTFE hoses. To reduce the radon emanation from the detector itself, and to realize easily cleanable inner detector surfaces, all metal parts in contact with the gas batch during screening were electropolished.

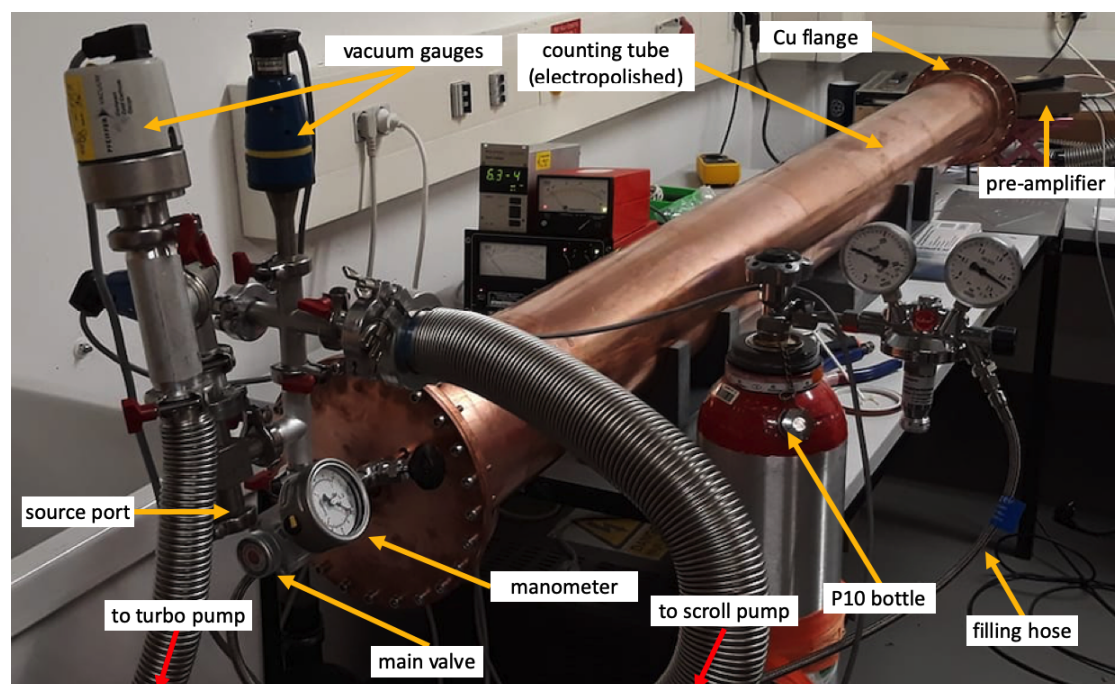


**Figure 7.20:** Photo of the RaMS large volume proportional counter during its commissioning. The detector with a length of 2.3 m realizes a counting gas volume of 42.3 l. All essential components visible in the figure are labeled directly in the picture while a detailed description can be found in the text.

Since during the demonstrator phase the HV feedthrough turned out to be a critical component which probably caused most of the micro-discharges, a special UHV feedthrough specified up to voltages of 5 kV was used here. This component features a MHV connector which is directly welded onto a KF-16 stainless steel flange. The soldering within the detector was done with lead and fluxing agent free tin. To avoid any discharges from sharp edges on the soldered connections or from bad insulation, all connections within the detector were covered with PTFE heat shrinkable tubing.

The holding bars for the counting wire were reduced in size and fixed by custom made copper screws in the flanges. During fabrication all edges were rounded off with large radii. The brass pins in the PTFE insulators have been replaced by copper ones with a 0.5 mm hole in their centre. The chamber was equipped with a 20  $\mu\text{m}$  straightened tungsten counting wire with a 0.2  $\mu\text{m}$  gold coating. This wire provided by LUMA METALL features a diameter variation below 2 %. To prevent the wire from sagging, the tension weight was increased to 5 g.

Also the vacuum system was upgraded. In addition to the dry scroll pump, an additional pumping station equipped with a TMH521 turbo molecular booster pump from Pfeiffer Vacuum was connected. To be able to determine the achievable vacuum, a UHV gauge (Pfeiffer IKR251) was added as well. In the blind flange, which closes the port for the connection of the calibration pot, a small recess is milled, which allows a direct mounting of the  $^{226}\text{Ra}$  source in the blind flange. This allows much faster calibrations than with the source pot. Nevertheless, this vessel is not obsolete, since it can be filled with material samples for an examination of their radon emanation.

Since dust could cause  $\alpha$  backgrounds as well as micro-discharges, all detector components were cleaned before mounting with acetone, isopropanol and de-ionized water. For the removal of dust particles also extensive rinsing with liquid nitrogen was performed for the detector parts in contact with the counting gas.

### 7.2.2 Calibrations with radon loaded counting gases

Before the detector was calibrated, it has been pumped down to  $2.1 \times 10^{-6}$  mbar and kept at this vacuum level for two days. Then the  $^{226}\text{Ra}$  source with an activity of 3.7 kBq was placed directly into the source port. After pumping out the source port, the detector and the port were filled with P10 and subsequently pumped down again to  $3.3 \times 10^{-4}$  mbar. Following on this flushing procedure, the detector was filled with its counting gas with an absolute pressure of 1.2 bar.

#### Calibration in P10:

After waiting  $\sim 10$  h, the bias HV was switched on and optimized using the live-spectrography system in a series of short measurements containing only a minor amount of pulses. It turned out, that the best energy resolution and linearity of the detector response was achieved at 520 V. During this investigation no micro-discharges were visible on the oscilloscope at this low bias voltage. Therefore, this bias voltage was used during the investigations described in the following.

Figure 7.21 shows the recorded energy spectrum (left) with 6000 events which was calibrated to the  $^{222}\text{Rn}$  line as well as a two-dimensional histogram of the pulses' risetimes and energies (right). The energy histogram contains three well separated

peaks of the three  $\alpha$  lines from  $^{222}\text{Rn}$ ,  $^{218}\text{Po}$  and  $^{214}\text{Po}$ . The energy resolution was greatly improved compared to the demonstrator detector. From a fit with the sum of two Gaussian functions and an additional constant, a resolution (FWHM) of  $(195.8 \pm 3.8)$  keV at 5.5 MeV and  $(128.1 \pm 3.4)$  keV at 6.0 MeV was calculated. The increased resolution of the  $^{218}\text{Po}$  peak can be explained by the distribution of the  $\alpha$  emitters along the counting wire and with that very similar drift paths of the electron avalanches and the resulting positive ions.

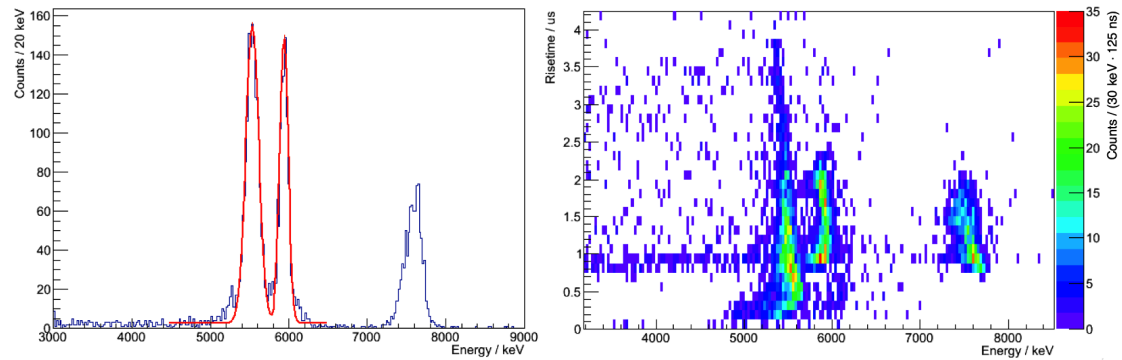


**Figure 7.21: Left:** Shown is a energy spectrum of the calibration pulses recorded with the waveform digitizer. The three characteristic lines of the alpha decays from radon and its short-lived daughters are visible. The red line represents a fit of the  $^{222}\text{Rn}$  and the  $^{218}\text{Po}$  peaks with the sum of two Gaussian functions and an additional constant. **Right:** Two-dimensional histogram of the pulses' risetimes and energies showing three populations as well. However, only minor amounts of pulses with short risetimes ( $<100$  ns) are visible.

To evaluate the detection efficiency for this enlarged proportional counter and to check further the Monte Carlo simulation described in 7.1.6, the intensities of the visible lines were compared. Within the  $^{222}\text{Rn}$  peak (5.3 MeV - 5.7 MeV) 1671 events were observed, while the polonium lines contain 1273 (5.8 MeV - 6.2 MeV) and 910 (7.2 MeV - 7.9 MeV) entries respectively. Assuming a detection efficiency for the radon of 96.5 % (as previously used), the efficiencies for the polonium decays follows to be  $(76.2 \pm 4.0)$  % for  $^{218}\text{Po}$  and  $(52.6 \pm 3.1)$  % for  $^{214}\text{Po}$ .

The right plot in Figure 7.21 is a two-dimensional histogram of the pulses' risetimes and energies. While the energy calibration was obtained from the radon line, the risetime calculation was done from the difference of the time values when the leading edge reaches 10 % and 50 % of the maximum pulse height. The diagram shows three separated populations. While the radon population is smeared over a wide range of risetimes, the polonium populations are less widely distributed. However, only a minor amount of events with risetimes below 100 ns was recorded.

### Calibration in N<sub>2</sub>:

The same calibration was performed with N<sub>2</sub>. However, the optimization of the bias voltage before the waveform recording revealed that effective measurements with a sufficiently low threshold require higher voltages of at least  $\sim 600$  V. Since the optimal resolution was reached between 600 V and 800 V the bias voltage was set to 700 V. Figure 7.22 shows an energy spectrum of the recorded pulses on the left, while on the right a two-dimensional histogram of the risetimes and energies of the events is shown.

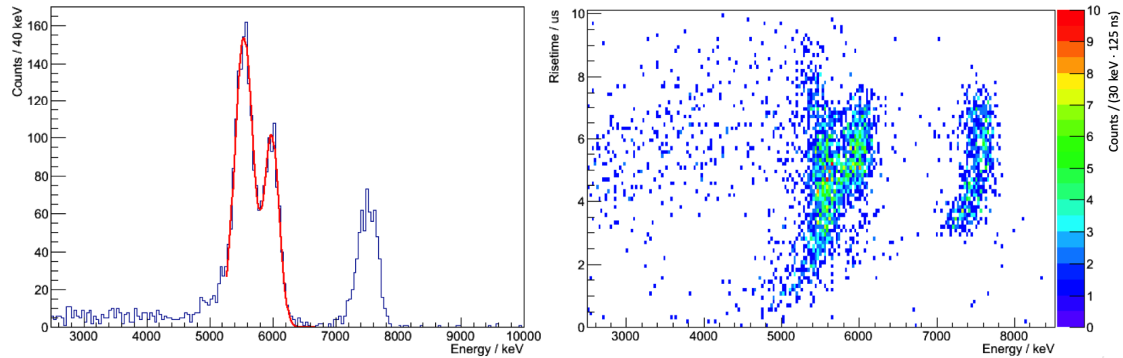


**Figure 7.22: Left:** Shown is a energy spectrum of the calibration pulses recorded with the waveform digitizer. The three characteristic lines of the alpha decays from  $^{222}\text{Rn}$  and its short-lived daughters are visible. The red curve represents a fit of the double peak structure using two Gaussian functions. The better resolution compared to the RaMS demonstrator is still not sufficient to separate the  $^{222}\text{Rn}$  and the  $^{218}\text{Po}$  peaks completely. **Right:** Two-dimensional histogram of the pulses' risetimes and energies showing three populations as well, while the two low energetic ones are partly overlaying each other. Furthermore, only minor amounts of pulses with short risetimes ( $<1000$  ns) are visible.

According to a fit of the double peak structure with the sum of two Gaussian functions the resolutions (FWHM) of this peaks are  $(342.8 \pm 1.8)$  keV for  $^{222}\text{Rn}$  and  $(278.7 \pm 2.2)$  keV for  $^{218}\text{Po}$ . The better resolution of the higher energetic peak can be explained by the distribution of the  $\alpha$  emitter along the counting wire and with that very similar drift paths of the electron avalanches and the resulting positive ions. The mean visible energy of the  $^{218}\text{Po}$  population lies at  $(5.982 \pm 0.003)$  MeV in well agreement with a nearly linear detector response. However, the  $^{214}\text{Po}$  peak is shifted to a mean visible energy of  $(7.511 \pm 0.005)$  MeV. The resolution (FWHM) obtained from a Gaussian fit is  $(366.7 \pm 3.4)$  keV.

The two-dimensional histogram (Figure 7.22 right) shows three populations in the energy range of the  $\alpha$  lines. The energy axis was calibrated to the radon peak only, while the risetimes were calculated from 10 % up to 50 % of the pulses' rising

edges. This would allow the implementation of a dedicated cut. However, it has to be mentioned that only single events show risetimes below 1000 ns and the micro-discharge background can be considered to be greatly reduced by the new detector construction.

### 7.2.3 Background and sensitivity determination

Before the background in the detector was measured, the chamber was pumped down to  $2.1 \times 10^{-6}$  mbar. To further increase the detector resolution and to reduce the amount of water vapour and the emanation of quenching organic compounds from the rubber and viton O-rings, the spectrometer was carefully heated up using an adjustable heating tape. By this procedure a vacuum of  $4.6 \times 10^{-7}$  mbar could be realized. After flushing and subsequent evacuation, the chamber was filled with the counting gas. It has to be mentioned, that the background run in  $N_2$  was done, directly after the first calibration to ensure a low  $^{210}\text{Po}$  activity. The background in P10 was determined after all calibrations.

#### Background and sensitivity with P10:

The background was recorded during 11 h at a bias voltage of 520 V. Figure 7.23 shows the resulting spectrum, where all events with risetimes above 100 ns were accepted as signal.

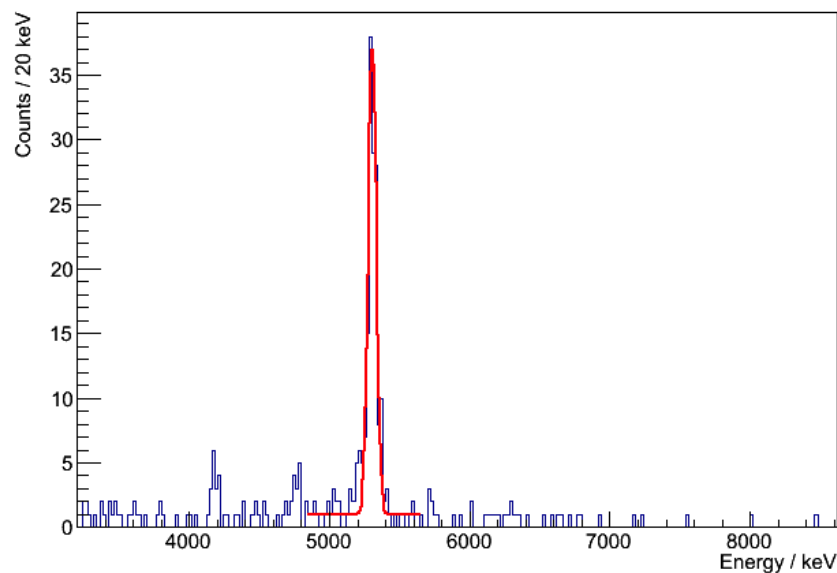


**Figure 7.23:** Spectrum of a detector filled with pure P10 gas. A sharp line from  $^{210}\text{Po}$  is visible at an energy of  $(5304 \pm 28)$  keV. The red line represents a fit of this peak using a Gaussian function with an additional constant. The ROI for the radon related events shows no defined population and only single events.

The spectrum shows a peak at  $(5304 \pm 28)$  keV with a resolution (FWHM) of  $(68.6 \pm 5.0)$  keV. This line is caused by  $^{210}\text{Po}$  decays since  $^{210}\text{Pb}$  remains in the detector as artefact from the calibration measurements. Within the ROIs for the  $^{222}\text{Rn}$ ,  $^{218}\text{Po}$  and  $^{214}\text{Po}$  peaks a total number of 16 entries was recorded. This corresponds to a total activity of  $(0.4 \pm 0.1)$  mBq. Assuming a constant radon activity in the detector and an initially radon free batch of counting gas, the sensitivity to the radon content of P10 at atmospheric pressure can be estimated to be  $(1.75 \pm 0.13)$  mBq/m<sup>3</sup> (95 % C.L.) for a 11 h lasting gas screening.

### Background and sensitivity with N<sub>2</sub>:

To ensure a low contamination with  $^{210}\text{Pb}$  on the wire leading to  $^{210}\text{Po}$  events at 5.3 MeV, the investigation of the background was performed following the commissioning of the detector directly after the first calibration runs. The background evaluation measurement was recorded during 10 h at a voltage of 700 V and a gas pressure of 1.2 bar (abs.). Nonetheless, the resulting energy spectrum shown in Figure 7.24 contains a peak due to  $^{210}\text{Po}$ .

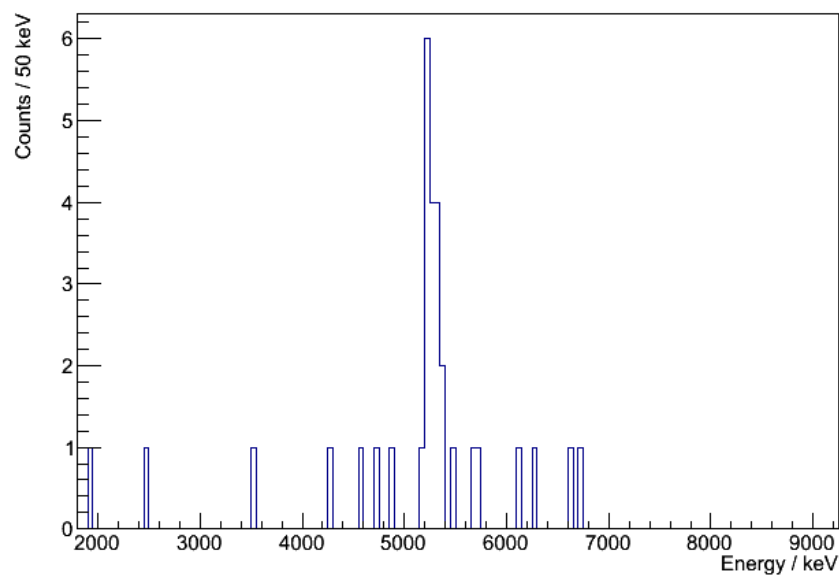


**Figure 7.24:** Spectrum of a detector filled with pure nitrogen. The line from  $^{210}\text{Po}$  is visible but with a lower intensity compared to the investigation in P10 (see Figure 7.23) because the measurement took place after the very first calibrations. This should ensure a low contamination on the counting wire. To avoid a contribution of the peak to the radon sensitivity of the counter, the limit is calculated from 5700 keV to 8200 keV on the expense of detection efficiency.

To reduce the micro-discharge background only events with a risetime above 500 ns and below 10  $\mu\text{s}$  were considered to be alpha related events. According to the

calibrations, the signal acceptance of this cut can be considered to be close to one. Between 4.8 MeV and 8.2 MeV 25 counts were registered. The resulting total activity can be calculated to be  $(0.69 \pm 0.14)$  mBq. Due to avoid a negative contribution of the peak to the radon sensitivity, the ROI is reduced to 5.7 MeV - 8.2 MeV on the expense of detection efficiency. Within this range 6 histogram entries are found. However, it has to be mentioned that even with the resolution reached in  $N_2$ , the two bins between 6600 keV and 6800 keV lie more than  $2\sigma$  away from the two  $\alpha$  lines at 6.00 MeV and 7.69 MeV. Furthermore, the spectrum above 6750 keV is empty.

Assuming that Poisson statistics is still applicable and further assuming a constant Rn-decay rate during the 10 h of measurement as well as an initially radon free counting gas a rough sensitivity estimation can be calculated. The observed 6 counts of background allow a detection of  $(2.07 \pm 0.36)$  mBq/m<sup>3</sup>  $^{222}Rn$  at a confidence level of 95 % within 10 h. Nevertheless, if the two counts between the Po lines are neglected and if counting statistics still holds, one obtains a sensitivity of  $(1.69 \pm 0.30)$  mBq/m<sup>3</sup> (95 % C.L.) in good agreement with the P10 results. Due to the low background rate, the RaMS large volume proportional counter will be able to provide an early warning also for minor air leaks or other radon related contaminations in the  $N_2$  supply system.

# Chapter 8

## Liquid scintillator characterization experiments

Besides, working on the LS production and purification as well as on the liquid handling systems, this thesis is also dedicated to the characterization of liquid scintillator samples in laboratory measurements. The precise knowledge of the LS properties is crucial for the interpretation of JUNO's data. For instance, it is essential to know its attenuation length for the scintillation light, typical scintillation quenching factors and pulse shapes for different particle interactions. Moreover, also the knowledge about the formation probability and lifetime of ortho-positronium (o-Ps) might be a beneficial input to JUNO's reconstruction algorithms. To address all these questions, experiments were set up during this and other theses at TUM. The following chapter will describe them in detail and will give an overview on present results.

### 8.1 Attenuation lengths measurements

Based on previous works at TUM [140, 141, 142] LS-purification with respect to the attenuation length was studied with an UV/Vis spectrometer [143]. LAB samples were measured, using a 10 cm long fused silica cuvette, before and after filtration through an aluminum oxide powder column. Both, acidic and alkaline powders over a broad range of particle sizes were investigated. In the same way the purification properties of QuadraSil TA [144] were studied. Due to the small base length of the fused silica cuvette, the attenuation lengths measurements performed with the commercial spectrometer are limited to about 10 m.

During the past four years, a new setup called PALM (Precision Attenuation Length Measurement) with a base length of approx. 2.5 m has been developed [145, 146] with the goal to enable measurements of about 30 m attenuation length with a

precision better than 10 % over a broad range of wavelengths. Within this section, the PALM setup is reviewed as well as first measurements by Sabrina Franke for LAB provided by SINOPEC Jinling Petrochemical Company before and after purification in the Daya Bay purification pilot plants.

### 8.1.1 The PALM setup - a brief overview

The setup (schematic drawing shown in Figure 8.1) uses a halogen light bulb (Osram HLX 64623) as light source focused via a mirror and quartz optics to a CCD light sensor in a distance of approx. 4 m. A monochromator is used to select a wavelength from the continuous light and with a deflection mirror, the monochromatic light beam is coupled into a vertically mounted stainless steel tube acting as sample cuvette.

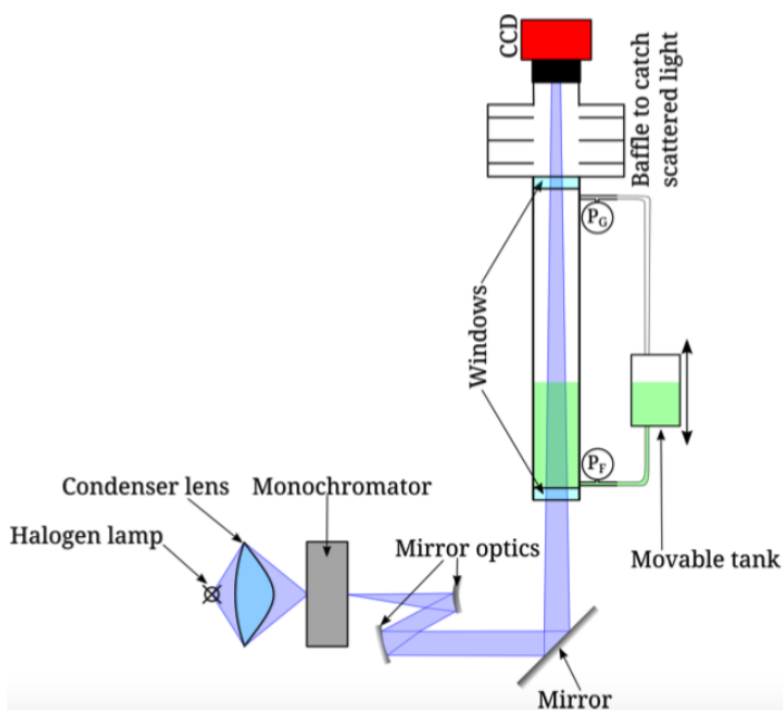


**Figure 8.1:** Schematic drawing of the PALM experiment. The light of a halogen lamp is focused by a condenser lens into a monochromator. The selected light with a wavelength between 180 nm and 3500 nm [146] is guided by a Cassegrain telescope and a deflection mirror into the sample tube equipped with quartz glass windows. After passing the sample tube the intensity of the remaining light is measured by a CCD camera. The fill height in the tube can be continuously adjusted by the usage of a movable tank exploiting the principle of communicating vessels. By the usage of two pressure sensors (one for the gas phase  $P_G$  and one for the liquid  $P_F$ ) the level within the vertical pipe can be determined. Figure taken from [146].

This tube is equipped with a special stray light suppressing coating on the inner walls. Quartz glass windows are used to enable the passing of UV-light as well. By the principle of communicating vessels the sample tube can be filled continuously with a movable tank. After the light passes the sample tube and its medium, it traverses a stray light suppressing baffle, before being detected by the CCD sensor (size  $1.3 \times 1.8$  cm). The CCD detector gives intensity as well as spatial information, which allows to monitor the intensity, shape and position of the light beam on the sensor. The operation of the experiment and the correct adjustment of the optics for the long light paths through the sample tube turned out to be complicated. Occurring vibrations in particular at the interface at the upper end of the LS column were difficult to control and prevented a full intensity deposition on the CCD sensor. These vibrations have different amplitude and frequency profiles since they are caused by a broad variety of sources. Some of them could be identified (e.g. neighboured vacuum pumps in the lab) and eliminated. To treat the vibrations originating by sources, which cannot be eliminated by default, the holding structure of the tube (solid metal clamps directly connected to the laboratory wall) was replaced by a custom made vibration damped holder directly mounted on the ceiling while the tube's lower end is now hanging freely over the optics. The CCD was also decoupled from the tube with a vibration damped adapter to reduce the in-coupling of the vibrations from the camera's cooler. After final optimization of the optics the vibrational perturbations were decreased to an acceptable level.

### 8.1.2 Results for LAB from the purification pilot plants

After the PALM setup was commissioned and extensively tested, the systematic uncertainties characterized and significantly reduced during the PhD thesis of Sabrina Franke [146], first batches of LAB from the Daya Bay site were investigated. To determine the influence of the LS pilot plant purification chain (see section 4.1), raw LAB from Daya Bay's storage tank (for details on this solvent see section 4.2) as well as LAB after undergoing all purification steps were measured with respect to the light attenuation at 420 nm, 430 nm, 440 nm and 633 nm wavelengths [146]. Once the wavelength was set at the monochromator and the optics have been adjusted with the empty setup, the tube was filled to  $\sim 0.8$  m. During the measurement procedure, the liquid level was increased in  $\sim 20$  cm steps up to  $\sim 2.6$  m. However, due to the filling height change, the optics have to be re-adjusted to ensure a central light beam spot in the CCD sensor. Subsequently several pictures were taken with the camera. Each one is selected manually during the offline analysis. In case of beam shifts of several mm, occurring reflections or visible diffraction, the picture was rejected. It has to be mentioned, that the possibility of this data selection turned out to be a great advantage of using a CCD sensor based pixelated camera system as light detector. Furthermore, the camera allows to check directly if the

optical conditions allow a meaningful measurement, which is especially beneficial during the delicate adjustment procedure of the optics [146].

The intensity of the light on the CCD camera was calculated by integrating over the sensor's pixels. To get rid of position dependencies a pixel-by-pixel gain calibration was applied as well as a dark noise correction. Also broken pixels were not taken into account in the intensity integral of the camera pictures. To eliminate the problem of intensity losses on the sensor's edges, caused by vibrations and mechanical instabilities of the setup, an intensity reconstruction was applied to the data (for details see [146]).

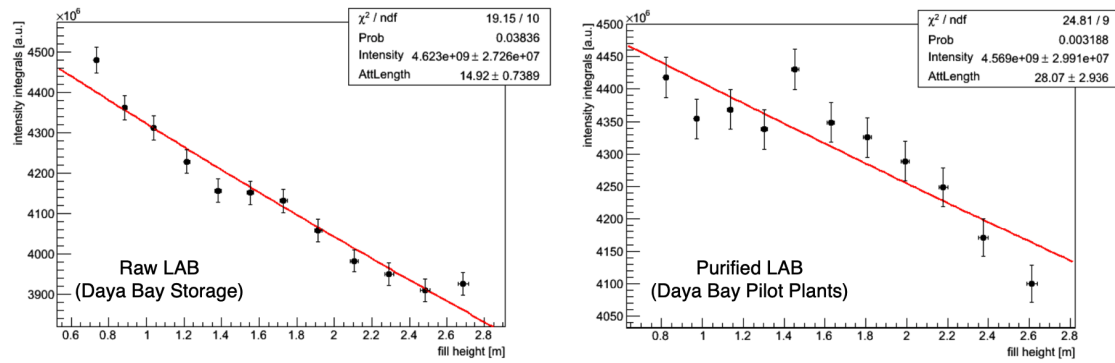


**Figure 8.2: Left:** Data obtained of raw LAB from the Daya Bay storage tank. The intensity on the CCD sensor is plotted versus the fill height in the sample tube. The data points were recorded at different filling heights. The red curve represents a fit of the data using the Beer-Lambert law. **Right:** Attenuation length measurement of the purified LAB after  $\text{Al}_2\text{O}_3$  filtration, vacuum distillation, water extraction and nitrogen stripping. Also here the red line represents a Beer-Lambert fit of the data. Both plots were taken from [146].

Figure 8.2 shows the measurement series for untreated raw LAB from the Daya Bay storage tank (left) as well as for the LAB after undergoing all purification steps (right) realized in the Daya Bay pilot plant facility. The light wavelength for this investigation was set to 430 nm. The vertical uncertainties of the data points are mainly caused by intensity fluctuations of the light bulb, uncertainties in the intensity reconstruction on the sensor edges as well as in the gain calibration. Beyond that there is also a statistical contribution from averaging several images per data point. The horizontal uncertainties are caused by the determination uncertainty of the fill height determination by two pressure sensors (see  $P_G$  and  $P_F$  in Figure 8.1) connected to the sample tube. From a data fit with the Beer-Lambert law the attenuation lengths for raw  $\Lambda_{raw}^{430} = (14.92 \pm 0.74)$  m and purified LAB  $\Lambda_{pur}^{430} = (28.07 \pm 2.94)$  m were obtained [146].

Table 8.1 summarizes the results of the entire measurement series for all four selected wavelengths. For all of them a clear increase in the attenuation length due

to the purification was found. However, also the raw LAB shows excellent transparency compared to European LAB products (e.g. LAB provided by the HELM AG:  $\Lambda_{HELM}^{420} = (6.02 \pm 0.24)$  m at 420 nm [147]). The cleaning effect is particularly strong in the range of 420 nm - 440 nm, which is beneficial since most of the LS' light emission takes place at these wavelengths.

Wavelength [nm]	Attenuation Length Raw LAB [m]	Attenuation Length Purified LAB [m]
420	$13.26 \pm 0.68$	$25.97 \pm 2.52$
430	$14.92 \pm 0.74$	$28.07 \pm 2.94$
440	$16.04 \pm 0.85$	$34.62 \pm 4.53$
633	$13.99 \pm 0.74$	$18.29 \pm 1.26$

**Table 8.1:** Summary of the results for raw and purified LAB from the Daya Bay storage tank. All values were taken from [146].

The measurements show that the cleaning techniques tested in Daya Bay effectively reduce optical impurities in the LS. Furthermore, they also show that the pure LAB already meets the LS transparency requirements of the JUNO experiment. Nevertheless, it has to be mentioned that the admixture of PPO and BisMSB might have a negative influence on the attenuation length.

## 8.2 Orthopositronium lifetime and formation probability

As mentioned in chapter 3, JUNO's main detection channel for electron antineutrinos is the inverse beta decay (IBD) process according to equation 3.1. A positron  $e^+$  and a neutron  $n$  are generated by this CC process. The  $e^+$  deposits its kinetic energy  $E_{e^+}$  in the scintillator, which leads to a prompt scintillation signal. The neutron is thermalized and finally captured by a proton which releases 2.2 MeV in  $\gamma$  radiation as a delayed second signal (about 236  $\mu s$  after the  $e^+$  signal).

After depositing their kinetic energies in the LS, positrons either annihilate with electrons or form positronium (Ps), a bound state consisting of a positron and an electron [148]. The singlet state, parapositronium (p-Ps), which is generated with a probability of 25% has a lifetime of 125 ps in vacuum [149], while the triplet state, orthopositronium (o-Ps), has a vacuum lifetime of 142 ns [150]. Parapositronium decays dominantly via the diametrical emission of two 511 keV gammas, while o-Ps dominantly produces three gammas during its decay in vacuum. However, there are three main processes shortening the lifetime of o-Ps in matter: conversion

(spin-flip of the positron [151]), pickoff (annihilation of the positron of o-Ps with an electron of the surrounding medium) and chemical reactions [152]. These processes cause two-body decays of o-Ps, shortening the effective lifetime to values of approx. 3 ns in organic liquids like LAB. Due to these short lifetimes compared to the vacuum lifetime of o-Ps, the fraction of o-Ps undergoing three-gamma decays can be neglected in LS.

In a LS detector like JUNO, the formation of o-Ps results in a delay between the signal from the deposition of the positron's kinetic energy and the signal caused by the two diametrical gammas. Thus, the pulse shape (photon emission time distribution) is different compared to the direct annihilation. The PSD between electron end positron related events by this pulse shape difference was proposed [153] and successfully applied in Borexino [154]. JUNO would benefit from this technique, since it enables the discrimination between IBD events and  $\beta$ -n decays caused by the cosmogenic isotopes  $^8\text{He}$  and  $^9\text{Li}$ , which are expected to be the main background component for this neutrino detection channel [59]. Moreover, for the detection of  $\nu_e$  the discrimination between electron and positron signals provides a significant reduction of backgrounds caused by  $\beta^+$  emitters as shown in Borexino [154]. To tune JUNO's event reconstruction algorithms and the Monte Carlo simulation framework enables a later discrimination of these backgrounds, a precise determination of the orthopositronium lifetime and its formation probability is crucial.

Therefore, a novel experimental setup called PoLiDe (Positronium Lifetime Determination) was developed at TUM in the frame of Mario Schwarz's master's thesis [155]. In a later measurement campaign, the lifetime and formation probability in a JUNO like LS mixture was determined and the result was published in [156]. To achieve a higher precision the experiment was upgraded in a second master's thesis by Oliver Dötterl [157]. Within this section, the PoLiDe setup is introduced and explained in detail. Furthermore, the results from the first measurement campaigns are reviewed as well as the realized upgrade with its first experimental data.

### 8.2.1 The PoLiDe setup

The PoLiDe setup, shown in Figure 8.3, consists of three scintillation detectors. A central detector measures the scintillation light caused by the interactions of positrons in the liquid scintillator sample, which gives the start signal for the time measurement. Two further detectors equipped with plastic scintillators (PS) measure the coincident emitted  $\gamma$ s. The mean of the onset times of these coincident pulses provide the stop signal for the lifetime determination. All three detectors are mounted on an optical table to allow adjustment of distances and with that adjustment of the solid angle for the  $\gamma$  detection. Furthermore, this table is located within a dark box also acting as faraday cage against high frequency noise. The following list summarizes the design of these detectors and gives an overview on the readout electronics as well [155, 156].

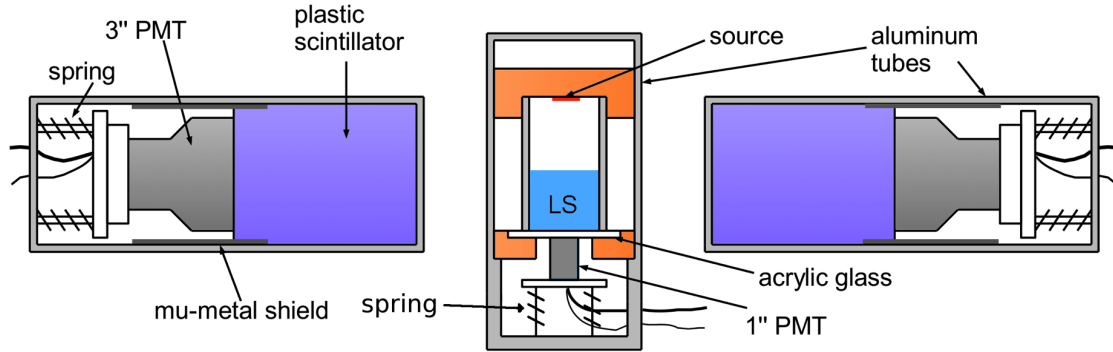


**Figure 8.3:** Scheme of PoLiDe. A Kapton encapsulated  $^{22}\text{Na}$  positron emitting source irradiates the LS sample. Its light output as well as interactions of the two 511 keV gammas are detected in coincidence. Therefore, the LS vessel is equipped with a 1" PMT, which is pressed by springs against the acrylic glass window of the sample container. The  $\gamma$ s are detected in two custom-made plastic scintillator detectors with 3" PMTs. Each of these detectors contains a cylindrical plastic scintillator block (Saint Gobain BC-400) with 3" diameter and a length of 16 cm. To reduce the air gap between the block and the PMTs, they are pressed by springs against the polished scintillator surface. To shield magnetic fields, all photon detectors are housed in mu-metal shields. All three detectors are mounted in light tight and grounded aluminum tubes acting as individual dark boxes and as shield against high frequency noise. Figure taken with courtesy from [156].

### The $\gamma$ detectors:

To detect the 511 keV gammas from the annihilation of the positron efficiently when traversing the PS the outer detectors were designed in a way, that the probability for undergoing a Compton scattering in it is  $\sim 80\%$ . Therefore, 16 cm long cylindrical blocks with a diameter of 3" were used as gamma absorbers. To ensure a good light yield (65 % of Anthracene) and fast scintillation light emission, Saint Gobain BC-400 [158] plastic scintillator with a risetime of 0.9 ns and a fastest decay time component of  $\tau = 2.4$  ns was selected. To read out the light from the PS, ETEL 9821B PMTs with 3" diameter and a flat entrance window are used. This PMT type features good timing capabilities (single PE risetime: 2.1 ns, single PE jitter: 2.2 ns) and a dark count rate below 500 Hz [159]. To reduce the air gap between PS and PMT, a dedicated holding structure with springs presses the glass tube against the plastic. A mu-metal shield is placed around the tube reducing signal distortions due to magnetic fields. The entire detector is housed within a 4 mm thick aluminum tube, acting as individual dark enclosure.

**The central LS detector:**

The LS in the central detector is stored within a polished aluminum tube with a length of 104.4 and an inner diameter of 26.8 mm. This material was selected because of its high reflectivity, which reduces light absorption losses on the vessel's walls. This should ensure a sufficient energy and time resolution. On top of the tube the positron emitting  $^{22}\text{Na}$  source enclosed by a thin Kapton foil is placed. The bottom of the LS vessel is closed by a window made from optical acrylic glass. A fast 1" inch PMT (ETEL 9112B) with a transition time spread for single electrons below 1.2 ns (FWHM) and a corresponding risetime of 1.8 ns [160] is pressed by springs against this window. The PMT is housed within a mu-metal cylinder. The central LS vessel is sealed by rubber O-rings and can be constantly flushed through dedicated valves with a protective nitrogen atmosphere. The vessel with its PMT is housed in an aluminum tube with 4 mm wall thickness. A fully detailed description of the vessel can be found in the PhD thesis of Sabrina Franke [146] as well as in the Master's Thesis of Mario Schwarz [155].

**Readout electronics:**

To read out the detector pulses, a robust and flexible trigger logic was designed on the basis of NIM modules which can be seen in Figure 8.4. The pulses of the outer  $\gamma$  detectors were amplified by a fast amplifier (Caen N979) with a fixed gain of 10 and signal rise and fall times below 1.5 ns [161]. One of the two outputs of the amplifier is directly fed into the waveform digitizing FADC (Acqiris DC282) with a sampling rate of 2 GS/s and a resolution of 10 bit [136]. The other output goes to a constant fraction discriminator (CF 8000) provided by Ortec [162]. When the signal exceeds the threshold (typically set to -30 mV), the discriminator provides a NIM logic gate with a set length of  $\sim 15$  ns. The gates from both detectors are fed into a coincidence logic unit (LeCroy 365AL) which was jumpered to a coincidence level of two. When signals on both active inputs are present simultaneously (coincidence window:  $\sim 23$  ns [155]), a logic signal with a duration of 20 ns is triggering the waveform digitizer. The waveform of the third central PMT will be digitized as well, when this trigger is present. If required an additional delay line (not in Figure 8.4) between PMT 3 and the input of the fast amplifier can be used to compensate the different transition times of the small 1" and the large 3" PMTs. Also the runtime of the signals through the fast amplifier can be compensated by fine adjusting the delay. These measures allow recording shorter traces and exploiting the full sampling rate of the FADC.

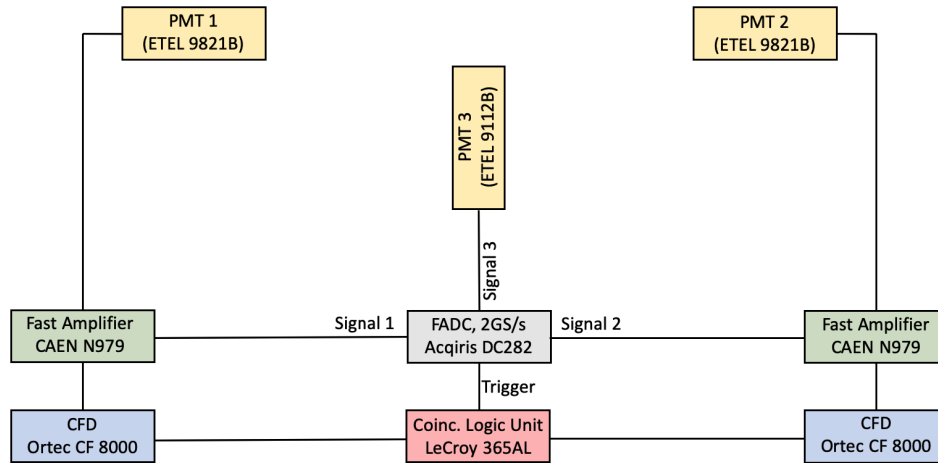


**Figure 8.4:** Block diagram of PoLiDe’s trigger logic. The signals from the outer  $\gamma$  detecting PMTs (yellow) are amplified. One output of each channel of the fast amplifier (green) is directly connected to the FADC (grey), while the other is furnished into a constant fraction discriminator (blue). When the threshold is exceeded by the signals, a NIM logic signal is generated. When a coincidence of these logic NIM pulses from both outer detectors is observed by the coincidence module (red) a trigger signal is generated and fed into the external trigger input of the FADC. Then the third PMT (yellow) is read out with the two others. The events with a pulse in the third channel are searched in the later offline analysis by dedicated algorithms (see also [155]).

### 8.2.2 Geometry optimization and background studies

Since the decay of  $^{22}\text{Na}$  releases beside the positron also a high energetic gamma with 1275 keV, source-induced backgrounds were expected. Therefore, a detailed Monte Carlo simulation of PoLiDe was created in [155] to optimize the  $\gamma$  detector distances as well as the fill height with LS of the central vessel. Beyond that, scintillation processes were implemented in order to generate hit-time spectra for each PMT. In addition, the response of the tubes itself was studied beforehand in a dedicated characterization campaign described in [155]. Other backgrounds could be identified as well. The two plots in Figure 8.5 show the pulse integral spectra obtained from the simulation with an optimized distance of the outer detectors (20 cm) to the central axis of the LS vessel and for an optimized filling level of 55 mm (corresponding to 35 ml LS). The following list summarizes all identified backgrounds briefly (for details see [155, 156]).

- Triple coincidence events including a hit of the 1275 keV  $\gamma$  in (at least) one scintillating volume. These events dominate the spectra in the high-energy region above 17 Vns for the 3” PMTs and above 0.5 Vns for the 1” detector.

- A minor source of correlated background is contributed by backscatter events, where one single 511 keV gamma hits both outer detectors.
- Outside annihilations: A positron deposits energy in the LS, but annihilates outside the LS. These events are the dominant background component in the low energy region of the spectra shown in Figure 8.5.
- A second background component in the low energy regime is provided by triple coincidences caused by the both 511 keV gammas only. These events typically have small energy depositions in the LS.

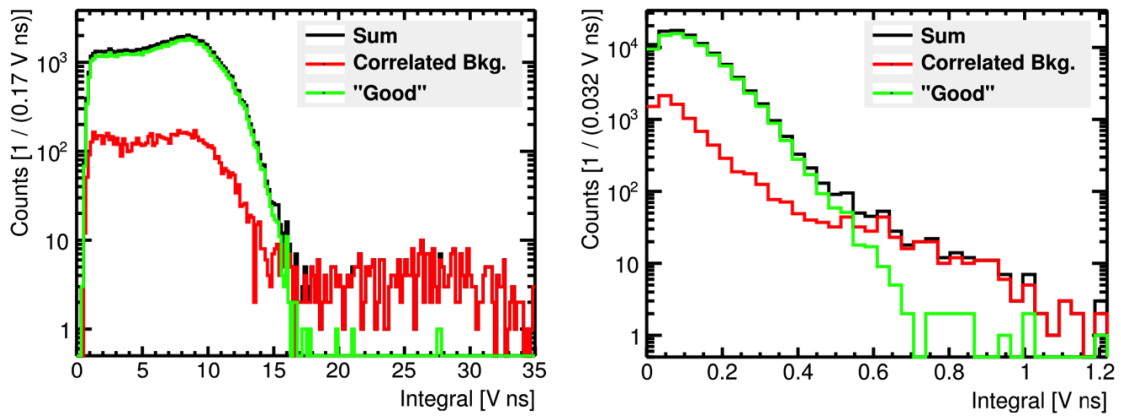


**Figure 8.5: Left:** Simulated pulse integral spectra for one outer 3" detector. The spectrum of all hits is drawn in black while the spectrum of the correlated backgrounds is shown in red. The high energy tail of the background is mainly caused by the 1275 keV gamma emitted in the  $^{22}\text{Na}$  decay. The "Good" events correspond to triple coincidences of all three detectors, where both 511 keV  $\gamma$ s are causing signals in the outer detectors without undergoing backscattering into an other active volume and the positron annihilates in the LS. **Right:** Shown is the corresponding spectrum of the central 1" PMT. Due to its lower gain, the spectrum lies at lower pulse integral values. Also here the background caused by the 1275 keV gammas is dominating the spectrum at high energies. Both plots taken with courtesy from [156].

### 8.2.3 Results for the lifetime and formation probability

The experimental data published in [156] was recorded in two runs of the experiment. Run 1 was carried out about 1 day after filling the LS vessel. The second data taking (run 2) took place about 35 days after the first run in order to investigate the temporal stability of the results. Run 1 consists of 16 million and run 2 of

15 million events containing 6817547 and 6148912 triple coincidences respectively. Data quality cuts were applied after removing events without a pulse from PMT 3. The pulse integral spectra of the uncut triple coincidences are shown in Figure 8.6. For the outer detectors events within a range from 2 Vns up 16 Vns were accepted. Furthermore, events are rejected, if the time difference of the two signals from the  $\gamma$  detectors exceeds 0.7 ns. Nonetheless, due to the limited time resolution of  $(1487.6 \pm 7.1)$  ps for the 511 keV coincidence in the outer detectors [155], not all backscatter events could be eliminated by the cut. In run 1 about 76 % and in run 2  $\sim 79$  % of all triple coincidences passed the energy cut and of those about 69 % and 68 % passed the time difference cut as well.

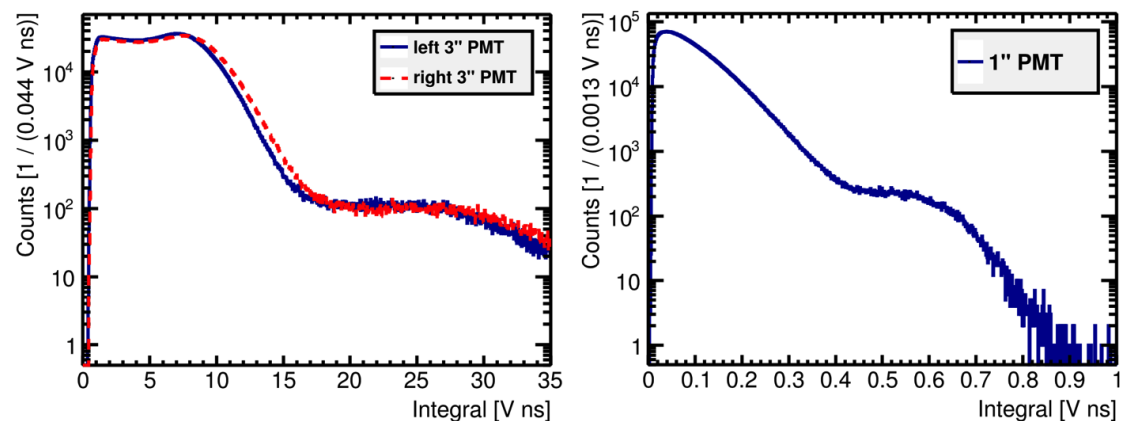


**Figure 8.6: Left:** Pulse integral spectra for the outer 3''  $\gamma$  detectors obtained from all triple coincidences in run 1. The high energy tail caused by the 1275 keV gammas emitted in the  $^{22}\text{Na}$  decay is clearly visible. **Right:** Shown is the corresponding spectrum of the central 1'' PMT. Also here the background caused by the 1275 keV gammas is dominating the spectrum at high energies. Both plots taken with courtesy from [156].

By comparing the simulated spectra (Figure 8.5) with the measured ones (Figure 8.6), it can be seen that the events of the outer detectors are dominantly caused by 511 keV gamma interactions, while most signals in the LS are caused by positrons. The so called "Good" events, from which the o-Ps lifetime will be calculated, dominate the spectra below the 1275 keV gamma regime. However, there is a discrepancy between the simulation of the outer detectors and the measurement in the region of the Compton edge of the 511 keV gammas (at  $\sim 13$  Vns). In the simulation it appears to be more steep, than observed in the measurement. The reason for this discrepancy is not fully understood yet, but it is likely that the Monte Carlo overestimates the reflectivity of the tube enclosing the PS and with that the achievable resolution. The small effective light yield of the LS detector results in a major decrease in its energy resolution [155, 156].

A typical signal candidate for the lifetime determination is shown in Figure 8.7. The pulses of the outer detectors are in coincidence while the signal of the central PMT occurs before them. In the offline analysis this time difference is reconstructed by a constant fraction timing algorithm. It determines the point in time when the corresponding signal is exceeding 20 % of its maximum height above the baseline. The start signal for the time measurement is the so calculated value for the pulse from PMT 3, while the stop signal is gained from the mean of the times extracted from the waveforms recorded from the outer detectors.

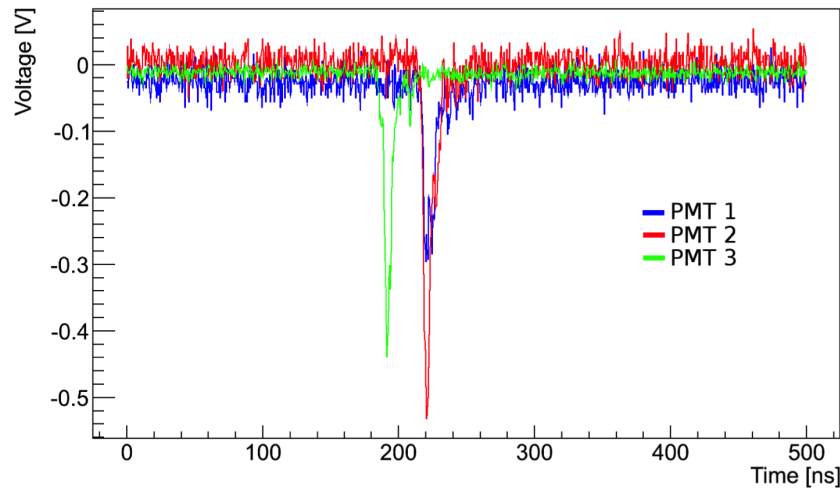


**Figure 8.7:** A triple coincidence event which contains a pulse in all three waveforms. The blue and red pulses are signals from the 3" detectors while the green trace corresponds to the 1" central PMT. To be better visible, the waveform of PMT 3 is multiplied by a factor of 30. The plot was taken from [155].

The data of each run was divided into several groups, depending on the events' energy deposited in the LS. This measure was necessary since the signal-to-background ratio shows a dependence on the energy deposition. Figure 8.8 is a lifetime spectrum of events from run 1, which passed all data quality cuts and showed a pulse integral value in the LS detector between 0.1 Vns and 0.15 Vns. The lifetimes and formation probability of o-Ps is extracted of the spectra by fitting the data points with the function

$$f(t) = \left( n_1 e^{-\frac{t}{\tau_1}} + n_2 e^{-\frac{t}{\tau_2}} \right) * \left( \frac{\eta_1}{\sqrt{2\pi\sigma_1^2}} e^{-\frac{(t-\mu)^2}{2\sigma_1^2}} + \frac{\eta_2}{\sqrt{2\pi\sigma_2^2}} e^{-\frac{(t-\mu)^2}{2\sigma_2^2}} \right) + n_3. \quad (8.1)$$

The first term in brackets contains an exponential function for the short lived (p-Ps and direct annihilations) and another for the long lived (o-Ps) decay component. Here  $\tau_1$  denotes the short and  $\tau_2$  the long lifetime. The second bracket contains the resolution model which is described in detail in [155] and was obtained from the Monte Carlo simulation and detector characterization measurements. The additional constant  $n_3$  accounts for the constant background in the spectra. The formation probabilities  $I_1$  for p-Ps and  $I_2$  for o-Ps can be calculated by integrating over the corresponding components of the fit.

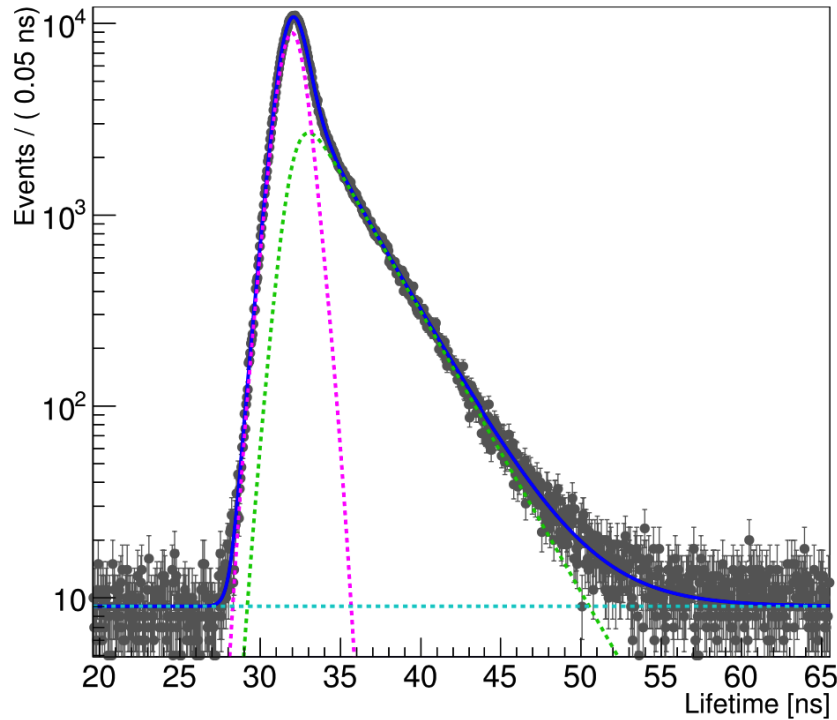


**Figure 8.8:** A lifetime spectrum of 634,861 events recorded in run 1, which passed all data quality cuts and showed pulse integrals in the LS detector between 0.1 Vns and 0.15 Vns. The blue line is a fit of the data points using equation 8.1. The dashed lines represent components of this equation. The magenta one represents the short lived, the green the long lived and the cyan a constant background component. The plot was taken with courtesy from [156].

Figure 8.9 shows the results for lifetime  $\tau_2$  and formation probability  $I_2$  of o-Ps from both runs. Fits were performed in the LS-energy range from 0.05 Vns to 0.45 Vns for each of the sections with a width of 0.05 Vns separately. The horizontal uncertainties of the data points are the statistical uncertainty of the fit results. The lifetimes of o-Ps show just a minor dependency on the LS-energy region. However, the observed behaviour can be attributed to effects caused by the increasing influence of the 1275 keV  $\gamma$  background towards higher pulse integral values.

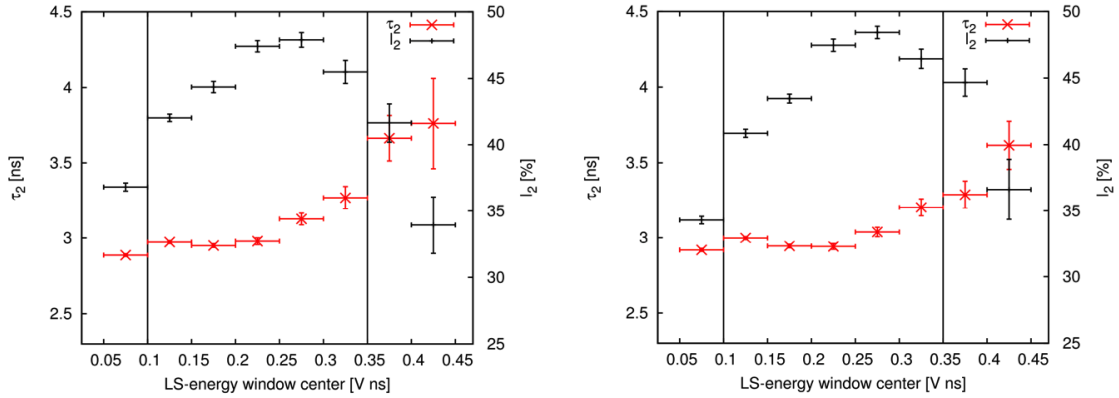


**Figure 8.9: Left:** Fit results for formation probability and lifetime of o-Ps in the different LS energy sections obtained from run 1. The solid vertical black lines represent the analysis window for the calculation of the final PoLiDe result. **Right:** The corresponding plot for the data from experimental run 2. No significant differences between run 1 and 2 were found. Both plots were taken from [156].

Since the simulation predicts a high number of background events in the high energy regime as well as a low number of photons at low energy depositions in the LS would distort the time resolution for the start signal, an analysis window between 0.1 Vns and 0.35 Vns was chosen. The final results for formation probability and lifetime were calculated by arithmetically averaging the individual results, weighted with their statistical uncertainties. A fully detailed description of the analysis can be found in the publication of the two runs [156]. By combining the data from both runs, results for the o-Ps lifetime

$$\tau_2 = (2.98 \pm 0.05) \text{ ns} \quad (8.2)$$

as well as the corresponding formation probability

$$I_2 = (44 \pm 3) \% \quad (8.3)$$

were obtained for the investigated LS mixture containing LAB, 3 g/l PPO and 15 mg/l BisMSB.

The measured o-Ps lifetime can be compared to literature values for pure LAB. The PoLiDe result is slightly lower than both results  $\tau_2=(3.10\pm0.07)$  ns [163] and  $\tau_2=(3.08\pm0.03)$  ns [164] found in recent publications. This deviation can be attributed to the added wavelength shifting molecules present in the LS. The result for the formation probability reported in [164] of  $I_2=(54.2\pm0.5)$  % is significantly

larger than the PoLiDe result. This discrepancy might be caused by the different experimental method used by D. Franco et al., known as the PALS technique, where positron interactions in other materials as the LS can not be suppressed directly. Especially annihilations in the relatively dense materials of the source encapsulation or the sample container walls are critical. Nonetheless, the result from Cheng et al. for the formation probability  $I_2=(43.7\pm 1.2)\%$  is in well agreement with the PoLiDe measurements.

### 8.2.4 The upgraded PoLiDe setup

In order to better understand the uncertainties in the formation probability and the energy dependencies of the results, the PoLiDe experiment is currently being upgraded. The main goal of these measures is to significantly improve the time resolution of the external detectors in order to better suppress the source-induced backgrounds described in 8.2.2. Special attention is paid to the reduction of the 1275 keV gamma quanta.

#### Detector Upgrades:

Therefore, the outer  $\gamma$  detectors were replaced completely by new ones shown in Figure 8.10 in detail. Now a quenched plastic scintillator (Saint Gobain BC-422Q) on the basis of polyvinyltoluene with an admixture of 1 % of benzophenone is used, which is specially designed for ultra fast timing and counting applications [165]. The PS features a scintillation light risetime of 105 ps and a typical pulse width (FWHM) of 290 ps. Due to the quenching, a decay time of the light emission of 700 ps is realized by Saint Gobain. However, the faster timing comes at the expense of light yield, which is not exceeding 11 % of anthracene's emission. Since very high trigger rates of several 100 Hz could be achieved due to the strong  $^{22}\text{Na}$  source ( $\sim 1$  MBq) in PoLiDe, the length of the scintillators has been reduced to 5 cm. This is to counteract the smearing of the stop signal due to different light propagation times in the scintillators and also to reduce the loss of photons in the plastic. Furthermore, the diameter of these absorbers are reduced to 1" to match the diameter of the new fast timing PMTs. These PMTs are provided by ADIT (L25D19W) and feature a single electron jitter (FWHM) of 290 ps and a multi-electron risetime of 1.0 ns [166], which by far exceeds the performance of the previously used ETEL 9821B. Also the central LS detector is upgraded with one ADIT PMT, replacing the ETEL 9112B. However, the better timing capabilities come at the expense of a decreased nominal gain of  $6\times 10^5$ , which is mainly caused by the low number of 8 dynodes (linear focused) used in this tube.

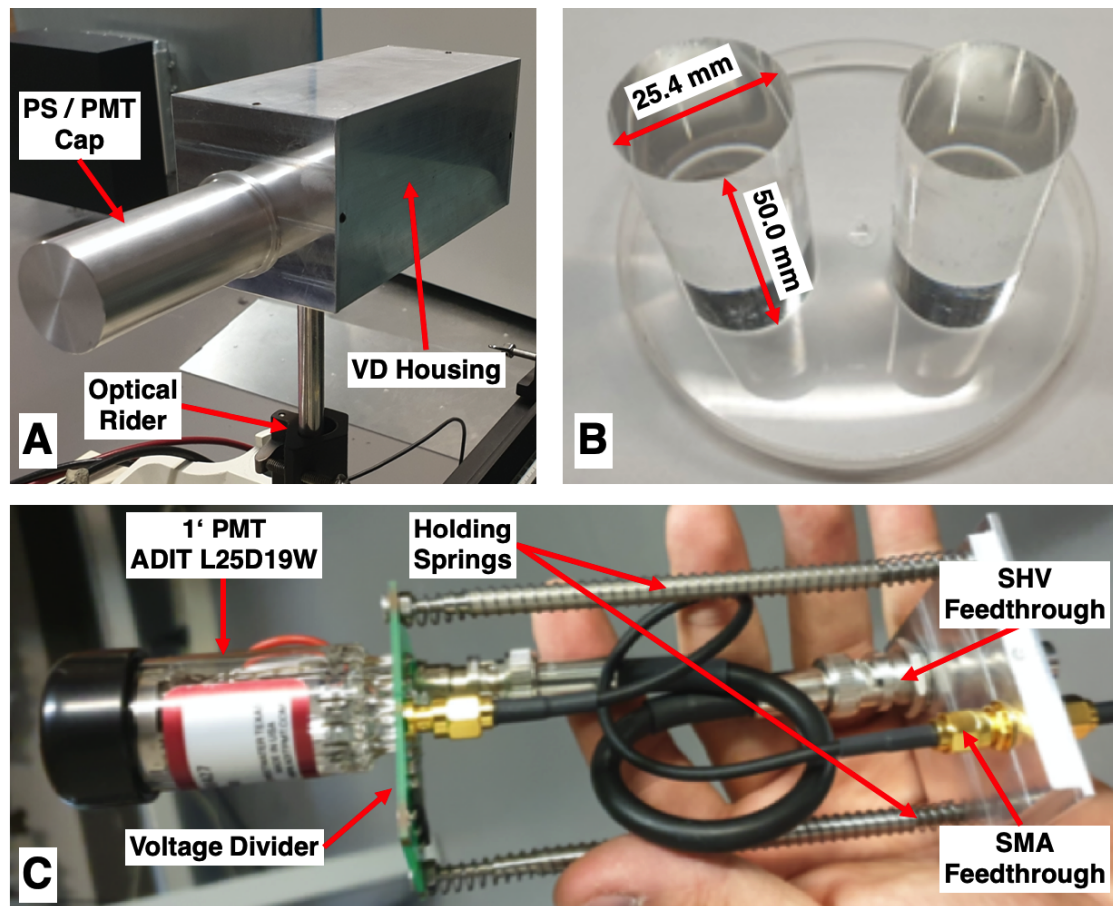


**Figure 8.10:** **A:** One of the outer  $\gamma$  detectors for the PoLiDe upgrade. The plastic scintillator (PS) and the PMT with its mu-metal shield are placed in a cylindrical aluminum cap. The cuboid housing provides space for the voltage divider and the retaining springs as well as for the cabling. **B:** The two Saint Gobain BC-422Q plastic scintillator cylinders with polished surfaces. In a later modification the surfaces might be painted with a highly reflective titanium dioxide paint (Saint Gobain BC-620) and the interface between PS and PMT can be equipped with refraction index matching optical pads (Saint Gobain BC-634A). **C:** One of the PMTs mounted on its insert. Dedicated holding springs, pressing the PMT against the PS, are directly screwed on the VD (Voltage Divider). The VD is directly soldered to the PMT socket to avoid any signal distortion by conventional connectors. The HV connection is realized via a SHV cable and a gas and also light tight feedthrough in the insert's aluminum baseplate. The signal connection is done similarly via a gold coated SMA feedthrough. The gap between the insert's base plate and the detector housing is closed and made light-tight by black sanitary silicone.

### Modifications on the readout electronics:

The readout electronics were also subjected to a comprehensive revision. A stepped triple coincidence logic is implemented in the new setup. A block diagram of the new arrangement is shown in Figure 8.11.

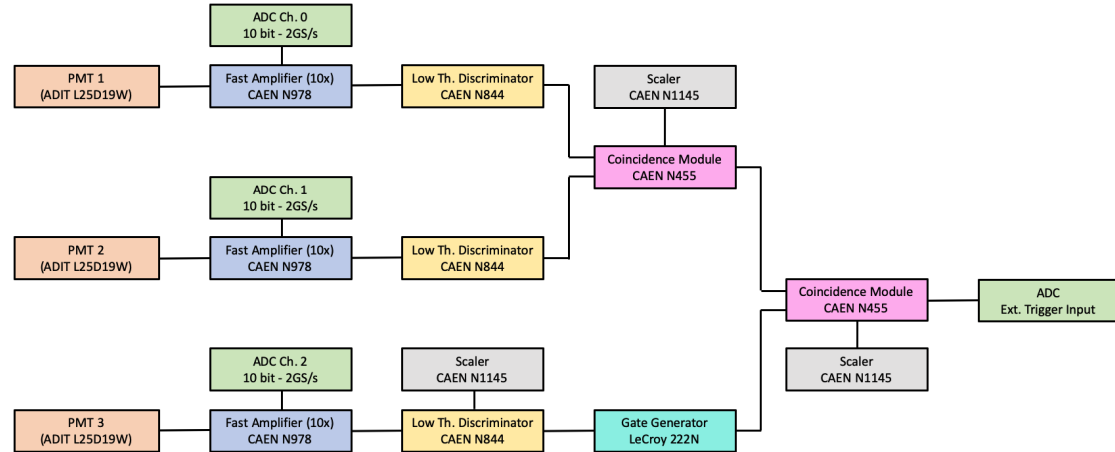


**Figure 8.11:** Block diagram of the upgraded readout electronics of the PoLiDe experiment. The pulses from the three PMTs (reddish brown) are amplified using a variable gain fast amplifier (blue) NIM module provided by CAEN. The constant fraction discriminator was replaced by a low threshold leading edge discriminator (yellow). To produce a 150 ns gate when a signal occurs in PMT 3, a gate generator (cyan) from LeCroy is used. The staged coincidence logic is realized by a quad coincidence module (pink). When a double coincidence of PMT 1 and PMT 2 is present simultaneously with the gate from PMT 3 a trigger signal is produced for the ADC (green). Channels of a CAEN N1145 scaler (gray) are connected to selected parts of the logic circuit to support adjusting the setup. A fully detailed description is given in the text.

The weak pulses are now amplified by a fast amplifier NIM module (Caen N978) with four channels. The input bandwidth reaches 250 MHz and the pulses' rise and fall times are typically below 1.5 ns. The gain for each channel is variable and can be set by rotary switches. If necessary, 2 amplifiers with 4 channels each are available [167]. By cascading two channels amplification factors up to  $10^2$  are possible. One output of the amplifier is directly fed to the ADC, while the second one goes to the discriminator. In the upgraded electronics, the CF8000 constant fraction discriminator is replaced by a low threshold leading edge discriminator (Caen N844) which allows triggering down to a threshold level of -1 mV, while the minimum detectable signal is a -3 mV pulse [168]. By the usage of this device, discrimination of single PE pulses is possible even with low gain amplification.

For the upgrade the length of the logic signals at all discriminator stages was set to 10 ns allowing short coincidence windows. Once, a signal is observed in the LS detector (PMT 3) the discriminator logic pulse is led into a gate generator (LeCroy 222N), which opens a gate of 150 ns, waiting for a coincidence signal of the outer two  $\gamma$  detectors. For the coincidence of these detectors one stage of a quad coincidence logic unit (CAEN N455, see [169]) is used. If two signals from the discriminators are present simultaneously, a NIM logic output signal with a set length of 20 ns is generated. Subsequently, it is directly fed with the gate from the gate generator into a second stage of the coincidence module. If the long gate and the short logic signal from the first coincidence stage are present at the same time a trigger signal is fired and furnished into the external trigger input of the ADC. To evaluate the signal rates at the corresponding stages of the coincidence logic, a four channel scaler (Caen N1145 [170]) is used, which simplifies adjusting of the setup's geometry and discrimination thresholds. It has to be mentioned here, that for the first tests, the Acqiris DC282 with 2 GS/s has been used, but in a further extension of the setup this device will be replaced by a DRS4 Evaluation Board with 5.12 GS/s [171], which is able to save up to 2048 sampling points per waveform. The board makes use of a Switched Capacitor Array (SCA) provided by the Paul Scherrer Institute (PSI). The array is read out with a 14 bit ADC (AD9245 from Analog Devices) and a FPGA (Xilinx Spartan 3). Currently, a software for spline interpolation between the voltage sampling points (which are not equidistant for this type of digitizers) is prepared in the frame of a forthcoming master's thesis. This will allow even more precise timing.

### 8.2.5 First results from the commissioning tests

During commissioning of the upgraded setup, the achievable time resolution and the background suppression achievable by exploiting this property were examined more closely.

#### **Time resolution of the 511 keV $\gamma$ detection:**

Special attention was paid to the achievable time resolution of the 511 keV  $\gamma$  detection, since it is highly influencing the discrimination capability of the experiment against the backgrounds caused by the 1275 keV gammas or by backscattering. Therefore, a direct comparison measurement with the old  $\gamma$  detectors was carried out. The 3" detectors were placed on an optical bench in a distance of 110 cm to each other and connected to the upgraded electronics. The  $^{22}\text{Na}$  source was placed in the middle between them. To record a coincidence spectrum, the ADC was triggered on the coincidence of these two PMTs. After this measurement was completed, the same was done with the new upgraded  $\gamma$  detectors. However, due to

the smaller PSs the distance between their front sides was reduced to 30 cm (which corresponds to 15 cm distance to the radioactive source). A comparison of the hit time difference spectra for the old and new detectors is shown in Figure 8.12. These spectra were acquired with a sampling rate of 2 GS/s and the time was reconstructed with the same constant fraction algorithm as used for the previous PoLiDe runs.

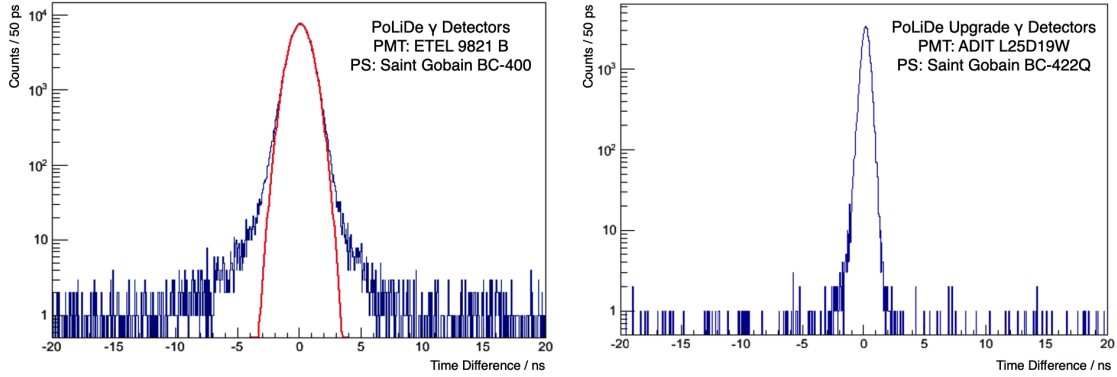


**Figure 8.12: Left:** Hit time difference spectrum for the PoLiDe 3”  $\gamma$  detectors. The red line represents a Gaussian fit to the data. The background to the left and right of the peak can be attributed to backscattered gammas as well as to muons simultaneously traversing both large PS blocks. **Right:** The same measurement but with the upgraded detectors and in a shorter distance to the source. The increased resolution is clearly visible. However, due to the smaller solid angle with respect to the source and the lower muon flux through the smaller scintillator blocks, the background to the left and right of the peak is reduced.

By fitting Gaussian functions to the data, the time resolutions for the 3” detectors

$$\sigma_{3''} = (775.4 \pm 3.2) \text{ ps} \quad (8.4)$$

and for the 1” upgrade

$$\sigma_{1''} = (303.6 \pm 1.2) \text{ ps} \quad (8.5)$$

were determined.

### Background reduction by a coincidence cut:

Also the full setup with the central LS detector was tested during its commissioning. Therefore, the LS vessel was filled with 35 ml of a mixture of LAB with 3g/l PPO and 15 mg/l BisMSB produced for the first phase of the PoLiDe ex-

periment. The  $^{22}\text{Na}$  source was placed above the LS and the central detector was placed in the middle between the two upgraded  $\gamma$  detectors. The distance of the outer detectors to each other was kept at 30 cm. The readout electronics were connected according to Figure 8.11. In a short data taking campaign 300000 triple coincidences were recorded. To suppress the background, a strict coincidence cut was applied to the data. Only events where the two outer detectors were hit simultaneously within a window of  $1\sigma$  to the left and to the right of the Gaussian distribution's mean have been accepted. This results in a coincidence window of 608 ps for the offline analysis, which is excluding events caused by backscattering that would have a minimum time difference of 1 ns. The resulting energy spectra for one of the  $\gamma$  detectors and the central LS detector are shown in Figure 8.13.

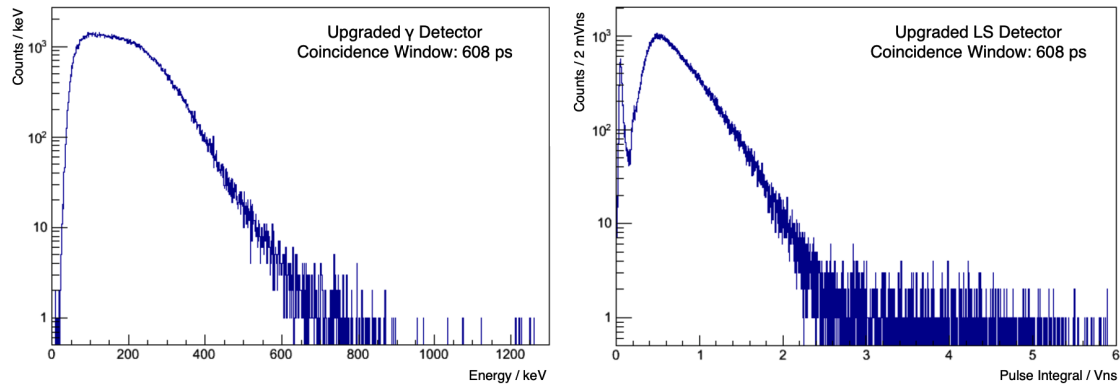


**Figure 8.13: Left:** Energy spectrum from one of the outer  $\gamma$  detectors. The 1275 keV background plateau was efficiently reduced by cutting on the coincident arrival of hits on the both PS detectors. The spectrum shows a Compton edge caused by the 511 keV gammas which was used for a rough calibration. **Right:** Pulse integral spectrum of the inner LS detector. By comparing the spectral shape with the Monte Carlo result presented in Figure 8.5 a reduction of the high energetic background can be observed here as well.

The spectrum of the outer detector was roughly calibrated on the Compton edge of the 511 keV gammas. Due to the coincidence cut, the entire 1275 keV plateau is removed. The same can be observed in the spectrum of the central detector. Both spectra are now in well agreement with the shape of the "Good" events from the Monte Carlo simulation presented in Figure 8.5.

The upgraded setup showed in the first test measurements improved background suppression capabilities. In a dedicated forthcoming master's thesis a new data taking campaign for the JUNO LS mixture and further investigations for other scintillation cocktails will be carried out. Beyond that, the Monte Carlo simulation will be upgraded. Based on the commissioning results, improved precision especially for the o-Positronium formation probability determination can be expected.

## 8.3 Fluorescence time profile measurements

One of the most powerful background suppression techniques in LS detectors is pulse shape discrimination. Pulses, that PMTs record, are influenced by the hardware itself as well as more fundamentally are built up by the intrinsic fluorescence time profile of the LS. This profile depends on the one hand on the scintillator's composition and on the other on the differential energy loss  $dE/dx$  of the particles traversing the LS (for theoretical descriptions and further empirical details see [69, 70, 71]). The time distribution of the fluorescence light emission can be described by a probability density distribution (PDF) comprising several exponential decay functions. However, the PSD performance of a LS is closely related to differences in the time spectrum of the photon emission for different particle species. The precise knowledge of the PDF for a broad variety of particles is a necessity for the implementation of a realistic scintillation model in the global JUNO simulation framework. Furthermore, this knowledge is crucial for event position reconstruction algorithms and tuning of the pulse shape analysis algorithms.

For the  $\alpha/\beta$  separation, investigations on the time profile of the fluorescence of  $\alpha$  particles interacting with the LS in comparison with  $\beta$ s were carried out by P. Lombardi et al. for a JUNO like LS mixture which showed good pulse shape discrimination capabilities [172]. Beyond that, the fluorescence decay times are highly affecting JUNO's sensitivity in the proton decay search (see also [65]) for the channel  $p \rightarrow K^+ + \bar{\nu}$ , since the expected signal shows a narrow double peak structure in time, which could only be resolved with a fast scintillator. The details on the proton decay signal can be found in section 3.1.9 of the present thesis as well as in the Conceptual Design Report of the JUNO experiment [32]. A study of the emission time spectra of the fluorescence photons for different LS solvents and fluor concentrations was carried out by T. Marrodan et al. in the frame of the LENA project. Therefore, the LSs were excited with secondary betas produced by the interaction of  $\gamma$  quanta. Moreover, the work presented an empirical model for the prediction of the fastest scintillation decay component [65].

Furthermore, the detection of the DSNB in JUNO (see section 3.1.7 and [32]) is feasible, according to Monte Carlo simulations within the energy range from 10 MeV up to 30 MeV. There, we need to identify the DSNB signal in the presence of neutron background events induced by neutral current interactions of atmospheric neutrinos or cosmic muons.

To investigate the fluorescence time profiles for the planned LS cocktail of JUNO, an experiment to measure the PDF and directly extract its parameters was developed in the frame of this and another PhD project currently realized by M. R. Stock. The setup using a pulsed neutron beam produced at a heavy ion particle accelerator allows the simultaneous study of the PDFs of recoil electrons induced by gamma radiation as well as recoil protons induced by the interaction of fast neutrons. The

following section gives an overview of the experimental setup, the generation of the pulsed neutron beam at the MLL (Maier-Leibnitz-Laboratorium) 15 MV tandem accelerator as well as first results from the currently ongoing data analysis of the first two beam times in April and September 2019. Moreover, a brief introduction in the theoretical models for the energy transfer mechanisms in multi-component LSs is given, since they are essential for an understanding of the measurements presented in the following sections.

### 8.3.1 Energy transfer in organic scintillators

The phenomenon of scintillation of organic compounds (such as the ones in the JUNO LS) is caused by properties of their molecular structure. Liquid scintillating substances are hydrocarbon molecules containing benzene rings. In this planar ring structure, one s- and two p-orbitals combine ( $sp^2$  hybridization) and form three equivalent hybrid orbitals. The electrons in them are called  $\sigma$ -electrons and form the so called  $\sigma$ -bonds, which are strong and responsible for the rigidity of the molecular skeleton. These  $sp^2$  hybrid orbitals do not contribute to the luminescence. The remaining third 2p-orbital is symmetric to a nodal plane, which coincides with the plane formed by the three  $\sigma$ -bonds. These orbitals are called  $\pi$  orbitals and contain the so called  $\pi$ -electrons. In a benzene ring the six  $\pi$ -electrons form three double-bonds ( $\pi$ -bonds), which are weaker than the  $\sigma$ -bonds. Moreover, these  $\pi$ -orbitals overlap each other so that the six electrons are combined in one single delocalized orbital around the ring. In most organic scintillators the luminescence is caused by the transitions from the excited states of these  $\pi$ -orbitals to the ground state. Nonetheless, it has to be mentioned here, that also triply bounded molecules featuring sp hybridization show luminescence [70].

#### 8.3.1.1 Luminescence related to excited $\pi$ -states

Figure 8.14 shows a Jablonski energy diagram of a general aromatic or conjugated organic molecule. Relative spin orientations of the excited electron are defined commonly in comparison with the spin of the unpaired electron in the ground state as parallel or anti-parallel. Both configurations are at different energy levels and therefore the singlet and triplet spin states are shown separately. The vibrational levels ( $S_{00}$ ,  $S_{01}$ ,  $S_{02}$ , ...) of the molecule show energy differences of about 0.1 eV, while the spacings between electronic levels ( $S_0$ ,  $S_1$ ,  $S_2$ , ...) are larger and typically in the range of 2 eV up to 4.5 eV [70].

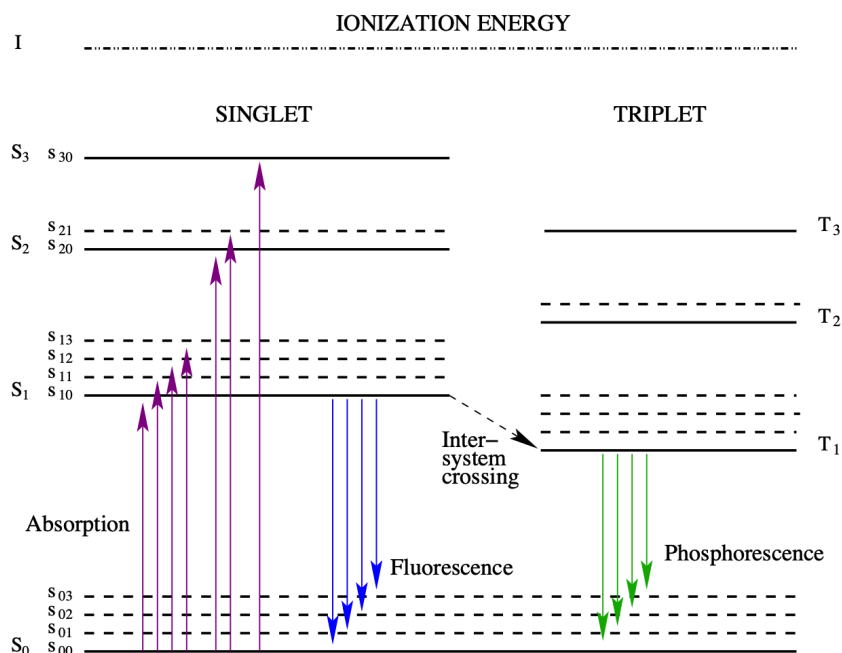


**Figure 8.14:** Jablonski diagram of the  $\pi$ -electron energy levels in an organic molecule containing a benzene-ring.  $S_0$  denotes the ground state, while the excited singlet spin states are written as  $S_1$ ,  $S_2$  and  $S_3$ . The excited triplet spin states are represented by  $T_1$ ,  $T_2$  and  $T_3$ . The corresponding vibrational substates are indicated with double indices.  $I$  is the ionization energy of the molecule. The figure was taken from [72].

When the molecule is excited by photons or ionizing particles to the higher singlet state, it rapidly ( $10^{-12}$  s) dissipates its energy by collisions with other molecules until the  $S_1$  level is reached. Vibrational states are also decaying in the same time frame by vibrational relaxation under heat dissipation. The relative intensities of the transitions from  $S_1$  to different vibrational states of  $S_0$  are given by the Franck-Condon factors [173, 174] which take the overlap of the vibrational wave functions into account. As shown in Figure 8.14 the radiation emitted in the transition from  $S_1$  to the  $S_0$  states is called fluorescence. It accounts for the fast luminescence component occurring in organic LSs. Between the states of identical multiplicity also radiation-less processes can occur, which are commonly referred to as internal conversion or electronic relaxation. These processes lead to losses in the conversion of excitation energy to fluorescence light.

Populating excited triplet states ( $T_1$ ,  $T_2$ , ...) is not possible directly since a spin-flip of one of the contributing  $\pi$ -electrons is required. Nevertheless, by the transition of  $S_1 \rightarrow T_1$ , where the spin of the electron flips to the parallel configuration, the first excited triplet state  $T_1$  can be populated which is indicated in Figure 8.14 as

inter-system crossing with a dashed arrow. According to J. B. Birks, triplet states are preferably populated, when ionized molecules recombine with electrons. In this recombination process about 75 % of the resulting states are triplets. Similar to the singlet states, higher excited triplet states rapidly decay to the  $T_1$  state by internal conversion followed by a quick de-excitation of the vibrational substates. The radiative transition of the  $T_1$  state to one of the vibrational substates of  $S_0$  is highly forbidden, which results in a lifetime of some  $10^{-4}$  s. This light emission at a rather long timescale compared to fluorescence is called phosphorescence. Especially at higher temperatures, the lifetime of the  $T_1$  state can be reduced by numerous processes. A molecule excited to this state may gather enough thermal energy during its lifetime to return to  $S_1$ . Moreover, by the interaction of two molecules in the  $T_1$  state via



both can de-excite under the emission of light. In these processes fluorescence from the  $S_1$  to  $S_0$  transition occurs, but with a delay, which accounts for the time required for  $T_1$  to gather enough energy to be transferred to  $S_1$  or for two excited molecules in  $T_1$  to meet and react with each other. Typical lifetimes for these processes are  $10^{-7}$  up to  $10^{-6}$  depending on the ionization density, the temperature and the  $S_1/T_1$  energy gap. Furthermore, the ionization density affects the density of excited triplet states and with that the probability for the process shown in equation 8.6. The so delayed fluorescence mainly accounts for the slow component of the light production in organic scintillators. Due to its long decay time compared to the delayed fluorescence, the phosphorescence plays only a minor role.

### 8.3.1.2 Multi-component scintillators

Due to a significant overlap of the emission and absorption spectra of single component scintillators, absorption reduces the amount of detectable luminescence photons. Therefore, in organic liquid scintillation cocktails one or two additional components are added to the solvent which have a smaller energy gap between the ground state  $S_0$  and the first excited singlet state  $S_1$ . Typical concentrations for the fluor are 1-10 g/l. The emission spectrum of the solute is shifted to longer wavelengths compared to that of the solvent. Therefore, the fluor is also referred to as primary wavelength shifter. As mentioned in 3.2.4, the JUNO LS will contain 2.5 g/l PPO acting as fluor. Due to its low concentration, self-absorption of the solute plays a minor role even in large scale detectors. Since JUNO's CD has a diameter of 35.4 m the secondary wavelength shifter BisMSB is added in concen-

trations of 1-3 mg/l, which shifts the light to even longer wavelengths in order to further reduce the self-absorption. Figure 8.15 shows a simplified diagram of the energy transfer processes in a three-component LS mixture according to [70, 71].

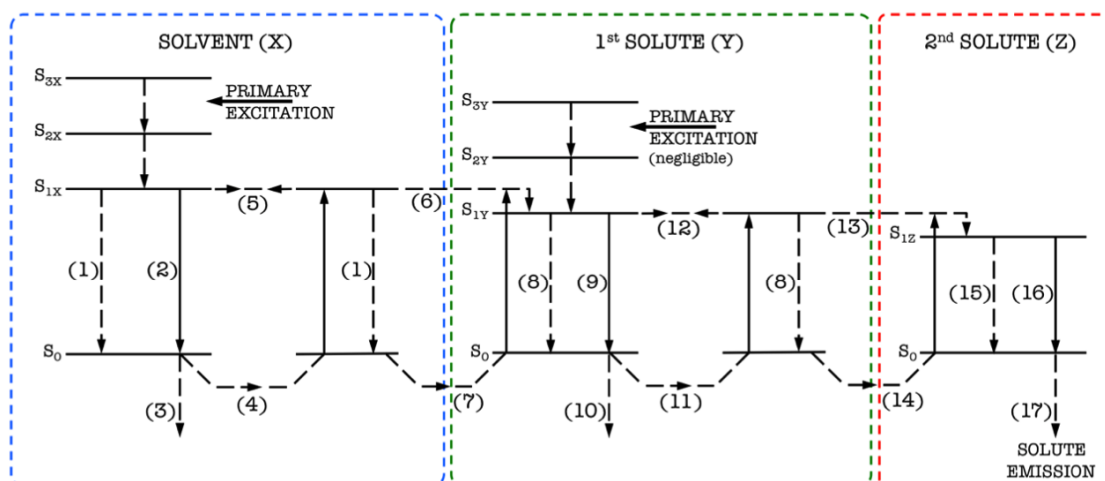


**Figure 8.15:** The transfer processes of the solvent molecules (blue box) are: internal quenching (1), emission (2), escape of light (3), radiative migration (4) and nonradiative migration (5). The excitation energy can be transferred to the first solute either nonradiatively (6) or radiatively (7). The transfer processes within and between molecules of the first solute (green box) are the same as for the solvent, which are: internal quenching (8), emission (9), escape of light (10), radiative migration (11) and nonradiative migration (12). Nonradiative and radiative transfer from the first to the second solute are indicated by (13) and (14) respectively. The processes within molecules of the 2<sup>nd</sup> solute (red box) are: internal quenching (15), emission (16) and escape of light (17). The figure was taken from [175].

As described in 8.2.1.1 the excitation energy of molecules in higher singlet states dissipates energy by internal conversion and thermalization of vibrational states until  $S_{1X}$  is reached. For de-exciting  $S_{1X}$  four different processes are possible: decay to  $S_{0X}$  with or without fluorescence emission, energy transfer via collisions to another solvent molecule (known as energy hopping [72]) or direct energy transfer to a solute molecule. The fast transfer mechanisms dominate since the lifetime of the excited states of the solvent are typically much longer (10-30 ns) [70, 176]. The energy transfer to the fluor molecules happens mainly nonradiative by dipole-dipole interactions. The rate  $k$  of this transfer mechanism which is also called Förster interaction is given for two molecules in a distance  $R$  apart from each other by

$$k = \frac{1}{\tau_{1x}} \cdot \left( \frac{R_0}{R} \right)^6 \quad (8.7)$$

where  $\tau_{1x}$  is the lifetime of the solvents  $S_{1X}$  level. Moreover,  $R_0$  (the so called Förster radius) represents the critical distance at which the excitation transfer has an equal probability as the other de-excitation processes via photon emission or internal quenching. For distances below  $R_0$  the probability for the excitation transfer rapidly increases. Typical Förster radii lie between 20 Å and 60 Å, which is large compared to the molecular diameter of typical solvent molecules of about 6 Å. Due to the low concentration of the secondary wavelength shifter, it is unlikely to find a molecule in the vicinity of an excited fluor molecule. Therefore, the energy transfer via dipole-dipole interaction from the fluor to the second solute has a reduced probability. Here, radiative transfer via photon emission of the fluor and subsequent absorption by the secondary wavelength shifter dominates [70]. However, the probabilities of these processes can be fine-adjusted by tuning the concentration of the second solute.

### 8.3.1.3 Light output and quenching

The amount of photons emitted for an energy deposition in the LS is given by the light output parameter. This figure is crucial as it influences the detection threshold and the energy resolution of a scintillator detector directly. The light output is not strictly proportional to the energy deposited by an ionizing particle. Moreover, the number of emitted photons follows a complex function of the energy, which is not necessarily linear and depends on the particle type and the corresponding specific ionization. It has to be considered, that by the combination of the excitation energy of several molecules additional molecule ions may be generated. In case of two excited molecules in the state  $S^*$  the production of the ionized molecule  $S^+$  can be denoted as



where  $S_0$  represents the ground state [70, 72]. As mentioned before, excited  $\pi$ -electrons recombine with a probability of about 75 % to excited triplet states and by that this mechanism decreases the fluorescence light yield of an initial excitation even further. Since the ionization density is high for heavy charged particles as  $\alpha$ s, protons or heavy nuclei their specific light output is reduced, since the probability for excited molecules in the LS to undergo reaction 8.8 is increased. Furthermore, this effect called ionization quenching causes nonlinearities in the scintillation light

yield for energy depositions of a certain particle type. The semi-empirical Birk's formula

$$\frac{dL}{dx} = \frac{A \frac{dE}{dx}}{1 + kB \frac{dE}{dx}} \quad (8.9)$$

describes the number of photons emitted per unit length  $\frac{dL}{dx}$  as a function of the energy deposition per unit length  $\frac{dE}{dx}$ .  $A$  is the absolute scintillation efficiency, which is defined as the number of photons per energy unit.  $B \frac{dE}{dx}$  denotes the specific density of excited and ionized molecules along the particle path through the LS. The strength of the quenching effect is represented in the equation by  $k$ . Today, the unified parameter  $kB$  is called Birk's parameter and is the common figure for comparing the nonlinearities of different scintillation cocktails. In organic LSs like the one foreseen for JUNO, low  $kB$  values of  $\sim 0.01$  cm/MeV are typical. Nonetheless, this results in a reduction of the light emission of protons by a factor of  $\sim 2$  compared to electrons depositing the same amount of energy [175]. For  $\alpha$  particles higher quenching factors of 9-11 are typical.

#### 8.3.1.4 Fluorescence time profile

Commonly the PDFs of the photon emission process contain more than one exponential decaying component. Therefore, the fluorescence time profile is described by the sum of typically 2 to 4 exponential functions

$$n(t) = \sum_i n_i \cdot e^{-\frac{t}{\tau_i}} \quad (8.10)$$

where  $\tau_i$  are the decay constants and  $n_i$  are the values of the corresponding exponential functions at  $t = 0$ . The parameters  $\tau_i$  and  $n_i$  and with that the composition of the PDF are characteristic for each scintillator and have to be determined experimentally. However, the first short component has usually a large amplitude and is caused by the transition of the lowest excited singlet spin state  $S_1$  in the solute to its ground state  $S_0$ . Further effective decay time constants arise from further molecular processes such as the de-excitation of electrons in triplet spin-states [70, 177]. It has to be mentioned that, the precise origin of these additional long-lived components is not well understood and has to be determined by experiments for each scintillator mixture. Nonetheless, the fastest scintillation component for commonly used LSs can be predicted by a model based on the energy hopping. It was successfully applied to LAB, PC and PXE based two and three component mixtures with different fluors and also with admixtures of the secondary wavelength shifter BisMSB in [177] by T. Marrodan et al.

In this model the excitation of a solvent molecule propagates to neighbouring solvent molecules by collisions occurring with a rate  $k_t$  [ $\text{s}^{-1}$ ]. The excitation energy moves spatially until a fluor molecule is encountered. Then the excitation is transferred by dipole-dipole interaction [69]. The fastest decay constant of a scintillator  $\tau_1$  is mainly determined by the sum of the energy hopping time

$$\tau_t(c) = \frac{n(c)}{k_t} \quad (8.11)$$

and the intrinsic lifetime of the fluor  $\tau_s$ , which was determined in [177] for PPO dissolved in LAB to be  $\tau_{s,PPO}=(1.19\pm 0.15 \text{ ns})$ . So for a mixture of two components, the shortest decay time can be expressed by

$$\tau_1 = \tau_s + \tau_t(c). \quad (8.12)$$

The number  $n$  of solvent-solvent interactions (by collision) decreases for larger fluor concentrations  $c$ . With that the energy is transferred faster from the solvent to the solute. With smaller fluor concentrations the scintillation process happens more slowly and  $\tau_1$  is enlarged. With the assumption of a linear dependence of the transfer rate on the solute concentration [178, 179] and with the definition of an effective hopping rate  $k_h$  follows

$$\frac{k_t}{n(c)} = k_h \cdot \frac{c}{c_0} \quad (8.13)$$

where  $c_0 = 1 \text{ g/l}$ . With that, the fastest component of the fluorescence time profile of a mixture of a solvent and one solute can be expressed by

$$\tau_1(c) = \tau_s + \frac{c_0}{k_h \cdot c}. \quad (8.14)$$

With the parameters determined in the measurements of T. Marrodan et al. [177] for the system of LAB and PPO, the shortest decay time component of the JUNO LS containing 2.5 g/l PPO can be predicted to be  $(4.41\pm 0.56) \text{ ns}$ . Due to its low concentration (1-3 mg/l), the influence of the intrinsic lifetime of the secondary wavelength shifter BisMSB  $\tau_{s,Bis}$  can be neglected for this prediction.

### 8.3.1.5 Particle identification

According to J. B. Birks, the shape of the fast and the slow components are nearly unaffected by differences of the excitation and ionization density of incident

particles [70]. Nevertheless, the relative amplitudes of the components are characteristic for different particle species. As already pointed out, for heavy charged particles like  $\alpha$ s or protons with higher excitation and ionization densities the fraction of excited triplet states is increased. As a consequence slow scintillation components occur with an enhanced amplitude. This discrepancy of the scintillation time profile between particles with different  $\frac{dE}{dx}$  leads to the possibility of distinguishing between different types of particles by their characteristic pulse shape. A qualitative comparison of the pulse shapes for the interactions of  $\alpha$ s, protons and electrons in an organic scintillator is shown in Figure 8.16. The amplitudes are normalized and plotted using a logarithmic scale. This measure highlights the increased fraction of the slow component emission for particles with larger  $\frac{dE}{dx}$ .

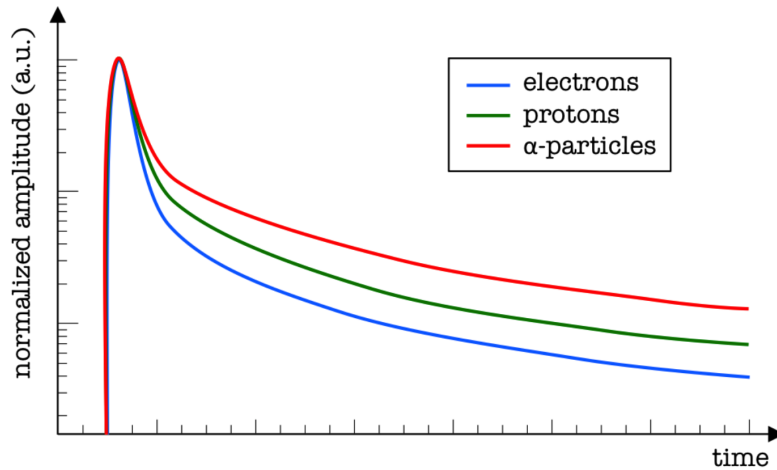


**Figure 8.16:** Qualitative comparison of the emission pulse shapes for  $\alpha$  particles, protons and electrons interacting with a LS. The amplitude of the pulses is normalized and plotted logarithmically versus the time. The figure was taken from [175].

Since the time profiles of the fluorescence caused by different particles cannot be predicted completely with current models, the determination of the corresponding PDFs in laboratory experiments for each particle species is required. As mentioned before, this was done for LS mixtures comparable to the one of JUNO with excitation by  $\alpha$  and  $\beta$  particles [172]. Therefore, the experimental setup presented in the following sections was especially designed to investigate the pulse shape of recoil protons induced by fast neutrons interacting with the LS. Moreover, the time profiles of scintillation caused by secondary betas induced by  $\gamma$  quanta undergoing scattering in JUNO's scintillator mixture can also be studied setup.

### 8.3.2 Experimental setup at the MLL

Today, the production of neutrons via (p,n)-reactions at proton or heavy ion accelerators is commonly used to characterize detector materials. Depending on the realized nuclear reaction, neutrons with a continuous energy spectrum or quasi-monoenergetic neutrons can be obtained. By pulsing the incident beam, a time-of-flight (ToF) measurement allows the discrimination between neutrons and gamma radiation unavoidably produced in the target material and furthermore, the ToF provides additional information on the neutron energy. The neutron scattering facility at the Maier-Leibnitz-Laboratorium (MLL) provided (until the laboratory was finally closed in January 2020) an unique environment to investigate proton recoils in detector materials with quasi-monoenergetic neutrons from 4.7 MeV up to 11.2 MeV. The pulsed neutrons are produced at the MLL scattering facility by guiding a bunched  $^{11}\text{B}^{5+}$  beam with  $\sim 61.5$  MeV energy on a gaseous hydrogen target where the reaction



takes place. Within the following subsections the accelerator setup, the ion beam production, the applied beam pulsing and the production of neutrons in the mentioned gaseous hydrogen target cell are introduced.

#### 8.3.2.1 Overview on the accelerator facility of the MLL

The Tandem accelerator installed at the MLL in 1970 is one of the “Emperor” (MP) series manufactured by High Voltage Engineering corporation (HVEC). During the years the machine was continuously upgraded. A Pelletron charging system was installed followed by extended acceleration tubes. These measures increased the achievable acceleration voltage from initially 10 MV to 14 MV. A detailed description of the MLL accelerator and most of the permanently installed experiments can be found in [180].

The beamlines and essential parts of the accelerator facility are shown in Figure 8.17. The neutron scattering facility is placed in experimental Hall II. Therefore, the beam has to be guided all the way from the Tandem Hall to the experiment through the  $90^\circ$  analysing magnet and two switcher magnets. Several magnetic quadrupole lenses and magnetic beam steering devices were required to ensure a sufficient beam transmission to the experiment. A quadrupole lens close to the beamline’s end in Hall II focuses the  $^{11}\text{B}$  beam to the hydrogen target cell which acts also as beam stop.

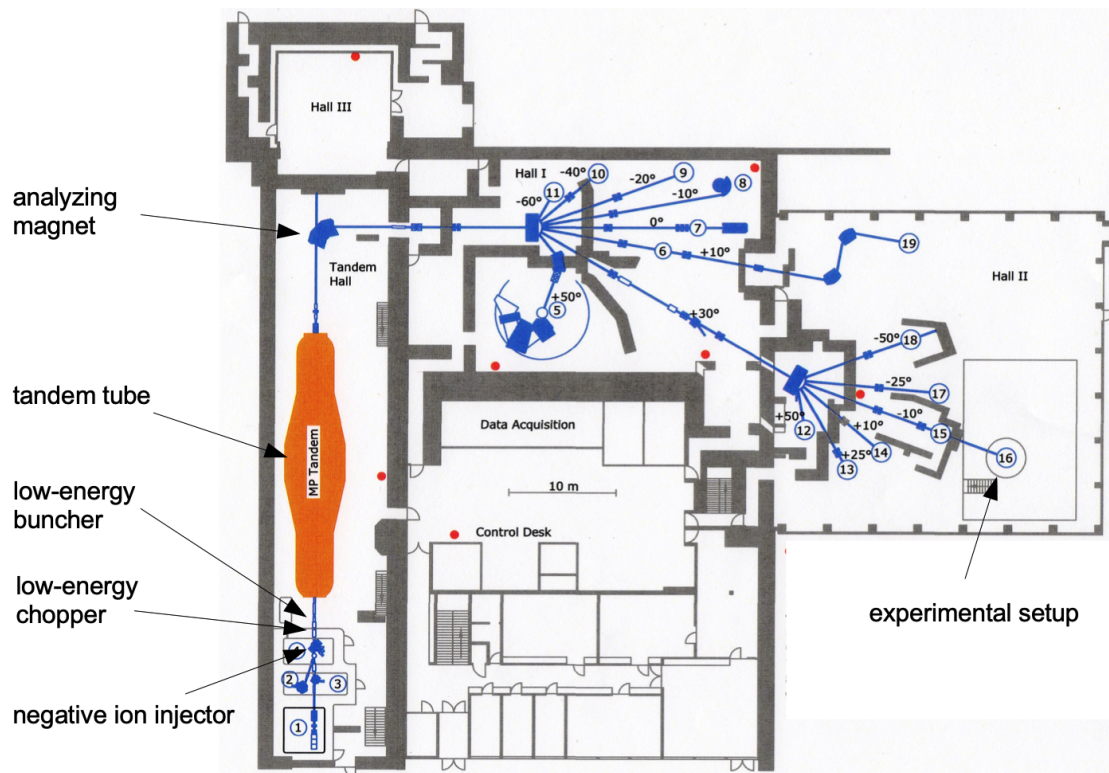


**Figure 8.17:** Top view of the Tandem Hall and the experimental Halls I and II of the Munich Maier-Leibnitz Tandem accelerator facility. Important parts are indicated with arrows. The hydrogen target for the production of quasi-monoenergetic pulsed neutron beams is located at the end of the longest beamline in experimental Hall II (see experimental setup). The figure was taken with courtesy from the MLL visitors information material [181].

### 8.3.2.2 Ion beam production and acceleration

The ion injectors of the MLL are equipped with several different sources. A single-cathode sputter source suitable for most ions which is able to provide beams with moderate intensity is used for the production of the initial  $^{11}\text{B}^-$  ions. A hollow and on the front side open copper cone filled up completely with a mixture of boron powder and silver is placed in an evacuated vessel, where a heater produces neutral Cs vapour. By that, Cs is deposited everywhere in the entire source vessel and also on the surface of the source as well as on an ionizer. By heating the ionizer up to  $1400\text{ }^\circ\text{C}$   $\text{Cs}^+$  ions are generated and due to a high voltage sputtered onto the source cone as well as on the exposed boron silver powder. There the fast  $\text{Cs}^+$  ions knock out atoms from the target, especially boron and silver. Since these atoms have to pass the previously evaporated Cs on the source, they easily pick up an electron

from the loosely bound outermost Cs electron shell. The produced conglomerate of negative ions is extracted by a second high voltage from the source and subsequently separated in an analysing magnet, to get rid of beam contaminants and gain a pure  $^{11}\text{B}^-$  beam.

The ions pass the pre-accelerator (80 kV), the beam pulsing systems (described in the following subsection) and then they enter the tandem. The terminal voltage is set to  $\sim 10.2$  MV. By passing the stripper foil in the terminal the negatively charged particles get stripped and the beam becomes a mixture of positively charged ions (mainly  $^{11}\text{B}^{4+}$  and  $^{11}\text{B}^{5+}$ ). Due to the different charges, the energies of the particles become miscellaneous. By a quadrupole lens behind the tandem accelerator the beam is roughly focused into the  $90^\circ$  analysing magnet, where by a fine adjusted magnetic field the  $^{11}\text{B}^{5+}$  state with 61.25 - 61.55 MeV is selected. By a feedback signal from an slit aperture, the terminal voltage is stabilized so that the energies of the ions are matching perfectly the applied field in the magnet. By this measure the stability of the beam energy and its intensity is significantly enhanced.

### 8.3.2.3 Low energy beam pulsing

After the pre-accelerator, the beam is pulsed. Therefore, a chopper and a bunching system are mounted before the low energy input of the tandem accelerator. The low energy chopper consists of five synchronized AC coupled capacitors arranged consecutively in the beam line. Behind the last capacitor an aperture is placed. When the capacitors wiggle the beam over the aperture, beam slices of  $\sim 70$  ns can be generated. The repetition frequency for the slices passing the aperture can be selected according to  $5 \text{ MHz}/2^i$ . For the fluorescence time profile measurements  $i = 2$  was chosen, which results in one bunch every 800 ns. Regulating the amplitude of the voltage on the capacitors and the phase with respect to the buncher is required to optimize the length of the resulting bunches as well as the achievable beam intensity. The low energy buncher consists of several consecutive drift tubes. In the gaps between them, high voltages are applied similar to the working principle of a conventional linear accelerator. By applying a saw-tooth voltage in the gap between the tubes, beam slices passing the chopper are compressed to a sharp bunch as early arriving ions are decelerated, while late arriving particles are accelerated. Since the generation of a high frequency saw-tooth signal with high voltages is challenging, it is approximated by two sine waves with 5 MHz and 10 MHz applied at two separated gaps. The amplitudes of the two waves as well as their phases relative to each other are adjusted such, that a stable well approximated saw-tooth shaped voltage is realized. If the low energy buncher and chopper are synchronized properly, bunches with a duration of 2-3 ns can be generated.

It should not be concealed that the accelerator facility also has an additional high energy chopper placed behind the  $90^\circ$  analysing magnet. This enables pulse widths

of less than 1 ns even with a wide open window on the low energy chopper. However, as the device did not function reliably at any of the beam times described here, it was not used. Since the experiment turned out to require higher beam currents at the hydrogen cell, the length of the low energy chopper window was enlarged to 100 ns. Due to the defective high energy chopper, this comes at the cost of time resolution. However, with the 100 ns window approx. 5 ns pulses were generated routinely during the beamtimes.

#### 8.3.2.4 Neutron production on a gaseous H<sub>2</sub> target

To produce monoenergetic neutrons the nuclear reaction  $p(^{11}\text{B},n)^{11}\text{C}$ , suggested by M. Drosg [182] especially for heavy ion accelerators, is used. Therefore, a hydrogen target cell was developed in 2004 by T. Jagemann during his PhD thesis [183] in the frame of the CRESST experiment. A schematic drawing of this cell is shown in Figure 8.18.

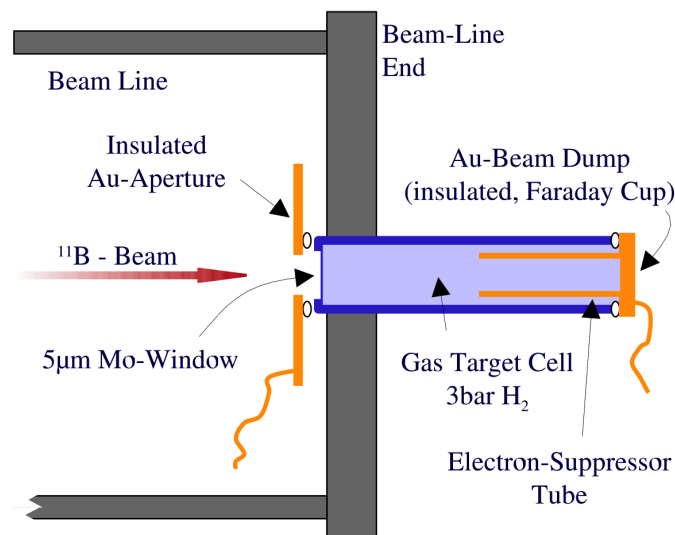


**Figure 8.18:** Schematic drawing of the hydrogen gas target mounted on the end of the beamline. A description of the major parts can be found in the text, while a fully detailed report can be found in [183], where the figure was taken from.

Gaseous H<sub>2</sub> with an absolute pressure of 3 bar is separated against the vacuum by a 5 µm thick molybdenum window. An incident boron particle from the beam with ~61.5 MeV loses about ~4.9 MeV in this metallic foil and typically another ~1.3 MeV before undergoing the nuclear reaction. The remaining ~55.3 MeV are enough to produce neutrons resonantly and therefore with a high yield. Moreover, the energy is low enough to avoid an excitation of the first excited state of the <sup>11</sup>C

daughter nucleus [182, 183] which would result in an additional production of low energetic neutrons. A plot of the energy dependence of the neutron production is shown in Figure 8.19. Due to the inverse kinematics, the neutrons are scattered in the forward direction of the initial beam. As a consequence of momentum and energy conservation, the neutron energy decreases with rising scattering angle with respect to the beam axis. This can be exploited if neutrons with lower energies are needed.

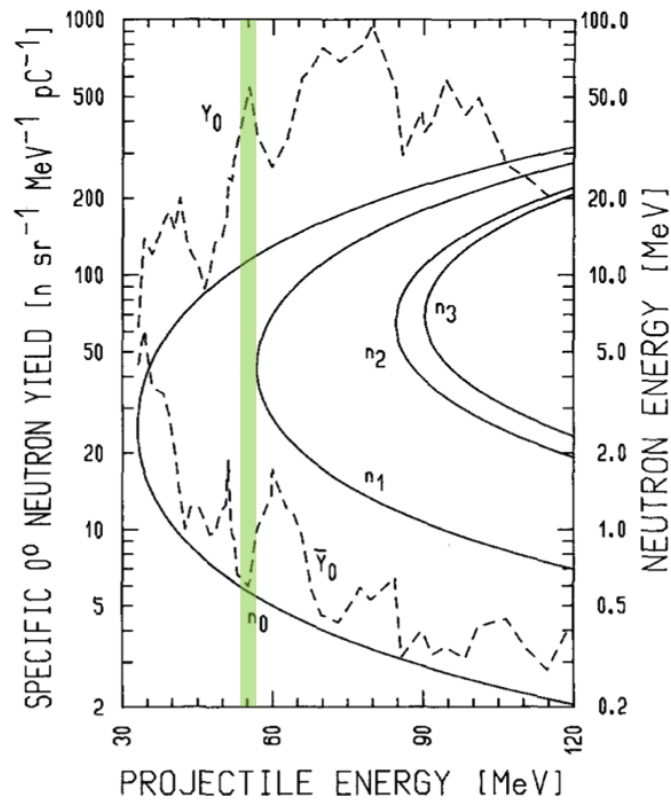


**Figure 8.19:** Plotted is the dependence of the neutron production on the energy of the  $^{11}\text{B}$  ion in the reaction  $p(^{11}\text{B},n)^{11}\text{C}$  as solid curves. The dashed curves represent the specific neutron yields at  $0^\circ$ , so directly in the axis of the incident beam. The high energy branch is indicated with  $Y_0$ , while the low energetic one is labelled as  $\tilde{Y}_0$ . The region highlighted by the green bar corresponds to the  $^{11}\text{B}$  energy of  $\sim 55$  MeV used for the resonant neutron production at the MLL. The plot was taken from [182] and modified.

The entrance window is surrounded by an Au aperture, which was found to be the best material to minimize the background neutron production by the beam corona. The aperture is electrically insulated against the end of the beamline by

a dedicated PTFE washer. This assembly serves as a Faraday cup in form of a ring aperture for easier guiding the beam spot onto the foil window. The beam dump is a 1.5 mm thick electrically insulated removable Au disk insulated as well by a PTFE washer against the cell. An inner electron-suppressor tube prevents backscattered electrons from leaving the Au disc. Otherwise such electrons would lead to an increased current picked up from the target. This would result in wrong estimates of the beam intensity.

After the cell was irradiated for several hours, a refill with fresh H<sub>2</sub> gas is required to remove the contamination caused by boron particles hitting the inner structure of the cell. Therefore, the cell can be evacuated by a small piston pump and can be refilled by a dedicated gas transfer system equipped with a pressure gauge. A detailed description of these parts can be found in [183].

If the molybdenum foil is used extensively and not replaced during several beam-times, gold atoms from the beam stop are sputtered onto the window leading to a broadening of the boron beam and with that the neutron energy distribution. It should be mentioned here, that due to a lack of spare parts, previously used old foil windows with a visible gold deposition were used for both beamtimes presented in the present thesis.

### 8.3.3 Experimental method and detector setup

The main goal of the experiment is to sample the photon emission time profile after the LS is excited by the neutrons or the gammas produced in the cell. Therefore, the so called single photon technique is used. In this method, the start signal of the time measurement is the starting point of the light emission. This is approximately the time of the energy deposition in the LS. If a light detector setup is able to detect a large number of photons from a particle interaction, the start time can be extracted from the first detected photon. The stop signal for the time measurement is provided by an additional detector which is monitoring the same event. This detector should be designed such, that the probability of detecting a single photon of an event is a few percent. This ensures an almost zero probability to detect more than one photon. The time difference between the start and the stop signals of an event provides the information about the PDF. The measuring principle was realized in the setup described in the following, which is similar to the ones used by T. Marrodan et al. [177] and P. Lombardi et al. [172]. However, the setup presented here is adapted to the requirements of the operation at the end of a beam tube of a particle accelerator. Beam-induced backgrounds as well as signal distortions due to unavoidable magnetic fields and high frequency noise should be efficiently decreased.

The detectors for the fluorescence time profile measurement are placed onto optical benches in a darkbox (wall thickness 1 mm) made of aluminum that is also acting as

a faraday cage. A schematic drawing of the experiment is presented in Figure 8.19. A spherical borosilicate glass vessel with an outer diameter of  $\sim 72$  mm and wall thickness below 1 mm contains a sample of  $\sim 150$  ml LS (see Figure 8.19 right). To prevent oxidation of the LS, the remaining volume in the sphere is filled with a protective nitrogen atmosphere with an overpressure of some millibar. The vessel is enclosed by two gas-tight stopcocks with PTFE plugs. The sphere with the LS is placed between two ETEL 9821B PMTs [159] with a 3" photocathode. The coincident pulsing of these tubes provides the start signal for the time measurement. The time of the energy deposition in the LS is then determined by calculating the mean of the pulses' onsets.

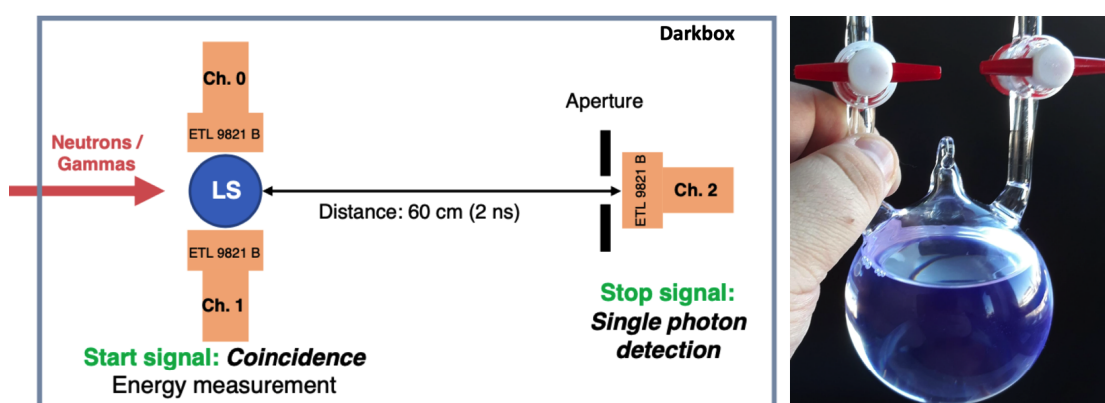


**Figure 8.20:** **Left:** The experimental setup for the determination of the fluorescence time profile of the LS. The start signal of the time measurement is gained from the coincident pulsing of two PMTs (Ch. 0 and Ch. 1) directly on the LS vessel. A stop signal is generated, when a PMT (Ch. 2) in a distance of 60 cm placed behind an aperture detects a single photon. The opening's diameter of the aperture is adjusted such, that the probability for a signal in the distant PMT following a coincidence of Ch. 0 and Ch.1 is below 3 %. **Right:** Photography of the LS vessel made from borosilicate glass (type 3.3). It is filled with approx. 150 ml of a LS sample, which is excited here to its blue coloured light emission by the UV content of sunlight. The visible  $N_2$  gas blanket at an overpressure of several millibars protects the sample from oxidation.

Using two PMTs for the start signal determination instead of one has the advantage that accidental backgrounds by beam-caused particles directly hitting one of the close PMTs is reduced. Furthermore, typical PMT induced backgrounds for the start time measurement like after- and pre-pulsing as well as late and early occurring pulses can be efficiently reduced by a strict cut on the coincidence of both tubes. To avoid a negative influence of magnetic fields on the timing performance of the PMTs, they are mounted in dedicated mu-metal shields provided by ETEL. Moreover, a fully encapsulated voltage divider E638PFP-01 which is well shielded against high frequency noise is used. A third PMT of the same type (with identical shielding and high voltage divider) is placed in a distance of approximately 60 cm

from the sphere and behind an adjustable aperture. By varying the aperture's opening diameter, the single photon detection probability at the distant PMT can be fine adjusted to  $\sim 3\%$  for beam induced events in the LS sample. The darkbox with the entire setup, is placed in a distance of  $\sim 1.5$  m to the hydrogen target cell. Thereby, the LS vessel is exactly aligned in the beam axis.

### 8.3.4 Readout electronics for the experiment

Figure 8.20 shows a block diagram of the electronics used for the data recording. Instead of digital data filters in the recording computer, robust and flexible analog trigger logic based on NIM models is used.

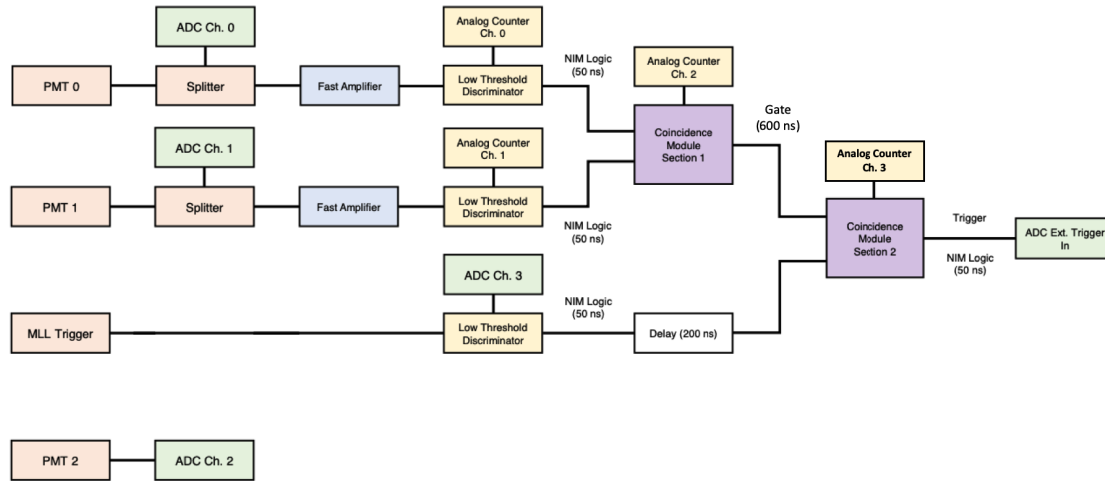


**Figure 8.21:** Block diagram of the readout electronics used for the experiment at the MLL accelerator. PMTs and the corresponding signal splitters as well as the trigger input from the chopper/buncher electronics (MLL Trigger) are drawn as reddish brown boxes. The ADC input channels and the external trigger input are shown in green. The amplifier channels are depicted in blue, while the discriminators and scalers are highlighted by yellow color. The staged coincidence logic is indicated by purple boxes. A white rectangle in the MLL signal path represents the used delay line. For a detailed description of the functionality refer to the text.

At first, the signals of the PMTs 0 and 1 are split by means of a resistive divider. Half of each signal is fed directly into the ADC (Agilent Acquiris 4 Ch., 10 bit, 2 GS/s [136]), to avoid signal distortions by the trigger logic modules. The other half of the signal is amplified by a factor of six using a variable gain fast amplifier (Caen N978, see [167]) with 250 MHz bandwidth and with pulse rise and fall times smaller than 1.5 ns. Then, the signals are discriminated using a low threshold leading edge discriminator (Caen N844, see [168]). The signal of the beam chopper/buncher electronics (MLL Trigger) is directly fed into the third channel of the discriminator

module. For all discriminator channels the lengths of the rectangular logic output signals were set to 50 ns. Subsequently, these signals are brought into a stepped structure of two double coincidence logic sections of the quad coincidence logic unit N455 provided by CAEN [169]. In case of a coincidence of PMT 0 and 1 a long 600 ns gate is generated. By a delay line (of  $\sim 200$  ns) the 50 ns logic signal from the accelerator is placed in the middle of the long 600 ns gate. When a coincidence of these two signals is present, a trigger signal (length: 50 ns) is generated in the second stage of the coincidence logic module and fed into the external trigger input of the ADC. Then for all three PMTs as well as the rectangular MLL chopper/buncher signal a 1000 ns long waveform is recorded. A qualitative drawing of typical signals in the acquisition window can be found in Figure 8.22. The trigger delay at the digitizer is adjusted such, that enough baseline before the pulses can be recorded and that fluorescence decay time measurements for neutrons and gammas are possible up to 600 ns.

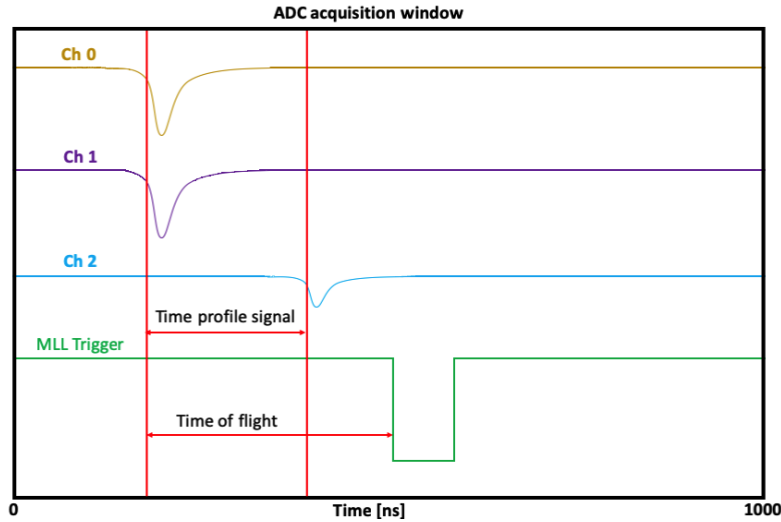


**Figure 8.22:** Qualitative drawing of a typical event in its acquisition window of 1000 ns length. The trigger delay at the ADC is set to a value, that allows a digitization of enough baseline before the pulses. The coincidence of the PMTs close to the LS (Ch 0 draw in in gold and Ch 1 in purple) defines the start signal for the time of flight measurement as well as for the fluorescence time profile investigation. The difference from this start signal to the pulse from the distant PMT (Ch 2, light blue line) provides the information on the PDF for the fluorescence light emission, while the time of flight is calculated as time difference to the logic signal provided by the MLL chopper/buncher system (shown as green line). These values in time are indicated by vertical solid red lines as well as by red double arrows. It has to be mentioned, that the logic signal occurs later compared to the pulses in Ch 0 and Ch 1. Due to that and due to the fixed trigger delay, neutron pulses occur later in the acquisition window and therefore have the lower time differences to the MLL signal. Early arriving  $\gamma$ s show a larger distance to this logic NIM pulse.

Scalers (CAEN N1145, see [170]) connected to the discriminators and the coincidence logic units simplify the setups adjustment. It has to be mentioned here, that during the adjustment of the apertures opening diameter the signal of PMT 2 was split up, discriminated and counted as well. Since this leads to weakening of the small single photon pulses, this was avoided during the data recording phase.

### 8.3.5 Time resolution determination

The time resolution achievable in fluorescence time profile measurements depends mainly on the single photoelectron transit time spread of the distant PMT. According to the data sheet [159] and the test protocol provided by the supplier, the used 3" PMT reaches values below the specification of 2.2 ns (FWHM). This jitter is mainly caused by the photoelectrons produced at different positions of the cathode. They have different path lengths to the first dynode and with that a smearing of the transit time through the tube is caused. Nonetheless, this effect is reduced in the setup, due to the usage of an aperture directly in front of the PMT, as this decreases the area of the photocathode which can be illuminated by the photons from the LS. However, a minor contribution to the loss in time-resolution is caused by the electronic readout chain. Nonetheless, the LS composition has a direct influence on the timing of the experiment, as higher PPO concentrations lead to an increased light yield and also to a faster energy transport. By that, the start signal is obtained more accurately from the PMTs close to the sample sphere as the increased amount of produced light causes a better photon statistics.

As the timing performance is a crucial quantity for the success of the experiment, it was determined using slight modifications of the setup. The far PMT was optically decoupled from the LS sphere with its close PMTs by several layers of black felt. Then a cylindrical block (length: 5cm, diameter: 2.5 cm) of Saint Gobain BC-422Q plastic scintillator which is suitable for ultra-fast timing applications [165] was placed in front of the single-photon PMT. This quenched PS provides a nearly instantaneous light emission (risetime: 105 ps), which has a negligible width in time (FWHM pulse width: 290 ps) compared to the jitters of the used PMTs. In the middle between the LS sphere and the PS a  $^{22}\text{Na}$  source was placed where it emits diametrically coincident  $\gamma$ s with 511 keV energy from the  $e^+$  annihilation. The distance of the PS to its PMT was fine adjusted to ensure that only single photons are hitting the photocathode for most of the  $\gamma$  scatterings. The ADC was triggered for this measurement on the triple coincidence of all three PMTs to efficiently record simultaneous interactions of  $\gamma$ s in the LS and PS. Using the time difference between the time mean value calculated from the pulses' onsets in PMT 0 and 1 and the onset of the small pulse in PMT 2, the time resolution of the setup can be determined. Figure 8.23 shows a plot of the time differences obtained from 28.900 triple coincidences. All timing values were obtained by the same constant fraction algorithm that was used for the PoLiDe experiment described in section 8.2.

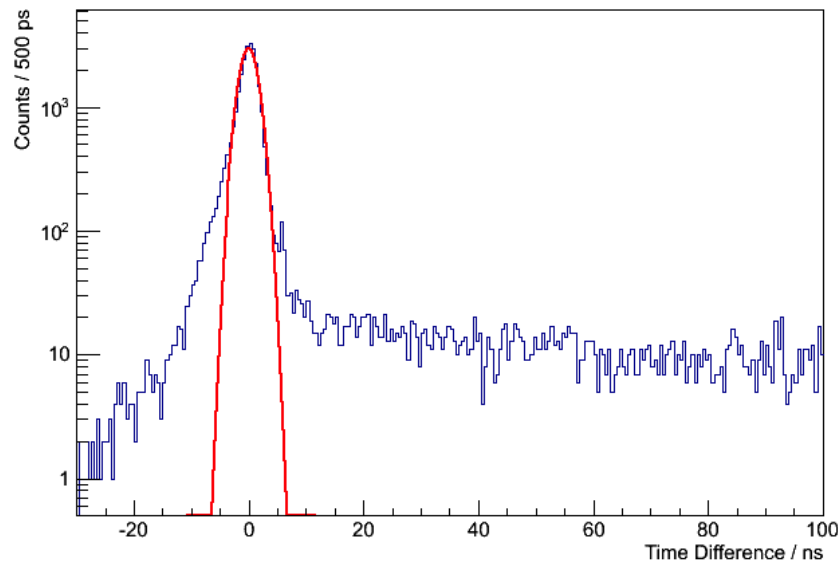


**Figure 8.23:** Distribution of the time differences between the start signal in the scintillator and the arrival of single photons from the PS block. The time resolution of the system with a LS sphere filled with the JUNO mixture is well described by a Gaussian curve (fit of the peak shown as red line).

Although the peak dominating the spectrum is well described by a Gaussian function, there are small contributions at lower and higher time differences. The shoulder on the left side of the Gaussian curve is caused by pre-pulses of the single-photon tube. Further to the left, there is a second background contribution which can be interpreted according to [177] as photons which cross the cathode of PMT 2 and produce subsequently a photoelectron on the dynode-chain. On the right side of the peak additional events can be explained by the reflection of photoelectrons on the first dynode back to the cathode, which was observed in [177] and described in detail in [184]. However, these pulses typically show a slightly decreased pulse height. Therefore, most of the corresponding events were removed efficiently by a simple cut on this quantity before plotting the spectrum. The pulses at later times ( $t > 20$  ns) are caused by fast afterpulses and by weak light emission of the photomultiplier window (see also [177]) induced by the intensive radioactive source (1 MBq) which was placed very close to the tube. This background is only visible on the right side of the peak, as the gate of the discriminator connected to PMT 2 was set to 20 ns. Since the gate produced by the coincidence unit connected to PMT 0 and 1 was set to 600 ns, only very late pulses from PMT 2 are recorded. Moreover, if the PS (or the LS) is hit a second time (before or after a 511 keV related triple coincidence) within the acquisition window of  $1 \mu\text{s}$ , events with an arbitrary time difference can be generated.

For the setup with the JUNO LS mixture (LAB, 2.5 g/l PPO, 3 mg/l BisMSB) a time resolution of

$$\sigma = (1.608 \pm 0.008) \text{ ns} \quad (8.16)$$

was determined by a Gaussian fit of the peak. The uncertainty of this value is purely statistical and directly obtained from the fit.

### 8.3.6 Time of flight particle identification

The ToF measurement allows an efficient discrimination between neutrons from the hydrogen cell and unavoidable gammas produced by the beam. As the fluorescence time profile experiment was found to be critical in rate and the beam current is significantly reduced by the low repetition rate of the beam pulses (1.25 MHz), the distance to between LS sphere and H<sub>2</sub> target was set to  $(150 \pm 5)$  cm. Figure 8.24 shows a time of flight spectrum of events recorded in one of the 9 data runs (here 2 million events before cuts) from the beamtime in September 2019 with the JUNO LS mixture. The hits of the LS plotted here, were identified by offline analysis as events which contain a single photon in the distant PMT.

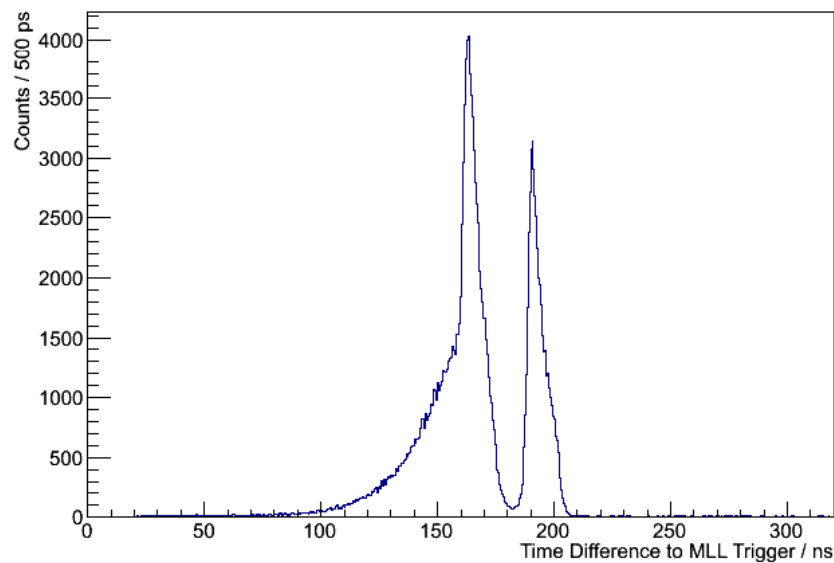


**Figure 8.24:** Time difference between the coincidence of PMT 0 and 1 and the logic signal from the MLL chopper/buncher system present after this coincidence. By using this reference point in time, the neutrons occur at lower time difference values as the gammas. As this plot contains information about the time of flight of the particles from the H<sub>2</sub> target cell, it is referred to in the following as ToF spectrum. Detailed explanations of the spectral shape are given in the text.

Clearly visible are two strong peaks in the spectrum. As a rectangular signal from the beam chopper/buncher system after the events in the detector was selected for the timing, the neutrons show up at lower time difference values to this MLL trigger signal as the beam gammas. So the left large peak is caused by neutrons, while the smaller right one originates from the gammas produced at the beam stop. The tail of the two peaks on the right side is a consequence of early arriving  $^{11}\text{B}^{5+}$  ions at the hydrogen cell. This was found to be caused by the enlarged chopper window on the low energy side of the tandem, while no high energy chopping was applied. The long tail on the left of the neutron peak has its origin in  $^{11}\text{B}$  particles hitting the hydrogen nuclei with lower energies. This was expected, as the molybdenum foil of the cell window showed a visible gold deposit. By that, the thickness of the foil is enlarged, and the  $^{11}\text{B}$  energy is smeared out towards lower values. As lower energetic neutrons require more time for travelling the  $\sim 150$  cm, they show up as tail towards lower time differences to the MLL trigger.

By fitting Gaussian functions to the peaks their position was determined in the spectrum. The gamma peak's mean is  $(191.19 \pm 0.03)$  ns, while the neutrons with the full energy are placed at  $(163.78 \pm 0.04)$  ns. The time difference of  $(27.41 \pm 0.07)$  ns is in well agreement with a neutron energy of 11.2 MeV. From the fit of the  $\gamma$  peak the time resolution of the low energy pulsing system in combination with the detectors of the experiment was determined to be

$$\sigma_{\text{ToF}} = (2.27 \pm 0.02) \text{ ns}, \quad \text{Res}_{\text{ToF}} = (5.33 \pm 0.05) \text{ ns} \quad (8.17)$$

which is in well agreement with the expectation of a pulse width of  $\sim 5$  ns for the 100 ns low energy chopper window.

For the fluorescence decay time profile determination, neutrons with ToF values from 140-180 ns were accepted. The corresponding gamma sample is composed of events between 180 ns and 200 ns. However, neutrons and gammas which are backscattered of the walls from the experimental hall to the LS sphere, as well as  $\gamma$ s and neutrons produced elsewhere in the beamline close to the cell produce a contamination in the ToF populations. Furthermore, cosmic muons and other natural radiation hitting the LS would produce a 600 ns long gate at the coincidence unit connected to PMT 0 and 1. As the MLL trigger signal is produced regularly every 800 ns, this radiation is expected to cause accidental triple coincidences with a random ToF value. To evaluate these contaminations of the neutron and gamma populations the flat background to the left of the  $\gamma$  peak was fitted and a mean bin-content of  $(5.96 \pm 0.17)$  Counts/(500 ps) was obtained. This results in a contamination of the neutron sample in the acceptance region of  $(0.42 \pm 0.01)$  %, while the backgrounds contribute  $(0.50 \pm 0.02)$  % to the gamma population.

Table 8.2 shows an overview for the produced neutrons with a single photon depos-

ited in PMT 2 for the 9 data runs with the JUNO LS sample in September 2019. In total  $13 \times 10^6$  events (coincidences of PMT 0 and 1 with the MLL beam trigger) were recorded during 2 days of data taking.

Data Run	Raw Events	Neutrons with single PE	Fraction [%]
1	2,000,000	64,961	$3.248 \pm 0.013$
2	1,000,000	32,548	$3.255 \pm 0.018$
3	1,000,000	31,708	$3.171 \pm 0.018$
4	2,000,000	108,486	$5.424 \pm 0.016$
5	2,000,000	94,103	$4.705 \pm 0.015$
6	2,000,000	89,725	$4.486 \pm 0.015$
7	2,000,000	95,116	$4.756 \pm 0.015$
8	500,000	23,178	$4.636 \pm 0.030$
9	500,000	21,968	$4.394 \pm 0.030$
<b>Total</b>	13,000,000	561,793	$4.321 \pm 0.006$

**Table 8.2:** Table of the 9 data runs for the JUNO LS mixture with 2.5 g/l PPO and 3 mg/l BisMSB from the beamtime at the neutron scattering facility of the MLL tandem accelerator laboratory in September 2019. The second column shows the number of events which were recorded. These are triple coincidences of the beam trigger signal and the two PMTs directly at the LS sphere. The third column shows the number of neutron events selected by the ToF method, which show a single photon in the distant PMT. These events can be used for the fluorescence time profile determination. The last column shows the fraction of these events contained in the raw data.

In total  $13 \times 10^6$  events (coincidences of PMT 0 and 1 with the MLL beam trigger) were recorded during 2 days of data taking. Trigger rates at the experiment of 100 Hz up to 350 Hz were achieved, when the beam was hitting the target cell centrally. However, as the current from the  $^{11}\text{B}$  sputter source was unstable, due to several technical problems in the cooling loop, large fluctuations and beamtime interruptions happened. If well adjusted, the current of the pulsed beam at the experiment exceeds 1.3 nA, while reaching values up to 2.8 nA in times where the ion source provided larger amounts of ions. Therefore, the duration of the data runs was nearly unpredictable.

At the end of data run 3, the power supply of the magnetic lens, which focuses the beam on the target window failed as well as the power supply for the magnetic steering device guiding the beam to the hydrogen cell. After the repair a complete re-adjustment of the beam spot's shape and focal point was required. Since the size of the beam was significantly reduced and with that less boron ions hit the target's ring aperture, the neutron production rate was significantly enhanced. During data

run 5 readjustments of the  $90^\circ$  analysing magnet as well as on both beam switchers were necessary due to a power failure on the beam focusing quadrupole lens between the tandem accelerator and the bending magnet. Therefore, the beam showed a slightly broader shape close to the experiment and with that the fraction of neutron events in this and the following runs was slightly reduced compared to run 4. The remaining fluctuations are mainly caused by an unavoidable random beam walk over the target, which is mainly caused by fluctuations of the magnetic fields in the second beam switcher, the magnetic steering devices and the quadrupole lens focusing the ions to the hydrogen cell.

As visible in the ToF spectrum shown in Figure 8.24, the peak of  $\gamma$  events with a single photoelectron in PMT 2 contains less events compared to the neutron peak and by that the data set for the  $\gamma$  fluorescence time profile determination is smaller. In total 297,920 gamma hits with a single photon in PMT 2 were accepted for further analysis. As observed in the data,  $\gamma$  quanta with their spectrum from the multi-MeV regime down to several keV are depositing typically lower amounts of energy in the LS, than the quasi-monoenergetic neutrons. By that, the probability of a single photon hit on PMT 2 is lower for  $\gamma$ s than for neutrons from the  $H_2$  target cell.

### 8.3.7 Current results for neutron and gamma interactions

Since the analysis of the beamtime data is still ongoing while this thesis has been written, only the currently available results for the JUNO mixture are shown in the following section. The investigation of the systematic uncertainties is currently ongoing in laboratory test measurements with radioactive  $\gamma$  sources. These investigations and also the final analysis are being carried out as part of Raphael Stock's PhD thesis. The results for the second organic LAB-based LS with 3 g/l PPO and 20 mg/l BisMSB and for the JUNO mixture will be presented in a forthcoming publication [185].

#### 8.3.7.1 Single photon selection

As mentioned before, it is crucial for the so called single photon technique, to use single photoelectron events in the distant PMT for the sampling of the fluorescence time profile. As the event rates presented in Table 8.2 show, the diameter of the aperture was well adjusted. To further purify the data, the pulse height spectra for all neutron and gamma events of all waveforms recorded from PMT 2 is investigated. The corresponding plot of the maximum pulse height above the baseline (mean) of the waveform for all neutron hits of the LS from data run 7 is shown in Figure 8.25. The high peak on the left of the logarithmically plotted spectrum is caused by the

empty waveforms without a single photon. The broad peak to the left corresponds to the single photon interactions. Within this measurement a single electron peak to valley of  $\sim 1.5$  was realized. This is in well agreement with the characteristics of the used PMT equipped with the E638PFP-01 voltage divider. The spectrum shows no indication for double-photon peaks. However, to avoid contributions from noise as well as potential double-photon caused large pulses, only events with a height between 2.8 mV and 16 mV were accepted for further analysis.

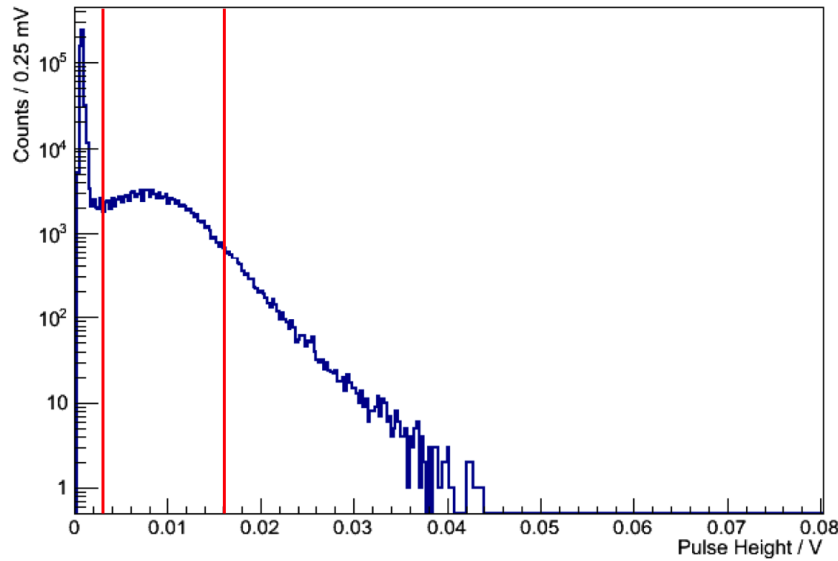


**Figure 8.25:** Spectrum of the pulse heights of all recorded waveforms for the distant PMT. Clearly visible is the noise peak on the left caused by the large amount of empty traces. The peak at  $\sim 0.01$  V corresponds to single photon hits. The acceptance region from 2.8 mV to 16 mV for pulses used for the fluorescence time profile determination is indicated by red vertical lines.

### 8.3.7.2 Fluorescence time profiles for neutrons and $\gamma$ s

As mentioned above the onset time of the start and stop signal is derived by a constant fraction method. The starting point of each pulse is defined by the point in time where the leading edge exceeds 20 % of the maximum pulse height above the baseline. The distribution of the photon emission time is then determined by the difference between these starting points and that of the single photon PMT. The plot presented in Figure 8.26 shows the resulting fluorescence time profiles for the JUNO LS mixture for 561,793 neutron events (red histogram) and 297,920 gammas (blue spectrum) from the beam. To avoid an influence of the ADC recording window length, the analysis of the spectra was only performed up to a time difference of

500 ns. Even for a coincidence of the PMTs 0 and 1, which is placed very late in the recording window (typically at  $\sim 400$  ns for neutrons with reduced energy), a single PE, which is emitted 500 ns after the start signal, is detected for sure.

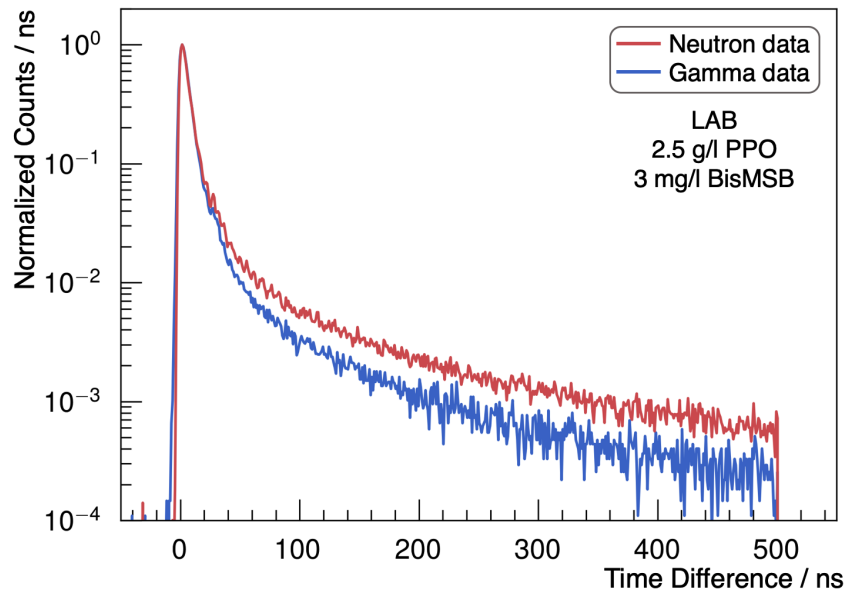


**Figure 8.26:** Comparison of the fluorescence time profiles for proton (red histogram) and  $\beta$  interactions (blue spectrum) with the planned JUNO LS. The proton events were induced by neutron scattering, while the  $\beta$ s are produced by the  $\gamma$ s undergoing Compton scattering in the LS sample.

To allow a direct comparison of the spectral shape, both curves were normalized to their peak. Both spectra are well overlapping each other in the part of the fast fluorescence decay. At later times the curves deviate from each other substantially as the spectrum of the recoil protons induced by the fast neutrons show a more pronounced tail. These different tails underline the PSD capabilities of JUNO's LS for neutron and gamma interactions.

### 8.3.7.3 Determination of the PDF parameters

To determine the effective fluorescence decay times  $\tau_i$  and their contribution to the absolute scintillation light emission, the data is fitted with a probability density function  $F(t)$ . As mentioned in 8.3.1.4 and pointed out in equation 8.10, the scintillation-light emission can be described by several exponential decay functions. Here, also the detector resolution  $R(t)$  has to be considered. Therefore, the function

$$F(t) = R(t) * \left( \sum_{i=1}^4 \frac{n_i}{\tau_i} \cdot e^{-\frac{(t-t_0)}{\tau_i}} \right) \quad (8.18)$$

is a convolution of a Gaussian function

$$R(t) = e^{-\frac{t^2}{2\sigma^2}} \quad (8.19)$$

as model for the resolution and (for the JUNO LS) the sum of four exponential decays. The contributions of the decay time components to the scintillation light emission are defined such, that the equation  $\sum_{i=1}^4 n_i = 1$  holds. Figure 8.27 shows the fluorescence time profiles with the fitted probability density functions for neutron and gamma interactions separately in two plots.

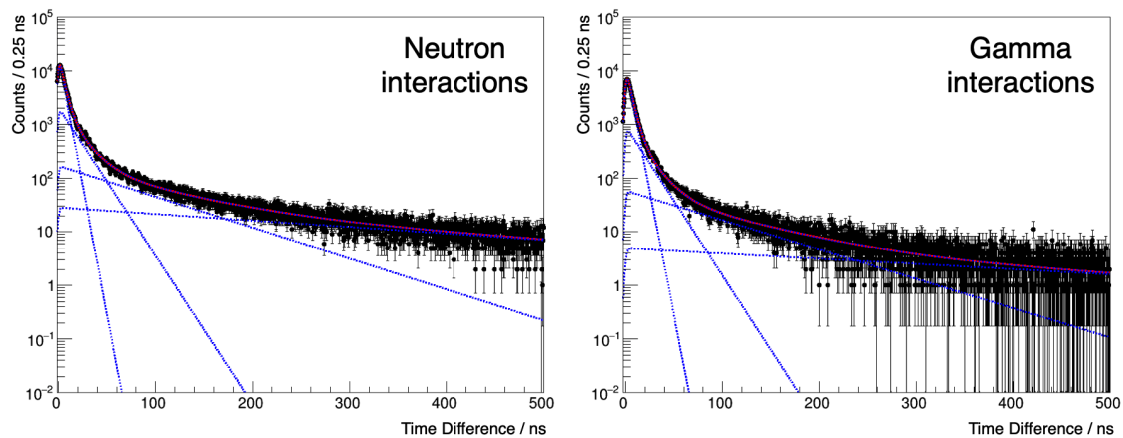


**Figure 8.27:** Datapoints for neutron induced proton recoils (left plot) and  $\beta$  events (right plot) caused by Compton scattering of  $\gamma$  radiation in the LS. The dotted red lines represent data fits with the PDF described in equation 8.18. The contributions of the effective fluorescence decay times to the PDF are plotted separately as blue dotted lines. The gamma spectrum contains significantly less events, especially towards larger time difference values. This results in a larger statistical uncertainty for the largest effective decay time component in the fluorescence time profile.

The fit according to equation 8.18 was realized by using the ROOT-based toolkit RooFit [186]. This software performs in its default configuration a maximum likelihood fit by minimizing  $-\log(L)$  where  $L$  is the likelihood function. Therefore, RooFit makes use of the Minuit [187] package from the CERN libraries. The results for the PDF parameters obtained from the neutron and gamma induced events are listed in Table 8.3.

i	Neutron	Neutron	Gamma	Gamma
	$\tau_{i,N} \pm \Delta\tau_{i,N}$ [ns]	$n_{i,N} \pm \Delta n_{i,N}$	$\tau_{i,G} \pm \Delta\tau_{i,G}$ [ns]	$n_{i,G} \pm \Delta n_{i,G}$
1	4.51±0.05	0.607±0.007	4.71±0.05	0.718±0.008
2	15.72±0.42	0.242±0.005	15.65±0.57	0.199±0.007
3	75.4±5.7	0.095±0.004	79.5±8.8	0.063±0.004
4	358±51	0.057±0.009	447±204	0.021±0.010

**Table 8.3:** The first and second column to the left contain the effective fluorescence decay times and their fraction of contribution to the PDF. The listed statistical uncertainties were obtained from the fit. The two columns on the right show the corresponding parameters for the beam induced gamma radiation. The large uncertainties for the longest effective decay time component and its contribution to the  $\gamma$  PDF are caused by the lack of events with large time differences in the corresponding spectrum in Figure 8.27. The values for the shortest decay component are in excellent agreement with the phenomenological prediction of  $(4.41 \pm 0.56)$  ns (for details see subsection 8.3.1.4).

The resolution obtained from the PDF fit is  $\sigma_N = (1.62 \pm 0.02)$  ns for the neutron events and  $\sigma_G = (1.68 \pm 0.02)$  ns for the gamma events. Both values are in good agreement with the experimentally determined value presented in 8.3.5. The results for the shortest effective decay time are in excellent agreement with the expectation  $(4.41 \pm 0.56)$  ns based on the energy hopping model with the parameters for LAB reported by T. Marrodan et al. [177]. As reported in [70] and confirmed by the data, different ionization densities of incident particles have only a minor influence on the effective decay times. The results obtained from the two fits show similar decay time values for neutron and gamma interactions. However, the contributions of long effective decay time components to the fluorescence time profile of neutron induced proton recoils are significantly larger compared to them of  $\beta$  events caused by  $\gamma$  scattering. It has to be mentioned, that the large uncertainties for the  $\gamma$  data are caused by the low number of events with a large difference between start and stop signal. In the measurements currently carried out for the PhD project of R. Stock, more  $\gamma$  data is recorded using a  $^{137}\text{Cs}$  source.

## 8.4 Proton quenching factor determination

Proton recoils caused by fast neutrons are a background component for the detection of electron antineutrinos from the nuclear reactors or from the earth's internal radioactivity. Furthermore neutrons provide a background in the energy region of interest in diffuse supernova neutrino searches. Beyond that, neutrino-proton

scattering is a major detection channel for neutrinos from core collapse supernovae. Due to the higher ionization quenching for protons compared to electrons with equal kinetic energy, the light output of the scintillator shows a stronger nonlinearity. On the one hand, profound knowledge about the quenching of proton recoils is crucial for reconstructing the real energy scale from the visible energy in the JUNO detector. On the other hand the quenching factors are an important input to Monte Carlo simulation studies. Especially the visible energy spectrum and expected rate for these backgrounds require informations on the effective light yield. Therefore, experimental studies for LAB-based LSs were carried out in 2013 and 2014 by V. Zimmer in the frame of a PhD project [175]. For this investigations the neutron scattering facility with the hydrogen target cell described in subsection 8.3.2.4 was used. During the following section a brief overview on the detector design, the measurement principle as well as on the results for a LS containing LAB with 3 g/l PPO and 20 mg/l BisMSB is presented, while a full detailed description of these experiment can be found in [175].

### 8.4.1 Detector design with improved light collection

As a high light collection efficiency and with that a good energy resolution is crucial for achieving a good precision in the quenching factor determination, the detector shown in Figure 8.28 was designed to meet this requirement.

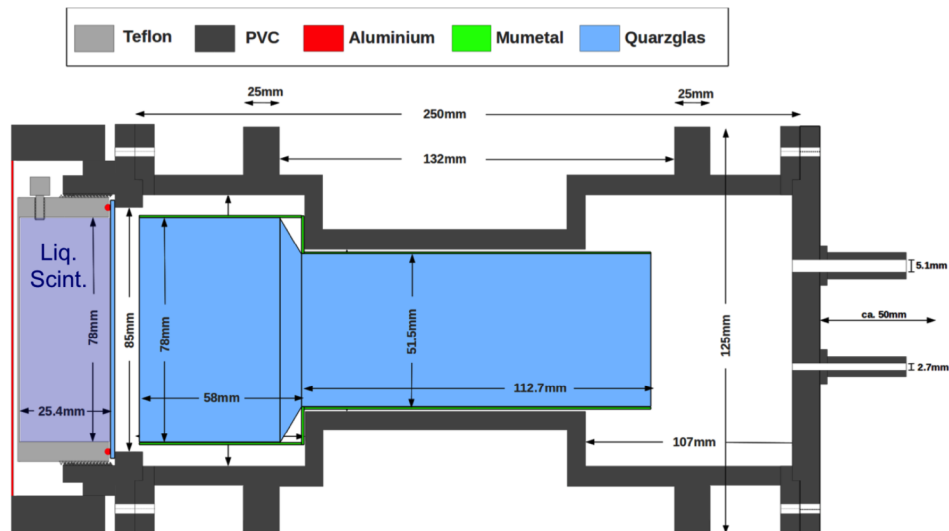


**Figure 8.28:** Coloured technical drawing of the detector design used for the determination of the effective light yield of protons in the LS. The material composition of the setup's parts are indicated by their color in the drawing. The LS in the sample cell is shown in purple. For details on the major parts refer to the text or to [175], where this Figure was taken from.

To detect the scintillation light from the LS sample, one ETEL 9822KB [188] photomultiplier tube (PMT) which features good timing capabilities and a wide dynamic range was used. The 3" PMT was placed within a custom made mu-metal shield. The LS sample is contained in a PTFE cell with a diameter of 3" and a height of 1". This results in a sample volume of approx. 120 ml. The base of the cell, which pointed to the H<sub>2</sub>-target during the data taking, was made with a thickness of only 1 mm to reduce scattering of the neutrons before entering the liquid scintillator volume. The cell is mounted into a PVC flange and sealed with a PTFE coated O-ring which is placed between the cell's PTFE wall and the 2 mm thick quartz glass window. As exchanging the sample quickly during the beamtimes was necessary, no refractive index matching optical pads or glue was used between the windows of PMT and cell. The entire assembly is placed within a light tight PVC housing. The empty space behind the PMT contains the voltage divider which is not shown in Figure 8.28. To further decrease light leaking into the system, the outer housing was wrapped into several layers of black felt. A black PVC cap and an additional 1 mm thick aluminum plate make the front side of the detector light tight.

The detector was extensively calibrated by several radioactive  $\gamma$  sources. Due to multiple scattering of the gamma quanta in the scintillator the determination of the Compton edge position in the recorded energy spectra is not trivial. Therefore, a reconstruction method based on detailed Monte Carlo simulations of the detector was developed during the diploma thesis of L. Prade [189]. A detailed description of all calibrations can be found in [175], while the reconstruction method is extensively discussed in [189].

### 8.4.2 Experimental setup at the neutron scattering facility

A precise determination of the effective light yield of recoil protons requires measurements with several different neutron energies. Therefore, the detector was placed at certain angles to the axis of the initial beam as it is shown in Figure 8.29. The full detector module is mounted on an Item-rail. By moving the detector to pre-defined positions on this rail, angles between 1° and 35.3° were realized, which correspond to neutron energies from 4.7 MeV up to 11.2 MeV for <sup>11</sup>B<sup>5+</sup> particles with an energy of ~61.5 MeV hitting the hydrogen target cell. The distance between detector and beam stop was precisely measured by a laser distance sensor. When the LS cell is placed in the beam axis, this distance is (3.592±10) mm. By this larger distance compared to the fluorescence time profile experiment, the ToF provides information on the neutron energies with good resolution. Moreover, during the beamtimes in 2013 and 2014 beam bunches with a length (FWHM) of 2-3 ns were realized using a 70 ns low energy chopper window. Nonetheless, both improvements come at the expense of a decreased neutron flux through the LS cell. Therefore, the bunch re-

petition rate was set to 2.5 MHz. Since a monoenergetic neutron spectrum emitted by the target cell is crucial for the success of the measurements, new molybdenum foil windows without any gold deposition were used for each of the beamtimes.

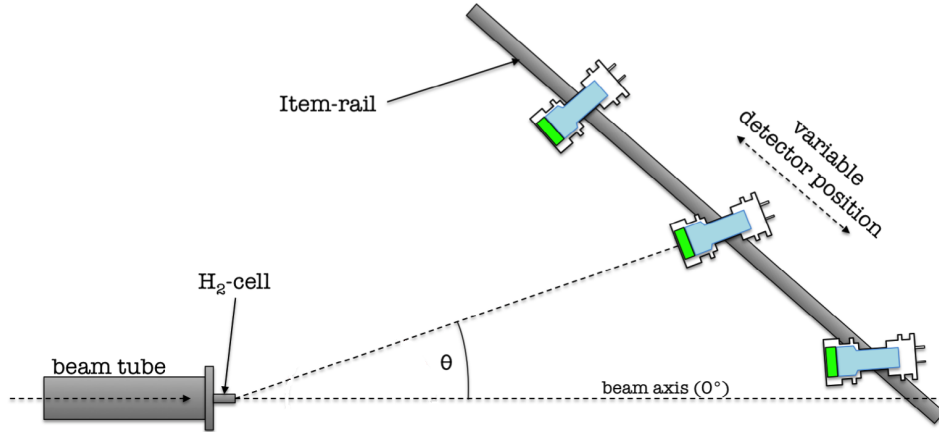


**Figure 8.29:** Schematic drawing of the detector installation at the neutron scattering facility of the MLL. The LS detector can be moved between  $1^\circ$  to  $35.3^\circ$  with respect to the beam axis ( $0^\circ$ ). As a consequence the available neutron energies can be selected from 4.7 MeV up to 11.2 MeV at will. The figure was taken from [175] and subsequently modified.

### 8.4.3 Results for the Birk's factor $k_B$ of protons

As mentioned in 8.3.1.3, the influence of the ionization density of a particle interacting with LS can be described by the semi-empirical Birk's model. By substituting the absolute light output  $L$  in equation 8.9 with the visible energy  $E_{vis}$  an equation

$$E_{vis} = \int_0^{E_{dep}} \frac{A}{1 + kB \frac{dE}{dx}(E)} dE \quad (8.20)$$

for the scintillation answer to an energy deposition can be calculated.  $E_{vis}$  is the energy obtained from the energy scale provided by a calibration of the detector with  $\gamma$  radiation induced electron recoils. The parameter  $A$  corresponds to  $E_{vis}/E_{dep}$  in case of no quenching ( $k_B=0$ ). Since the detector was calibrated, it can be set to unity. Nonetheless, an uncertainty is caused by the energy calibration of the detector. In equation 8.20 the Birk's factor is denoted as  $k_B$  (for details see also 8.3.1.3).

The maximum energy of the recoil protons  $E_{rec}^{max}$  in the scintillator is approximately equal to the initial neutron energy  $E_n$  as the proton and neutron masses are

almost identical. The energy dependent energy loss  $\frac{dE}{dx}(E)$  of protons in the LS was calculated from data taken from the NIST PSTAR database [190]. The energy from the neutron interactions recorded under 8 different angular positions with respect to the boron beam axis is shown in the left plot of Figure 8.30. Clearly visible is the reduction in energy for larger angles. By fitting a complementary error function with an additional background to the region around the spectra's edges, the maximum visible proton recoil energy  $E_{Vis}^{max}$  is determined. The left plot in Figure 8.30 is the spectrum recorded directly in the beam axis. The fit of the high energetic edge (red line) provides  $E_{Vis}^{max} = (5.713 \pm 0.024)$  MeV.

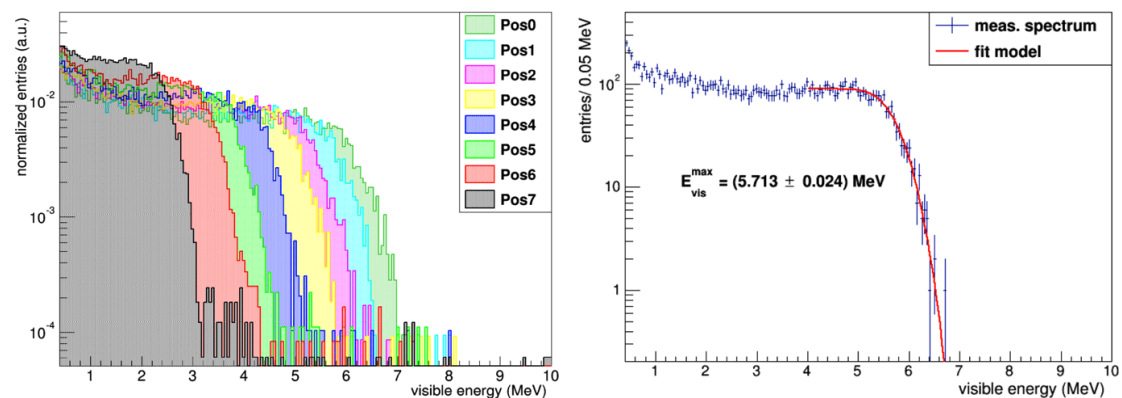


**Figure 8.30: Left:** Spectra of the visible energy  $E_{Vis}$  in the LS detector for recoils of free protons induced by neutron scattering. The colors of the normalized histograms correspond to the position relative to the beam axis. From Pos0 to Pos7 the angle increases and with that neutron energy decreases. **Right:** Recoil spectrum of the free protons in the LS recorded in the beam axis. The red line represents a fit of the high energetic edge by a complementary error function with an additional background. Both plots were taken from [175].

By fitting all the eight spectra, the data points for the maximum visible energies of the neutrons emitted with a defined energy under the angles corresponding to the positions Pos0 to Pos7 were obtained. The uncertainties of the data points are dominated by the systematic errors from the detector calibration and the uncertainties related with the models for the extraction of  $E_n$  and  $E_{Vis}^{max}$ . The fit of these data points with Birk's model (using the assumptions described above) is shown in Figure 8.31. As already mentioned, the quenching effect for protons in the LAB-based scintillator was measured in two beam times at the MLL in September 2013 and February 2014 for a mixture containing 3 g/l PPO and 20mg/l BisMSB. The values for the Birk's factor  $k_B = (0.0103 \pm 0.0005)$  cm/MeV (Sept. 13) and  $k_B = (0.0098 \pm 0.0005)$  cm/MeV (Feb. 2014) are in good agreement [175].

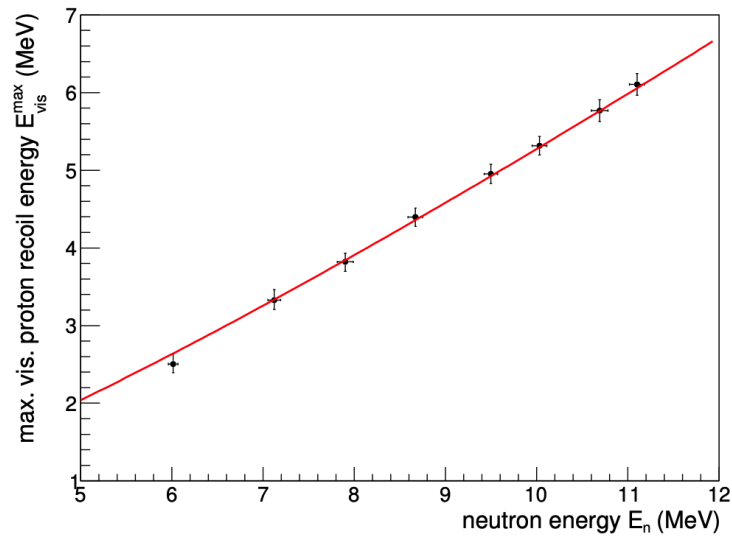


**Figure 8.31:** Data points for the maximum visible proton recoil energy obtained by fitting the high energetic edges of the corresponding recoil spectra with a comprehensive error function containing also a constant background. The red line in the present plot represents a fit of all data points with the Birk's model. The plot was taken from [175] and subsequently modified.

#### 8.4.4 Pulse shape discrimination performance

Since the experimental data contains clearly separated neutron and gamma populations, which can be identified by their characteristic ToF, an evaluation of the PSD performance based on the data set was carried out by V. Zimmer in [175]. A 'tail-to-total' (T2T) method for the discrimination between the pulse shapes of neutrons and gammas was applied. Therefore, the ratio between the integral over the tail region and the total area of the recorded pulses is calculated. The region used for the total pulse integral [ $t_{max} - 50$  ns,  $t_{max} + 350$  ns] and the upper boundary for the tail integral [ $t_{max} + 350$  ns] were fixed with respect to the time  $t_{max}$  when the pulse reaches its maximum. The lower boundary for the integral calculation of the tail was optimized for the LS mixture with 3 g/l PPO and 20 mg/l BisMSB to a value of  $t_{max} + 28.5$  ns, which was found to maximize the PSD performance. The distribution of the T2T-parameter as a function of the visible energy for each event is shown Figure 8.32. The nicely separated bands pointing out the good PSD capabilities of this LAB based scintillator, which is well comparable with JUNO's recipe. In the region between 1.0-1.5 MeV a neutron leakage into the gamma population of  $(0.175 \pm 0.006)$  % was observed for a fixed  $\gamma$  selection efficiency of 99 %. As visible in Figure 8.32, the separation of the bands between 3 MeV to

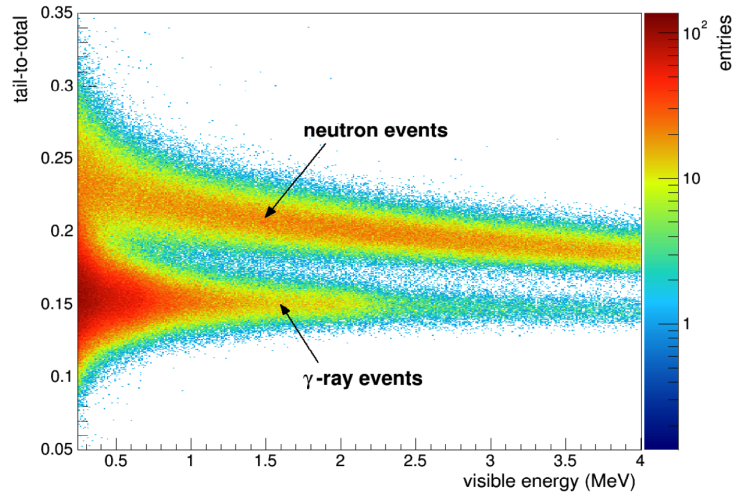


**Figure 8.32:** Two-dimensional distribution of the tail-to-total parameter as a function of the visible energy. The band at lower T2T values around 0.15 corresponds to  $\gamma$ -ray induced events, while the band at higher values correspond to recoils of free protons caused by neutron scattering. Figure taken from [175].

4 MeV is increased. Here the neutron leakage reached a value of  $(0.0116 \pm 0.005) \%$  at a  $\gamma$  detection efficiency of 99 % [175]. So, PSD with LAB-based scintillators comparable to the JUNO LS works even down to low energies. For comparability of the PSD results, the photoelectron yield of the detector was determined. By using the detector resolution extracted from the energy calibration data ( $628 \pm 40$  pe/MeV) were found for the investigated sample in the reflective LS cell. As JUNO aims for photoelectron yields of  $\sim 1100$  pe/MeV very promising PSD capabilities of the CD can be expected. This is especially important for the planned DSNB search in JUNO, since even in the region of interest between  $\sim 10$  MeV and  $\sim 30$  MeV, the faint DSNB signal has to be extracted in the presence of strong backgrounds.

# Chapter 9

## Conclusions

The Jiangmen Underground Neutrino Observatory (JUNO) is a 20 kton multi-purpose liquid scintillator detector currently being built in a dedicated underground laboratory in Jiangmen (PR China). JUNO aims for an unprecedented energy resolution of 3 % at 1 MeV. With these properties, JUNO as the largest liquid scintillator detector ever built will be the world leading experiment in low energy neutrino physics during the upcoming decade. JUNO's main goal is the determination of the neutrino mass ordering at a confidence level of  $3-4\sigma$ . Besides this fundamental aim, JUNO will have a very rich physics program. It includes the measurement of the solar neutrino oscillation parameters, the detection of low-energy neutrinos coming from galactic core-collapse supernovae, the first measurement of the diffuse supernova neutrino background, the detection of neutrinos coming from the sun, the earth and the earth's atmosphere. Moreover, JUNO will be sensitive to searches for nucleon decays and neutrinos resulting from dark matter annihilation in the sun. The present thesis is focused on the development of key technologies for the success of the experiment: the development and characterization of JUNO's high-purity liquid scintillator (LS) and the liquid handling systems for the central detector.

For the JUNO LS, purification using aluminum oxide filtration, vacuum distillation, water extraction and steam stripping is foreseen. The program for the design and construction of these plants with a purification capacity of 10.000 l/h has two stages, a pilot plant testing phase in Daya Bay (Shenzhen, PR China) realizing prototype plants (capacity 100 l/h) and the final plant construction with the LS production phase on the JUNO site in Jiangmen. During the pilot plant phase (2016-2018), all types of LAB purification facilities foreseen for JUNO were successfully set up, commissioned and operated in several testing campaigns. In 2017 a total amount of 24 t of purified LS was produced and filled in one of the DYB antineutrino detectors. In the subsequent data taking campaign the light yield and content of radioactive isotopes in the LS was evaluated. Nevertheless, the goals of the LS production test could be reached only partially. While the optical transparency and light yield of the JUNO LS was measured to comply with the specifications, the

radiopurity levels did not reach the required  $10^{-15}$  g/g for the uranium and thorium concentrations. This discrepancy is at least partially due to certain inadequacies of the used Daya Bay detector and the filling setup. Both were not designed to reach the background levels specified for the JUNO LS.

Based on the experiences from the pilot plant phase, an online monitoring detector, called OSIRIS, for the radiopurity of the LS, placed in the underground liquid scintillator hall between water extraction and steam stripping plant will be realized. The purpose of this detector are measurements of the LS internal radioactivity during the commissioning of the purification plants, LS production phase and the CD filling. According to current Monte Carlo simulations, the design presented in the present thesis, meets the sensitivity requirement to study the LS down to JUNO specifications.

For the liquid handling system of the JUNO detector and the OSIRIS detector, liquid level monitoring systems were developed. Amongst others, a multi-purpose testing facility for hydrostatic pressure sensors with a very flexible readout electronics based on a Raspberry-Pi single board computer was set up. Within the test stand two types of HPSs were investigated. Both showed promising performances and will be considered for usage in JUNO and OSIRIS. To reach highest demands on precision and range, an optical liquid level measurement system based on an IR-laser distance meter was also investigated and a dedicated readout software developed. Irradiation tests with a JUNO Hamamatsu PMT in Tübingen showed compatibility of the laser operation in the presence of running PMTs. The precision and stability of the sensor readings was extensively tested in the laboratory with LAB and distilled water. The distance measurements showed precisions better than  $\pm 10$  mm. In a second test during the decommissioning of the Double Chooz detectors, the sensor demonstrated its usability in a real detector environment. Currently the integration of this type of IR laser level meter into the LHSs of JUNO and OSIRIS is ongoing. As the temperature of the detector liquids is a crucial parameter for the OSIRIS project, a temperature sensor grid based on PT-1000 sensors was developed for the LHS prototype, which is currently under construction at JGU Mainz. A software, allowing live plotting and data storage of the entire sensor grid was developed and will be used in the forthcoming operation of the prototype.

Beyond that, a large volume proportional counter operated as  $\alpha$  spectrometer for radon monitoring in the nitrogen supply system of JUNO was built. The development was carried out in two phases, a demonstrator phase realizing a counter with 4.3 l active volume and a full scale detector with 42.3 l. Moreover, a dedicated electronics for the stabilisation of the supply voltage and the readout of the small detector pulses were developed. The properties of this type of radon monitor were studied extensively and the detection efficiency determined by a Monte Carlo simulation and in experimental investigations. To further reduce the

---

background of micro-discharges observed in the demonstrator phase, pulse shape analysis techniques were successfully applied. The risetime of the detector pulses was identified as powerful particle discrimination parameter. With PSD the demonstrator detector reached a sensitivity for the radon activity of  $\sim(82.5\pm 8.7)$  mBq/m<sup>3</sup> (95 % C.L.) within a 14 h screening of a nitrogen batch. For the final radon monitor, the background from the detector materials was efficiently reduced by careful material selection. All inner detector surfaces made from metal and in contact with the sample have been electropolished. By the usage of a refined suspension of the counting wire and a high voltage feedthrough directly welded on a KF flange the amount of micro-discharges was greatly reduced. Due to the increased homogeneity of the electric field (compared to the demonstrator) excellent energy resolutions of  $(68.6\pm 5.0)$  keV at 5.3 MeV in P10 and  $(278.6\pm 2.2)$  keV at 6 MeV in pure nitrogen gas was reached. Sensitivities for radon decays down to  $(1.75\pm 0.13)$  mBq/m<sup>3</sup> (95 % C.L.) were achieved within 11 h for a batch of P10. In pure N<sub>2</sub>  $(2.07\pm 0.36)$  mBq/m<sup>3</sup> (95 % C.L.) were demonstrated in a 10 h lasting measurement. The low backgrounds and the good sensitivity are pointing the way beyond the usage of the large volume proportional counter as an early warning system for radon contaminations and air leaks in the gas handling system of JUNO. By the usage of a radon trap, quality controls and acceptance tests for JUNO's highly pure gases down to the  $\mu$ Bq/m<sup>3</sup> level are in range. Beyond that, the radon emanation of materials (e.g. the Al<sub>2</sub>O<sub>3</sub> substrate for the LS filtration) might be studied in the future. Since N<sub>2</sub> filled proportional counters are sensitive to thermal and fast neutrons, a use of RaMS as low background neutron spectrometer with PSD based  $\alpha$  suppression is also conceivable.

Moreover, the characterization of liquid scintillator samples in laboratory measurements using self-designed experiments was a central part of this thesis as the precise knowledge of the scintillator properties is crucial for the interpretation of JUNO's data. For instance, it is essential to know the typical scintillation quenching and pulse shape for different particle interactions. The pulse shape discrimination (PSD) performance is closely related to differences in the time spectrum of the photon emission of the LS for different particle species. The precise knowledge of the fluorescence time profile is a necessity for the implementation of a realistic scintillation model in the global JUNO simulation framework. Furthermore, this knowledge is crucial for event position reconstruction and tuning of pulse shape analysis algorithms. Beyond that, the fluorescence decay times are highly affecting JUNO's sensitivity in proton decay searches. To study the fluorescence time profile for gamma and neutron interactions an experimental setup exploiting the single photon technique was developed. In two beamtimes at the neutron scattering facility of the Maier-Leibnitz-Laboratorium a huge data set was gained. The analysis showed a clear separation of the fluorescence time profiles of neutrons and gamma

radiation. The values for the shortest decay time component are in well agreement with phenomenological predictions. The final results will refine the global JUNO simulation framework. Beyond that, the quenching factor of protons (induced by neutron scattering) in a LAB based LS with a recipe similar to the one foreseen for JUNO was determined to be  $k_B = (0.0098 \pm 0.0005)$  cm/MeV. Moreover, with this detector, featuring a photoelectron yield of  $628 \pm 40$  pe/MeV, the PSD performance using the tail-to-total technique was evaluated. The promising results of these measurements performed by V. Zimmer in 2014 are well compatible with the fluorescence time profile measurements.

Reactor neutrinos are detected via the inverse beta decay (IBD) of a proton in the LS. In this reaction a positron and a neutron are generated. The formation of positronium changes the time distribution of the photon emission, which affects positron reconstruction algorithms and allows the application of PSD to distinguish electron from positron events. In order to determine the lifetime and formation probability of ortho-positronium in the liquid scintillator, a novel experimental setup with positrons from a  $^{22}\text{Na}$  source was developed in a master's thesis closely related to the present PhD project. With this setup the effective ortho-positronium lifetime in LAB with 3 g/l PPO and 15 mg/l BisMSB was determined to be  $(2.98 \pm 0.05)$  ns. The corresponding formation probability was found to be  $(44 \pm 3)$  %. Nonetheless, the background of backscattered  $\gamma$  radiation (mainly 1275 keV  $\gamma$ s) limited the precision especially for the investigation on the formation probability. To address these problems, the setup was substantially upgraded with faster detectors reaching a time resolution of the  $\gamma$  detectors of  $\sigma = (303.6 \pm 1.2)$  ns. As observed in first test measurements, the background especially in the 1275 keV gamma plateau was greatly reduced. Forthcoming data taking runs of the experiment are expected to increase the precision of the formation probability value significantly.

Beyond these properties, the attenuation length at the emission wavelengths of the LS is an important parameter and has to be well known to allow the reconstruction an event's position and energy in the detector precisely. Moreover, the attenuation length has a direct impact on the feasibility of a detector of JUNO's diameter. Therefore, the PALM setup, allowing measurements of the attenuation lengths of highly transparent liquids at a percent level, was developed in the frame of another PhD project. In PALM several LAB samples were investigated. The measurements of unpurified and purified LAB samples showed the great improvement of the solvents transparency achieved by cycling them through the Daya Bay pilot plants. The attenuation length reaches  $(28.07 \pm 2.94)$  m at a wavelength of 430 nm.

In summary, all data obtained on the LS indicate its excellent properties. Moreover, they are pointing the way to the realization of the JUNO detector with its unprecedented dimensions and energy resolution.

# Bibliography

- [1] J. Chadwick, *Intensitätsverteilung im magnetischen Spektrum der Betastrahlen von Radium B+C*, Verh. der Deutschen Physikalischen Ges. **16**, 383 (1914)
- [2] C.D. Ellis and W.A. Wooster, *The Average Energy of Disintegration of Radium E*, Proc. Roy. Soc. (A) **117**, 109 (1927)
- [3] L. Meitner and W. Orthmann, *Über eine absolute Bestimmung der Energie der primären  $\beta$ -Strahlen von Radium E*, Z. Phys. **60**, 143–155 (1930)
- [4] W. Pauli, *Liebe Radioaktive Damen und Herren*, Offener Brief an die Gruppe der Radioaktiven bei der Gauvereins-Tagung zu Tübingen. (1930)
- [5] G. W. Rodeback and J. S. Allen, *Neutrino Recoils Following the Capture of Orbital Electrons in  $A^{37}$* , Phys. Rev. **86**, 446 (1952)
- [6] A. H. Snell and F. Pleasonton, *Spectrometry of Recoils from Neutrino Emission in Argon-37*, Phys. Rev. **97**, 246 (1955)
- [7] F. Reines and C. L. Cowan, Jr., *Detection of the Free Neutrino*, Phys. Rev. **92**, 830 (1953)
- [8] C. L. Cowan, Jr. et al., *Detection of the Free Neutrino: a Confirmation*, Science **124**, 103 (1956)
- [9] C. S. Wu et al., *Experimental Test of Parity Conservation in Beta Decay*, Phys. Rev. **105**, 1413 (1957)
- [10] M. Goldhaber, L. Grodzins, and A. W. Sunyar, *Helicity of Neutrinos*, Phys. Rev. **109**, 1015 (1958)
- [11] M. Schwartz, *Feasibility of Using High-Energy Neutrinos to Study the Weak Interactions*, Phys. Rev. Lett. **4**, 306 (1960)

- 
- [12] G. Danby et al., *Observation of High-Energy Neutrino Reactions and the Existence of Two Kinds of Neutrinos*, Phys. Rev. Lett. **9**, 36 (1962)
- [13] R. Davis, Jr., *Solar Neutrinos. II. Experimental*, Phys. Rev. Lett. **12**, 303 (1964)
- [14] R. Davis, Jr., *A review of the Homestake Solar Neutrino Experiment*, Prog. Part. Nucl. Phys. **32**, 12 (1994)
- [15] R. Davis, Jr., *A review of measurements of the solar neutrino flux and their variation*, Nucl. Phys. B (Proc. Suppl.) **48**, 284 (1996)
- [16] B. T. Cleveland et al., *Measurement of the solar electron neutrino flux with the Homestake chlorine detector*, Astrophys. J. **496**, 505 (1998)
- [17] W. Hampel et al., *GALLEX solar neutrino observations: Results for GALLEX IV*, Phys.Lett. B **447**, 127 (1999)
- [18] V. N. Gavrin for the SAGE collaboration, *Measurement of the solar neutrino capture rate in Sage*, Nucl. Phys. B (Proc. Suppl.) **118**, 39 (2003)
- [19] J. N. Abdurashitov for the SAGE collaboration, *Measurement of the solar neutrino capture rate with gallium metal. III. Results for the 2002–2007 data-taking period*, Phys. Rev. C **80**, 015807 (2009)
- [20] DONUT Collaboration, K. Kodama et al., *Observation of tau neutrino interactions*, Phys. Lett. B **504**, 218 (2001)
- [21] The ALEPH Collaboration, the DELPHI Collaboration, the L3 Collaboration, the OPAL Collaboration, the SLD Collaboration, the LEP Electroweak Working Group, the SLD electroweak, heavy flavour groups, *Precision Electroweak Measurements on the Z Resonance*, Phys. Rept. **427**, 257 (2006)
- [22] The Super-Kamiokande Collaboration, Y. Fukuda et al, *Precision Electroweak Measurements on the Z Resonance*, Phys. Rev. Lett. **81**, 1562 (1998)
- [23] SNO Collaboration, *Direct Evidence for Neutrino Flavor Transformation from Neutral-Current Interactions in the Sudbury Neutrino Observatory*, Phys. Rev. Lett. **89**, 011301 (2002)
- [24] KamLAND Collaboration, *First Results from KamLAND: Evidence for Reactor Anti-Neutrino Disappearance*, Phys. Rev. Lett. **90**, 021802 (2003)
- [25] G. Alimonti et al., *The Borexino detector at the Laboratori Nazionali del Gran Sasso*, Nucl. Instrum. Meth. A **600**, 568 (2009)

- 
- [26] The Borexino Collaboration, *Comprehensive measurement of pp-chain solar neutrinos*, Nature **562**, 505 (2018)
- [27] M. G. Aartsen et al. (IceCube Collaboration), *First Observation of PeV-Energy Neutrinos with IceCube*, Phys. Rev. Lett. **111**, 021103 (2013)
- [28] IceCube Collaboration, *Neutrino emission from the direction of the blazar TXS 0506+056 prior to the IceCube-170922A alert*, Science **361**, 147 (2018)
- [29] D. Akimov et al., *Observation of coherent elastic neutrino-nucleus scattering*, Science **357**, 1123 (2017)
- [30] J. Hakenmüller et al., *Neutron-induced background in the CONUS experiment*, arXiv: 1903.09269 (2019)
- [31] R. Strauss et al., *The  $\nu$ -cleus experiment: A gram-scale fiducial-volume cryogenic detector for the first detection of coherent neutrino-nucleus scattering*, European Physical Journal C **77(8)**, 506 (2017)
- [32] The JUNO Collaboration, *JUNO Conceptual Design Report*, arXiv: 1507.07166v2 (2015)
- [33] S. Bilenky, *The Neutrino. History of a unique particle*, European Physical Journal **H38**, 345 (2013)
- [34] K. A. Olive et al. (Particle Data Group), Chin. Phys. C **38**, 090001 (2014)
- [35] B. Povh et al., *Teilchen und Kerne*, Springer Berlin Heidelberg, Wiesbaden (2009)
- [36] N. Schmitz, *Teilchen und Kerne*, Teubner Studienbücher, Stuttgart (1997)
- [37] Y. Fukuda et al., *Evidence for Oscillation of Atmospheric Neutrinos*, Phys. Rev. Lett. **81**, 1562 (1998)
- [38] Q. R. Ahmad et al., *Direct Evidence for Neutrino Flavor Transformation from Neutral-Current Interactions in the Sudbury Neutrino Observatory*, Phys. Rev. Lett. **89**, 011301 (2002)
- [39] K. Eguchi et al., *First Results from KamLAND: Evidence for Reactor Anti-neutrino Disappearance*, Phys. Rev. Lett. **90**, 021802 (2003)
- [40] S. M. Bilenky et al., *On Oscillations of Neutrinos with Dirac and Majorana Masses*, Phys. Lett. B **94**, 495 (1980)

- 
- [41] J. Oberauer and L. Oberauer, *Neutrino physics*, Springer Spektrum, Berlin (2019)
- [42] M. Zralek, *From Kaons to Neutrinos: Quantum Mechanics of Particle Oscillations*, Acta Phys. Polon. B **29**, 3925 (1998)
- [43] S. M. Bilenky, C. Giunti, W. Grimus, *Phenomenology of Neutrino Oscillations*, Prog. Part. Nucl. Phys. **43**, 1 (1999)
- [44] B. Kayser, *Neutrinos in Particle Physics, Astrophysics and Cosmology*, CRC Press, Boca Raton (2009)
- [45] Particle Data Group, C. Amsler et al., *The Review of Particle Physics*, Phys. Lett. B **667**, 1 (2008)
- [46] K. Abe et al., *Search for CP violation in Neutrino and Antineutrino Oscillations by the T2K experiment with  $2.2 \times 10^{21}$  protons on target*, Phys. Rev. Lett. **121**, 171802 (2018)
- [47] The DUNE Collaboration, *The DUNE Far Detector Interim Design Report Volume 1: Physics, Technology and Strategies*, arXiv:1807.10334 (2018)
- [48] L. Wolfenstein, *Neutrino oscillations in matter*, Phys. Rev. D **17**, 2369 (1978)
- [49] B. Kayser, *Neutrino Oscillation Phenomenology*, arXiv: 0804.1121v3 (2008)
- [50] E. K. Akhmedov, R. Johansson, M. Lindner, T. Ohlsson and T. Schwetz, *Series expansion for three flavor neutrino oscillation probabilities in matter*, JHEP **0404**, 078 (2004)
- [51] Super-Kamiokande Collaboration, J. Hosaka et al., *Solar neutrino measurements in Super-Kamiokande-I*, Phys.Rev. **D73**, 112001 (2006)
- [52] SNO Collaboration, B. Aharmim et al., *Electron energy spectra, fluxes, and day- night asymmetries of  $^8\text{B}$  solar neutrinos from measurements with NaCl dissolved in the heavy-water detector at the Sudbury Neutrino Observatory*, Phys.Rev. **C72**, 055502 (2005)
- [53] J. Hewett et al., *Fundamental Physics at the Intensity Frontier*, arXiv:1205.2671 (2012)
- [54] X. Qian and P. Vogel, *Neutrino Mass Hierarchy*, arXiv:1505.01891v3 (2015)
- [55] IceCube-Gen2 Collaboration, T. Birkenfeld et. al., *Combined sensitivity to the neutrino mass ordering with JUNO and PINGU/IceCube Upgrade*, arXiv:1911.06745 (2019)

- 
- [56] S. Bilenky, *On the phenomenology of neutrino oscillations in vacuum*, arxiv: 1208.2497 (2012)
- [57] S. Bilenky et al., *Constraints on  $|U_{e3}|^2$  from a three-neutrino oscillation analysis of the CHOOZ data*, Physics Letters B **538**, 77 (2002)
- [58] H. Schlattl, *Can three flavor oscillations solve the solar neutrino problem?*, Phys. Rev. **D64**, 013009 (2001)
- [59] The JUNO Collaboration, *Neutrino Physics with JUNO*, J. Phys. **G 43**, 030401 (2016)
- [60] Th. Mueller et al., *Improved Predictions of Reactor Antineutrino Spectra*, Phys.Rev. **C 83**, 054615 (2011)
- [61] I. Esteban et al., *Global analysis of three-flavour neutrino oscillations: synergies and tensions in the determination of  $\theta_{23}$ ,  $\delta_{CP}$ , and the mass ordering*, JHEP **01**, 106 (2019)
- [62] M. Sisti on behalf of the JUNO Collaboration, *Physics prospects of the JUNO experiment*, TAUP2019 Proceedings, IOP Conference Series, submitted for journal review (Nov. 2019)
- [63] J. Sawatzki, PhD Thesis in preparation, Technical University of Munich (Nov. 2019)
- [64] A. D. Sakharov, *Violation of CP Invariance, C asymmetry, and baryon asymmetry of the universe*, JETP Lett. **5**, 24 (1967)
- [65] T. Marrodan Undagoitia et al., *Search for the proton decay  $p \rightarrow K^+ + \bar{\nu}$  in the large liquid scintillator low energy neutrino astronomy detector LENA*, Phys. Rev. D **72**, 075014 (2005)
- [66] H. Steiger on behalf of the JUNO Collaboration, *Design and Status of JUNO*, Topics in Astroparticle and Underground Physics (Toyama 2019), Journal of Physics: Conference Series (JPCS), to be published (2019)
- [67] T. Sterr, PhD Thesis in preparation, Eberhard Karls Universität Tübingen (2019)
- [68] H. Zhang et al., *Tested Performance of JUNO 20-inch PMTs*, Topics in Astroparticle and Underground Physics (Toyama 2019), Journal of Physics: Conference Series (JPCS), to be published (2019)

- [69] T. Förster, *Transfer Mechanisms of Electronic Excitation*, Discuss. Faraday Soc. **27**, 7 (1959)
- [70] J. B. Birks, *The Theory and Practice of Scintillation Counting*, Pergamon Press, First Edition (1964)
- [71] D. L. Horrocks, *Application of Liquid Scintillation Counting*, Academic Press (1974)
- [72] T. Marrodan Undagoitia, *Measurement of Light Emission in Organic Liquid Scintillators and Studies Towards the Search for Proton Decay in the Future Large-Scale Detector LENA*, PhD thesis, Technische Universität München (2008)
- [73] I. B. Berlman, *Handbook of Fluorescence Spectra of Aromatic Molecules*, Academic Press, New York and London (1971)
- [74] Y. Ding et al., *A new gadolinium-loaded liquid scintillator for reactor neutrino detection*, Nucl. Instrum. Methods Phys. Res. Sect. Accel. Spectrometers Detect. Assoc. Equip. **548**, 238–243 (2008)
- [75] P. Lombardi et al., *Distillation and stripping pilot plants for the JUNO neutrino detector: design, operations and reliability*, NIM-A **925**, 6 (2019)
- [76] R. J. Ford for the SNO+ Collaboration, *A scintillator purification plant and fluid handling system for SNO+*, AIP Conference Proceedings **1672**, 080003 (2015)
- [77] The Daya Bay Collaboration, *A side-by-side comparison of Daya Bay anti-neutrino detectors*, NIM-A **685**, 78 (2012)
- [78] Jun Cao and Kam-Biu Luk, *An overview of the Daya Bay Reactor Neutrino Experiment*, arXiv:1605.01502 (2016)
- [79] D. Adey et al., *Optimizing the contents of the JUNO liquid scintillator at Daya Bay*, in preparation, under collaboration internal review (2019)
- [80] Boxiang Yu on behalf of the JUNO Collaboration, *Liquid Scintillator purification study for JUNO*, Contribution to the International Conference on Topics in Astroparticle and Underground Physics TAUP2017 (2017)
- [81] Q.-j. Li et al., *Front-End Electronics System of PMT Readout for the Daya Bay Reactor Neutrino Experiment*, Proceedings: IEEE Nuclear Science Symposium and Medical Imaging Conference: Orlando, Florida 1821–1823 (2009)

- 
- [82] Xiaofeng Zhang, Wenjie Wu and Zeyuan Yu, *Radioactive background analysis during LS replacement at Daya Bay*, Talk at the LS Workshop in the Frame of the 10th Juno Collaboration Meeting, IHEP, Beijing (2017)
- [83] A. Formozov and Emanuela Meroni, *Current status of the analysis of JUNO LS at Daya Bay*, Talk at the LS Workshop in the Frame of the 10th Juno Collaboration Meeting, IHEP, Beijing (2017)
- [84] Xiaofeng Zhang and Zeyuan Yu, *Radioactive Background Analysis in Liquid Scintillator Replacement (Stripping Test)*, Talk at the LS Workshop in the Frame of the 11th Juno Collaboration Meeting, Nanjing (2018)
- [85] S. Franke, *Optical Purification Study of the LAB-based Liquid Scintillator for the JUNO Experiment*, PhD Thesis, Technische Universität München (2019)
- [86] Ch. Genster, H. Steiger, M. Wurm et al., *OSIRIS - Preliminary Design*, unpublished, JUNO internal document (2018)
- [87] R. Othegraven, *OSIRIS - Collection of CAD Models*, unpublished, JUNO internal document (2019)
- [88] R. Wang, P. Zhang, et al., *Water pool lining bidding and CD truss foot sealing*, Talk at the CD Workshop in the Frame of the 12th Juno Collaboration Meeting, Beijing (2018)
- [89] M. Wurm, *The Status of the OSIRIS Detector Project*, Talk at the DFG Research Unit JUNO Retreat in Munich (2019)
- [90] H. Steiger, *OSIRIS: Introduction and Mechanics*, Talk at the JUNO Liquid Scintillator Purification Workshop at the LNGS (2019)
- [91] P. Hackspacher, PhD Thesis in preparation, JGU Mainz (2019)
- [92] H. Steiger, *Mechanical Construction and Liquid Handling System of the OSIRIS (Online Scintillator Internal Radioactivity Investigation System) Pre-detector Facility*, Talk at the DPG-Frühjahrstagung in Aachen (2019)
- [93] M. Wurm, *OSIRIS: Overview and Operations*, Talk at the 13th Juno Collaboration Meeting, Shanghai (2019)
- [94] P. Pfahler, *OSIRIS: Drawings of the Liquid and Gas Handling System*, unpublished, JUNO internal document (2019)
- [95] P. Lombardi, *Leakage work related with the LS production*, Talk in the frame of the monthly JUNO phone conferences (2019)

- [96] F. Gao, T. Kuhlbusch, J. Steinmann, C. Vollbrecht and C. Wysotzki, *OSIRIS Electronics Hardware status report*, Talk at the DFG Research Unit JUNO Retreat in Munich (2019)
- [97] A. Zambanini, *VULCAN Readout chip: Test Strategy for Low Failure Rates and Status of a Highly Integrated Readout Chip for PMTs in JUNO*, Contribution to TWEPP Topical Workshop on Electronics for Particle Physics (2018)
- [98] XILINX, *Zynq-7000 SoC Data Sheet: Overview*, [https://www.xilinx.com/support/documentation/data\\_sheets/ds190-Zynq-7000-Overview.pdf](https://www.xilinx.com/support/documentation/data_sheets/ds190-Zynq-7000-Overview.pdf) (2018)
- [99] C. Genster, *Software and hardware development for the next-generation liquid scintillator detectors JUNO and OSIRIS*, PhD Thesis, RWTH Aachen (2019)
- [100] J. Liu et al, *Automated calibration system for a high-precision measurement of neutrino mixing angle  $\theta_{13}$  with the Daya Bay antineutrino detectors*, NIM A **750**, 19–37 (2013)
- [101] J. Zhao, *Requirement to CD radioactive background*, unpublished, JUNO internal document (2017)
- [102] JUNO Collaboration, *JUNO Material Radioactivity Database*, unpublished, JUNO internal document (2019)
- [103] G. Feldman and R. Cousins, *A Unified approach to the classical statistical analysis of small signals*, Phys. Rev. **D57**, 3873–3889 (1998)
- [104] J. J. Gomez-Cadenas et al., *Sense and sensitivity of double beta decay experiments*, JCAP **1106**, 7 (2011)
- [105] J. Ling et al., *JUNO Filling Overflow and Circulation (FOC) System Control*, Talk in the frame of the FOC Pre-Bidding Review, 13th Collaboration Meeting in Shanghai, JUNO internal document (2019)
- [106] SISEN Automation, *Homepage*, <http://www.sisenchina.com> (2019)
- [107] Swagelok Deutschland, *Katalog: Manometer Industrieausführung*, <https://www.swagelok.de/downloads/webcatalogs/de/MS-02-170.pdf> (2019)
- [108] MICROCHIP, *2.7V 4-Channel/8-Channel 10-Bit A/D Converters with SPI Serial Interface*, MCP3004/MCP3008 Documentation 40 (2013)
- [109] STATRON, *Voltage Regulator Type 3250.1 Manual* (2019)

- 
- [110] The Raspberry Pi Foundation, *Raspberry Pi Documentation*, <https://www.raspberrypi.org/documentation/hardware/raspberrypi/> (2019)
- [111] M. Walter, *Construction of a Test Setup for the Characterization of Pressure Sensors on their Suitability for the JUNO Neutrino Experiment*, Bachelor's Thesis, Technische Universität München (2018)
- [112] M. Hoffmann, *Low-background gamma spectroscopy for the neutrino oscillation experiment DOUBLE CHOOZ*, Diplomas Thesis, Technische Universität München (2007)
- [113] M. Hoffmann, *Liquid Scintillators and Liquid Rare Gases for Particle Detectors*, PhD Thesis, Technische Universität München (2012)
- [114] M. Franke, *The neutrino experiment Double Chooz and data analysis with the near detector*, PhD Thesis, Technische Universität München (2016)
- [115] MEL-Mikroelektronik, *M10L/100 Laser Abstands-Sensor*, <http://new.melsensor.com/subversion/mel/Optische-Sensoren/pdf/DB-M10.pdf> (2019)
- [116] Laser Technology Inc, *TruSense S300 Series, User's Manual*, <https://www.lasertech.com/filedownloads/TruSense-S300-Documentation.zip> (2019)
- [117] Laser Technology Inc, *Homepage, TruSense Laser Sensors*, <https://www.lasertech.com> (2019)
- [118] A. Tietzsch, PhD Thesis, Eberhard Karls Universität Tübingen (2020)
- [119] T. Sterr, *Aufbau eines PMT Teststand-Prototypen für das JUNO-Projekt*, Bachelor's Thesis, Eberhard Karls Universität Tübingen (2016)
- [120] CAEN - Tools for Discovery, *Homepage for Modular Pulse Processing Electronics, Digitizers, V1742*, <https://www.caen.it/products/v1742/> (2019)
- [121] CAEN - Tools for Discovery, *Homepage for Modular Pulse Processing Electronics, Analog, Discriminators, V895*, <https://www.caen.it/products/v895/> (2019)
- [122] The Qt Company, *Qt Documentation*, <https://doc.qt.io/qt-5/qtgui-index.html> (2019)
- [123] Laser Technology Inc, *TruSense S200 Series, User's Manual*, <https://www.lasertech.com/filedownloads/TruSense-S200-Documentation.zip> (2018)
- [124] Otom Group GmbH, *Homepage and online shop for PT-1000 sensors, (Sensorshop24)*, <https://www.sensorshop24.de/temperaturfuehler/kabelfuehler/kabelfuehler-lebensmittelfuehler-mit-ptfe-leitung/> (2019)

- [125] Otom Group GmbH, *Homepage and online shop for active temperature sensors*, (*Sensorshop24*), <https://www.sensorshop24.de/temperaturfuehler/kabelfuehler/kabelfuehler-aktiv-mit-0-10v-oder-4-20ma/kabelfuehler-bis-260-c-aktiv-0-10v/a-97066/> (2019)
- [126] Nuclear Data Section, Vienna International Centre, Austria, *Live Chart of Nuclides*, <https://www-nds.iaea.org/relnsd/vcharthtml/VChartHTML.html> (2020)
- [127] KamLAND Collaboration (T. Araki (Tohoku U.) et al.), *Measurement of neutrino oscillation with KamLAND: Evidence of spectral distortion*, *Phys. Rev. Lett.* **94**, 081801 (2004)
- [128] Guangpeng An, *High pure nitrogen system PBR*, unpublished, JUNO internal document (2019)
- [129] Edwards, *nXDS Dry Scroll Pumps*, <https://www.edwardsvacuum.com/content/dam/brands/edwards-vacuum/edwards-website-assets/high-vacuum/documents/Edwards-nXDS-Dry-Scroll-Pump-Brochure-3601-0088-01.pdf> (2019)
- [130] P. Landgraf, *Development of a Radon Monitoring in gaseous Nitrogen used for the Filling of the Central Detector of JUNO*, Master's Thesis, Technische Universität München (2017)
- [131] ORTEC, *142PC brochure*, <https://www.ortec-online.com/-/media/ametektortec/brochures/142pc.pdf> (2019)
- [132] ORTEC, *556 and 556H brochure*, <https://www.ortec-online.com/-/media/ametektortec/brochures/556-556h.pdf> (2019)
- [133] CAEN - Tools for Discovery, *A483, HV Bidirectional Passive HV Filter, Product Page*, <https://www.caen.it/products/a483/> (2019)
- [134] ORTEC, *572A brochure*, <https://www.ortec-online.com/-/media/ametektortec/brochures/572a.pdf> (2019)
- [135] ORTEC, *EASY-NIM 928 Suite brochure*, <https://www.ortec-online.com/-/media/ametektortec/brochures/928.pdf> (2019)
- [136] Agilent Technologies, *Agilent U1065A Acqiris High-Speed cPCI Digitizers*, <https://literature.cdn.keysight.com/litweb/pdf/5989-7443EN.pdf?id=1306645> (2020)
- [137] A. Gardanow, *Detector Characterization and Pulse Shape Analysis for a Prototype Large Volume Proportional Counter for the Radon Monitoring in Gaseous Nitrogen in the JUNO Experiment and the OSIRIS Predetector Facility*, Bachelor's Thesis, Technische Universität München (2018)

- [138] T. J. Langford et al., *Event Identification in  $^3\text{He}$  Proportional Counters Using Risetime Discrimination*, Nucl. Instrum. Meth. A **717**, 51 (2013)
- [139] G. F. Knoll, *Radiation Detection and Measurement*, 2nd edition (1989)
- [140] L. Niedermeier et al., *Scintillator Purification by Silica Gel Chromatography in the Context of Low Counting Rate Experiments*, Proc. 8, Conf. Astroparticle, Particle, Space Physics, Detectors and Medical Physics Applications, World Scientific (2003)
- [141] P. Hackspacher, *Studies of Liquid Quenching Effects in Liquid Scintillators and Parameter Determination of the Buffer and Veto Fluids of the Double Chooz Near Detector*, Master's Thesis, Technische Universität München (2014)
- [142] T. Mannel, *Low-level radioactivity techniques for the neutrino oscillation Experiment Double Chooz*, Master's Thesis, Technische Universität München (2013)
- [143] PerkinElmer, Inc., *LAMBDA UV/Vis and UV/Vis/NIR Spectrophotometers*, [https://www.perkinelmer.com/lab-solutions/resources/docs/BR0\\_LAMBDA8509501050.pdf](https://www.perkinelmer.com/lab-solutions/resources/docs/BR0_LAMBDA8509501050.pdf) (2020)
- [144] Alfa Aesar, *QuadraSil, Product Flyer*, [http://www.reakor.ru/alfa/Product\\_Flyers/QuadraSil.pdf](http://www.reakor.ru/alfa/Product_Flyers/QuadraSil.pdf) (2020)
- [145] S. Prummer, *Precision Measurements of Optical Attenuation Lengths of LAB for the JUNO Neutrino Experiment*, Master's Thesis, Technische Universität München (2015)
- [146] S. Franke, *Optical Purification Study of the LAB-based Liquid Scintillator for the JUNO Experiment*, PhD Thesis, Technische Universität München (2019)
- [147] J. Eck, *Wavelength dependent measurements of the attenuation length in liquid scintillators with CELLPALS*, Bachelor's Thesis, Eberhard Karls Universität Tübingen (2019)
- [148] M. Deutsch, *Evidence for the formation of positronium in gases*, Phys. Rev. **82**, 455 (1951)
- [149] A. H. Al-Ramadhan, D. W. Gidley, *New precision measurement of the decay rate of singlet positronium*, Phys. Rev. Lett. **72**, 1632 (1994)
- [150] J. S. Nico, D. W. Gidley, et al., *Precision measurement of the ortho-positronium decay rate using the vacuum technique*, Phys. Rev. Lett. **65**, 1344 (1990)

- [151] S. J. Tao, *Positronium annihilation in molecular substances*, J. Chem. Phys. **56** (11), 5499 (1972)
- [152] S. J. Tao, *Ortho-Parapositronium quenching by paramagnetic molecules and ions*, Phys. Rev. **110**, 1355 (1958)
- [153] D. Franco, G. Consolati, et al, *Positronium signature in organic liquid scintillators for neutrino experiments*, Phys. Rev. C **83**, 015504 (2011)
- [154] G. Bellini et al, *Final results of Borexino Phase-I on low energy solar neutrino spectroscopy*, Phys. Rev. D **89** (11), 112007 (2014)
- [155] M. Schwarz, *First Measurements of Lifetime and Formation Probability of Orthopositronium in the JUNO Liquid Scintillator*, Master's Thesis, Technische Universität München (2017)
- [156] M. Schwarz et al, *Measurements of the lifetime of orthopositronium in the LAB-based liquid scintillator of JUNO*, Nucl. Instrum. Meth. A **922**, 64 (2019)
- [157] O. Dötterl, *A New Experimental Setup and Background Reduction for the PoLiDe Experiment*, Master's Thesis, Technische Universität München (2019)
- [158] Compagnie de Saint-Gobain, *Plastic scintillators BC-400, BC-404, BC-408, BC-412, BC-416 Data Sheets*, <http://www.crystals.saint-gobain.com/sites/imdf.crystals.com/files/documents/sgc-bc400-404-408-412-416-data-sheet.pdf> (2020)
- [159] ET Enterprises, *9821B series data sheet*, [http://et-enterprises.com/images/data\\_sheets/9821B.pdf](http://et-enterprises.com/images/data_sheets/9821B.pdf) (2020)
- [160] ET Enterprises, *9112B series data sheet*, [http://et-enterprises.com/images/data\\_sheets/9112B.pdf](http://et-enterprises.com/images/data_sheets/9112B.pdf) (2020)
- [161] CAEN - Tools for Discovery, *N979, 16Ch NIM fast Amplifier, Product Page*, <https://www.caen.it/products/n979/> (2020)
- [162] ORTEC, *Model CF8000, Octal Constant Fraction Discriminator, Operating and Service Manual*, <https://www.ortec-online.com/-/media/ametektortec/manuals/cf8000-mn1.pdf> (2020)
- [163] Y. P. Cheng, L. J. Wen et al.,  *$e^+/e^-$  discrimination in liquid scintillator and its usage to suppress  $^8\text{He}/^9\text{Li}$  backgrounds*, Chin. Phys. C **41** (1), 016101 (2017)

- [164] D. Franco, G. Consolati et al., *Positronium signature in organic liquid scintillators for neutrino experiments*, Phys. Rev. C **83**, 015504 (2011)
- [165] Saint-Gobain Ceramics and Plastics, Inc., *BC-422Q Ultra-Fast Timing Plastic Scintillators*, <https://www.crystals.saint-gobain.com/sites/imdf.crystals.com/files/documents/bc422q-data-sheet.pdf> (2016)
- [166] ADIT Electron Tubes, *L25D19 series data sheet*, [http://aditelectrontubes.com/images/data\\_sheets/L25D19.pdf](http://aditelectrontubes.com/images/data_sheets/L25D19.pdf) (2020)
- [167] CAEN - Tools for Discovery, *N978, 4 Channel Variable Gain Fast Amplifier, Product Page*, <https://www.caen.it/products/n978/> (2020)
- [168] CAEN - Tools for Discovery, *N844, 8 Channel Low Threshold Discriminator, Product Page*, <https://www.caen.it/products/n844/> (2020)
- [169] CAEN - Tools for Discovery, *N455, Quad Coincidence Logic Unit, Product Page*, <https://www.caen.it/products/n455/> (2020)
- [170] CAEN - Tools for Discovery, *N1145, Quad Scaler And Preset Counter / Timer, Product Page*, <https://www.caen.it/products/n1145/> (2020)
- [171] Paul Scherrer Institute, *DRS4 Evaluation Board User's Manual, Board Revision 5.1*, [https://www.psi.ch/sites/default/files/import/drs/DocumentationEN/manual\\_rev51.pdf](https://www.psi.ch/sites/default/files/import/drs/DocumentationEN/manual_rev51.pdf) (2018)
- [172] P. Lombardi et al., *Decay time and pulse shape discrimination of liquid scintillators based on novel solvents*, Nucl. Instrum. Meth. A **701**, 133 (2013)
- [173] J. Franck and E. G. Dymond, *Elementary Processes of Photochemical Reactions*, Trans. Faraday Soc. **21**, 536 (1926)
- [174] E. Condon, *A Theory of Intensity Distribution in Band Systems*, Phys. Rev. **28**, 1182 (1926)
- [175] V. Zimmer, *Studies of Proton Recoils in Organic Liquid Scintillators Used in Present and Future Neutrino Experiments*, PhD Thesis, Technische Universität München (2015)
- [176] C. Buck, F. X. Hartmann, D. Motta and S. Schönert, *Energy transfer and light yield properties of a new highly loaded indium(III)  $\beta$ -diketonate organic scintillator system*, Chem. Phys. Lett. **435**, 452 (2007)
- [177] T. Marrodan et al., *Fluorescence decay-time constants in organic liquid scintillators*, Rev. Sci. Instr. **80**, 043301 (2009)

- [178] I. B. Berlman, *Efficiency of Energy Transfer in a Solution of PPO in Xylene*, J. Chem. Phys. **33**, 1124 (1960)
- [179] I. B. Berlman, *Luminescence in a Scintillation Solution Excited by  $\alpha$  and  $\beta$  Particles and Related Studies in Quenching*, J. Chem. Phys. **34**, 598 (1961)
- [180] Günther Dollinger and Thomas Faestermann, *Physics at the Munich Tandem Accelerator Laboratory*, <https://www.bl.physik.uni-muenchen.de/forschung/laboratoryportrait.pdf> (2018)
- [181] MLL, Maier-Leibnitz-Laboratorium, *Besucherinformation, Strahlführung*, <https://www.bl.physik.uni-muenchen.de/tandem/besucherinfo/strahlfuehrung/index.html> (2020)
- [182] M. Drosig, *Novel monoenergetic neutron sources for energies between 2.5 and 25.7 MeV*, Nuclear Instruments and Methods in Physics Research A **254**, 466 (1987)
- [183] T. Jagemann, *Measurement of the Scintillation Light Quenching for Nuclear Recoils induced by Neutron Scattering in Detectors for Dark Matter Particles*, PhD Thesis, Technische Universität München (2004)
- [184] G. Ranucci et al., *Scintillation decay time and pulse shape discrimination of binary organic liquid scintillators for the Borexino detector*, Nucl. Instrum. Meth. A **350**, 338 (1994)
- [185] H. Steiger, M. R. Stock, L. Oberauer et al., *Fluorescence time profile studies for JUNO's liquid scintillator with a pulsed neutron beam and gamma radiation*, in preparation (2020)
- [186] W. Verkerke and D. Kirkby, *The roofit toolkit for data modeling*, <http://roofit.sourceforge.net/> (2020)
- [187] F. James and M. Roos, *MINUIT: a system for function minimization and analysis of the parameter errors and corrections*, Comput. Phys. Commun. **10**, 343 (1975)
- [188] ET Enterprises, *9821B series data sheet*, [http://et-enterprises.com/images/data\\_sheets/9822B.pdf](http://et-enterprises.com/images/data_sheets/9822B.pdf) (2020)
- [189] L. Prade, *Precise Determination of Quenching Factors and of the Energy Response Function of Liquid Scintillators for Future Neutrino-Astroparticle Physics Experiments*, Diploma Thesis, Technische Universität München (2013)

- [190] M. J. Berger et al., NIST, *Stopping-Power and Range Tables for Electrons, Protons, and Helium Ions*, <https://www.nist.gov/pml/stopping-power-range-tables-electrons-protons-and-helium-ions> (2014)

# Danksagung

Herrn Prof. Dr. Lothar Oberauer gilt mein besonderer Dank für das sehr interessante Thema im Rahmen des JUNO Experiments sowie für die großzügige Unterstützung meiner Arbeit mit Reise- und Sachmitteln. Ich danke meinem Doktorvater für die ständige Bereitschaft zur Diskussion experimenteller Ergebnisse, seinen Rat und das mir entgegengebrachte große Vertrauen.

Meinem Mentor Prof. Dr. Franz Freiherr von Feilitzsch danke ich für die wertvolle Unterstützung meiner Arbeit. Unsere Gespräche über Astroteilchenphysik und Wissenschaftspolitik waren stets eine Bereicherung für mich.

Herrn Prof. Dr. Michael Wurm (JGU Mainz) danke ich für die gute Zusammenarbeit bei der Realisierung des OSIRIS Detektors. In vielen gemeinsamen Besprechungen in München und Mainz habe ich viel gelernt.

Bei Prof. Dr. Achim Stahl (RWTH Aachen) bedanke ich mich für die freundliche Aufnahme in die DFG Forschergruppe JUNO sowie für das große Interesse an meiner Arbeit. Durch die gemeinsame Vorbereitung von Förderanträgen habe ich einen Einblick in die Welt der Wissenschaftsförderung erhalten.

Herrn Prof. Dr. Tobias Lachenmaier (Eberhard Karls Universität Tübingen) danke ich für die Unterstützung meiner Arbeit, insbesondere für die Hilfe bei den PMT-Bestrahlungstests mit dem Lasersensor.

Frau Prof. Dr. Caren Hagner (Universität Hamburg) möchte für die vielen Tipps zum Bau von Gasdetektoren danken. Darüber hinaus hat mich ihr positives Feedback schon in den frühen Phasen meiner Doktorarbeit sehr motiviert.

Für die Unterstützung im gesamten Arbeitszeitrum danke ich Herrn Dr. Giocchino Ranucci (INFN Milano). Die Diskussionen mit ihm und das Feedback zu meinen Resultaten haben meine Arbeit stets bereichert. Die Beschaffung von Szintillatorproben aus verschiedenen Experimenten sowie sein Einsatz für die Einwerbung von Strahlzeit am Beschleunigerlabor des INFN in Legnaro unterstützen meine Forschung noch über die Zeit der Doktorarbeit hinaus.

Bei Herrn Dr. Walter Potzel bedanke ich mich für die unermüdliche Bereitschaft zu fachlichen Diskussionen, sowie für die kontinuierliche Hilfe bei meiner Arbeit. Er hatte während meiner Zeit am E15 immer ein offenes Ohr für mich. In schwierigen Zeiten hat mir so manches aufmunternde Wort sehr geholfen.

Herrn Eng. Paolo Lombardi (INFN Milano) danke ich die großartige Zusammenarbeit sowohl bei der Durchführung der Daya Bay Tests als auch in der Flüssigszintillatorarbeitsgruppe. Ebenso haben mir die Gespräche über die Messung von Fluoreszenzspektren sehr geholfen.

Herrn M.Sc. Wilfried Depnering, Eng. Michele Montuschi, Augusto Brigatti, Sergio Parmeggiano sowie dem ganzen Pilot Plant Team danke ich für die interessante Zeit in Daya Bay. Hervorzuheben ist die stets gute und kollegiale Stimmung in zahllosen arbeitsreichen Tag- und Nachtschichten.

Für die gemeinsam durchgeführten Bestrahlungstests mit dem IR Lasersensor in Tübingen sowie für unsere Diskussionen über Elektronik und die Tücken von LabView und Root danke ich Herrn M.Sc. Tobias Sterr.

Ein ganz besonderer Dank gilt meinem Kollegen M.Sc. Raphael Stock, mit dem ich gerade im letzten Jahr intensiv zusammen gearbeitet habe. In kurzer Zeit haben wir, zum Teil mit Arbeit an Wochenenden und bis spät in die Nacht, ein Experiment zur Messung des Zeitspektrums der Photonenemission von Szintillatoren entwickelt. Während zweier Strahlzeiten in Garching haben wir das Beschleunigerlabor oft tagelang nicht verlassen. Der Kontrollraum wurde zu unserem temporären Zuhause. Diese produktiven Wochen werden mir immer in bester Erinnerung bleiben.

Herzlich danke ich den Herren Dr. Ludwig Beck, Walter Carli, Peter Ring und Michael Wiesheu für die zum Teil ehrenamtliche Tätigkeit und die vielen spontanen Überstunden am MLL während unserer Strahlzeiten.

Für die Unterstützung bei der Entwicklung des Radonmonitors danke ich M.Sc. Philipp Landgraf und B.Sc. Alexander Gardanow.

Bei Herrn B.Sc. Mathias Walter bedanke ich mich für die gute Zusammenarbeit bei der Realisierung des Teststandes für hydrostatische Drucksensoren.

Dr. Björn Wonsak, Dr. Kai Loo, M.Sc. Heike Enzmann, M.Sc. Michaela Schever, Dr. Christoph Genster, M.Sc. Paul Hackspacher, M.Sc. Tobias Heinz sowie allen Post-docs und Doktoranden der DFG Forschergruppe JUNO ein herzliches Dankeschön für die vielen schönen Stunden auf Dienstreisen.

Dem Werkstatt-Team des Lehrstuhls um Harald Hess danke ich für das Umsetzen meiner technischen Zeichnungen in die realen mechanischen Komponenten meiner experimentellen Aufbauten. Selbst unter Zeitdruck gelang immer eine saubere Ausführung aller Bauteile.

Meinem Bruder Andreas Steiger danke ich besonders für die Unterstützung meiner Arbeit im Chemielabor bei der Herstellung von Szintillatorproben. Vielen Dank auch dafür, dass er uns während der Strahlzeiten in zahlreichen Nachtschichten unterstützte. Er hat sich dabei nie gescheut auch beim Aufbau und Betrieb unserer physikalischen Experimente zu helfen und Hand an die Elektronik zu legen. Unsere gemeinsam durchgeführten mitternächtlichen Reparaturen des Beam-Bunchers und der Ionenquelle am Tandembeschleuniger werde ich nie vergessen.

Ganz besonders danke ich meinen Eltern. Ohne ihre Unterstützung wäre mein Studium und damit diese Arbeit nicht möglich gewesen. Sie haben stets an mich geglaubt und mir auf dem langen Weg des Studiums den dringend benötigten Rückhalt gegeben.